

# Ultra low cycle fatigue of welded steel joints under multiaxial loading

THÈSE N° 7501 (2017)

PRÉSENTÉE LE 20 MARS 2017

À LA FACULTÉ DE L'ENVIRONNEMENT NATUREL, ARCHITECTURAL ET CONSTRUIT  
LABORATOIRE DES STRUCTURES MÉTALLIQUES RÉSILIENTES  
PROGRAMME DOCTORAL EN GÉNIE CIVIL ET ENVIRONNEMENT

ÉCOLE POLYTECHNIQUE FÉDÉRALE DE LAUSANNE

POUR L'OBTENTION DU GRADE DE DOCTEUR ÈS SCIENCES

PAR

Albano António DE ABREU E PRESA DE CASTRO E SOUSA

acceptée sur proposition du jury:

Prof. J.-F. Molinari, président du jury  
Prof. A. Nussbaumer, directeur de thèse  
Prof. A. A. Benzerga, rapporteur  
Prof. L. Gardner, rapporteur  
Prof. A. Muttoni, rapporteur



ÉCOLE POLYTECHNIQUE  
FÉDÉRALE DE LAUSANNE

Suisse  
2017



For a successful technology,  
reality must take precedence over public relations,  
for nature cannot be fooled.  
— Richard P. Feynman





# Acknowledgments

It is unlikely that any worthy enterprise can be materialized without having the proper context and a confluence of auspicious factors. The development of this thesis is no different and I am truly grateful to the people that played a role in it, however contiguous, so much so that it hardly seems fitting to honor them with the parsimony that these pages demand. For that I apologize to them in advance.

First and foremost, I am deeply grateful to my supervisor Prof. Alain Nussbaumer for the opportunity, the guidance, the encouragement and the support that he gave me throughout these 4 years. It was a pleasure indeed.

The work conducted for this thesis was supported financially by the Swiss National Foundation (SNF) as part of a DACH collaboration project, grant number 200021L-141315, between École Polytechnique Fédérale de Lausanne (EPFL) in Switzerland, Graz University of Technology (TUG) in Austria and Karlsruhe Institute of Technology (KIT) in Germany. I would like to thank the SNF and the project partners for their input in the development of this work: Prof. Harald Unterweger, Prof. Andreas Taras, Clemens Tappauf, Prof. Thomas Ummenhofer, Prof. Peter Knödel, Katharina Rohr and Sven Nagel.

I am also very grateful to the members of my jury, Prof. Jean-François Molinari (President), Prof. A. Amine Benzerga, Prof. Aurelio Muttoni and Prof. Leroy Gardner, for their most valued comments and suggestions. With respect to Prof. Benzerga I cannot not mention a story that took place in October 2014 when I went to visit him for a week at Texas A&M. Due to a mix-up in scheduling we would be unable to meet as he wouldn't be in College Station during the period I was supposed to be there. He graciously changed his travel plans only to have a short meeting with me. That meeting would prove to be quite consequential to the work I conducted with micromechanical models for ductile fracture. I will always remember this.

During the last year of my Ph.D. I also had the pleasure of meeting Prof. Dimitrios Lignos with whom I had some memorable and stimulating discussions and who I would also like to thank for the financial support from the Resilient Steel Structures Laboratory (RESSLab) during the last stretch of the thesis.

## Acknowledgments

---

The work presented in this document involved a large number of different experiments that would not have been possible without the help of the superb teams in EPFL laboratories. Starting with the structural engineering group, I would like to thank Sylvain Demierre, Gérald Rouge, Frederique Dubugnon, Gilles Guignet, Armin Krkić, Patrice Gallay, François Perrin and Serge Despont. Here I would like to acknowledge in particular the contribution of Patrice Gallay in the development of the test-setup for the cyclic loading of single notched round bars. In mechanical engineering, I would like to thank Prof. John Botsis of the Laboratory of Applied Mechanics and Reliability Analysis (LMAF) that allowed the use of LMAF's test facilities to conduct tension-torsion experiments on double notched tubular specimens. Here, I would like to thank in particular the help of Robin Amacher in carrying out those tests. In material science, I would like to thank Dr. Emmanuelle Boehm-Courjault (of the Computational Materials Laboratory headed by Prof. Michel Rappaz - LSMX), Cyril Dénéréaz (of the Laboratory of Mechanical Metallurgy headed by Prof. Andreas Mortensen-LMM) and Raphaël Charvet (LMM) for their guidance in the preparation of specimens for metallographic analyses. For preparation and the analyses themselves I would like to acknowledge and thank the help of Sarah Burnand, Santosh Yadav and Rajesh Kandel, particularly in the rather laborious and monotonous task of CAD demarcations. With respect to Scanning Electron Microscopy (SEM) of fracture surfaces I would like to thank the help of Grégoire Baroz from the Interdisciplinary Center for Electron Microscopy (CIME). For the tube-to-plate tests, the base plates and welding work were offered pro-bono by Zwahlen & Mayr S.A., a significant donation that is both greatly appreciated and highly regarded for its contribution to steel research. Here, I would like to thank Nadir Moussaoui for developing the welding procedure specification and João Oliveira for managing the execution.

I would also like to thank my fellow colleagues at Texas A&M Nithin Thomas and Mohammad Torki for discussions on micromechanical models in ductile fracture and guidance in their implementation via UMATs in Abaqus.

During my time in the Steel Structures Laboratory I also had the opportunity to meet fellow researchers with whom I shared a number of valuable discussions. I would like to thank particularly Claudio Baptista, Jagoda Cupać, Martin Garcia, Gary Prinz, Raphaël Thiebaud, Farshid Zamiri and Luca d'Angelo not only for their input but also for making life in lab all the more enjoyable and memorable. I would also like to thank João Simões of the Structural Concrete Laboratory (IBETON) for discussions on plasticity theory and softening behavior.

Lastly, to close on a broader context, a special acknowledgment is due to my Mother and my Brother. Without their support and encouragement I would not have been able to write the very words you are now reading.

*Lausanne, February 22nd, 2017*

A.C.S.

# Abstract

Extreme loading scenarios such as earthquakes, exceptional wind gusts or tides are characterized by very high amplitude and multidirectional cyclic loads applied to a structure. Ultra Low Cycle Fatigue (ULCF) arises in such cases and can be summarily defined as the deterioration of material properties due to repetitive loading at large amplitudes. In the case of welded steel joints, failure is generally reached in just a few number of cycles – typically less than ten or twenty.

The importance of a comprehensive understanding of this phenomenon lies in the balance between safety or allowable damages and an economical design. For rare events with very high demands there is a need to use the material's properties to its fullest in order to obtain the most rational design. A common example of this is the use of material ductility to absorb the energy of earthquake loading in design standards. The goal of this thesis is to provide the engineer with both the understanding of the physical phenomenon involved in ULCF and the tools to design a structural component with flexibility and sufficient accuracy.

Failure of metals in the presence of high plastic strains is commonly observed to be of ductile nature. Micromechanical models based on homogenization theory are typically used to predict this type of fracture, because they attempt to capture the fundamental mechanisms involved in void growth to coalescence. In this thesis, two micromechanical models (Gologanu-Leblond-Devaux for void growth and Torki-Benzerga-Leblond for void coalescence), developed for monotonic loading, are studied in the context of large amplitude cyclic loadings and their predictions are compared with experimental results obtained on small scale specimens for a high strength steel – S770QL. Component scale specimens, namely welded tube to plate specimens of the same steel type, are tested in bending and torsion. Digital image correlation measurements of weld toe strains for over 60 tests are presented and used to recommend a design procedure using local strains in finite element modeling, with a Manson-Coffin type of approach.

Key words: Ultra low cycle fatigue, High-strength steel, Multiaxial loading, Welded joints, Void growth to coalescence, Gurson, Gologanu-Leblond-Devaux, Manson-Coffin



# Résumé

Les scénarios de sollicitations extrêmes tels que tremblements de terre, rafales exceptionnelles ou marées se caractérisent par des chargements cycliques multidirectionnels de très grande amplitude appliqués à une structure. L'endommagement à très faible nombre de cycles (ULCF) apparaît alors dans de tels cas et peut être défini sommairement comme la détérioration des propriétés du matériau due à des déformations répétées de grandes amplitudes. Dans le cas des joints soudés en acier, la rupture est généralement atteinte en quelques cycles - moins de dix ou vingt.

L'importance d'une compréhension globale de ce phénomène réside dans l'adéquation entre la sécurité ou les dommages admissibles et une conception économique. Pour les événements rares avec des sollicitations très élevées, il est nécessaire d'utiliser au maximum les propriétés du matériau afin d'obtenir la conception la plus rationnelle. Le but de cette thèse est de fournir à l'ingénieur à la fois une compréhension du phénomène physique à l'oeuvre dans l'ULCF, et des outils ayant une validité générale pour dimensionner un composant structural, tout en garantissant une précision suffisante.

La rupture de métaux en présence de déformations plastiques élevées est couramment observée comme étant de nature ductile. Des modèles micromécaniques basés sur la théorie de l'homogénéisation sont souvent utilisés pour prédire ce type de rupture car ces descriptions capturent les mécanismes fondamentaux impliqués dans la croissance des vides jusqu'à leur coalescence. Dans cette thèse, deux modèles micromécaniques (Gologanu-Leblond-Devaux et Torki-Benzerga-Leblond), développés pour des chargements monotones, sont étudiés dans le contexte de charges cycliques de grande amplitude et leurs estimations sont comparées avec les résultats expérimentaux obtenus sur des éprouvettes à petite échelle pour un acier à haute résistance - S770QL. Des éprouvettes à l'échelle d'un composant structural, soit des tubes du même acier soudés à une plaque, sont testées en flexion et en torsion. Les mesures de corrélation d'images numériques des déformations au pied de la soudure pour plus de 60 essais sont présentées et utilisées pour recommander une procédure de dimensionnement utilisant des déformations locales obtenues dans un modèle par éléments finis. Les déformations locales sont utilisées dans une approche du type Manson-Coffin.

## Acknowledgments

---

Mots clefs : Fatigue à très faible nombre de cycles, Acier à haute résistance, Chargements multiaxiaux, Joints soudés, Croissance et coalescence de vides, Gurson, Gologanu-Leblond-Devaux, Manson-Coffin

# Contents

<b>Acknowledgments</b>	<b>i</b>
<b>Abstract (English/Français)</b>	<b>iii</b>
<b>List of figures</b>	<b>ix</b>
<b>List of tables</b>	<b>xiii</b>
<b>1 Introduction</b>	<b>1</b>
1.1 Background and motivation . . . . .	2
1.2 Scope, objectives and approach to the problem . . . . .	4
1.3 Structure of the thesis . . . . .	5
1.4 Notation and abbreviations . . . . .	7
<b>2 Background and state of the art</b>	<b>9</b>
2.1 Finite strain plasticity . . . . .	9
2.2 Digital image correlation . . . . .	17
2.3 Ductile fracture in metals . . . . .	19
2.3.1 Experimental observations . . . . .	19
2.3.2 Modeling approaches . . . . .	22
2.4 Ultra low cycle fatigue . . . . .	28
2.5 Summary . . . . .	33
<b>3 Material characterization and behavior</b>	<b>35</b>
3.1 Characterization of basic material properties . . . . .	35
3.2 Inclusion content . . . . .	38
3.3 Single notched round bar specimens . . . . .	43
3.3.1 Monotonic loading . . . . .	44
3.3.2 Large amplitude cyclic loading - ULCF . . . . .	45
3.4 Double notched specimens . . . . .	50
3.4.1 Monotonic loading . . . . .	55

## Contents

---

3.4.2	Large amplitude cyclic loading - ULCF . . . . .	61
3.5	Conclusions . . . . .	63
<b>4</b>	<b>Welded component behavior</b>	<b>65</b>
4.1	Test Setup . . . . .	66
4.2	Digital image correlation . . . . .	70
4.3	Loading protocols . . . . .	73
4.4	Results and discussion . . . . .	76
4.5	Conclusion . . . . .	86
<b>5</b>	<b>A cyclic micromechanical material model</b>	<b>89</b>
5.1	An extension of the Gologanu-Leblond-Devaux (GLD) model to nonlinear kinematic hardening and its implementation . . . . .	90
5.2	Validation and additional comments . . . . .	99
5.3	Analysis of small scale tests . . . . .	105
5.3.1	Single notched bar specimens . . . . .	105
5.3.2	Double notched tubular specimens . . . . .	113
5.4	Conclusion . . . . .	121
<b>6</b>	<b>Design approach for welded structural components</b>	<b>123</b>
6.1	Description of the modeling approach . . . . .	123
6.2	Results and discussion . . . . .	127
6.3	Conclusion . . . . .	138
<b>7</b>	<b>Conclusion and future work</b>	<b>141</b>
<b>A</b>	<b>UMAT</b>	<b>147</b>
<b>B</b>	<b>Summary of data from metallographic analyses</b>	<b>161</b>
<b>C</b>	<b>Summary of data from single notched bar tests</b>	<b>167</b>
<b>D</b>	<b>Summary of data from double notched tube tests</b>	<b>173</b>
<b>E</b>	<b>Summary of data from tube to plate tests</b>	<b>185</b>
	<b>Bibliography</b>	<b>201</b>
	<b>Glossary</b>	<b>203</b>
	<b>Acronyms</b>	<b>213</b>
	<b>Curriculum Vitae</b>	<b>217</b>



# List of Figures

2.1	Mapping between configurations . . . . .	10
2.2	$\pi$ -plane representation of hardening rules . . . . .	15
2.3	FEM Non-linear isotropic and kinematic hardening in Abaqus and prescribed stress-strain curve in simple shear . . . . .	17
2.4	DIC methods . . . . .	18
2.5	Digital image correlation definitions . . . . .	19
2.6	Loading of a single notched bar - from [Benzerga and Leblond, 2010] . . . . .	20
2.7	Nucleation, void growth and coalescence . . . . .	21
2.8	Typical ductile fracture surfaces . . . . .	22
2.9	Fracture surfaces of Compact Tension (CT) specimens . . . . .	22
2.10	Schematic of porous body . . . . .	23
2.11	Spherical RVE with a spherical internal void . . . . .	24
2.12	Spheroidal void shapes . . . . .	25
2.13	Material ( $\mathbf{e}_i$ ) and void orientations ( $\mathbf{n}_i$ ) with respect to the undeformed reference frame ( $\mathbf{l}_i$ ) . . . . .	25
2.14	Cylindrical RVE for TBL coalescence criterion . . . . .	27
2.15	Illustration of Manson-Coffin type approaches in a hot-rolled S355J2H steel - from [Nip et al., 2010a] . . . . .	29
2.16	FEM modeling of weld fracture under ULCF of column to base plate connection - adapted from the work of [Myers et al., 2009] . . . . .	31
3.1	Micrographs of S770QL's microstructure . . . . .	36
3.2	True stress vs true strain curve for uniaxial tests and fitted Power Law . . . . .	37
3.4	Specimen designation for metallographic analyses . . . . .	39
3.5	Steps in metallographic analyses of inclusions . . . . .	40
3.6	Circular diameters and GEV distribution fitting for BM_LT_1 . . . . .	42
3.7	Specimen designation for single notched specimens . . . . .	43
3.8	Geometry of single notched specimen . . . . .	44
3.9	Example of monotonic force-displacement curves for single notched specimens . . . . .	45

## List of Figures

---

3.10	Schematic of cyclic test-setup for single notched specimens . . . . .	46
3.11	Example of hysteresis curves for single notched specimens . . . . .	47
3.12	Hysteresis curve for specimen <i>T2CA1_7_1</i> . . . . .	48
3.13	Single notched specimen fracture surfaces . . . . .	49
3.14	Scanning Electron Microscope (SEM) micrographs of typical fracture surfaces at the center of single notched specimens for high-strength structural steel S770QL under monotonic and large amplitude cyclic loading . . . . .	50
3.15	Nominal notch geometry for double notched tube - cross-section cut (dimen- sions in mm) . . . . .	51
3.16	Specimen designation for single notched specimens . . . . .	52
3.17	Speckle pattern and gauge sections in DIC measurements for double notch tube specimens - front view . . . . .	53
3.18	Schematic of a transverse cut of the tube and definition of rotation $\theta_{sec}^{DN}$ . . .	53
3.19	Example of torque angle measurement with DIC. ' <i>dTheta</i> ' corresponds to $\theta_{sec}^{DN}$ .	53
3.20	Double notched specimen monotonic paths . . . . .	55
3.21	Comparison of tests results to a similar type of steel . . . . .	56
3.22	Slant fracture in monotonic pure tension (path 1) double notched specimens .	57
3.23	Fracture surface in monotonic load path 3 in double notched specimens . . .	57
3.24	Fractography of a double notched specimen loaded in monotonic pure tension - <i>DN7M1_1</i> . . . . .	58
3.25	SEM micrographs of fracture surface for specimen <i>DN7M3_1</i> . . . . .	58
3.26	SEM micrographs of fracture surface for specimen <i>DN7M2_3</i> . . . . .	59
3.27	Fracture surface in monotonic pure torsion (path 2) double notched specimens	59
3.28	Fracture surface in monotonic load path 4 in double notched specimens . . .	60
3.29	Double notched specimen cyclic paths . . . . .	61
3.30	Comparison of hysteresis curves in double notch specimens for path 1 . . . .	62
3.31	Fracture surface in cyclic for load path 3 in double notched specimens . . . .	62
4.1	Tube to plate test setup - side view . . . . .	66
4.2	Tube to plate test setup - front view . . . . .	67
4.3	Tube to plate test setup - front view cut just before tube inclinometer . . . .	67
4.4	Detail of gap in the bending actuator's head . . . . .	68
4.5	Schematic of the lever arm around the torsion actuator . . . . .	69
4.6	Detail of weld region . . . . .	69
4.7	Composite of micrographs around the weld toe - Nital 2% . . . . .	70
4.8	Definition of effective rotation $\theta$ . . . . .	71
4.9	Deformed view of the test setup . . . . .	71

4.10 Precision in $\varepsilon_{yy}$ DIC measurements for specimen B7CA1_3 - pictures at rest vs reference picture . . . . .	73
4.11 Specimen designation for welded tube to plate tests . . . . .	74
4.12 Constant amplitude load paths . . . . .	75
4.13 Variable amplitude load protocols . . . . .	76
4.14 Impact of gap in bending jack head in the hysteresis of specimen B7CA1_3 .	77
4.15 First visible crack in specimen B7CA1_3 at picture number 520 - 5 <sup>th</sup> cycle .	77
4.16 Hysteresis curve for specimen B7CA1_3 . . . . .	78
4.17 Crack propagation on specimen B7CA2_2 . . . . .	78
4.18 Initiation ratios for tube to plate tests . . . . .	79
4.19 $\varepsilon_{yy}$ DIC measurements for specimen B7CA1_3 at the peak of the first load excursion - picture number 50 . . . . .	80
4.20 DIC measurements at section through point of maximum $\varepsilon_{yy}$ for specimen B7CA1_3 at the peak of the first load excursion - picture number 50 . . . . .	80
4.21 Influence of geometry on strains at weld toe for specimen C7CA1_2 . . . . .	81
4.22 DIC point measurement . . . . .	83
4.23 Equivalent strain - life curve for tube to plate CA tests - Proportional . . . .	84
4.24 Equivalent strain-life curve for tube to plate tests - Non-proportional . . . .	85
4.25 Damage for tube to plate tests . . . . .	86
5.1 Structure of the <i>gld</i> UMAT . . . . .	98
5.2 Element(C3D8R) and loading cases used in validation of <i>gld</i> Umat in Abaqus	100
5.3 Comparison between hardening directions . . . . .	101
5.4 Comparison between GLD Umat and Abaqus's implementation of the Gurson model . . . . .	102
5.5 Comparison between for tension load tranverse to prolate void . . . . .	103
5.6 Comparison between intended material response and different objective stress rates in kinematic hardening for simple shear . . . . .	104
5.7 FEM model and a typical porosity contour map for a single notched bar test (T2CA1_7_1 at the 17th half cycle) . . . . .	106
5.8 Simple notched tensile tests - experimental results vs modeling . . . . .	108
5.9 Example of comparison of hysteresis curves between tests and the GLD UMAT - $\varrho = 1.125$ . . . . .	109
5.10 Comparison of material model response at the integration point of the element at the center of the notch as a function of $\varrho$ for specimen T2CA1_7_1 . . . .	110
5.11 Nodal results through cross-section for specimen T2CA1_7_1 with $\varrho = 1.125$	111
5.12 Predicted number of half cycle versus experimental results . . . . .	112
5.13 FEM model for double notched tubes . . . . .	114

## List of Figures

---

5.14 Typical FEM results for a double notched tube simulation - <i>DN7M3_1</i> at load step corresponding to fracture in experiments . . . . .	114
5.15 Double notched tube tests - experimental results vs modeling . . . . .	117
5.16 Load history at the integration point of element of highest $\phi^{TBL}$ for specimen <i>DN7M1_1</i> . . . . .	118
5.17 Load history at the integration point of element of highest $\phi^{TBL}$ for specimen <i>DN7M3_1</i> . . . . .	119
5.18 Load history at the integration point of element of highest $\phi^{TBL}$ for specimen <i>DN7M4_3</i> . . . . .	120
6.1 FEM model of tube to plate test - general view, all elements C3D8R . . . . .	125
6.2 FEM model of tube to plate test - cut and boundary conditions . . . . .	126
6.3 FEM submodel of weld toe region . . . . .	127
6.4 FEM comparison of hysteresis curves for specimen <i>B7CA1_3</i> . . . . .	128
6.5 Comparison of DIC measurements and FEM results - 1 . . . . .	128
6.6 Comparison of DIC measurements and FEM results - 2 . . . . .	129
6.7 Comparison of DIC measurements and FEM results - 3 . . . . .	130
6.8 FEM comparison of hysteresis curves for specimen <i>A7CA1_3</i> . . . . .	130
6.9 Comparison of DIC measurements and FEM results - CA torsion . . . . .	131
6.10 Manson-Coffin curve for proportional CA tests with FEM results . . . . .	132
6.11 Illustration of the bending stiffness issue through loading history . . . . .	133
6.12 Comparison of loading history and FEM results . . . . .	133
6.13 FEM comparison of hysteresis curves for specimen <i>A7VA1_2</i> . . . . .	134
6.14 Comparison of DIC measurements and FEM results - VA torsion . . . . .	134
6.15 Stress - life curve for longitudinal attachment detail in high cycle fatigue . . .	136
6.16 Damage for longitudinal attachment . . . . .	136
6.17 Manson-Coffin curve for constant amplitude proportional tests and design value	137

# List of Tables

3.1	Summary table for smooth round bar tension tests and power law parameters	36
3.2	Chemical Composition of S770QL . . . . .	42
3.3	Summary of inclusion statistics . . . . .	42
3.4	Single notch specimens nominal geometry . . . . .	43
3.5	Double notched - path ratios . . . . .	52
4.1	Constant amplitude test matrix . . . . .	74
4.2	Variable amplitude test matrix . . . . .	75
5.1	Designation for internal variables used in the validation procedure with KB UMAT . . . . .	102
5.2	Data summary for monotonic tests . . . . .	107
5.3	Data summary for cyclic tests . . . . .	112
6.1	Summary of CA FEM parameters and results . . . . .	131
6.2	Design values of M-C curve for local approach for components with thicknesses below 10mm under proportional loading histories for S770QL . . . . .	137



# 1 Introduction

Many extreme loading scenarios such as earthquakes, exceptional wind gusts or tides are characterized by very high amplitude and multi-directional cyclic loads applied to a structure. Ultra Low Cycle Fatigue (ULCF) arises in such cases and can be summarily defined as the deterioration of material properties due to repetitive loading at very high strain amplitudes. In these situations, failure is typically reached in just a few number of cycles – typically less than ten or twenty.

The importance of a comprehensive understanding of this phenomenon lies in the delicate balance to be made between safety or allowable damages and an economical design. For rare events with very high demands, there is a need to use material properties to their fullest in order to obtain the most rational outcome. A common example of this are specifications in design standards regarding material ductility to absorb the energy of earthquake loading.

This work aims to make a contribution to this field by both providing insights into the physical mechanisms that govern ULCF (which can help tailor material properties to specific applications) and also practical recommendations to address the most immediate need for design criteria in welded high-strength steel joints.

One will begin this introductory chapter by discussing more specifically the background and motivations behind this study. Subsequently, a statement of objectives and scope of the research will be given as well as the outline of how the problem was approached. Finally, a detailed overview of how the thesis is structured is presented.

### 1.1 Background and motivation

The research presented in this study is part of a DACH collaboration project, grant number 200021L-141315, between École Polytechnique Fédérale de Lausanne (EPFL) in Switzerland, Graz University of Technology (TUG) in Austria and Karlsruhe Institute of Technology (KIT) in Germany.

The overall aim of the project was to understand ULCF behavior of welded connections under extreme multi-axial loading conditions on both conventional and high-strength steels. Project partners had different tasks that were roughly divided as follows: 1 - study deformation time-histories of typical welded connections in situations susceptible to ULCF (the demand side - TUG); 2 - provide a failure criterion to ULCF in welded joints under multi-axial loading for both these materials (the resistance side - KIT and EPFL). EPFL focused on the characterization of material resistance to ULCF in high-strength steels.

There are a number of examples that can be given to illustrate the need both for a fundamental understanding and for appropriate design procedures in ULCF but none, in the author's opinion, as clear as the case of thin walled shell structures. An economic design of these systems hinges on the judicious use of wall thicknesses throughout the structure, where a even slight variation in thickness selection can bring about important financial costs. Examples of this type of structure can be found in pressure vessels, pipelines and liquid storage tanks. If one looks into current codes of practice relevant for these structures, one can see that the design criteria provided therein are often conservative and/or insufficiently justified.

Such is the case for Eurocode 3 Part 1-6 [European Committee for Standardization, 2007], pertaining to the design of shell structures, where design to cyclic loading that is liable to happen for more than three cycles during the lifetime of the structure can follow either of the following two criteria: 1- the stress amplitudes cannot exceed two times the yield strength of the material; 2 - the accumulated equivalent plastic strain at any point in the structure (not closer to a notch than the thickest adjacent plate) should be limited to twenty-five times the elastic strain of the material. The first criterion's purpose is to limit the accumulation of plastic strain and is thus conservative. The second, besides bypassing the special care to be given in the presence of stress / strain risers such as welds, lacks, to the author's knowledge, a justification in literature.

Another paradigmatic case in ULCF is the seismic loading provisions for the design of unanchored liquid storage tanks. The problem with thin shelled unanchored tanks is that, due to their flexibility, during earthquake loading there is the possibility of certain regions of the tank wall to uplift, subjecting the base-plate to very high plastic deformations. The most up-



to-date standards ([European Committee for Standardization, 2006b] and [NZSEE, 2009]) try to address this issue by imposing a limit on the maximum allowable plastic strain of 5% in the cross-section over a postulated plastic hinge length of two times the thickness of the base plate. Again, a big issue in this provision is that the limit of 5% strain, to the author's knowledge, lacks justification in literature. Furthermore, this provision does not inform the designer over how many number of cycles this limit should be considered nor the type of steel it should be limited to. Experimental studies into this type of connection in mild-steel have shown that these design requirements are overly conservative [Cortes et al., 2011] thus underscoring a need for a more robust approach to ULCF.

Codes of practice are, however, inertial in the adoption of new ideas and thus those provisions might not necessarily reflect the current knowledge on the subject. There is, nonetheless, a need to deepen one's understanding of ULCF if one looks into the most up-to-date literature. Without getting into much detail on what will be covered more extensively in Chapter 2, the current state of the art on ULCF in civil engineering structures revolves around two main approaches.

The first approach, more phenomenological, follows some variation of the well known Manson-Coffin (M-C) relation for Low-Cycle fatigue. Most of the resistance curves rooted in M-C formulae are based on experimental testing of smoothly polished small scale specimens (typically bars of 5 to 8 mm diameter) of base material. Data concerning tests carried out on welded parts in the ULCF regime are scarce, particularly when it comes to multiaxial loadings. The validity of such an approach (or at least its extent) is therefore unknown and further investigation on the subject is warranted if one is to apply it to welded structural components.

The second approach, more physics based, follows the attempts of [Kanvinde and Deierlein, 2004] to bring micro-mechanically informed failure criteria developed for ductile fracture into the ULCF regime. The main idea of this approach is to reduce the resistance for monotonic loading by an empirical function that is representative of material degradation to cyclic loading. The parameters of this empirical function are generally fit to experimental data of tests on small scale specimens. Building upon this work, quite recently and after this research project started, a model was proposed to extend [Kanvinde and Deierlein, 2004]'s work to generalized stress states [Smith et al., 2014], thereby tackling the issue of multiaxiality in the ULCF regime. This work, however, similarly to the M-C test programs, is based on small scale tests of base material and, as will be seen in Chapter 4, tests conducted on welded structural components can behave in ways that are not captured fully with a small scale experimental program.

### 1.2 Scope, objectives and approach to the problem

With the context given in the previous section, one can now set the scope of this study. The focus of the work presented in this document will be to address the issue of ultra low cycle fatigue resistance in welded high-strength steel joints under multiaxial loading.

The statement of objectives is given as follows,

1. Understand the behavior of high-strength steel under ULCF
2. Provide a model capable of estimating failure in welded high-strength steel joints under multi-axial ULCF
3. Develop an appropriate framework for the structural verification of welded high-strength steel joints under multi-axial ULCF

The first objective is quite broad and what it covers needs to be discussed more specifically. Phenomenological or empirical formulations are never the ideal bedrock in which to base design rules. The most obvious reason is their limited range of application. Understanding the true mechanisms behind the material's response to ULCF can allow the engineer to make better decisions with respect to either the choice of materials or design rules, and thus it is important to focus at least some part of the effort on this topic. This objective will be addressed in this thesis by performing small scale specimen testing taken to be representative of material behavior and then, leveraging state of the art micromechanical solutions to ductile fracture, try to explain some part of the phenomenological character of ULCF of the two approaches mentioned in the previous section.

To arrive at a model capable of estimating failure in steel joints under multi-axial loading a large experimental campaign on welded tube-to-plate was conducted so as to provide it with the necessary basis. Ideally this model would build upon the work conducted for the first objective. As will be shown in the detailed discussion of the tests conducted on the welded component level, experimental observations led to the conclusion that a significant part of a component's life is spent in the propagation of a crack. Considering that material behavior in ULCF is already poorly understood<sup>1</sup> under fairly uniform strain fields, that problem is only aggravated in presence of very high strain gradients such as a sharp crack tip. For practical reasons a more phenomenological approach is thus employed to take into account the total life of the joint under ULCF (initiation and propagation).

---

<sup>1</sup>at length scales relevant for micromechanical models of ductile fracture and how they are able to describe the differences observed in fracture patterns under monotonic and ULCF

The third and final objective is to take the knowledge acquired in the welded component test campaign and the model for multiaxial ULCF resistance suggested in objective number two, and provide a methodology that can be used for design. This will mainly be achieved by reproducing experimental results of the welded component tests by appropriate finite element models. The specifics involved in building those finite element models will become the very definition of that methodology.

## 1.3 Structure of the thesis

### Chapter 2 - Background and state of the art

The purpose of this chapter is to provide the necessary background information to understand both the details involved in the model developed in Chapter 5 and in Digital Image Correlation (DIC) measurements that are essential to the interpretation of results in Chapter 4. A brief review of the state of the art on ductile fracture and ultra low cycle fatigue is also given.

### Chapter 3 - Material characterization and behavior

This chapter presents the methods and results of an experimental program conducted on small-scale specimens. The focus of this chapter is to characterize key micromechanical variables as well as define the small scale experiments that will serve as a proxy for material behavior. The experiments presented in this chapter attempt not only to describe failure under uniaxial loading with round notched bar tests, but also in multiaxial loading with double notched tubes under tension and torsion.

### Chapter 4 - Welded component behavior

In this chapter the methods and results of an experimental program to study the behavior of welded structural components under multiaxial ULCF are presented. These tests consist of a welded tube-to-plate configuration loaded in bending and in torsion. One of the most innovative aspects of this test program is the use of DIC measurements to assess large strain time-histories at the weld toe of a component in a very localized way . It will be shown that these measurements correlate well with a M-C type law thereby providing a suitable model for ULCF.

## **Chapter 1. Introduction**

---

### **Chapter 5 - A cyclic micromechanical material model**

This chapter is dedicated to the adaptation of state of the art micromechanical models in ductile fracture to the domain of ultra low cycle fatigue. Its implementation as a user defined material model (UMAT) in the commercial software package Abaqus v6.11-2 [Dassault Systèmes, 2011] is discussed at length and its performance is validated by comparing it with similar material models. Taking the experimental results presented in Chapter 3, the application of this cyclic micromechanical model will be shown to provide reasonable estimates in ULCF for single notched specimens. However, modeling the results of double notched tubes under multiaxial loads proved challenging with this methodology. Here only a qualitative assessment in monotonic loading cases will be presented.

### **Chapter 6 - Design approach for welded structural components**

Building on the data collected for welded structural components in Chapter 4, this chapter will provide a design guideline for the assessment of welded high strength steel joints under multiaxial ULCF. This will be achieved by postulating a specific mesh element size and type around the weld toe region that consistently reproduces the resistance curve given by the localized strain measurements obtained with DIC. The main argument behind this approach is that a consistent modeling method is able to reproduce consistently the experimental results. Local weld toe evaluation methods are not unprecedented in fatigue analysis. One need only look at the hot-spot stress method for high-cycle fatigue established in current design codes. The design proposal in this chapter, with all its assumed shortcomings, follows along those lines and represents a step towards improving what was discussed in Section 1.1.

### **Chapter 7 - Conclusion and future work**

This chapter briefly summarizes the work presented throughout the thesis and provides suggestions on areas to conduct future work.

## **Appendices**

The thesis is completed by a set of appendices containing key information on the UMAT that was developed, as well as a summary of the results of the experimental campaigns conducted on both small and component level specimens. For more detailed information on each test result and simulation, one refers to a companion report to the thesis [de Castro e Sousa and Nussbaumer, 2017]. In that document one can also find the Fortran code for the UMAT discussed in Chapter 5.

## 1.4 Notation and abbreviations

The following general notation rules are used. Lower case bold roman characters ( $\mathbf{a}$ ) are vectors, upper case bold characters ( $\mathbf{A}, \mathbf{\Sigma}$ ) are second-order tensors and lower case Greek bold characters ( $\boldsymbol{\sigma}$ ) are second-order tensors. Normal characters represent scalar quantities. Exceptions can be found to this notation but they will be explicitly noted with respect to their nature.

The Einstein summation convention is used, where repeated indices imply summation:  $(\mathbf{A}\mathbf{b})_i = A_{ij}b_j$ . The Frobenius product is defined as  $\mathbf{A} : \mathbf{B} = A_{ij}B_{ij}$ . The dyadic product of two vectors is expressed by  $(\mathbf{a} \otimes \mathbf{b})_{ij} = (\mathbf{a}\mathbf{b}^T)_{ij} = a_i b_j$

These standard abbreviations are used throughout the text: *w.r.t.* - stands for "with respect to"; *i.e.* - *id est*, stands for "that is"; *e.g.* - *exempli gratia*, stands for "for example"; *cf.* - stands for "confer".



## 2 Background and state of the art

This chapter will provide the background and the current state of the art on the subject of ultra low cycle fatigue. It is divided in four sections: plasticity; digital image correlation; micro-mechanical modeling of ductile fracture; and low and ultra low cycle fatigue. The first two sections provide some background on key concepts used throughout the thesis. Their aim is to provide context and basic definitions to the reader and are by no means extensive in their domains. The subsequent sections present a literature review of the work carried out by the community on the subject.

### 2.1 Finite strain plasticity

The purpose of this section is to provide background on finite strain plasticity. The detail afforded in describing this subject will be justified in the development of a cyclic micro-mechanical model in Chapter 5. Much of the concepts that are outlined in this section can be consulted more in depth in [Simo and Hughes, 1998] and [Lubliner, 2008] .

#### Basic kinematics

Consider an object defined in space by set  $\mathcal{B}$ , *i.e.* every material point defined by position  $\mathbf{X} \in \mathcal{R}^3$  in that object belongs to set  $\mathcal{B}$ . Furthermore, consider that this object can move in space such that there exists a function  $\varphi \rightarrow \mathcal{R}^3$  mapping position  $\mathbf{X}$  in the material configuration to position  $\mathbf{x}$  in the spatial configuration. Mathematically, this can be written as

$$\varphi(\mathcal{B}) = \{\mathbf{x} = \varphi(\mathbf{X}) \mid \mathbf{X} \in \mathcal{B}\} \quad (2.1)$$

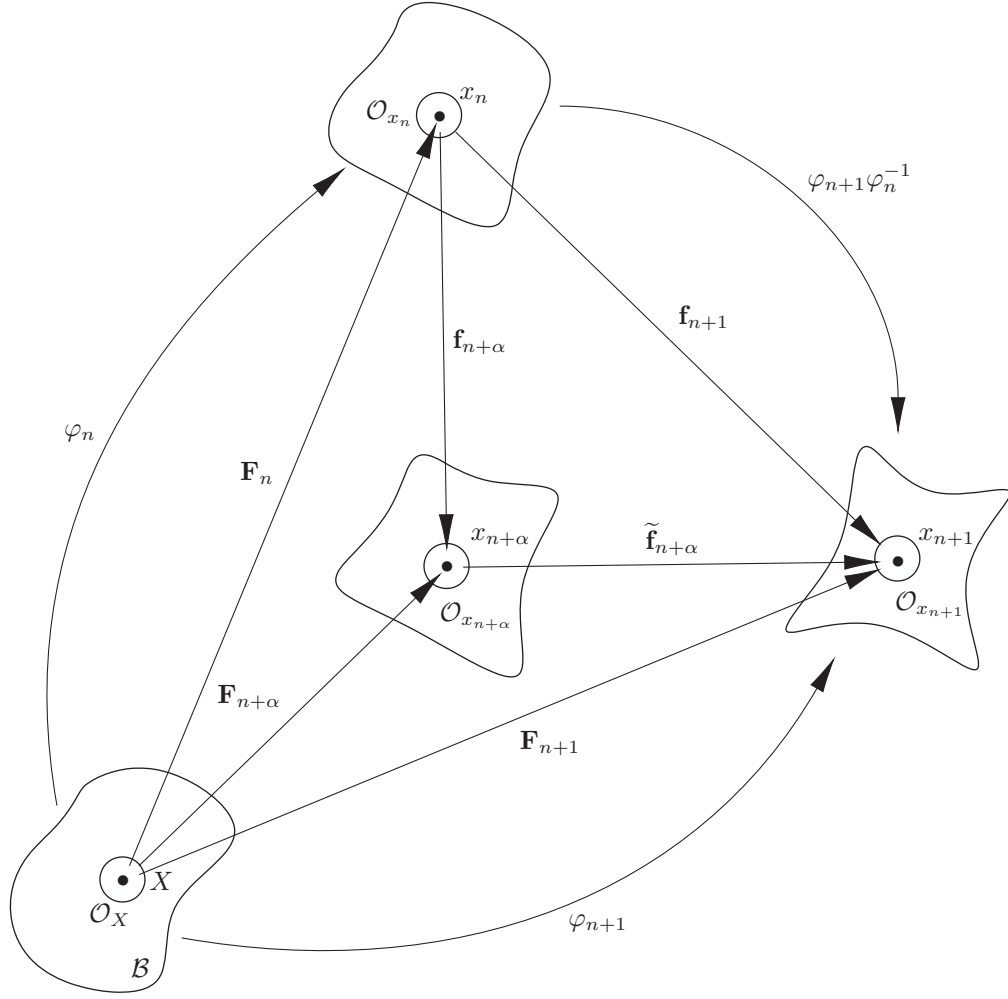


Figure 2.1 – Mapping between material and spatial configurations

Practical treatment of the mechanical problem of insuring equilibrium between internal and external work in body  $\mathcal{B}$  from the reference configuration to the final configuration usually involves dividing this path in appropriate step sizes. This becomes exceedingly important the more acute the material and geometric nonlinearities are. In rate formulations, variables at time  $t_{n+1}$  are equal to  $t_n + \Delta t$  where  $\Delta t$  defines the step size.

Let us define the mapping function ( $\varphi$ ) in an intermediate configuration  $n + \alpha$  as a linear combination of step  $n + 1$  and  $n$ ,

$$\varphi_{n+\alpha} = \alpha \varphi_{n+1} + (1 - \alpha) \varphi_n \mid \alpha \in [0, 1] \quad (2.2)$$

Let us also define the deformation gradient( $\mathbf{F}$ ) on the neighborhood of point  $X$  ( $\mathcal{O}_X$ ) at



$n + \alpha$  as,

$$\mathbf{F}_{n+\alpha} = \frac{\partial \varphi_{n+\alpha}}{\partial \mathbf{X}} \quad (2.3)$$

then from Eq. 2.2,

$$\mathbf{F}_{n+\alpha} = \alpha \mathbf{F}_{n+1} + (1 - \alpha) \mathbf{F}_n \mid \alpha \in [0, 1] \quad (2.4)$$

Defining  $\mathbf{F}$  in an intermediate configuration is a useful concept because it gives one flexibility in choosing how to integrate within time increment  $\Delta t$ . By setting  $\alpha = 0$ , one uses the forward Euler method (explicit time stepping). For  $\alpha = 1$  one uses the backward Euler method (implicit time stepping). For  $\alpha = \frac{1}{2}$  one uses the implicit midpoint rule (second order accurate, as opposed to the Euler method which is first order accurate).

Fig. 2.1 depicts the mapping between material and spatial configurations. All important are the relations between spatial configurations( $\mathbf{f}$ ) expressed in Eqs. 2.5, 2.6 and 2.7.

$$\mathbf{f}_{n+\alpha} = \mathbf{F}_{n+\alpha} \mathbf{F}_n^{-1} \quad (2.5)$$

$$\mathbf{f}_{n+1} = \mathbf{F}_{n+1} \mathbf{F}_n^{-1} \quad (2.6)$$

$$\tilde{\mathbf{f}}_{n+\alpha} = \mathbf{f}_{n+1} \mathbf{f}_{n+\alpha}^{-1} \quad (2.7)$$

The deformation gradient can be decomposed into two parts: one corresponding to a rigid body rotation and another representing the stretch around  $\mathcal{O}_{\mathbf{X}}$  that the material undergoes. This can be expressed in the following forms (Eqs.2.8 and 2.9).

$$\mathbf{F} = \mathbf{R} \mathbf{U} \quad (2.8)$$

$$\mathbf{F} = \mathbf{V} \mathbf{R} \quad (2.9)$$

where  $\mathbf{U}$  and  $\mathbf{V}$  are defined as the right and left stretch tensors, respectively, and  $\mathbf{R}$  the rotation associated with the rigid body movement on  $\mathcal{O}_{\mathbf{X}}$ .

The time rate of change of the deformation gradient relative to the spatial configuration, *i.e.* the spatial velocity gradient tensor ( $\mathbf{L}$ ), can be shown to be equal to,

$$\mathbf{L} = \dot{\mathbf{F}} \mathbf{F}^{-1} \quad (2.10)$$

The symmetric part of  $\mathbf{L}$  is defined as the spatial rate of deformation tensor  $\mathbf{d}$  and the anti-symmetric part, *i.e.* rotational unbalanced, is defined as the spin tensor  $\mathbf{W}$  of the material - see Eqs.

$$\mathbf{d} = \frac{1}{2} (\mathbf{L} + \mathbf{L}^T) \quad (2.11)$$

$$\mathbf{W} = \frac{1}{2} (\mathbf{L} - \mathbf{L}^T) \quad (2.12)$$

Another important definition in the subsequent discussion of objectivity is the rotation rate  $\mathbf{\Omega}$ .

$$\mathbf{\Omega} = \dot{\mathbf{R}}\mathbf{R}^T \quad (2.13)$$

This tensor also has the property that it is anti-symmetric, *i.e.*  $\mathbf{\Omega} + \mathbf{\Omega}^T = \mathbf{0}$  (belonging to a special orthogonal group  $so(3)$ ).

### Objectivity

With the spatial rate of deformation  $\mathbf{d}$  defined, an appropriate approximation for the increment in total strain can be given by,

$$\Delta\boldsymbol{\varepsilon}_{n+\frac{1}{2}} = \Delta t \mathbf{d}_{n+\frac{1}{2}} = \frac{1}{2} \tilde{\mathbf{f}}_{n+\frac{1}{2}}^T \left[ \mathbf{I} - (\mathbf{f}_{n+1} \mathbf{f}_{n+1}^T)^{-1} \right] \tilde{\mathbf{f}}_{n+\frac{1}{2}} \quad (2.14)$$

$\Delta\boldsymbol{\varepsilon}_{n+\frac{1}{2}}$  has the interesting property that if the deformation when going from configuration  $n$  to  $n+1$  consists solely of a rigid body rotation ( $\mathbf{\Lambda}$ ), *i.e.*  $\mathbf{f}_{n+1} = \mathbf{\Lambda} \mathbf{f}_n$  where  $\mathbf{\Lambda} \mathbf{\Lambda}^T = \mathbf{I}$  (belonging to special orthogonal group  $SO(3)$ ), then  $\Delta\boldsymbol{\varepsilon} = \mathbf{0}$ . As such, this quantity is considered to be incrementally objective. Having shown that the increment in strain is incrementally objective, let's turn now our attention to stress measures. Assume that the Cauchy stress tensor ( $\boldsymbol{\sigma}$ ) transforms objectively<sup>1</sup> such that,

$$\tilde{\boldsymbol{\sigma}} = \mathbf{\Lambda} \boldsymbol{\sigma} \mathbf{\Lambda}^T \quad (2.15)$$

where  $\tilde{\phantom{x}}$  represents a rotated quantity. The time derivative of Eq. 2.15 can be shown to be,

$$\dot{\tilde{\boldsymbol{\sigma}}} = \mathbf{\Lambda} \dot{\boldsymbol{\sigma}} \mathbf{\Lambda}^T + \dot{\mathbf{\Lambda}} \mathbf{\Lambda}^T \tilde{\boldsymbol{\sigma}} - \tilde{\boldsymbol{\sigma}} \dot{\mathbf{\Lambda}} \mathbf{\Lambda}^T \quad (2.16)$$

or more conveniently,

$$\dot{\tilde{\boldsymbol{\sigma}}} = \mathbf{\Lambda} (\dot{\boldsymbol{\sigma}} + \mathbf{\Lambda}^T \dot{\mathbf{\Lambda}} \boldsymbol{\sigma} - \boldsymbol{\sigma} \mathbf{\Lambda}^T \dot{\mathbf{\Lambda}}) \mathbf{\Lambda}^T \quad (2.17)$$

One can see comparing Eqs. 2.15 and 2.17 that whereas the Cauchy stress transforms objectively its rate of change does not.

Let us define the tensor  $\hat{\omega} \in so(3)$  as representing a quantity that characterizes the rigid body rotation rate on  $\mathcal{O}_{\mathbf{x}}$  such that,

$$\dot{\mathbf{\Lambda}} = (\hat{\omega} \circ \varphi) \mathbf{\Lambda} \quad (2.18)$$

---

<sup>1</sup>*i.e.* that there is a direct correspondence between reference frames under rigid body rotations that conforms to the rules of tensor calculus

Eq.2.17 becomes,

$$\dot{\boldsymbol{\sigma}} = \boldsymbol{\Lambda} (\dot{\boldsymbol{\sigma}} + \hat{\boldsymbol{\omega}} \boldsymbol{\sigma} - \boldsymbol{\sigma} \hat{\boldsymbol{\omega}}) \boldsymbol{\Lambda}^T \quad (2.19)$$

Two classical measures of rotation are of relevance in the present discussion,

1.  $\hat{\boldsymbol{\omega}} \equiv \mathbf{W}$  - Jaumann-Zaremba stress rate, leading to Eq. 2.20
2.  $\hat{\boldsymbol{\omega}} \equiv \boldsymbol{\Omega}$  - Green-McInnis-Naghdi stress rate, leading to Eq. 2.21

$$\dot{\boldsymbol{\sigma}}^* = \dot{\boldsymbol{\sigma}} + \mathbf{W} \boldsymbol{\Sigma} - \boldsymbol{\sigma} \mathbf{W} \quad (2.20)$$

$$\dot{\boldsymbol{\sigma}}^\circ = \dot{\boldsymbol{\sigma}} + \boldsymbol{\Omega} \boldsymbol{\sigma} - \boldsymbol{\sigma} \boldsymbol{\Omega} \quad (2.21)$$

One can now link stress and strain responses via an appropriately chosen constitutive law. Objectivity of integration algorithm hinges on formulating a constitutive law that is insensitive to rigid body rotations in the spatial configuration. This is usually done by defining its rate form in the material configuration, also known as the convected configuration, and then pushing-forward to the spatial configuration. Consider the hypo-elastic rate constitutive law in Eq. 2.22 in the material configuration,

$$\dot{\boldsymbol{\sigma}} = \mathcal{C} \mathbf{d} \quad (2.22)$$

where,  $\mathcal{C}$  is the fourth-order elastic stiffness tensor. Approximating Eq. 2.22 by the midpoint rule

$$\begin{aligned} \boldsymbol{\sigma}_{n+1} - \boldsymbol{\sigma}_n &= \Delta t \dot{\boldsymbol{\sigma}}_{n+\frac{1}{2}} \\ &= \Delta t \mathcal{C}_{n+\frac{1}{2}} \mathbf{d}_{n+\frac{1}{2}} \\ &= \mathcal{C}_{n+\frac{1}{2}} \boldsymbol{\Lambda}_{n+\frac{1}{2}}^T \Delta \tilde{\boldsymbol{\epsilon}}_{n+\frac{1}{2}} \boldsymbol{\Lambda}_{n+\frac{1}{2}} \end{aligned} \quad (2.23)$$

Rearranging 2.23 to express it incrementally in the spatial configuration yields,

$$\tilde{\boldsymbol{\sigma}}_{n+1} = \Delta \boldsymbol{\Lambda} \tilde{\boldsymbol{\sigma}}_n \Delta \boldsymbol{\Lambda}^T + \tilde{\mathcal{C}} \Delta \tilde{\boldsymbol{\epsilon}}_{n+1} \quad (2.24)$$

where,

$$\Delta \boldsymbol{\Lambda} = \boldsymbol{\Lambda}_{n+1} \boldsymbol{\Lambda}_n^T \quad (2.25)$$

$$\tilde{\boldsymbol{\epsilon}}_{n+1} = \tilde{\boldsymbol{\Lambda}}_{n+\frac{1}{2}} \tilde{\boldsymbol{\epsilon}}_{n+\frac{1}{2}} \tilde{\boldsymbol{\Lambda}}_{n+\frac{1}{2}}^T \quad (2.26)$$

$$\tilde{\boldsymbol{\Lambda}}_{n+\frac{1}{2}} = \boldsymbol{\Lambda}_{n+1} \boldsymbol{\Lambda}_{n+\frac{1}{2}}^T \quad (2.27)$$

and  $\tilde{\mathcal{C}}$  the stiffness matrix rotated to the spatial configuration at  $n+1$ . When elastic isotropy

## Chapter 2. Background and state of the art

---

is assumed,  $\mathcal{C} = \tilde{\mathcal{C}}$  because the operations only involve rigid body rotations.

The only thing left to define is how to obtain  $\mathbf{\Lambda}_{n+\alpha}$ . Considering that at  $t = 0 \rightarrow \mathbf{\Lambda}_0 = \mathbf{I}$ ,  $\mathbf{\Lambda}_{n+\alpha}$  can be found by integrating Eq. 2.18 as,

$$\mathbf{\Lambda}_{n+1} = e^{\Delta t \hat{\omega}_{n+\alpha}} \mathbf{\Lambda}_n \quad (2.28)$$

For  $\hat{\omega} \equiv \mathbf{\Omega}$ , from Eq. 2.28 follows that one only needs to perform three polar decompositions following Eq. 2.8,

$$\mathbf{\Lambda}_n = \mathbf{R}_n ; \mathbf{\Lambda}_{n+\alpha} = \mathbf{R}_{n+\alpha} ; \mathbf{\Lambda}_{n+1} = \mathbf{R}_{n+1} \quad (2.29)$$

For  $\hat{\omega} \equiv \mathbf{W}$

$$\Delta t \hat{\omega}_{n+\alpha} = \frac{1}{2} [\mathbf{h}_{n+\alpha} + \mathbf{h}_{n+\alpha}^T] \quad (2.30)$$

$$\mathbf{h}_{n+\alpha} = \nabla_{n+\alpha} \tilde{\mathbf{u}} = (\mathbf{F}_{n+1} - \mathbf{F}_n) \mathbf{F}_{n+\alpha}^{-1} \quad (2.31)$$

It can be shown that the widely used Hughes-Winget formula [Hughes and Winget, 1980] is an approximation to Eqs. 2.28 and 2.30 [Simo and Hughes, 1998].

### Yield surfaces and hardening laws

Modeling plasticity typically involves assuming an additive decomposition of the strain rate tensor into elastic and plastic parts, as per Eq. 2.32

$$\mathbf{d} = \mathbf{d}^e + \mathbf{d}^p \quad (2.32)$$

Yield functions (henceforth generally denote as  $\phi$ ) serve to assess the boundary between elastic ( $\phi < 0$ ) and plastic deformation ( $\phi = 0$ ). Plasticity in metals is usually expressed in terms of  $J_2$  flow theory.  $J_2$  stands for the second invariant of the deviatoric stress tensor ( $\boldsymbol{\sigma}'$ ; where the apostrophe implies  $\mathbf{S}' = \mathbf{S} - \frac{1}{3} S_{kk} \mathbf{I}$ ). The Von Mises yield criterion appears in this theory as Eq. 2.33.

$$\phi^{VM} = \sigma_{vm}^2 - \sigma_y^2 = 0 \quad (2.33)$$

$\sigma_{vm}$  is the Von Mises equivalent stress (given by  $\sqrt{3/2 \boldsymbol{\sigma}' : \boldsymbol{\sigma}'}$ ) and  $\sigma_y$  is denoted as the matrix yield stress.  $\sigma_y$  defines a limit on the yield function in Eq. 2.33 whose surface defines a cylinder in principal stress space, with its axis of revolution along the hydrostatic axis. One defines the  $\pi$ -plane as the plane normal to the hydrostatic axis that passes through the origin. To describe a hardening material, there are two common approaches - isotropic and kinematic hardening. Fig. 2.2 presents the projection of  $\phi^{VM} = 0$  onto the  $\pi$ -plane for those two scenarios. The first and most immediate solution is to increase the size of the yield

surface (or circle in the  $\pi$ -plane) as the material undergoes plastic deformation. The second solution would be to move the yield surface along with the loading. Eq. 2.34 expresses those two options mathematically, where  $\alpha$  is a stress tensor that shifts the center of the surface - this tensor is also known as the backstress. If one is to try to model a metal's plastic response in monotonic loading, an isotropic hardening is sufficient. In cyclic loading, however, because of the Bauschinger effect, kinematic hardening is usually employed to some extent.

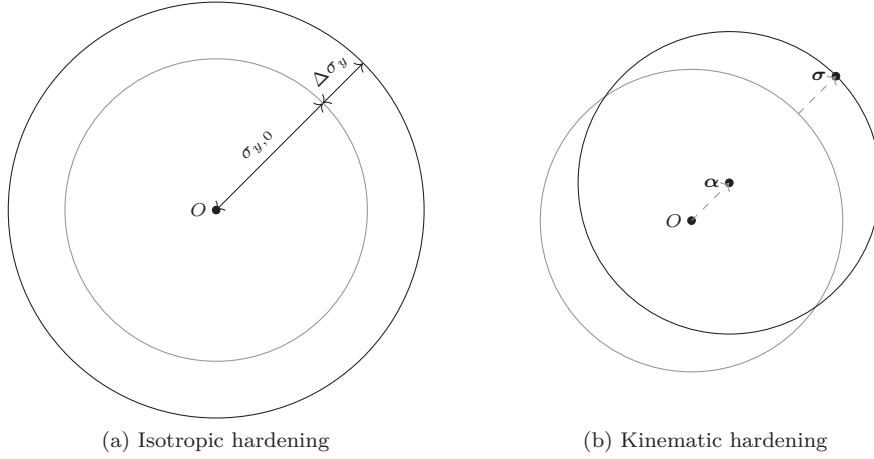


Figure 2.2 –  $\pi$ -plane representation of hardening rules

$$\phi^{VM} = \frac{3}{2} (\sigma - \alpha)' : (\sigma - \alpha)' - (\sigma_{y,0} + \Delta\sigma_y)^2 = 0 \quad (2.34)$$

Once one has reached the limit set by the yield function, a direction of plastic flow needs to be defined. This is normally imposed by another function commonly denoted as the plastic potential. When the plastic potential equals the yield function one is in the presence of associated plasticity. Such is the case for  $J_2$ -theory. Following Drucker's postulate and principle of maximum plastic dissipation, the plastic strain rate obeys normality to the yield function  $\phi$ , leading to the following associated flow rule,

$$d^P = \lambda \frac{\partial \phi}{\partial \sigma} \quad (2.35)$$

where  $d^P$  is proportional to the normal to the yield function by a factor commonly called the plastic multiplier  $\lambda$ . Hardening laws, as the name suggests, serve to describe how the material hardens. A number of hardening laws exist. Pervasive in most of them, is a scalar strain measure known as the equivalent plastic strain  $\varepsilon_{eq}^p$ . This quantity is obtained by enforcing work conjugacy in the rate of plastic dissipation, see Eq. 2.36

$$\sigma : d^P = \sigma_{vm} \dot{\varepsilon}_{eq}^p \quad ; \quad \dot{\varepsilon}_{eq}^p = \sqrt{\frac{2}{3} d^P : d^P} \quad (2.36)$$

## Chapter 2. Background and state of the art

---

In isotropic hardening, this scalar variable is sufficient for a description of the material behavior. The simplest nonlinear isotropic power law due to [Ludwik, 1909] is presented in Eq. 2.37.

$$\sigma_y = \sigma_{y,0} + K (\varepsilon_{eq}^p)^n \quad (2.37)$$

For the case of kinematic hardening, one also needs a direction where to move the yield surface. A widely used non-linear kinematic law due to [Armstrong and Fredrick, 1966] is given in Eq. 2.38, expression in which the direction of the backstress rate ( $\dot{\alpha}$ ) is set by the plastic strain rate ( $d^p$ ) and previous backstress values. Here,  $C$  is a linear hardening parameter on the plastic strain rate and  $\gamma$  the so-called relaxation term that introduces non-linearity to the law. The well-known Chaboche model [Chaboche et al., 1979] takes the Armstrong-Fredrick law and defines backstress as the sum of a number component backstresses ( $\alpha_k$ )- see Eq. 2.39.

$$\dot{\alpha} = \frac{2}{3} C d^p - \gamma \alpha \dot{\varepsilon}_{eq}^p \quad (2.38)$$

$$\begin{cases} \alpha = \sum_k \alpha_k \\ \dot{\alpha}_k = \frac{2}{3} C_k d^p - \gamma_k \alpha_k \dot{\varepsilon}_{eq}^p \end{cases} \quad (2.39)$$

Non-linear kinematic hardening laws in hypo-elastic finite strain formulations are known to be sensitive to shear oscillations [Xiao et al., 2006]. A manifestation of the problem can be seen in Fig. 2.3. Here a Finite Element Method (FEM) simulation is made on the software Abaqus Standard [Dassault Systèmes, 2011] on an 8-node reduced integration cubic element on which simple shear is applied. A prescribed material law is given (marked *Intended* in the figure) and the response in terms of accumulated plastic strain and Von Mises stress is registered for the built-in material models corresponding to non-linear isotropic and kinematic hardening. One can see that, for the same hardening curve in simple shear, different material models will give different results. Abaqus Standard's finite strain formulation is hypo-elastic and based on the Jaumann-Zaremba stress rate. One should therefore be cognizant of this fact when performing FEM analyses that involve large shear strains.

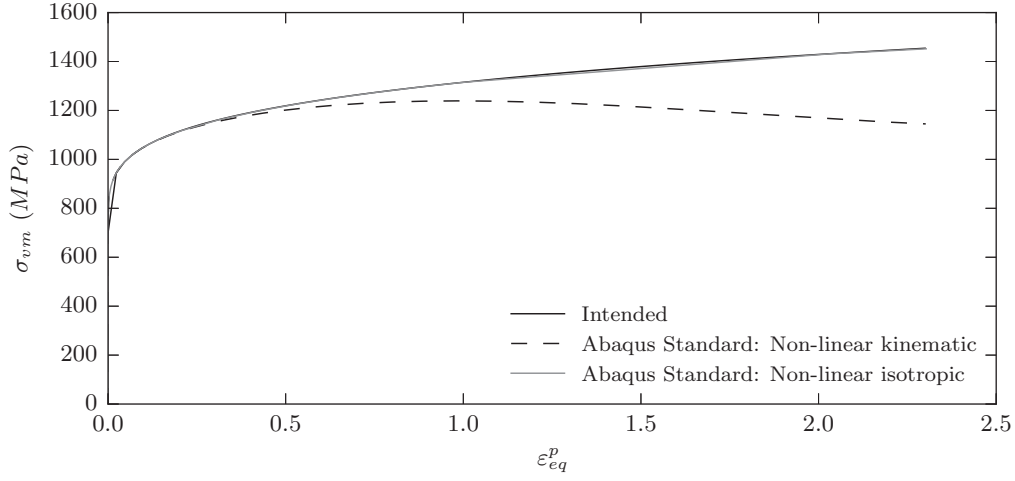


Figure 2.3 – FEM Non-linear isotropic and kinematic hardening in Abaqus and prescribed stress-strain curve in simple shear

## 2.2 Digital image correlation

DIC is a measurement technique that was used throughout the experimental programs made during this work. Due to its importance, it is useful to have a few dedicated remarks on the procedures that are at the root of this method.

The two different methods of DIC used were: stereo DIC with speckle pattern (Fig. 2.4a) and target recognition (Fig. 2.4b). The latter is a simple technique that consists of an in-house image recognition program that, by analyzing contrast between white and black pixels, defines the outlines of circular targets and fits the best circle that represents the data. This can be done continuously at sample rates of 10Hz. Displacements on uni-axial tests are expressed in difference in pixels *w.r.t.* a reference configuration. A scaling factor must therefore be applied and this is done so by using a ruler as wide as the picture itself to get a correspondence between pixels and actual length scale.

A more complex method involves the use of a randomized speckle pattern on the surface of a specimen. The working principle can be understood by interpreting Fig. 2.5 with the help of Eq. 2.40. One begins by establishing a *subset size* (Fig. 2.5a) in a reference image ( $I$ ) that defines a box with center  $(x, y)$  of  $n \times n$  pixels. In Fig. 2.5b one finds a picture in the deformed configuration ( $I^*$ ) with an idealized pattern having moved by  $(u, v)$  pixels. Now, each pixel has associated with it a numerical value ( $I(x, y)$ ) corresponding to its greyscale (say 0 is white, 1 is black). Out of all  $n \times n$  boxes that can be placed in the deformed picture, there is one whose difference, pixel by pixel, *w.r.t.* the reference picture is minimum. That is

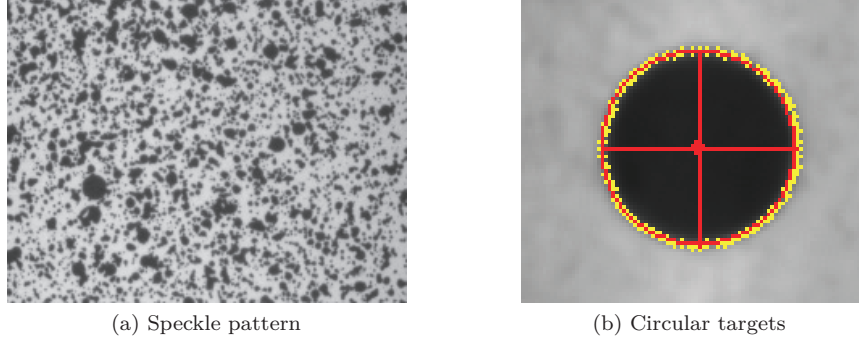


Figure 2.4 – DIC methods

a measure of correlation between the two pictures and is, essentially, what can be interpreted from Eq. 2.40.

$$C^{DIC}(x, y, u, v) = \sum_{i,j=-n/2}^{n/2} (I(x+i, y+j) - I^*(x+u+i, y+v+j))^2 \quad (2.40)$$

Two extra parameters contribute a great deal to DIC speckle measurements. The first is the *step size*<sup>2</sup> that one chooses between the boxes, *i.e.* the grid spacing of  $(u, v)$  measurement points (Fig. 2.5c). The second is the *filter size* that sets a window of  $m \times m$   $(u, v)$  points over which data is averaged ( $m$  being an odd number of points; *c.f.* Fig. 2.5d). With a field measurement of displacements values, strain fields can be calculated.

Stereo correlation systems add another level of sophistication in so far as with two camera systems one can produce full-field measurements in 3D. This involves knowing precisely the relative position of each camera. It should be noted that accuracy in the in-plane direction is generally better than the out-of-plane. Specialized software (in this study VIC3D from Correlated Solutions [McGowan et al., 2001]) and calibration procedures have to be employed for reliable results. More details can be found in [Schreier et al., 2009].

---

<sup>2</sup>step size can be inferior to subset size, *i.e* boxes may overlay



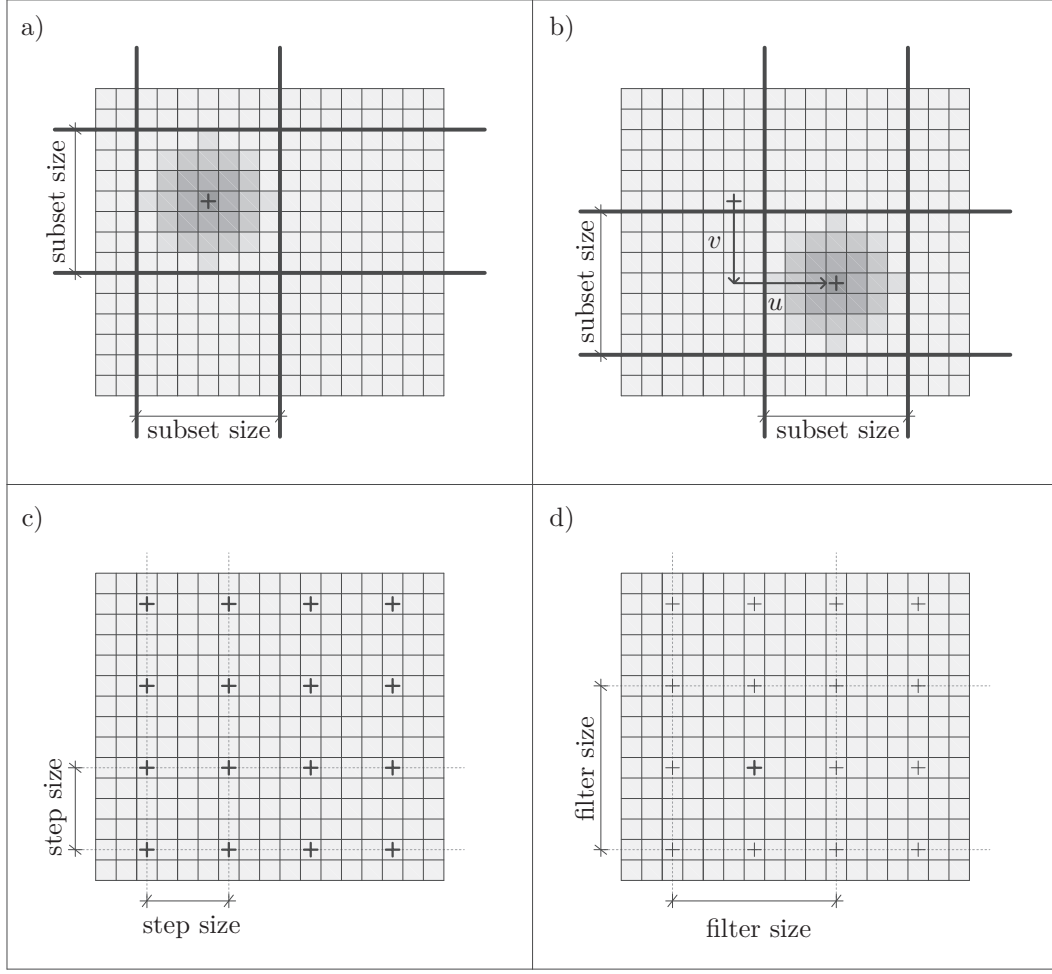


Figure 2.5 – Digital image correlation definitions

## 2.3 Ductile fracture in metals

This section presents a synopsis of the state of the art in ductile fracture by void growth to coalescence. Its objective is to summarize the work in the field and to put the current study into context. For a comprehensive treatment of the subject one refers to [Benzerga and Leblond, 2010] and [Pineau et al., 2016].

### 2.3.1 Experimental observations

One starts by presenting pertinent experimental observations in literature. Consider Fig. 2.6 which presents a force-displacement curve for a single notched round tube along with cross sectional cuts representative of key points during the loading. What is apparent from this test is the diffuse formation of voids in the material, followed by an appreciable increase in

size until their volume becomes such that they start to coalesce to form a full-sized crack in the material. This full-sized crack will propagate until ultimate failure of the specimen. In this succinct description lies the foundation for micro-mechanical based models of void growth to coalescence.

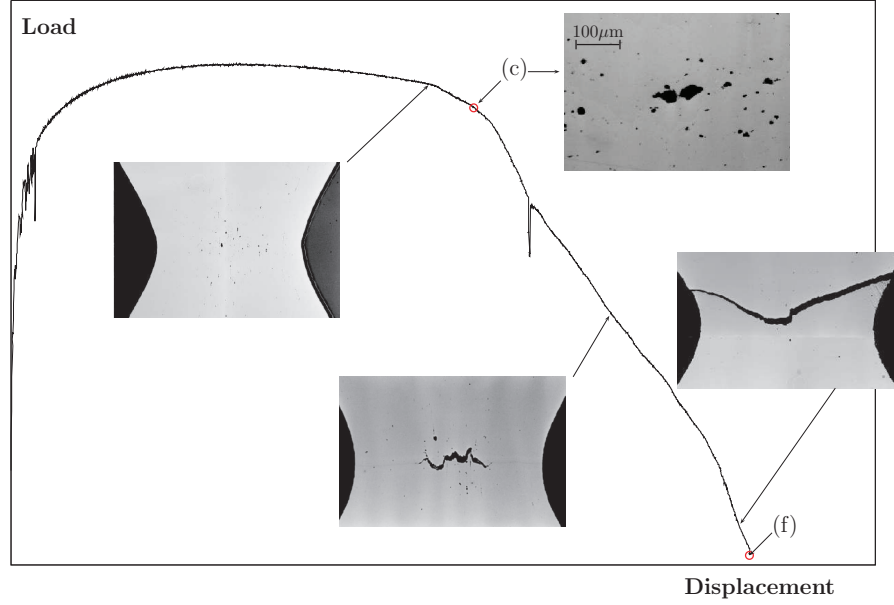


Figure 2.6 – Loading of a single notched bar - from [Benzerga and Leblond, 2010]

This process is schematically represented in Fig. 2.7. The process of formation of voids around inclusions or second-phase particles have been reported as far back as [Argon and Im, 1975]. During loading, voids tend to form around those particles (Fig. 2.7a) either by decohesion (Fig. 2.7c) of the matrix or by particle cracking (Fig. 2.7b). Then voids grow (Fig. 2.7d) up to a point where plastic instability ensues and necking in the inter-void ligament is observed (Fig. 2.7e). A crack is then formed by the coalescence of these voids. The fracture surface is then characterized by pockets of ellipsoidal depressions henceforth called dimples.

Different modes than the coalescence of voids by necking in the inter-void ligament have been reported in literature. These include shearing of the inter-void ligament and coalescence in columns (often associated with material delamination) [Benzerga, 2000].

Experiments also show that the fracture behavior is highly dependent on the stress state ([Bao and Wierzbicki, 2004], [Mohr and Henn, 2007], [Dunand and Mohr, 2011], [Barsoum et al., 2012], [Faleskog and Barsoum, 2013], [Smith et al., 2014]). The two most commonly used measures of the stress state to describe material ductility (as represented by the fracture strain) are the stress triaxiality ( $T$  - Eq. 2.41) and the Lode parameter ( $L$  - Eq.

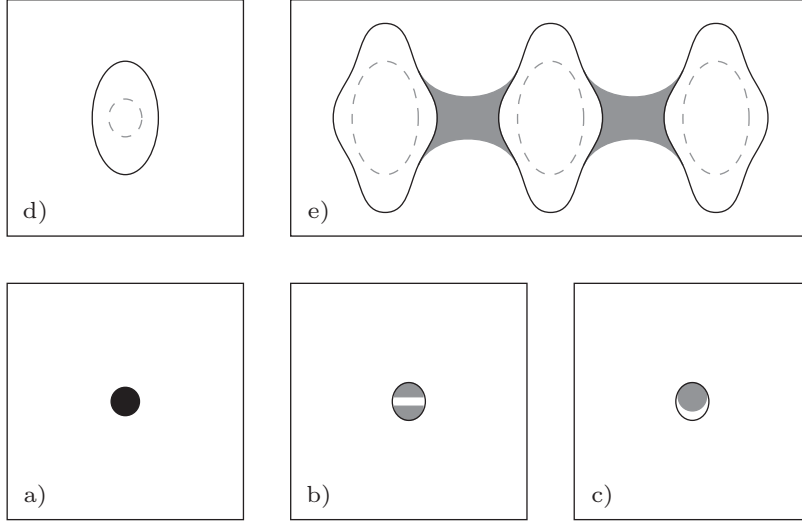


Figure 2.7 – Nucleation, void growth and coalescence

2.42).

$$T = \frac{\sigma_h}{\sigma_{vm}} \quad (2.41)$$

$$L = \frac{2\sigma_2 - \sigma_1 - \sigma_3}{\sigma_1 - \sigma_3} \quad (2.42)$$

where  $\sigma_h$  is the hydrostatic stress ( $\sigma_h = \frac{1}{3}\sigma_{kk}$ ) and  $\sigma_1$ ,  $\sigma_2$  and  $\sigma_3$  are the principal stresses. Physically the triaxiality can be interpreted as a measure of the relationship between hydrostatic and deviatoric stress states. The Lode parameter, being closely related to the third invariant of the deviatoric stress tensor, acts as a measure of the axisymmetry of the loading. It is a bounded measure going from  $L = -1$  in uniaxial tension to  $L = 1$  in equi-biaxial tension.

In so far as larger values of triaxiality imply a larger hydrostatic component in the loading, which intuitively implies a greater rate of growth of voids, large triaxiality values are associated with decreased ductility. A typical fracture surface in the tensile regime can be seen in 2.8a. Fracture surfaces for low triaxiality values, which are predominantly shear loadings, are associated with shearing instability of the inter-void ligament and can be seen in Fig. 2.8b. Phenomena such as crack tunneling in CT specimens can be viewed in this perspective. Triaxialities in front of a crack tip in plane strain conditions are greater than in plane stress conditions. This justifies a greater rate of crack growth in the middle of CT specimens as seen in 2.9.

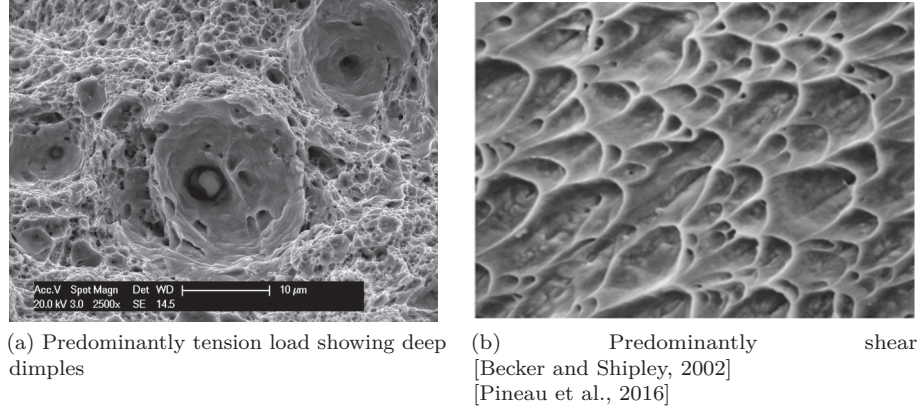


Figure 2.8 – Typical ductile fracture surfaces

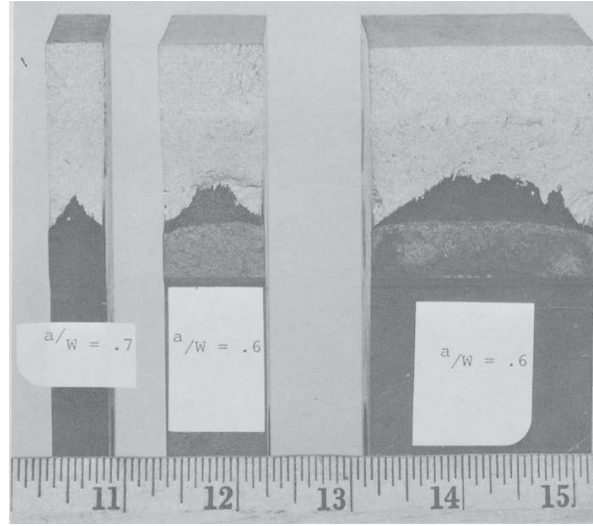


Figure 2.9 – Fracture surfaces of CT specimens illustrating crack tunneling. From bottom to top: 1 - Fatigue crack; 2 - monotonic ductile crack propagation; 3 - brittle failure [Vassilaros et al., 1980]

### 2.3.2 Modeling approaches

This subsection summarizes current approaches to modeling of the experimental observation made in the previous section. For a comprehensive review one refers to [Benzerga and Leblond, 2010].

Homogenization theory plays a central role in the derivation of micromechanical models. Consider 2.10 where a schematic of a porous body is presented and an arbitrary velocity field is applied on the boundaries of body  $\partial\mathcal{B}$  as per Eq. 2.43.

$$\forall \mathbf{x} \in \partial\mathcal{B}, \quad v_i = D_{ij}x_j \quad (2.43)$$

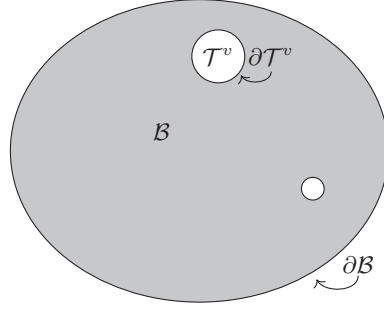


Figure 2.10 – Schematic of porous body

The Hill-Mandel Lemma (Eq. 2.44) allows one to express the macroscopic rate of dissipation  $(\boldsymbol{\Sigma} : \mathbf{D})$  as the average microscopic dissipation in the matrix of body  $\mathcal{B}$ .

$$\begin{aligned}\boldsymbol{\Sigma} : \mathbf{D} &= \langle \boldsymbol{\sigma} : \mathbf{d} \rangle_{\mathcal{B}} \\ &= (1 - f) \langle \boldsymbol{\sigma} : \mathbf{d} \rangle_{\mathcal{B} \setminus \mathcal{T}^v}\end{aligned}\tag{2.44}$$

where  $f$  is defined as the porosity of the material given by  $\mathcal{T}^v / \mathcal{B}$ .

The principle of maximum plastic dissipation and the upper bound theorem allow one to make the following statement: among the set of microscopic strain rate fields  $\mathbf{d}^+$  that are kinematically admissible with the macroscopic strain rate field  $\mathbf{D}$  ( $\mathbf{d}^+ \in \mathcal{K}(\mathbf{D})$ ), together with a statically admissible stress field  $\boldsymbol{\sigma}^*$ , the tightest upper bound to the actual plastic dissipation rate  $(\boldsymbol{\Sigma} : \mathbf{D})$  is given by Eq. 2.45.

$$\boldsymbol{\Sigma} : \mathbf{D} \leq \Pi(\mathbf{D}) = \inf_{\mathbf{d}^+ \in \mathcal{K}(\mathbf{D})} \left\langle \sup_{\boldsymbol{\sigma}^*} \boldsymbol{\sigma}^* : \mathbf{d}^+ \right\rangle_{\mathcal{B}}\tag{2.45}$$

By selecting an appropriate Representative Volume Element(s) (RVE) and corresponding velocity field, it can be shown (*c.f.* [Benzerga and Leblond, 2010]) that one can use Eq. 2.45 to obtain a set of macroscopic stress states that characterize the elastic domain, thereby defining a yield criterion.

### Void growth models

The popular Gurson model [Gurson, 1975] uses a spherical RVE with a spherical internal void as depicted in Fig. 2.11 in a perfectly plastic J2-plasticity matrix to obtain the well known yield function given in Eq. 2.46

$$\phi^G(\boldsymbol{\Sigma}; f) = \frac{\Sigma_{vm}^2}{\sigma_y^2} - 1 + 2f \cosh \left( \frac{1}{2} \frac{\boldsymbol{\Sigma} : \mathbf{I}}{\sigma_y} \right) + f^2\tag{2.46}$$

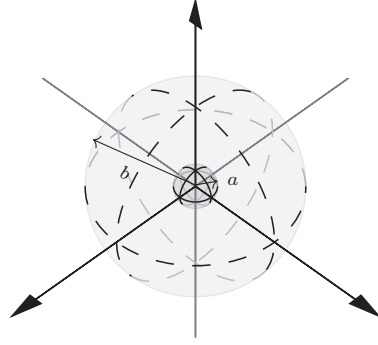


Figure 2.11 – Spherical RVE with a spherical internal void

Since its appearance, the Gurson model has been the target of intense study and enhancements starting with the corrections of [Tvergaard, 1982] to account for void interaction effects. Recently, attempts have been made to address the shortcomings of the Gurson in low triaxiality regimes either by heuristic extensions incorporating additional stress measures (like the Lode parameter - [Nahshon and Hutchinson, 2008]) or by making use of second-order homogenization models [Danas and Castaneda, 2012] .

Other models have tried to incorporate void shape effects explicitly. Such is the case of the GLD model [Gologanu and Leblond, 1993], [Gologanu et al., 1994], [Gologanu, 1997], [Gologanu et al., 1997] (see Eq. 2.47), where the yield function  $\phi^{GLD}(\boldsymbol{\Sigma}; f, w, \boldsymbol{\Upsilon})$  is dependent not only on the porosity ( $f$ ) but also on the aspect ratio of a spheroidal void ( $w$ ) and its orientation ( $\boldsymbol{\Upsilon}$  as given by Eq. 2.50 in correspondence with Figs. 2.12 and 2.13).

$$\begin{aligned} \phi^{GLD} = & C \frac{\|\boldsymbol{\Sigma}' + \eta(\boldsymbol{\Sigma} : \mathbf{X})\mathbf{Q}\|^2}{\sigma_y^2} + \\ & 2(g+1)(g+f) \cosh\left(k \frac{\boldsymbol{\Sigma} : \mathbf{X}}{\sigma_y}\right) - \\ & (g+1)^2 - (g+f)^2 \end{aligned} \quad (2.47)$$

where  $\mathbf{X}$  and  $\mathbf{Q}$  are given by,

$$\mathbf{X} = \alpha_2 (\mathbf{n}_1 \otimes \mathbf{n}_1 + \mathbf{n}_2 \otimes \mathbf{n}_2) + (1 - 2\alpha_2) \mathbf{n}_3 \otimes \mathbf{n}_3 \quad (2.48)$$

$$\mathbf{Q} = -\frac{1}{3} (\mathbf{n}_1 \otimes \mathbf{n}_1 + \mathbf{n}_2 \otimes \mathbf{n}_2) + \frac{2}{3} \mathbf{n}_3 \otimes \mathbf{n}_3 \quad (2.49)$$

and  $\|\mathbf{S}\| = \sqrt{3/2 \mathbf{S}' : \mathbf{S}'}$ .  $C$ ,  $\eta$ ,  $g$ ,  $k$  and  $\alpha_2$  are functions of the aspect ratio  $w$  and the

porosity  $f$  given in Appendix A.

$$\mathbf{\Upsilon} = \begin{bmatrix} | & | & | & | \\ \mathbf{n}_1 & \mathbf{n}_2 & \mathbf{n}_3 & \\ | & | & | & | \end{bmatrix} \quad (2.50)$$

with  $\mathbf{n}_1, \mathbf{n}_2$  and  $\mathbf{n}_3$  being the void's axes and  $\mathbf{n}_3$  being the void's principal direction.

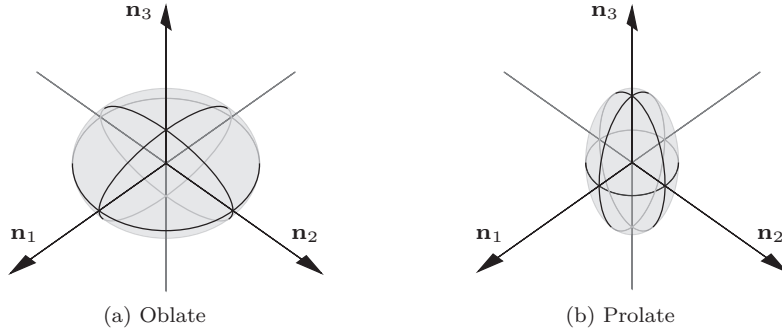


Figure 2.12 – Spheroidal void shapes

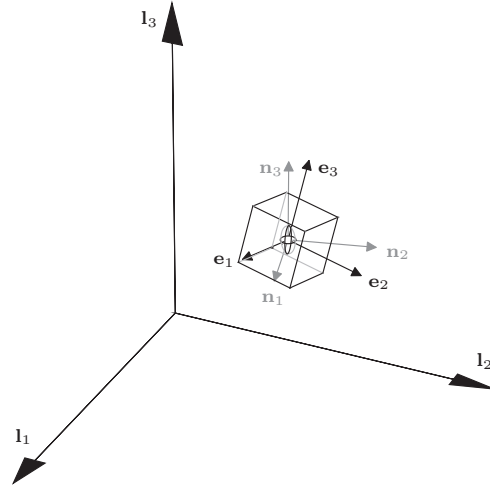


Figure 2.13 – Material ( $\mathbf{e}_i$ ) and void orientations ( $\mathbf{n}_i$ ) with respect to the undeformed reference frame ( $\mathbf{l}_i$ )

Models also attempt to describe the evolution of the internal state variables. Porosity is a classic case for which, assuming the matrix is incompressible, one can state that  $\dot{\mathcal{T}}^v = \dot{\mathcal{B}}$  thus implying Eq. 2.51.

$$\dot{f} = \frac{d}{dt} \frac{\mathcal{T}^v}{\mathcal{B}} = \left(1 - \frac{\mathcal{T}^v}{\mathcal{B}}\right) \frac{\dot{\mathcal{B}}}{\mathcal{B}} = (1 - f) D_{kk} = (1 - f) \dot{\lambda} \frac{\partial \phi}{\partial \Sigma_{kk}} \quad (2.51)$$

Although not used in this thesis, the porosity evolution rate is often seen to be supplemented

with terms accounting for void nucleation [Chu and Needleman, 1980].

Void shape evolution laws have been derived in the work of [Gologanu et al., 1997], and are presented in Eq. 2.52 as per [Kweon et al., 2016]. One defines  $S = \ln w$ .

$$\dot{S} = \mathbf{Z} : \left[ (1 + k_w k_f k_T) \mathbf{D}^p + \left( \frac{1}{f} \mathbf{X}_v - \mathbf{X} \right) D_{kk}^p \right] \quad (2.52)$$

where,

$$\mathbf{Z} = -\frac{1}{2} (\mathbf{n}_1 \otimes \mathbf{n}_1 + \mathbf{n}_2 \otimes \mathbf{n}_2) + \mathbf{n}_3 \otimes \mathbf{n}_3 \quad (2.53)$$

$$k_w = \frac{9}{2} \frac{\alpha_1 - \alpha_1^G}{1 - 3\alpha_1} \quad (2.54)$$

$$k_f = (1 - \sqrt{f})^2 \quad (2.55)$$

$$k_T = \begin{cases} 1 - \frac{T^2 + T^4}{9} & \text{for } \text{sgn}(\Sigma_{kk} \Sigma'_{33}) = 1 \\ 1 - \frac{T^2 + T^4}{18} & \text{for } \text{sgn}(\Sigma_{kk} \Sigma'_{33}) = -1 \end{cases} \quad (2.56)$$

with  $\alpha_1$  and  $\alpha_1^G$  as parameters given in Appendix A.  $\mathbf{X}_v$  is defined as in Eq. 2.48 with  $\alpha_2$  replaced by  $\alpha_1$ . Here void evolution is influenced by factors such as stress triaxiality as well as the porosity ( $f$ ) and the void's aspect ratio itself ( $w$ ). This expression was calibrated so as to give similar results to the evolution observed in cell models.

Evolution of the orientation of the void is usually associated with the evolution of the material's rotation itself as per Eq. 2.57.

$$\dot{\mathbf{n}}_3 = \mathbf{\Lambda} \mathbf{n}_3 \quad (2.57)$$

When  $\mathbf{\Lambda}$  is associated with the material's spin ( $\mathbf{W}$ ), corrections based on [Kailasam and Castaneda, 1998] are usually employed to take into account plastic distortion effects [Kweon et al., 2016]. To the author's knowledge, when  $\mathbf{\Lambda}$  is tied to the material's rotation rate ( $\mathbf{\Omega}$ ), such corrections are unavailable in literature.

Extensions of the GLD model to include plastic anisotropy effects were developed by [Keralavarma and Benzerga, 2010] and a numerical implementation of that study in the form of an Abaqus User-defined subroutine can be found in [Kweon et al., 2016]

One of the shortcomings of the GLD model is the fact that it assumes a spheroidal shape for the voids. This issue was addressed recently by [Madou and Leblond, 2013a], [Madou and Leblond, 2013b] that obtained solutions to the more general case of ellipsoidal



void shapes.

### Void coalescence models

Micromechanical models for void coalescence hinge upon representative volume elements that localize strains within a narrow band representing the inter-void ligament. Early works on the subject include the well-known Thomason model [Thomason, 1985]. Thomason's model attempts to describe the limit load in square-prismatic and cylindrical voids in homomorphic RVE's, following much of the methodology that has been outlined (upper bound estimate by arbitrating kinematically admissible velocity fields within the inter-void ligament). Over the years, several corrections have been proposed to better describe its behavior in, for example, the limit of penny-shaped cracks [Benzerga, 2002].

Quite recently, a model for coalescence has been proposed that combines both tension and shear loading. The representative volume element of the Torki-Benzerga-Leblond (TBL) model [Torki et al., 2015] can be seen in Fig. 2.14.

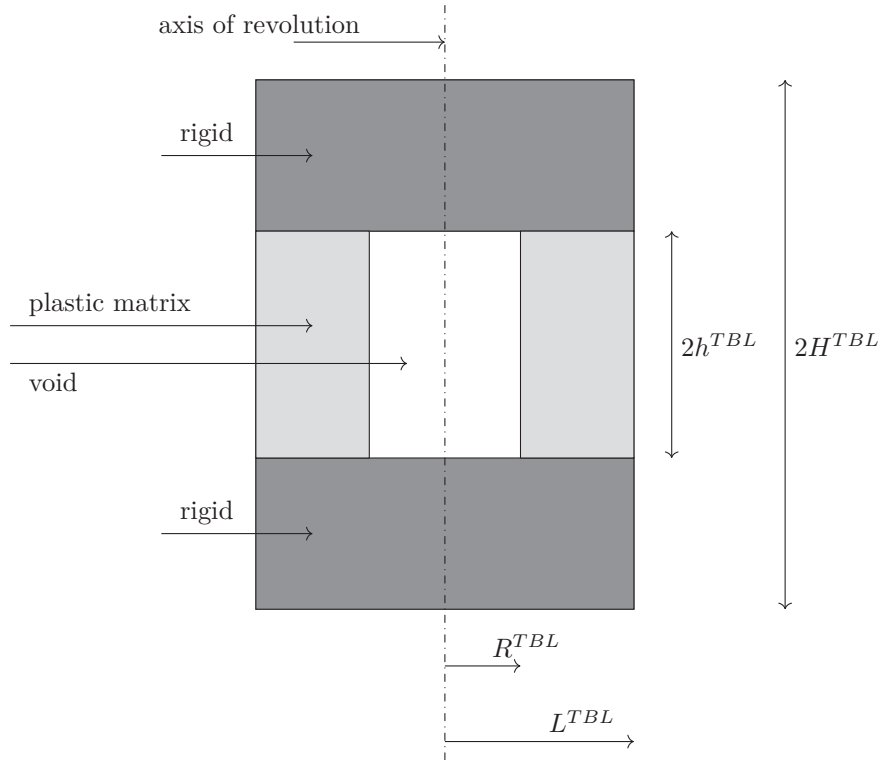


Figure 2.14 – Cylindrical RVE for TBL coalescence criterion

The TBL's' RVE consist of a cylindrical volume with a cylindrical void volume in its interior bordered at the top and bottom by a rigid layer. Limit analysis allowed the authors to define

the following yield surface  $\phi^{TBL}(\Sigma^v, \chi_{TBL}, w_{TBL})$ ,

$$\phi^{TBL,mod} = \begin{cases} \frac{(|\Sigma_{33}| - t^{TBL}\Sigma^{surf})^2}{b^2(\Sigma^{vol})^2} + 4\frac{\Sigma_{31}^2 + \Sigma_{32}^2}{l^2\tau^2} - 1 & , |\Sigma_{33}| \geq \Sigma^{surf} \\ 4\frac{\Sigma_{31}^2 + \Sigma_{32}^2}{l^2\tau^2} - 1 & , |\Sigma_{33}| \leq \Sigma^{surf} \end{cases} \quad (2.58)$$

where,  $\Sigma^{vol}(\chi_{TBL})$ ,  $\Sigma^{surf}(\chi_{TBL}, w_{TBL})$  and  $t^{TBL}(\chi_{TBL})$  are weighted values of the limit stress in the matrix ( $\sigma_y$ ) that depend on the key geometric quantities in Eq. 2.59.  $t^{TBL}$ ,  $b$  and  $l$  are parameters fit to cell model calculations. All parameters can be found in Appendix A.

$$\chi_{TBL} = \frac{R^{TBL}}{L^{TBL}} \quad ; \quad w_{TBL} = \frac{h^{TBL}}{R^{TBL}} \quad ; \quad \lambda_{TBL} = \frac{L^{TBL}}{H^{TBL}} \quad (2.59)$$

## 2.4 Ultra low cycle fatigue

Ultra low cycle fatigue is defined here as the deterioration of material properties under large amplitude cyclic loading of typically less than 10 or 20 cycles. Currently there are two common approaches used in the characterization of ultra low cycle fatigue life of structural components in civil engineering structures.

The first approach, phenomenological in nature, dates back as far as [Manson, 1953] and [Coffin, 1954] with the widely known Manson-Coffin relation for low-cycle fatigue given in Eq. 2.60.

$$\frac{\Delta \varepsilon^p}{2} = b(2N_f)^c \quad (2.60)$$

where  $\frac{\Delta \varepsilon^p}{2}$  represents the cyclic amplitude of plastic strain and  $2N_f$  the number of reversals or twice the number of cycles to failure ( $N_f$ ).

Extensions of Eq. 2.60 to multiaxial fatigue appeared shortly thereafter with an approach proposed by [Yokobori et al., 1965] to use as strain measurement the octahedral shear strain. Other empirical methods include energy models which express fatigue life as a function of the plastic work performed during loading ([Garud, 1981]), and critical plane models whose aim is both to predict fatigue life and the dominant failure plane ([Fatemi and Socie, 1988]). A comprehensive review of multiaxial fatigue from the low to high cycle can be found in [Socie and Marquis, 1999].

In so far as the validity of Eq. 2.60 can be put into question in the presence of large scale yielding <sup>3</sup>, more recently work has been carried out to investigate properties of M-C

---

<sup>3</sup>most of the experimental results in literature's had been conducted within a range between  $10^2$  and

type laws in the ultra low cycle fatigue regime (*c.f.* [Kuroda, 2002], [Tateishi et al., 2007], [Xue, 2008]). It was found that around 50 cycles if one wishes to unify ULCF and low-cycle fatigue predictions, certain corrections have to be employed to take into account an observed decrease in ULCF in that range (*w.r.t.* to the low cycle fatigue regime under  $10^4$  cycles). However, the predictions to ULCF considering only cycles below that transition regime using this type of empirical formulae remain remarkably consistent - see Fig. 2.15. Since ULCF applications (*e.g.* earthquake induced failure) typically experience a low number of cycles of amplitudes whose resistance falls within the range of low-cycle fatigue, M-C relationships are deemed a suitable approach to ULCF.

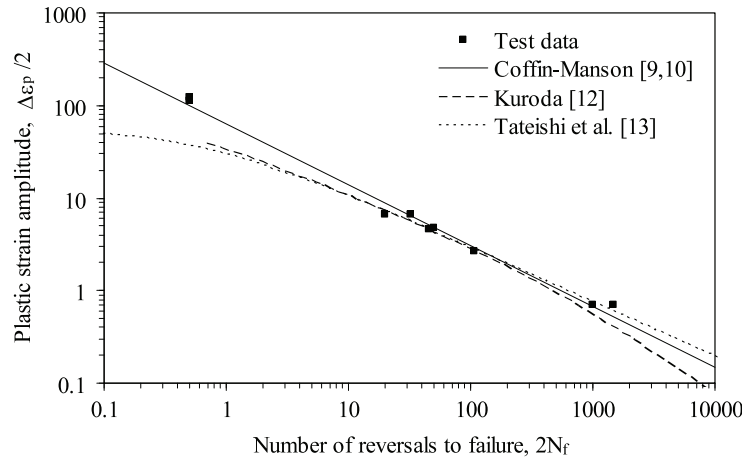


Figure 2.15 – Illustration of Manson-Coffin type approaches in a hot-rolled S355J2H steel - from [Nip et al., 2010a]

Examples of applications to structural components of M-C type of relations include the ULCF resistance of base plate liquid storage tanks [Prinz and Nussbaumer, 2012a], [Prinz and Nussbaumer, 2012b] and braces for steel frames [Nip et al., 2010b].

The second approach, more physics based, draws on insights provided by micromechanical models. In [Kanvinde and Deierlein, 2004] an ULCF design criterion was developed that drew on the works of [McClintock, 1968], [Rice and Tracey, 1969], [Hancock and Mackenzie, 1976] where for monotonic loading fracture strain is characterized by its relation with the stress triaxiality (*cf.* Eq. 2.61).

$$\eta_f^{mon} = \int_0^{\varepsilon_{eq,f}^p} \exp(1.5T) d\varepsilon_{eq}^p \quad (2.61)$$

$\eta_f^{mon}$  represents a material property that defines fracture over a minimum volume of material.

---

$10^4$  cycles

## Chapter 2. Background and state of the art

---

This minimum volume is inherently linked to the length scale most relevant to the fracture process. Different measures for this so called characteristic length ( $l^*$ ) have been proposed like the average material grain size or void diameter at failure ([Kanvinde and Deierlein, 2004]). In [Kanvinde and Deierlein, 2004] it is also proposed that the resistance set by  $\eta_f^{mon}$  should be decreased as a function of *damage* processes happening in the material. Those *damage* processes, it is proposed, are closely related to the accumulation of plastic strain as measured by  $\varepsilon_{eq}^p$ . This relation is mathematically expressed in

$$\eta_f^{cyclic} = f(damage) \cdot \eta_f^{mon} = \exp(-\lambda_D \varepsilon_{eq}^p) \cdot \eta_f^{mon} \quad (2.62)$$

where  $\lambda_D$  is a constant parameter to be estimated with experiments. Note the exponential decay nature tied to the increase in demand, a characteristic also present in 2.60. This is also consistent with maximum entropy estimations of a damage accumulation processes [Bhate et al., 2012].

Characterization and calibration of parameters that define  $\eta_f^{cyclic}$  have been the subject of intense research ([Myers et al., 2005], [Myers et al., 2010], [Myers et al., 2014], [Cooke and Kanvinde, 2015]).

Weld influence in ULCF has also been studied in [Myers et al., 2009]. In this work, it was found that the variability of  $\eta_f^{cyclic}$  in the Heat Affected Zone (HAZ) was greater than in base material by a factor of almost two. Although that conclusion was based on few test results, it is an important account to take note of. Fig. 2.16 summarizes the FEM approach in that report, where analyses in the commercial software package Abaqus of a welded column-to-base-plate connection with a complete joint penetration weld along the flange was made. Here, a strategy was used where a coarse mesh model of the connection simulates with sufficient accuracy the global moment-rotation curves measured in tests. Subsequently, sub-models of critical zones with refined meshes were conducted as to evaluate laws of the type shown in Eq. 2.62. Of particular interest to this thesis is the element size and type used in those analyses. Here, quadratic reduced integration hexahedra elements with reduced integration (element C3D20R) were used throughout the sub-models. The size of the elements were picked so that the volume sampled by an integration point would be consistent with a volume representative of the characteristic length  $l^*$  (taken to be within the range defined by [Kanvinde and Deierlein, 2004] between  $60\mu m$  and  $500\mu m$  for most structural steels).

Recently an extension of this micromechanical approach to characterize ULCF in low-triaxiality regimes has been proposed in [Smith et al., 2014].

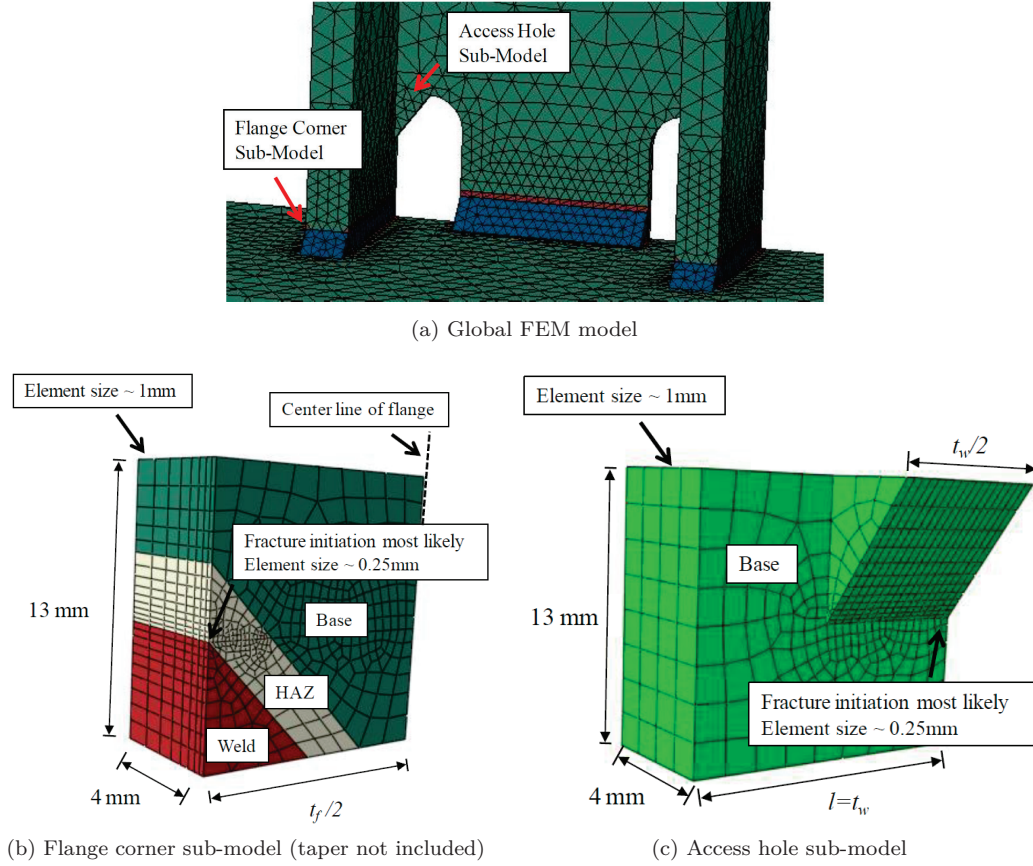


Figure 2.16 – FEM modeling of weld fracture under ULCF of column to base plate connection - adapted from the work of [Myers et al., 2009]

Applications of this approach have been reported in modeling beam to column connections in moment resisting frames ([Zhou et al., 2012], [Zhou et al., 2014]), column base plates ([Myers et al., 2009]), forensic examinations of failures in earthquake events ([Kanvinde et al., 2011]) as well as bracing members [Fell et al., 2008]

Less used in the context of civil engineering for ULCF are explicit<sup>4</sup> micromechanical models. Cyclic loading of metals is often associated with modeling the material's plastic response with kinematic hardening to some extent because of the Bauschinger effect. An important consideration in modeling porous ductile media with kinematic hardening versus isotropic hardening is the sensitivity to the yield surface curvature to the load path. For materials that exhibit a significant amount of work-hardening, non-proportional load paths can lead to significant differences in predicting the evolution of porosity inside a material [Mear and Hutchinson, 1985].

<sup>4</sup>by which it is meant that material degradation is taken into account by an explicit physical variable such as the void volume fraction

In so far as it is known that fracture strains under ULCF are lower than in monotonic load, one can envision that this can be modeled in the context of the Gurson model as increase in porosity due to cyclic loading - henceforth denoted porosity ratcheting. One fact that is important to note is that the original Gurson model does not predict ratcheting effects on the porosity due to cyclic loading under constant triaxiality and a rigid-ideally-plastic material ([Devaux et al., 1997]).

Unit cell calculations similar to the ones by [Koplik and Needleman, 1988] have been reported by [Besson and Guillemer-Neel, 2003] which suggest that unit cells with a matrix of nonlinear isotropic power law material show porosity ratcheting under cyclic loading. Similar results have also been reported in [Gilles et al., 1992] and [Devaux et al., 1997].

An extension of the Gurson model proposed by [Leblond et al., 1995] that can qualitatively simulate the effects of porosity ratcheting can be seen in Eq. 2.63

$$\phi^{LDP} = \frac{\|\boldsymbol{\Sigma} - \mathbf{A}\|^2}{(\rho\sigma_{y,0} + (1-\rho)\Sigma_1)^2} + 2q_1 f \cosh\left(\frac{q_2}{2} \frac{(\boldsymbol{\Sigma} - \mathbf{A}) : \mathbf{I}}{(\rho\sigma_{y,0} + (1-\rho)\Sigma_2)}\right) - 1 - (q_1 f)^2 \quad (2.63)$$

where  $\mathbf{A}$  is the macroscopic backstress tensor,  $q_1$  and  $q_2$  constant parameters fit to unit cell calculations ([Tvergaard, 1982], [Tvergaard and Needleman, 1984], [Tvergaard, 1990]),  $\rho$  a parameter between 0 and 1 that weighs the amount of isotropic and kinematic hardening (purely isotropic  $\rightarrow \rho = 0$ ; purely kinematic  $\rightarrow \rho = 1$ ) and  $\Sigma_1, \Sigma_2$  are history dependent parameters that are able to qualitatively incorporate porosity ratcheting. Although proposing an extension of the Gurson model to kinematic hardening that does not incorporate explicitly ratcheting, [Besson and Guillemer-Neel, 2003] also suggests using parameters  $q_1$  and  $q_2$  to take this phenomenon into account.

It is important to take note that the evolution law associated with the backstress (chiefly its direction) is not as trivial a subject as it might seem due to the fact it may have both deviatoric and mean stress components. For example, [Mear and Hutchinson, 1985] suggests that the backstress rate should be co-directional with  $\boldsymbol{\Sigma} - \mathbf{A}$ , whereas [Besson and Guillemer-Neel, 2003] suggests  $\mathbf{D}^p$  for that direction. Influence regarding this choice will be discussed more explicitly in Chapter 5 for the GLD model. More recently [Klingbeil et al., 2016] proposed a direction equal to the deviatoric part of  $\mathbf{D}^p$ .

## **2.5 Summary**

This chapter presented the necessary context to the work carried out in this study.

It addressed the issues involved in finite strain plasticity that one needs to understand the implementation of the material model in Chapter 5. It focused on the question of objectivity and showed an example of a well known problem in kinematic hardening that arises in the presence of large body rotations.

This chapter also provided an introduction to DIC to understand the measurements made throughout the experiments presented in Chapters 3 and 4. This synthesis is important in particular for the speckle pattern methodology because full-field measurements in the presence of high strain gradients depend significantly on the distance of sample points and the area over which the measurements are averaged. Here, precise definitions were given to unambiguously set the scope for the discussions in Chapter 4.

A brief state of the art that described current approaches to modeling ductile fracture as well as ultra low cycle fatigue was given. That discussion will be able to put into context the decisions made in modeling of small-scale specimens with void growth to coalescence models in Chapter 5 and also the FEM models of tube-to-plate joints in Chapter 6 suggested as a design approach.





## 3 Material characterization and behavior

This chapter presents the results of an experimental campaign designed to gather data on the structural steel used in this thesis to study ultra low cycle behavior. The chapter will focus on two main themes: firstly on the characterization of basic material and microstructural properties (Sections 3.1 and 3.2); secondly on describing the fracture behavior of small scale experiments under monotonic and large amplitude cyclic loading (Sections 3.3 and 3.4). The main idea behind the small scale experimental testing program is that the geometric properties of the specimens assure a reasonably uniform state of applied load through a controlled cross-section (a notch). This fact would allow to state that the material's behavior can be satisfactorily approximated by the behavior of the small scale specimen itself. Interpretation of test results within Sections 3.3 and 3.4 will discuss to which extent it is reasonable to do so and provide insights for the micromechanical model presented in Chapter 5.

### 3.1 Characterization of basic material properties

The material studied in the thesis is the high strength structural steel S770QL (not included in EN10210-1 [European Committee for Standardization, 2006a] for tubular sections but whose properties can be derived from EN10025-6 [European Committee for Standardization, 2009] for flat plate products). Steel specimens were cut out of circular hot rolled seamless tubes of two different diameters ( $101.6 \times 10mm$  and  $219.1 \times 22.2mm$ ) produced by the same supplier but from different plants. Two diameters were used because in order to be able to machine a double notched specimen geometry a minimum of  $15mm$  diameter tube had to be used (see Section 3.4). Smooth round bar and single notched round bar specimens were cut out of the  $101.6 \times 10mm$  tubes because this is the tube diameter used in the welded tube to plate test campaign in Chapter 4.

### Chapter 3. Material characterization and behavior

The steel's chemical composition for both tubes is presented in Table 3.2, as provided by the inspection certificates, and later confirmed by Energy Dispersed X-ray Spectroscopy (EDX) conducted at the Interdisciplinary Center for Electron Microscopy at EPFL (CIME) <sup>1</sup>. It is a quenched and tempered steel with martensitic microstructure and a grain size on the order of  $10\mu m$  (between 5 to  $15\mu m$  - see Fig. 3.1a).

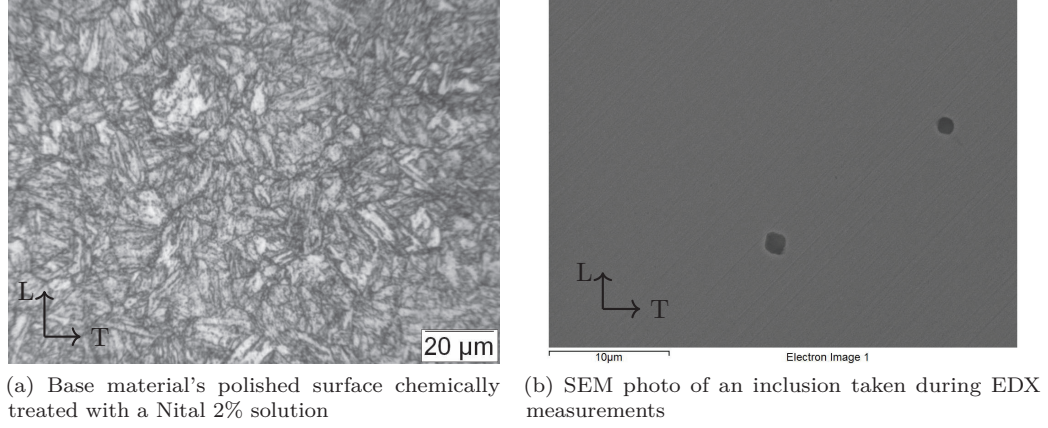


Figure 3.1 – Micrographs of S770QL's microstructure

Smooth bar tension tests of  $6mm$  diameter were conducted in accordance with [ASTM, 2013b]. Strains were measured using DIC by tracking targets laid on the specimens similar to what is shown in the single notched tests in Fig. 3.8a. 5 tests were conducted and the average results are summarized in Table 3.1.

Table 3.1 – Summary table for smooth round bar tension tests and power law parameters

	$\sigma_{y,0}$ (MPa)	$\sigma_u$ (MPa)	$E_{mod}$ (GPa)	$\Delta L/L_0$	$\bar{\epsilon}_f$	$K$ (MPa)	$n$
Mean	915	1024	197	20.79%	115.0 %	615	0.245
StD	11.6	11.02	4.0	1.35%	2.8%	27.82	0.015
COV	1.27%	1.08%	2.02%	6.47%	2.44%	4.54%	6.02%

StD - standard deviation; COV - coefficient of variation

In Table 3.1,  $\sigma_y$  is the yield stress<sup>2</sup>,  $\sigma_u$  is the ultimate stress,  $E_{mod}$  the modulus of elasticity,  $\Delta L/L_0$  the elongation to fracture,  $\bar{\epsilon}_f$  the logarithmic strain after failure (given by  $2 \ln D_0/D_f$ )<sup>3</sup>. Also given in this Table are  $K$  and  $n$  the coefficients of an isotropic hardening power law defined in Eq. 3.1 with a  $\sigma_{y,0}$  equal to 700 MPa - see Fig. 3.2. The material exhibits a small yield plateau and a ratio between ultimate and yield stress on the order of

<sup>1</sup>although an extensive analysis was not conducted, *w.r.t* the nature of inclusions, measurements by EDX detected the presence of aluminum oxides and calcium sulfides

<sup>2</sup>subscript 0 stands for initial value

<sup>3</sup> $D_0$  is the initial diameter of the round bar and  $D_f$  the diameter after failure

1.10.

$$\sigma_y = \sigma_{y,0} + K(\varepsilon_{eq}^p)^n \quad (3.1)$$

Fig. 3.2 shows the results of the 5 tests and an average power law in terms of uniaxial true stress ( $\sigma$ ) vs. true strain ( $\varepsilon$ ). These measures were derived from the classical considerations of material volume conservation represented by Eq. 3.2 and the engineering stress <sup>4</sup> and strain <sup>5</sup> measured during the tests. Note that these relationships are only valid up to necking of the specimens.

$$\sigma = \sigma_{eng} (1 + \varepsilon_{eng}) \quad , \quad \varepsilon = \ln(1 + \varepsilon_{eng}) \quad (3.2)$$

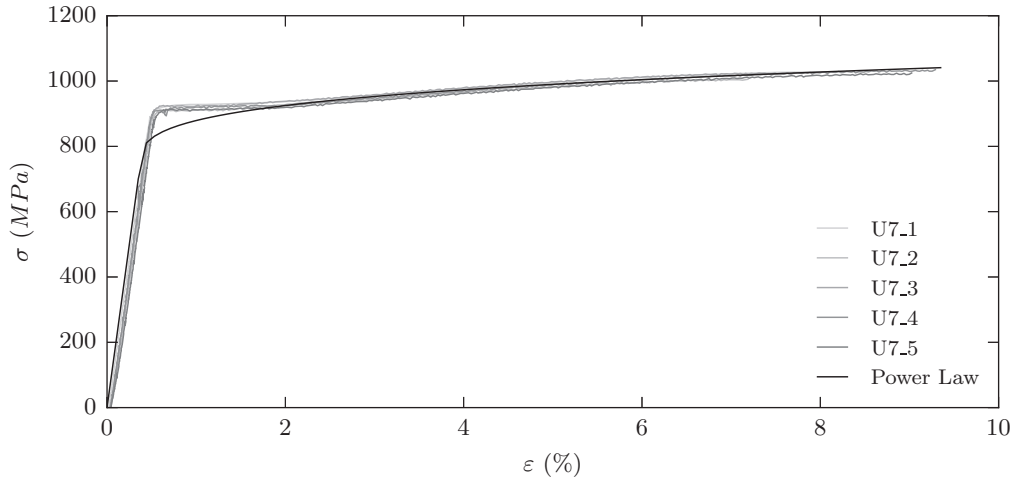


Figure 3.2 – True stress vs true strain curve for uniaxial tests and fitted Power Law

The power law depicted in Fig. 3.2 plays a fundamental role in this thesis because all the FE analyses in Chapters 5 and 6 follow exactly the same uniaxial half-cycle curve, albeit with a nonlinear kinematic hardening model (the Chaboche model presented in Chapter 2, whose coefficients can be consulted in Table A.1). The main justification for this fact is to give a uniform basis of comparison in the analyses for the material hardening properties. Although some variability in those results can be associated with the variability of hardening properties, having a uniform basis of comparison was deemed more important. Another relevant consideration to be made is the fact that due to the lack of knowledge of yield stress values above the necking strain, these are often inferred from FE analyses by changing material

<sup>4</sup>  $\sigma_{eng} = F/A_0$  with  $F$  the force measured in,  $A_0$  the initial cross-sectional area

<sup>5</sup>  $\varepsilon_{eng} = \Delta L/L_0$ ,  $L_0$  being the initial length between the two DIC sights (gauge size)

parameters like  $\sigma_{y,0}$ ,  $K$  and  $n$  to match force-displacement test curves (the variables that are actually measured). This can potentially lead to non-unique solutions and considerable errors in estimating plastic strains as discussed in [Cooke and Kanvinde, 2015]. This epistemic shortcoming is indeed something to be underlined but, in the absence of better and more local measurements, a fact one has to resign to and make the best of. Although not covered in this thesis, calibration procedures for material laws are all important. Here, a simple procedure to try to minimize the difference between force-displacement curves in tests and FEM using a global optimization algorithm (Probabilistic Global Search Lausanne (PGSL) [Raphael and Smith, 2003]) was used to obtain the set of values presented in Table 3.1 but a detailed exposition of it is deemed unnecessary. A comprehensive discussion of a variant of the same methodology using Particle Swarm Optimization (PSO) can be found in [Smith et al., 2014].

As a complementary note, it may be observed that non-linear cyclic hardening parameters were determined solely based on the half cycle curve in Fig. 3.2 and not based on a stabilized cyclic hysteresis curve. This simplification is considered sufficient for this steel as will be clear in chapters to come. This is mainly due to the fact that the amount of isotropic hardening was found to be negligible.

## 3.2 Inclusion content

This section presents the work done in determining the inclusion content of S770QL steel. Determining the inclusion content is an important step in the material characterization because it serves as a proxy measurement of an initial void volume ratio. Procedures are here briefly summarized and main results reported.

Fig. 3.3 presents a schematic of the geometry and orientation of metallographic specimens cut out from tube to plate specimens used in Chapter 4.

Fig. 3.4 shows a convention followed for naming of the specimens used for determining the inclusion content. The following region designations were used: BM - Base Material (BM); W - Weld (W) material; WT - near Weld Toe (WT) of a loaded tube specimen. For WT cases, unfortunately representative samples near the weld toe were hard to get, leading to sampling away from the weld toe. This means that the statistics that are presented are closer to the BM than to the actual weld toe. All specimens were cut and placed in a resin mold and then polished to within  $1\mu m$  of abrasive (diamond) particles. No etching was used. Two types of analyses were conducted - see Fig. 3.5.

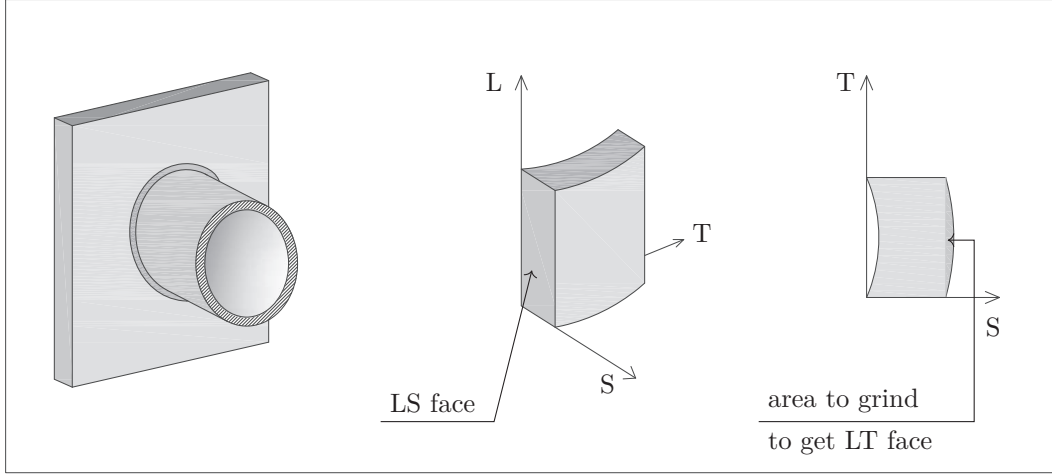


Figure 3.3 – Orientation of micrographs *w.r.t.* to tube sample

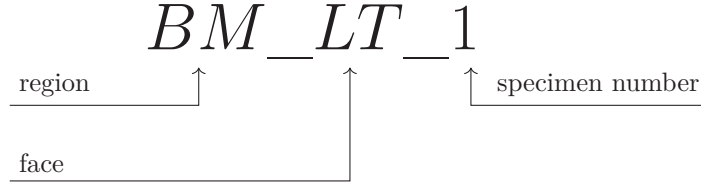


Figure 3.4 – Specimen designation for metallographic analyses

The first is designated by Automatic Image Processing (AIP) and consists of a script that for each micrograph of a given specimen executes the following procedure: 1 - opens the file; 2 - removes the scale; 3 - converts the image to black and white; 4 - given a certain threshold of greyscale (depends on the lighting conditions and the camera sensor of the optical microscope) recognizes a certain pixel as being an inclusion and marks it as pure black and all other pixels as white; 5 - counts the number of black pixels in the image and divides it by the total number of pixels of that image to obtain an estimate of the void volume fraction  $f_0^{AIP}$ . The total area surveyed with this method follows [ASTM, 2013a] *i.e.* a minimum of  $160mm^2$ .

The second method consists of building a digital drawing file(*e.g.* *dxf*) in a Computer-Aided Design (CAD) software with demarcations of inclusions taken manually over the micrographs. Two types of basic elements were used in the demarcations: circles and ellipses (for more elongated inclusions). Using a script that is able to parse through the *dxf* file, one is able to obtain key geometric information like the position and areas for circles (from the inclusion's diameter  $D_{inc}$ ) as well as Aspect Ratio (AR) and orientation for ellipses ( $\theta_{ell}$ ). Due to the high number of inclusions in a certain micrograph only about 1 to 5% of the AIP area is

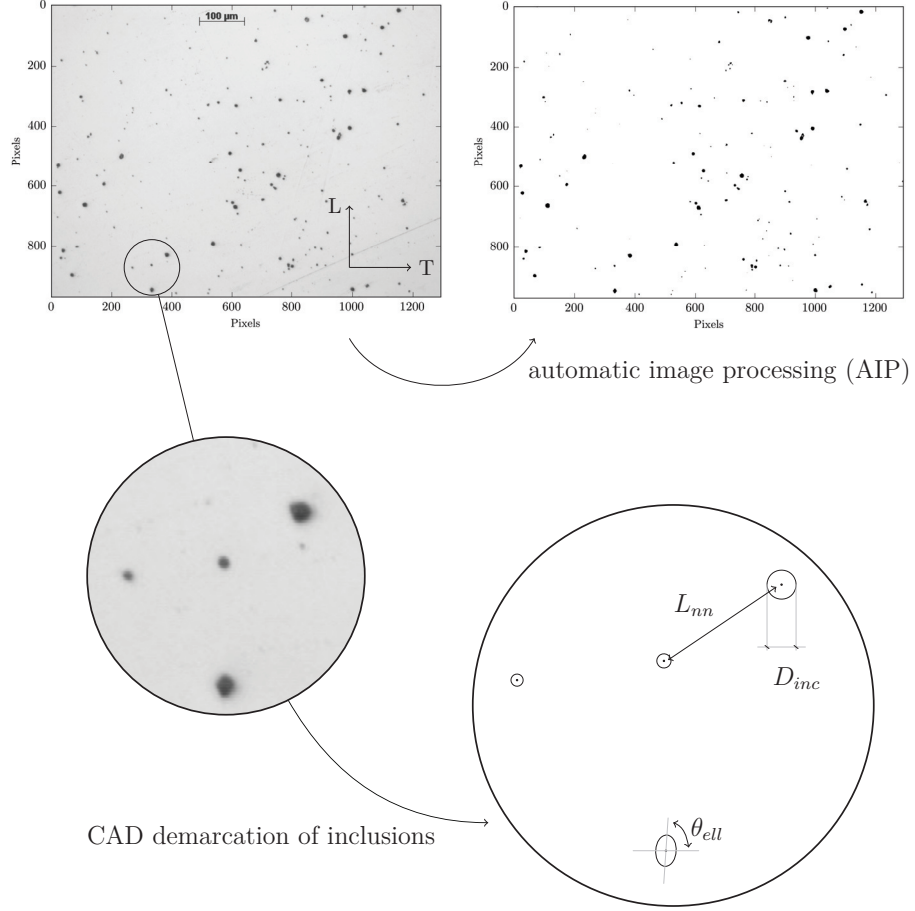


Figure 3.5 – Steps in metallographic analyses of inclusions

covered.

A statistical analysis was carried out on the variables obtained with the CAD method and probability distribution functions were fit to the observed data. Parameters for these functions (namely Generalized Extreme Value (GEV) and Beta distributions) were obtained using maximum likelihood estimation integrated in the scientific library package SCIPY [Oliphant, 2007] for the scripting language Python within the IPython environment [Pérez and Granger, 2007]. Probability-Probability (PP) plots and parameters can be found in Appendix B as well as more detailed data. Nearest neighbor calculations were also conducted with SCIPY using a spatial KDTree search, which organizes a set of spatial points according to the closest euclidean distance ( $L_{nn}$ ). Searches were conducted using both circles and ellipses drawn over micrographs. For the definition of the inclusion ligament size ratio, *i.e.* the inclusion diameter divided by its corresponding nearest neighbor distance ( $\chi_{inc}$ ), only circles were used.

Table 3.3 summarizes the data obtained for both methods by specimen. Fig. 3.6 gives an example of the frequency of observed  $D_{inc}$  and compares it to a GEV probability density function fit with maximum likelihood estimation to specimen BM\_1\_1.

Some key observations can be made with the data from the CAD analyses. The inclusion content does not vary significantly between weld and base material. The mean size of circular inclusions is on the order of  $5\mu m$  in diameter. The inclusion volume ratio for AIP revolves around  $3e-3$  but can vary significantly *w.r.t* measurements done by CAD, chiefly because it involves a smaller sample size. Elongated inclusions measured on LT faces do not have a preferential orientation *i.e.*  $\theta_{ell}$  is just as likely to be found as 0 or 90 Deg. On LS (through thickness) faces a slight tendency was found for ellipses to be oriented in the longitudinal direction.

It is important at this stage to point out how this knowledge can be leveraged in micro mechanical models. In Chapter 2 it was seen that these models rely on internal variables such as the porosity, void aspect ratio, void orientation and intervoid spacing. One can now quantify these variables.

For the porosity, the inclusion content can serve as proxy measurements because voids will tend to nucleate and grow around them. Since not all inclusions will nucleate voids, it seems reasonable to assume as an initial void volume ratio ( $f_0$ ) a value on the order of magnitude of inclusion volume ratio, for example  $1e-3$ .

For the shape and orientation of the voids, since no preferential direction for ellipses was clearly observed, the hypothesis will be made that the material behavior will be best described by initially spherical voids.

In void coalescence models, such as the TBL presented in Chapter 2, a key quantity for defining the limit load on the inter-void ligament is the ratio between the void and the RVE's radii. The statistics performed in this section *w.r.t.* the void's size and nearest neighbor distance can arguably provide some insight into the order of ratios that can be considered in coalescence criteria. According to Table 3.3 for base material that value should arguably be around 0.2.

Table 3.2 – Chemical Composition of S770QL

	C	Mn	Si	Ni	Cr	Mo	V	Cu	P	S	$C_{eq}^{LIW}$	$C_{eq}^{AWS}$
101.6 × 10mm	0.16%	1.44%	0.39%	0.54%	0.10%	0.37%	0.07%	0.17%	0.012%	0.002%	0.55%	0.61%
219.1 × 22.2mm	0.15%	1.37%	0.25%	0.12%	0.40%	0.45%	0.00%	0.16%	0.012%	0.001%	0.57%	0.61%

Table 3.3 – Summary of inclusion statistics

Specimen	$\overline{D}_{inc} (\mu m)$	$\overline{L}_{nn} (\mu m)$	$\overline{AR}$	$\overline{\chi}_{inc}$	$f_0^{CAD}$	$f_0^{AIP}$
BM_LT_1	5.50	63.00	0.65	0.15	0.0023	0.0038
BM_LS_1	3.07	38.43	0.42	0.16	0.0016	0.0026
BM_LT_2	6.57	36.00	0.52	0.28	0.0080	0.0047
BM_LS_2	7.01	37.45	0.57	0.29	0.0108	0.0033
BM_LS_3	4.47	53.89	0.61	0.12	0.0027	0.0026
W_LT_1	4.66	31.50	0.54	0.31	0.0038	0.0037
WT_LT_1	3.30	31.52	0.43	0.17	0.0026	0.0013
WT_LT_2	5.76	31.50	0.59	0.29	0.0083	0.0036
WT_LS_1	7.40	41.91	0.57	0.28	0.0096	0.0042

(over line indicates the average measurement)

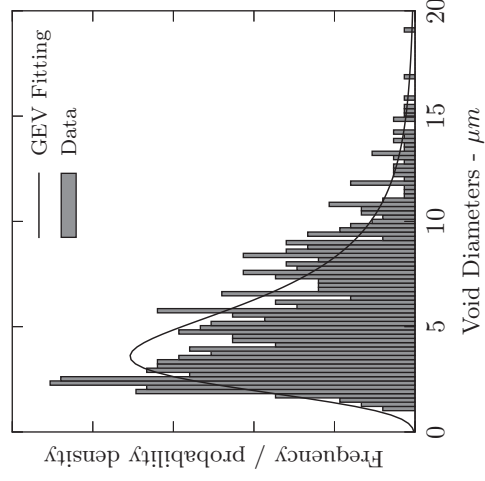


Figure 3.6 – Circular diameters and GEV distribution fitting for BM\_LT\_1



### 3.3 Single notched round bar specimens

This section presents the experimental program conducted on Single Notch (SN) round bar specimens and the main observations from those tests.

A picture of the test setup of a cyclically loaded specimen (see detailed description in Subsection 3.3.2) and a schematic of the geometry around the notch are presented in Fig.3.8. Fig. 3.7 shows the convention followed in the designations of the specimens. Table 3.4 presents the nominal geometries of the specimens. Two different nominal geometries were used in order to vary triaxialities at the center of the specimens.

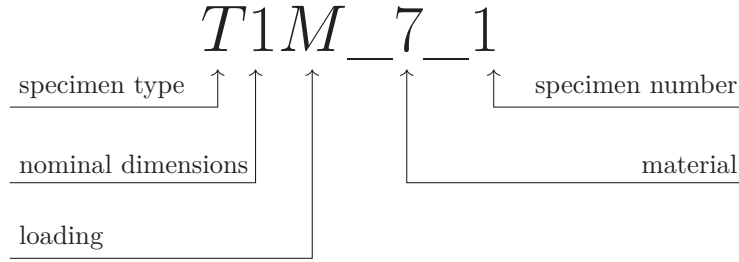


Figure 3.7 – Specimen designation for single notched specimens

Machining these specimens proved to be a delicate task given its steel grade. So much so that the surface roughness of the delivered specimens was deemed unacceptable and additional polishing of the notch area was required. This caused notch geometries to deviate significantly from the nominal dimension in Table 3.4. Definitive geometries, including the measurement height between DIC targets ( $h^{SN}$ ), and triaxialities at failure obtained by FEM models conducted in Chapter 5, are given in Appendix C for each specimen.

Tests were conducted in a 200 kN Walter and Bai (W+B) universal testing machine.

Results in this section will often be discussed in terms of the observed displacement; it is important to clarify what is meant by this. All tests are conducted using displacement control. But that displacement is controlled at the machine level, which is to say that it does not take into account two relevant variables: slippage occurring on the grips and elastic compliance of the specimen itself. In order to detach from those factors one needs to discuss

Table 3.4 – Single notch specimens nominal geometry

Type	$D^{SN}$ (mm)	$D_n^{SN}$ (mm)	$R_n^{SN}$ (mm)
T1	6	3	1.5
T2	6	2	2.0

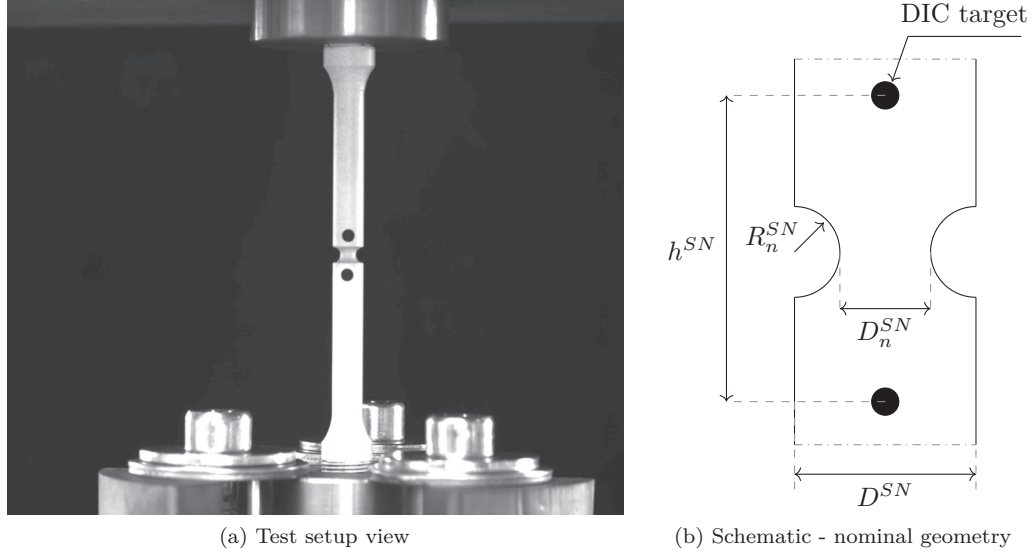


Figure 3.8 – Geometry of single notched specimen

test results using a more local displacement measure, like the one between two DIC targets. This is the measure that is used throughout the rest of the thesis when displacement is mentioned. It will be shown in Chapter 5 that FE models built with the length between the DIC targets can accurately capture the elastic part of the loading, hence incorporating implicitly the elastic compliance associated with that distance.

### 3.3.1 Monotonic loading

6 monotonic tests were conducted on single notch specimens. All tests were performed using displacement control at the machine level. Speed of the tests were conducted such that engineering strain rate using DIC targets is of the same order of magnitude as those conducted on the smooth bar tests which is in accordance with [ASTM, 2013b] - *i.e.* between 0.05 and 0.5  $mm/mm/min$ .

Fig. 3.9 shows force-displacement curves typically observed in these tests. Here one can observe that shortly after elastic loading, once the specimens start to yield at about 0.1mm displacement, the maximum force steadily decreases until a sudden change in slope occurs (abrupt loss of stiffness). That steady decrease in force is due to the non-linear geometric effect of cross sectional necking. This geometric effect is a phenomenon that can be modeled quite accurately in FE analyses as will be seen in Chapter 5. The abrupt loss of stiffness is associated with material failure, more specifically a transition between the more diffuse damage mechanism of void growth to the coalescence of voids and the formation of a crack in

### 3.3. Single notched round bar specimens

the material (see [Pineau et al., 2016] and Chapter 2). This transition will be the definition used for failure in monotonic tests - *cf.* Fig. 3.9 .

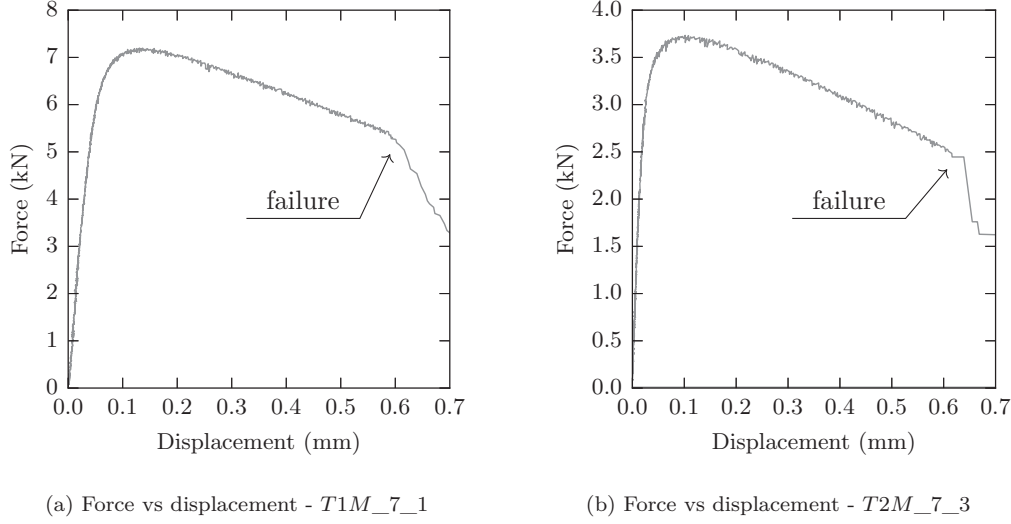


Figure 3.9 – Example of monotonic force-displacement curves for single notched specimens

The fracture surfaces were observed to follow the typical cup-cone shapes widely reported in literature. Fig. 3.13 shows the fractured surfaces for the examples above; they are accompanied by cyclically loaded specimens for comparison. More comments on this subject are given in subsection 3.3.2.

#### 3.3.2 Large amplitude cyclic loading - ULCF

Exceedingly important in conducting cyclic loading in single notch specimens is assuring their vertical alignment and minimizing slippage at the ends. The latter point will be evident when one compares cyclic loading between single notch and double notch tests in subsection 3.4.2.

Fig. 3.10 shows the test setup used in the cyclic tests. The W+B testing machine consists of a frame whose upper grip is fixed to the frame and the lower grip is attached to an hydraulic actuator. Two plates were bolted to the grips: the upper plate to the upper grip, the lower plate to the lower grip - see Fig. 3.10a. Both ends of SN specimens were threaded. A threaded hole was made on the upper plate so as to screw a specimen directly in it. By tightening a nut just below the upper plate one neutralizes the play in the threads between the plate and the specimen. It is important to note that this assures perpendicularity and close-to-fixed boundary conditions. On the lower end of specimen, a nut and its counter are

### Chapter 3. Material characterization and behavior

screwed onto the specimen and then the nut and counter tightened against each other to neutralize gaps in the threads. Then the lower end plate is raised by the hydraulic actuator to touch the counter nut, introducing a residual amount of compression in the specimen (around -0.1 to -0.2kN). Once this is achieved, a three-piece outer ring is placed around the nut and counter nut and then bolted to the lower plate - see Fig. 3.10b. This ensures that in tensile loading, tension goes through the specimen to the nut and counter nut, then through the bolts and into the lower plate which is attached to the hydraulic actuator. In compression, load is transferred directly from the counter nut to the lower plate.

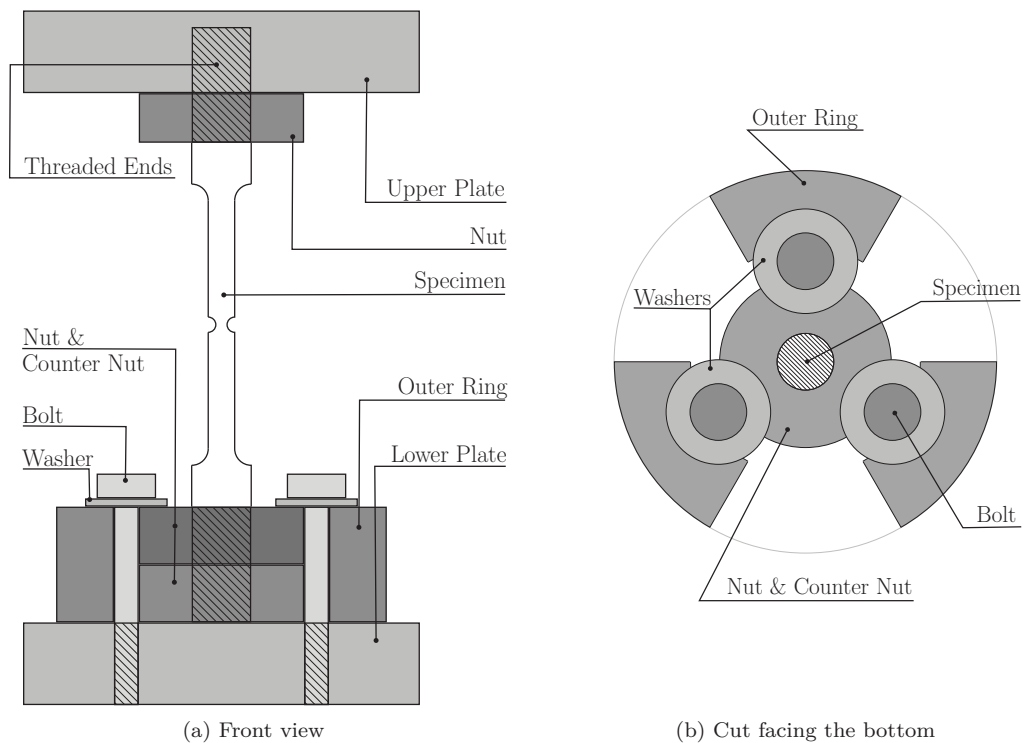


Figure 3.10 – Schematic of cyclic test-setup for single notched specimens

Specimens are loaded with a fixed displacement range at the machine level centered around the initial configuration. Fig. 3.11 shows two typical hysteresis curves for single notched specimens. Here, thanks to the setup, one can see that rigorous displacement ranges are measured at the notch, until a drop in stiffness is observed that causes a greater local displacement range at the notch level for the same machine level displacement range.

Of note is the fact that the stable cyclic behavior seen in Fig. 3.11b supports the statements made in Section 3.1 that this material is characterized by limited to no isotropic hardening. Also of note is the non-linear geometric behavior in compression. Notice the difference in slope after yielding when compression is involved due to the enlargement of the diameter

### 3.3. Single notched round bar specimens

of the notch versus the ever decreasing force after yielding in tension when the diameter is reduced.

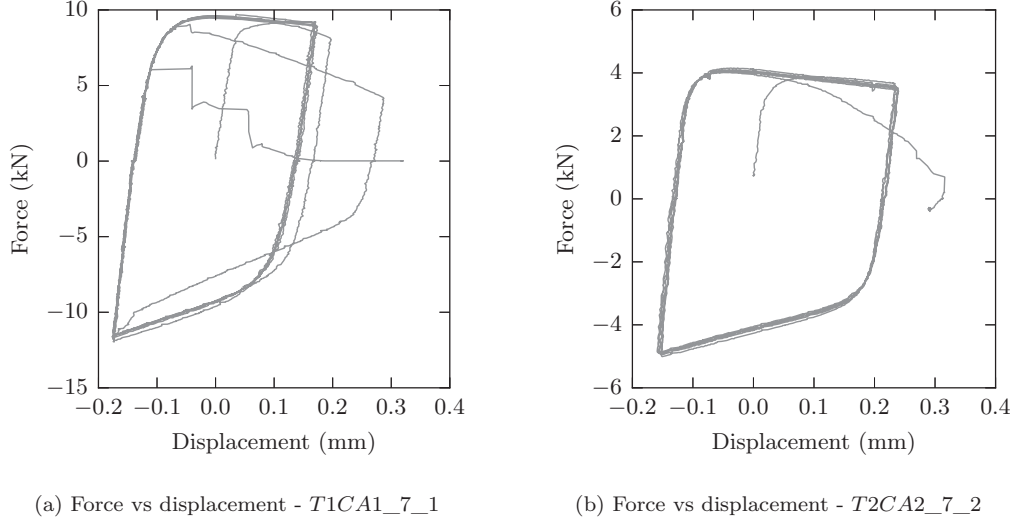


Figure 3.11 – Example of hysteresis curves for single notched specimens

Definition of failure in these specimens is more subtle than in the monotonic case, especially when discussing cases which involve more than five cycles (as the cases shown in Fig. 3.11). Consider the case of a test with 10 cycles to failure - Fig. 3.12. In the close-up view of the test (Fig. 3.12b) one can observe a gradual decrease in the load carrying capacity of the specimen. It is an illustration of the problem of differentiating phenomena near the boundaries of two categories - in this case between softening due to an increase in porosity and the formation of an actual crack inside the specimen. To establish a definite criterion, failure is defined as a 10% decrease in the load carrying capacity at constant amplitude. It is considered that such a bound is indicative of the incipience of fracture (*i.e.* the following cycle is characterized by a significant loss in stiffness).

As a side note, one can see a conspicuous artifact in the hysteresis curve in Fig. 3.12a in a tension half-cycle between -0.1 and 0 mm of displacement. This was due to a problem in the electronics of the W+B control system. It caused a very sudden jerk in the actuator that loaded and unloaded the specimen within the sample rate of 10 Hz. At the end of that sudden movement, the specimen was reloaded and resumed its path along the stable cycle.

With respect to fracture surfaces, consider Fig. 3.13. It depicts fractured single notch specimens in monotonic and cyclic loading for the purposes of comparison.

Featured in Fig. 3.13 are the fracture surfaces of specimens whose load displacement curves

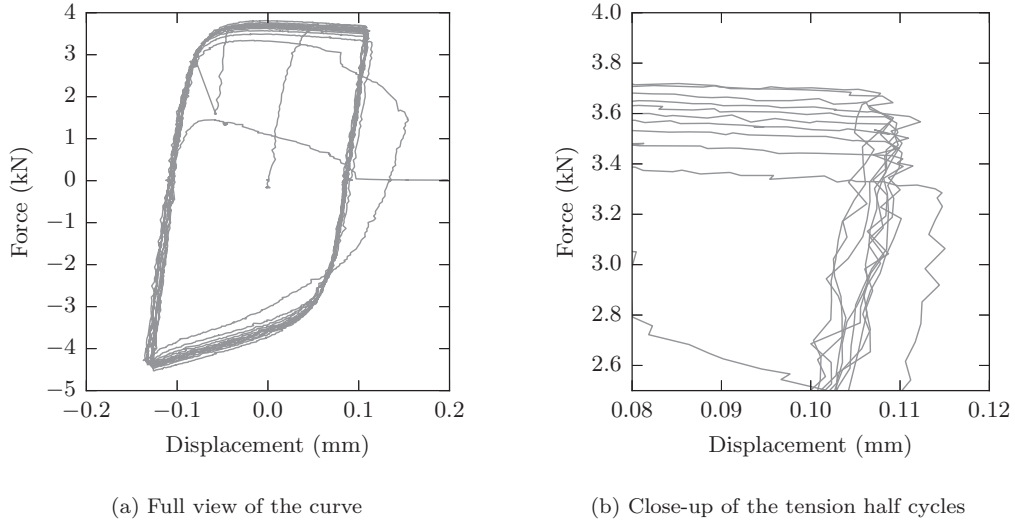


Figure 3.12 – Hysteresis curve for specimen *T2CA1\_7\_1*

can be seen in Fig. 3.9 and 3.11. For the monotonically loaded specimens, as was mentioned, one can observe a mix of flat and slant fracture reflected in the cup-cone shape. When compared to specimens loaded cyclically, a key observation can be made about the fracture surface at the center of the specimens: they are a shade of grey lighter than in the monotonic case. This statement comes in fact as a consequence of the type of fracture surface.

Consider Fig. 3.14 that shows SEM micrographs of the fracture surface at the center of some of the single notched specimens in Fig. 3.13. Cyclic loading fracture surfaces are observed to be in general flatter than their monotonic counterparts which are more rugged or castellated. For the monotonic case a smaller dimple diameter is observed *w.r.t.* to the cyclic loading in Fig. 3.14b, suggesting that failure<sup>6</sup> under monotonic loading happens at smaller porosities. Support for this statement can be found in Fig. 3.12b where a gradual decrease in the stiffness of the specimen suggests an increase in porosity which is quite stable. These observations, however, constitute merely an hypothesis. In fact in literature one can find precisely the opposite suggestion [Kanvinde et al., 2007]. Clarification of this issue is of interest for the definition of more precise failure criteria in future works and can be achieved by performing a series of interrupted tests<sup>7</sup> under ULCF where, at different stages of loading, the notch area would be cut and open and the evolution of porosity more objectively quantified.

Also observed in these fracture surfaces is the fact that dimples are in general shallower in *T2CA2\_7\_2* than in the monotonic case. This statement comes not only from vi-

<sup>6</sup>one recalls the definition of failure regarding a sizeable and abrupt loss in the stiffness of the specimen, which in cyclic loading the 10% drop in load carrying capacity is taken to be representative of

<sup>7</sup>similarly to Fig. 2.6

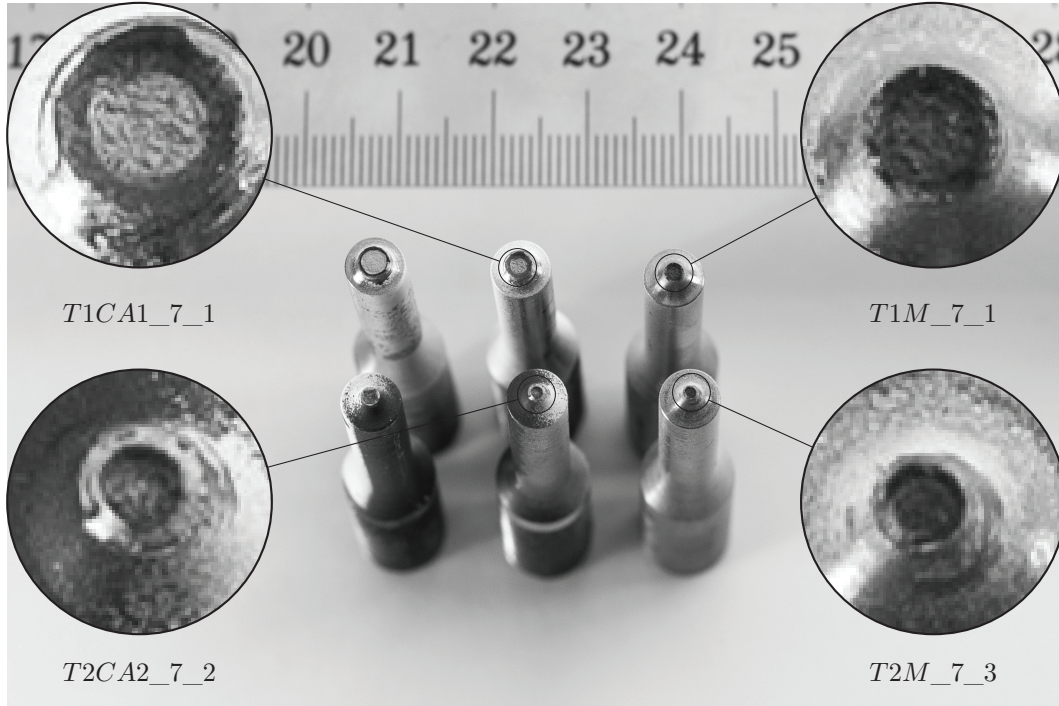


Figure 3.13 – Single notched specimen fracture surfaces

sual inspection of the micrographs but also from focal 'depth' measurements in the SEM. From ten randomly chosen measurements of dimple geometry on specimens *T2M\_7\_3* and *T2CA2\_7\_2*, the average aspect ratio ( $w$ ) was 3.16 and 0.52, respectively. Reports of shallower dimples as a result of ULCF in single notched specimens can also be found in [Kanvinde and Deierlein, 2004]. This observation will be important in informing the cyclic micromechanical model developed in Chapter 5. Shallower dimples intuitively also justify the higher degree of light reflectivity observed. For more micrographs at different scales one refers to Appendix C.1.

Turning back to Fig. 3.13, one can see for *T1CA1\_7\_1* an inner light grey circle surrounded by a darker grey ring. One would be tempted to name this a zone of very shallow dimples, but conferring with the hysteresis curve in Fig. 3.11a a more keen interpretation would be that before the last tensile half cycle there was a compression half cycle in a cross section which already possessed an internal full-fledged crack and so, in that compression half cycle, there are two fracture surfaces being pressed together that smooth out the microscopic roughness of the dimples. As such, in the case of *T1CA1\_7\_1*, one cannot state that the lighter grey area is due to shallower dimples. It is the result of two separate surfaces being crushed - see the flat planes in Fig. 3.14c. It seems to be, rather, a good measure of the internal crack size in the penultimate tensile half cycle.



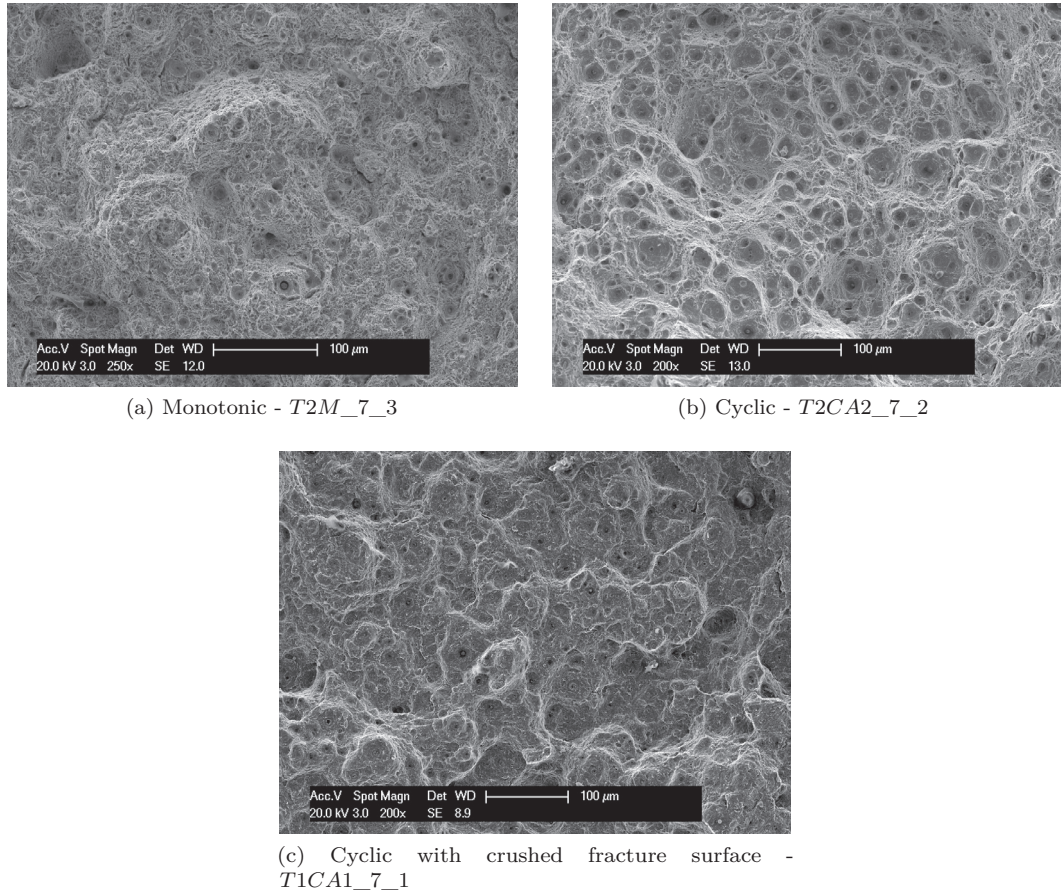


Figure 3.14 – SEM micrographs of typical fracture surfaces at the center of single notched specimens for high-strength structural steel S770QL under monotonic and large amplitude cyclic loading

## 3.4 Double notched specimens

This section presents the experimental program conducted on Double Notch (DN) tubular specimens. Tests were conducted in an MTS Tension-Torsion Fatigue machine at the Laboratory of Applied Mechanics and Reliability Analysis (LMAF) in EPFL. The machine's ranges are  $\pm 100\text{kN}$  maximum load for tension and  $\pm 1100\text{Nm}$  for torque. Machine grips consist of a segmented circular ring that is hydraulically tightened around the surface of a specimen. Load is transferred by friction in the grips.

As mentioned in Section 3.1, these specimens were cut out of a  $219.1 \times 22.2\text{mm}$  tube. Specimens were  $100\text{mm}$  in length. They were then machined to  $15\text{mm}$  diameter, drilled to create a tubular section and then an external and an internal notch were machined. The nominal dimensions of the notch area can be seen in Fig. 3.15.



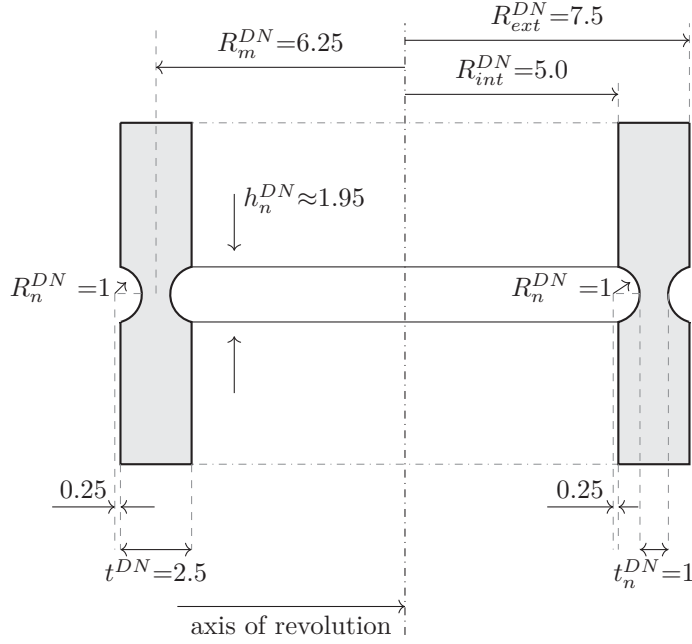


Figure 3.15 – Nominal notch geometry for double notched tube - cross-section cut (dimensions in mm)

An adapter piece (40mm in diameter) was used to provide higher contact area between the specimen (15mm in diameter) and the grips of the machine. This was an issue that came up from the fact that the testing machine's grips (15mm in diameter) could not achieve the required friction to be able to reach the ultimate load of the tubes in torsion. To address this problem, an adapter piece diameter was welded onto each specimen and a grip of 40mm in diameter was used. Care was taken to ensure that the central zone of the specimen (*i.e.* the notched part) was not heated up to values higher than 150 – 200°C, so as not to temper the micro-structure in this area. The resulting contact area was sufficient and testing was resumed.

All tests were performed in displacement/rotation control at the machine level. 4 different ratios were used. They were defined as follows. First tests in monotonic pure tension and pure torsion were performed. Second, the average displacement and rotation at failure was obtained for tension and torsion respectively ( $\delta_f^{DN,machine}$  and  $\theta_f^{DN,machine}$ ). Lastly, with these values one can define the measures  $\rho^{DN}$  and  $P^{DN}$  as path ratios given by the expressions in Eq. 3.3.

$$P^{DN} = 1 - \frac{1}{1 + \rho^{DN}} \quad ; \quad \theta_f^{DN,machine} = \rho^{DN} \frac{\theta_f^{DN,machine}}{\delta_f^{DN,machine}} \delta_f^{DN,machine} \quad (3.3)$$

### Chapter 3. Material characterization and behavior

Table 3.5 summarizes the path ratios used.

Table 3.5 – Double notched - path ratios

Measure \ Path	1	2	3	4
$P^{DN}$	0	1	1/3	2/3
$\rho^{DN}$	0	$\infty$	1/2	2
$\arctan(\rho^{DN})$ (Deg)	0	90	26.6	63.4

Naming convention for double notch specimens can be found in Fig. 3.16. It is important to remark that, unlike in single notch specimens, the number after the Constant Amplitude (CA) label indicates the number of the proportional load path that was followed, not a different amplitude.

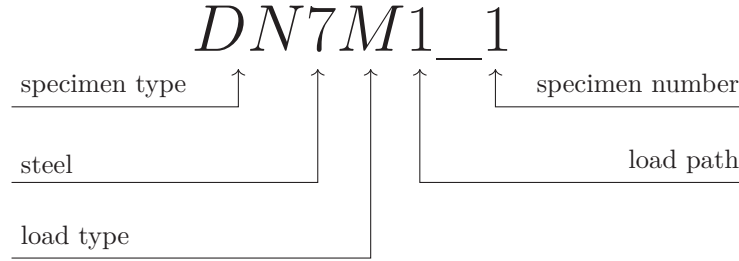


Figure 3.16 – Specimen designation for single notched specimens

Local measurements of displacement and rotation were captured using stereo DIC over a speckled pattern. Like in the case of single notched specimens, local measurements near the notch were used in the description of the loading that is applied to each specimen, as opposed to the testing machine's readings. This allows to remove the effects of slippage at the grip level in the analysis, as well as reducing the levels of elastic deformation of the specimen itself. The reference length used to measure the displacement and rotation is the same for all specimens and has a value of  $7.5mm$  - cf. Fig. 3.17.

One defines  $\delta^{DN}$  as the vertical displacement in the gauge length  $h^{DN}$ . To define a measure of rotation one should turn one's attention to Fig. 3.18. There one names  $\theta_{sec}^{DN}$  the rotation that a point on the surface goes through from the undeformed configuration to the deformed configuration *w.r.t.* its axis of revolution. The DIC software used in these tests can perform coordinate transformations and express displacement measures in cylindrical coordinates. One can observe an example of this in Fig. 3.19 for a specimen loaded in pure torsion ( $DN7M2\_2$ ). Standard calibration procedures were followed. Comparison of the elastic loading part (subject to higher errors because displacements are so small) with FEM models conducted with the same nominal geometry are a testament of the calibration procedure's

accuracy - *c.f.* Chapter 5.

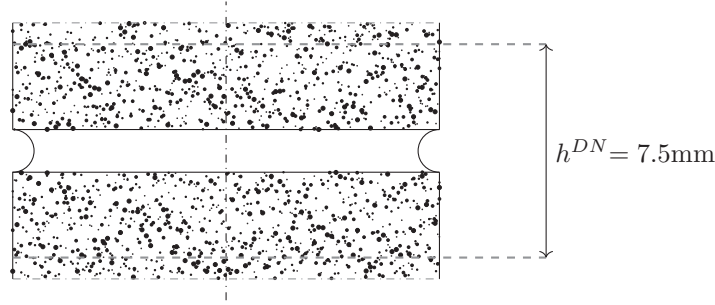


Figure 3.17 – Speckle pattern and gauge sections in DIC measurements for double notch tube specimens - front view

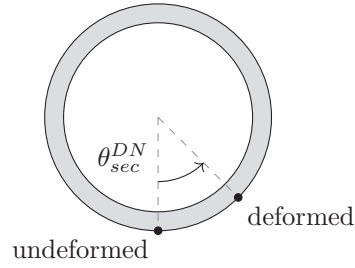


Figure 3.18 – Schematic of a transverse cut of the tube and definition of rotation  $\theta_{sec}^{DN}$

$\theta^{DN}$  is defined as the difference between the average of  $\theta_{sec}^{DN}$  along two horizontal lines on the surface of double notch specimens above and below the notch ('L0' and 'L1' in Fig. 3.19, respectively).

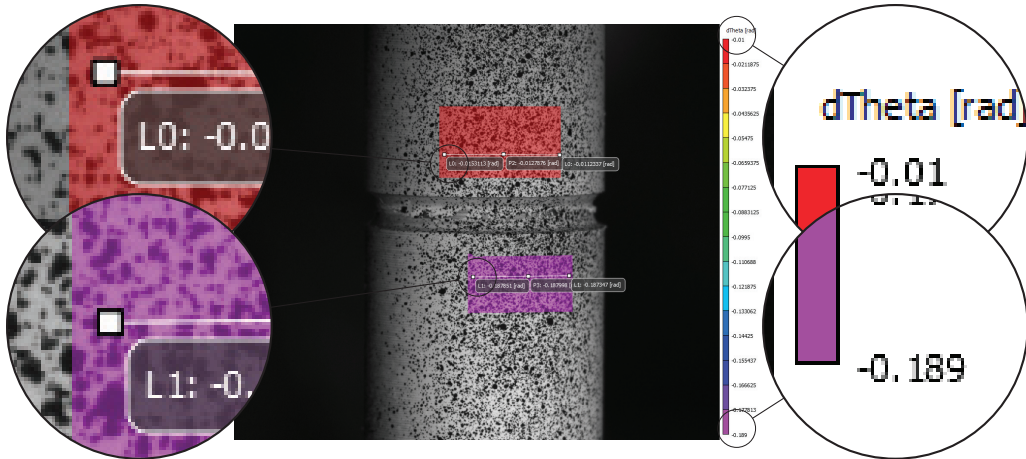


Figure 3.19 – Example of torque angle measurement with DIC. ' $d\theta_{sec}$ ' corresponds to  $\theta_{sec}^{DN}$

Axial force and torque measured in the load cell are denoted  $F^{DN}$  and  $M_t^{DN}$ , respectively.

### Chapter 3. Material characterization and behavior

---

Average axial stress ( $\sigma_n^{DN}$ ) and shear stress ( $\tau_n^{DN}$ ) over the notch section are defined by Eq. 3.4.

$$\sigma_n^{DN} = \frac{F^{DN}}{2\pi R_m^{DN} t_n^{DN}} \quad ; \quad \tau_n^{DN} = \frac{M_t^{DN}}{2\pi (R_m^{DN})^2 t_n^{DN}} \quad (3.4)$$

Key load ratios  $k^{DN}$  and  $k_T^{DN}$  are defined in Eq. 3.5.

$$k^{DN} = \frac{\sigma_n^{DN}}{\tau_n^{DN}} \quad ; \quad k_T^{DN} = \frac{\sigma_n^{DN}}{\tau_n^{DN} + \sigma_n^{DN}} \quad (3.5)$$

Let  $\delta_n^{p,DN}$  and  $\theta_n^{p,DN}$  be the plastic part of the displacement and rotation over notch, respectively, as defined by 3.6, where  $C_\sigma^{DN}$  and  $C_\tau^{DN}$  are elastic compliances that can be determined directly from test results. This expression assumes that all plastic deformation is concentrated in the notch area.

$$\delta_n^{p,DN} = \delta^{DN} - C_\sigma^{DN} F^{DN} \quad ; \quad \theta_n^{p,DN} = \theta^{DN} - C_\tau^{DN} M_t^{DN} \quad (3.6)$$

The total displacement and rotation ( $\delta_n^{DN}$  and  $\theta_n^{DN}$ , respectively) over the notch, however, still have contributions between the gauge section ( $g$ ) and the notch ( $n$ ). They are taken into account in Eq. 3.7

$$\delta_n^{DN} = \delta^{DN} - \frac{C_\sigma^{DN}}{1 + C_\sigma^{DN}/C_{\sigma g}^{DN}} F^{DN} \quad ; \quad \theta_n^{DN} = \theta^{DN} - \frac{C_\tau^{DN}}{1 + C_\tau^{DN}/C_{\tau g}^{DN}} M_t^{DN} \quad (3.7)$$

Approximate expressions for  $C_\sigma^{DN}/C_{\sigma g}^{DN}$  and  $C_\tau^{DN}/C_{\tau g}^{DN}$  can be found in [Barsoum and Faleskog, 2007].

Defining  $\dot{\varepsilon}_n^{p,DN}$  and  $\dot{\gamma}_n^{p,DN}$  as the rate of axial plastic strain and rate of plastic distortion (Eq. 3.8), one can provide a measure for the average equivalent plastic strain rate at the notch in 3.9 (additive decomposition of deformation rate, *cf.* [Faleskog and Barsoum, 2013]).

$$\dot{\varepsilon}_n^{p,DN} = \frac{\dot{\delta}_n^{p,DN}}{h_n^{DN} + \delta_n^{DN}} \quad ; \quad \dot{\gamma}_n^{p,DN} = \frac{R_m^{DN} \dot{\theta}_n^{p,DN}}{h_n^{DN} + \delta_n^{DN}} \quad (3.8)$$

$$\dot{\varepsilon}_{n,eq}^{p,DN} = \sqrt{\frac{4 \left( \dot{\varepsilon}_n^{p,DN} \right)^2 + \left( \dot{\gamma}_n^{p,DN} \right)^2}{3}} \quad (3.9)$$

The average equivalent plastic strain over the notch then becomes Eq. 3.10.

$$\bar{\epsilon}_{n,eq}^{p,DN} = \int \dot{\epsilon}_{n,eq}^{p,DN} dt \quad (3.10)$$

#### 3.4.1 Monotonic loading

A total of 12 monotonic tests were conducted on double notch tubular specimens, more precisely three per path ratio.

Fig. 3.20 shows the load path as applied at machine level and measured with the stereo DIC system. The differences in Fig. 3.20 are a clear example of the need to express tests on notched specimens in terms of the local measurements.

Another pertinent observation can be made on Fig. 3.20b *w.r.t.* the specimen's ability to deform. It is apparent that the path ratio between  $\delta^{DN}$  and  $\theta^{DN}$  strongly influences its ultimate fracture. For the purposes of comparison, one can express test results in terms of normalized stress ratios ( $k_T^{DN}$ ) and average plastic strain over the notch section. Since tests were performed in displacement/rotation control, the ratio between axial and shear stress is not assured to be kept constant throughout the test. A weighted average of  $k_T^{DN}$  with the equivalent plastic strain rate ( $\bar{k}_T^{DN}$  -see Eq. 3.11) was therefore used to express test results of the monotonic DN tests. Fig. 3.21 compares the monotonic tests results with that of [Faleskog and Barsoum, 2013] which were done on a similar type of high strength steel - Weldox960.

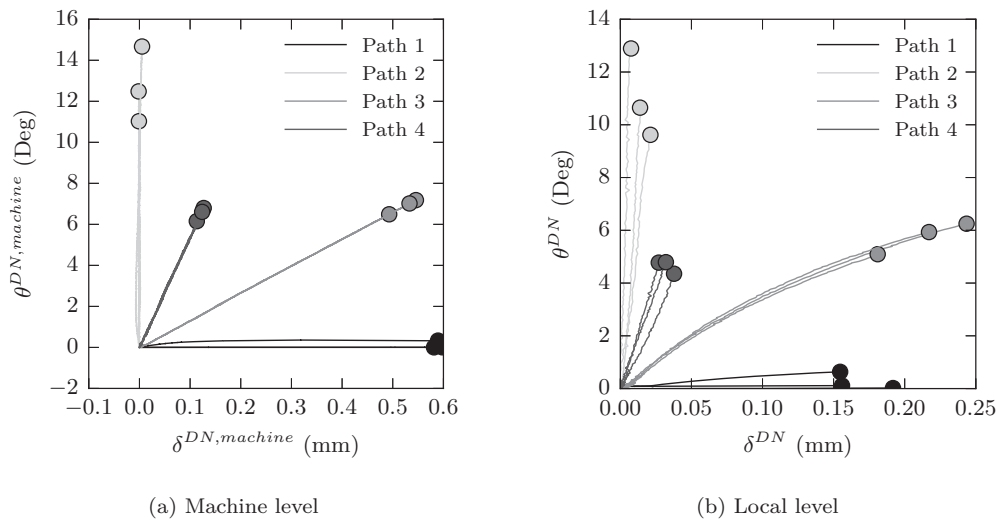


Figure 3.20 – Double notched specimen monotonic paths

$$\bar{k}_T^{DN} = \frac{\int \dot{\bar{\varepsilon}}_{n,eq}^{p,DN} k_T^{DN} dt}{\int \dot{\bar{\varepsilon}}_{n,eq}^{p,DN} dt} \quad (3.11)$$

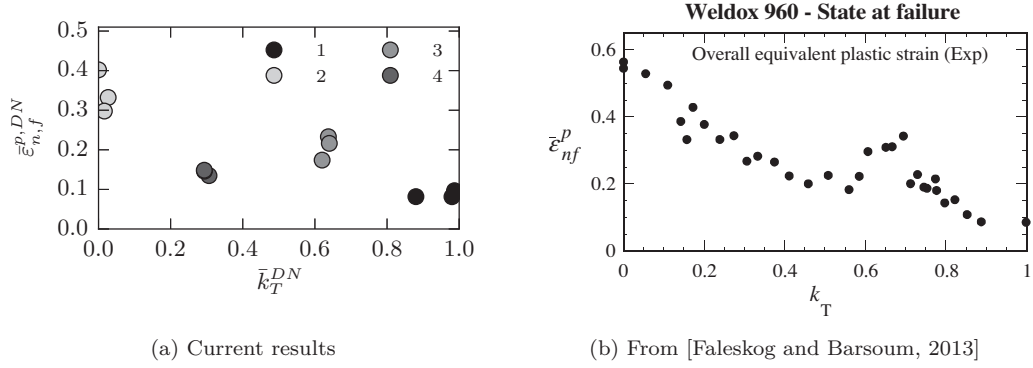


Figure 3.21 – Comparison of tests results to a similar type of steel

Average notch equivalent plastic strains were observed to be lower than that of Weldox 960. This correlates with a lower nominal fracture strains on smooth round bars - S770QL<sup>8</sup>:  $\bar{\varepsilon}_f = 115\%$ ; Weldox 960:  $\bar{\varepsilon}_f = 127\%$ . In both cases, there is a marked increase in ductility<sup>9</sup> around  $\bar{k}_T^{DN} = 2/3$  in comparison to uniaxial tests ( $\bar{k}_T^{DN} = 1$ ). In post-mortem inspections this was found to be correlated to two different modes of fracture. Comparing Fig. 3.22 to Fig. 3.23, one can see two different fracture surfaces: for the uniaxial case a slant fracture indicative of failure by plastic instability (Fig. 3.24); for  $\bar{k}_T^{DN} = 2/3$  a more rough and flat surface in the middle of the specimen is indicative of ductile tearing (Fig. 3.25) which subsequently becomes a slant type of failure. Also noteworthy in Fig. 3.24 is the fact that for a pure tension test one can observe the presence of elongated dimples in the circumferential direction of the tube, which is indicative of non-axisymmetric stress states (low Lode parameters).

The tendency of having rougher fracture surfaces associated with an increase in material ductility was also observed in shear dominated loadings (compare Fig. 3.27 to 3.28) which is natural considering it experiences more plastic deformation.

Fig. 3.26b shows the cross-section profile from a pure torsion test (load path 2). A clear distinction can be made between this case, which exhibits a flat surface perpendicular to the longitudinal axis of the tube, and tension dominated load paths (*c.f.* Fig. 3.24 and Fig. 3.25) where some form of slant fracture can be observed.

<sup>8</sup>the coefficients of the isotropic hardening law in that paper of the S770QL steel used in this study are the following:  $n=0.076$   $\varepsilon_N=0.0179$   $\varepsilon_S=0.0$

<sup>9</sup>taking  $\bar{\varepsilon}_{n,eq}^{p,DN}$  as a measure of the material's ductility

### 3.4. Double notched specimens

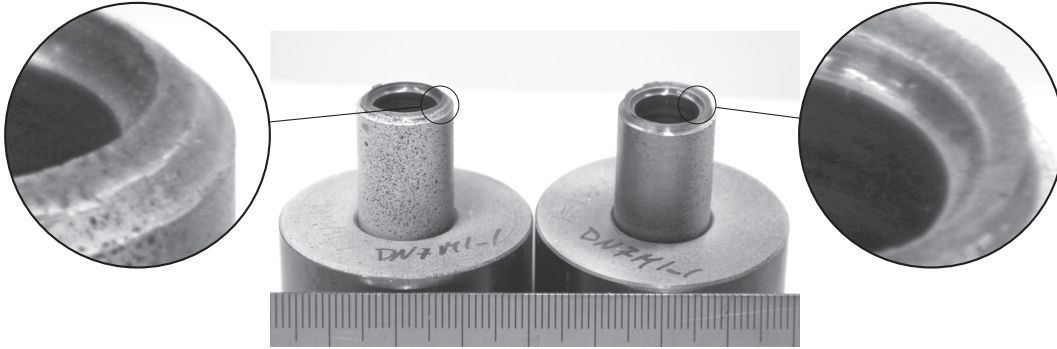


Figure 3.22 – Slant fracture in monotonic pure tension (path 1) double notched specimens

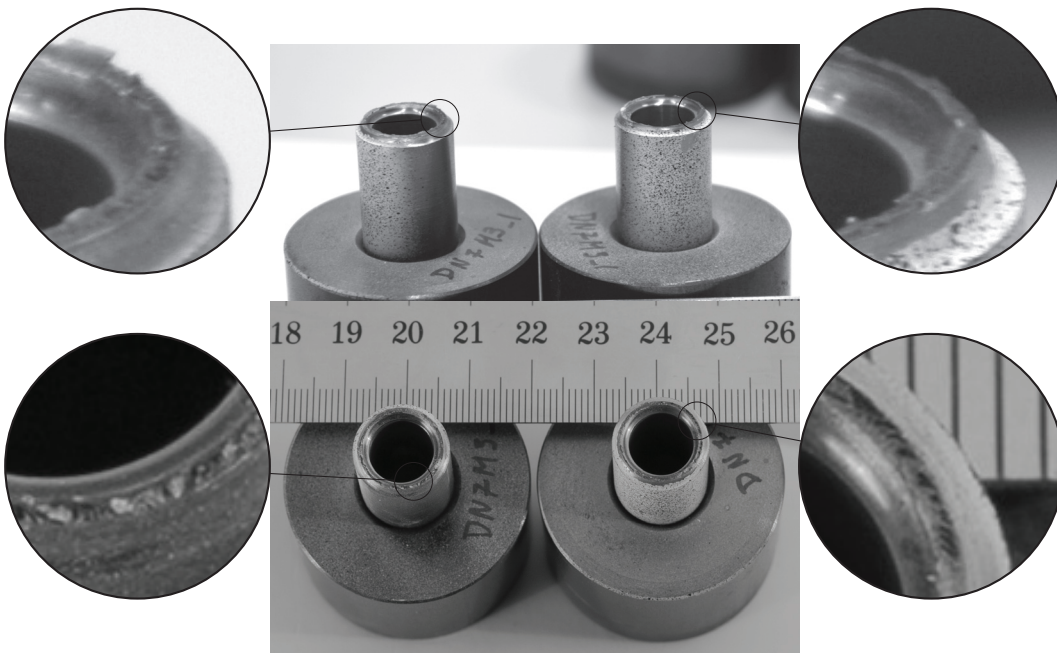


Figure 3.23 – Fracture surface in monotonic load path 3 in double notched specimens



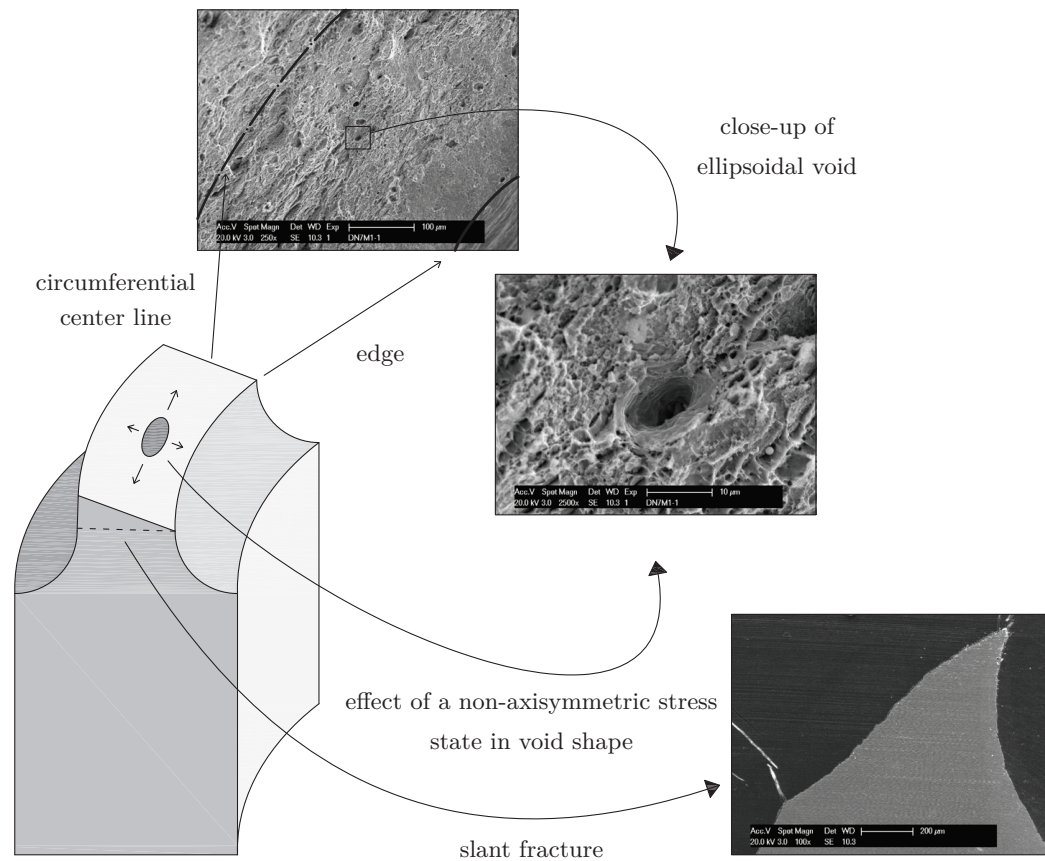


Figure 3.24 – Fractography of a double notched specimen loaded in monotonic pure tension - DN7M1\_1

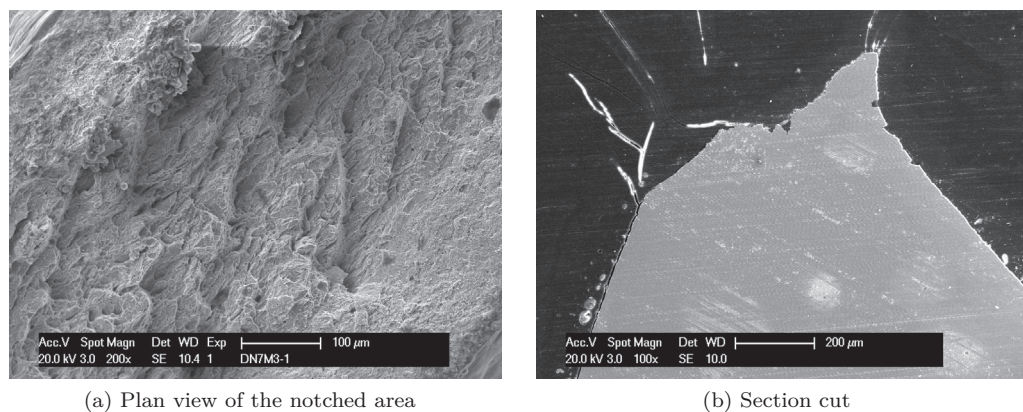


Figure 3.25 – SEM micrographs of fracture surface for specimen DN7M3\_1



### 3.4. Double notched specimens

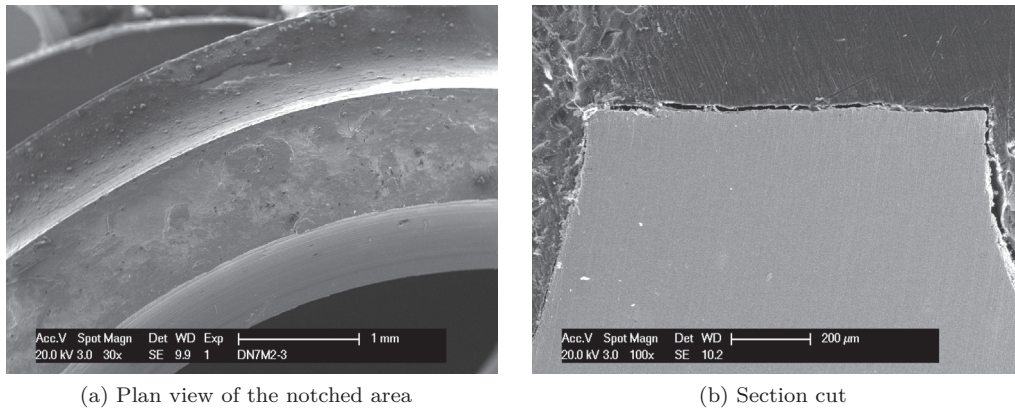


Figure 3.26 – SEM micrographs of fracture surface for specimen DN7M2\_3

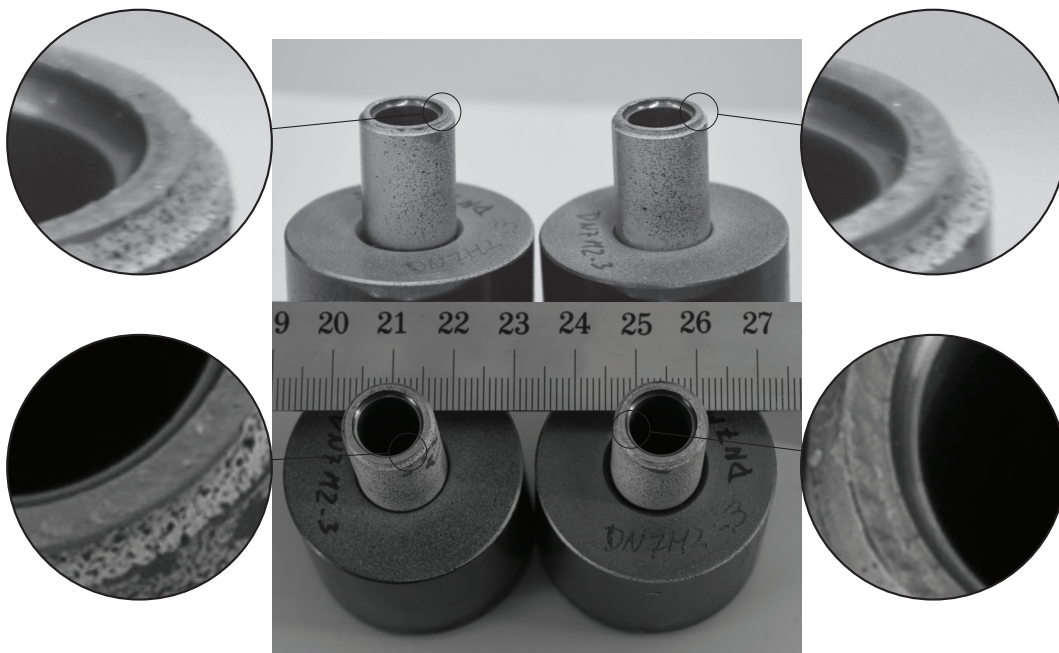


Figure 3.27 – Fracture surface in monotonic pure torsion (path 2) double notched specimens

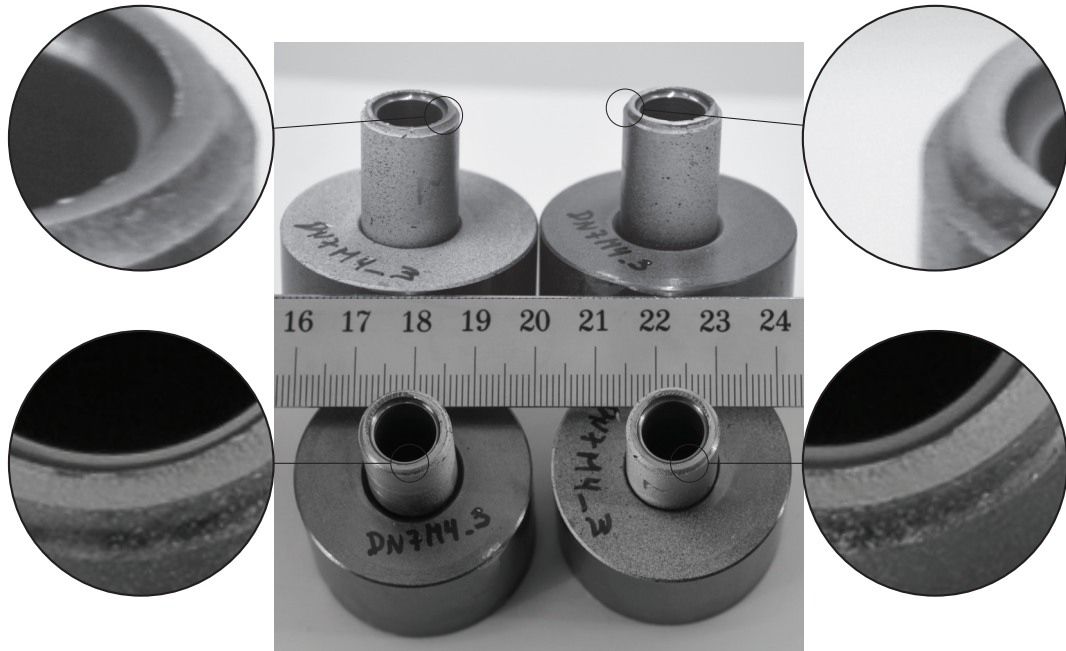


Figure 3.28 – Fracture surface in monotonic load path 4 in double notched specimens

### 3.4.2 Large amplitude cyclic loading - ULCF

In the sense that it can be of value to report less successful testing campaigns, this section presents some of the results under large amplitude cyclic loading in double notched tubes. 12 tests were performed with 3 tests per path ratio. A striking distinction in quality of results is seen in comparison to single notched specimens largely because of end conditions in loading the specimens. As can be seen in Fig. 3.29, this distinction comes from the difference in the prescribed boundary conditions at the grip level and the conditions observed at the notch.

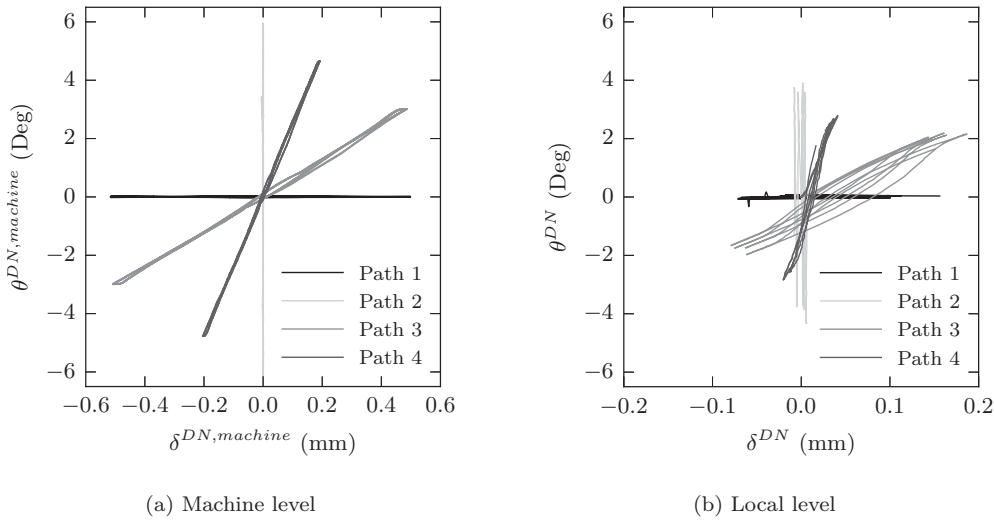


Figure 3.29 – Double notched specimen cyclic paths

As portrayed in Fig. 3.30, what were supposed to be constant amplitude grip level loading conditions, because of varying degrees of contact conditions between specimens, became significantly different loading histories applied to the notch. The smaller amplitudes of displacement at the notch led naturally to higher number of cycles.

Mixed load paths exhibited different modes of failure with respect to monotonic loading. This can be seen for path 3 in cyclic loading in Fig. 3.31 - to be compared with Fig. 3.23. A slant type fracture for pure tensile loading was still present.

Due to insufficient data from this campaign one will make an inference based on literature results and the data from the previous section under monotonic load. Consider, for example, the work of [Yokobori et al., 1965] that tested small thin-walled tubes of annealed mild steel in tension and torsion in low-cycle fatigue. These tests were conducted for numbers of cycles to failure ( $N_f$ ) as low as 100 and it was concluded that results when expressed in terms of

### Chapter 3. Material characterization and behavior

octahedral strains ranges vs  $N_f$  in double log-scale <sup>10</sup>, torsion is associated with a higher resistance curve than tension. From monotonic tests in the previous section that show the same trend for pure torsion and pure tension in terms of  $\bar{\varepsilon}_{n,eq}^{p,DN}$ , one will assume that this trend holds true also for the ULCF regime.

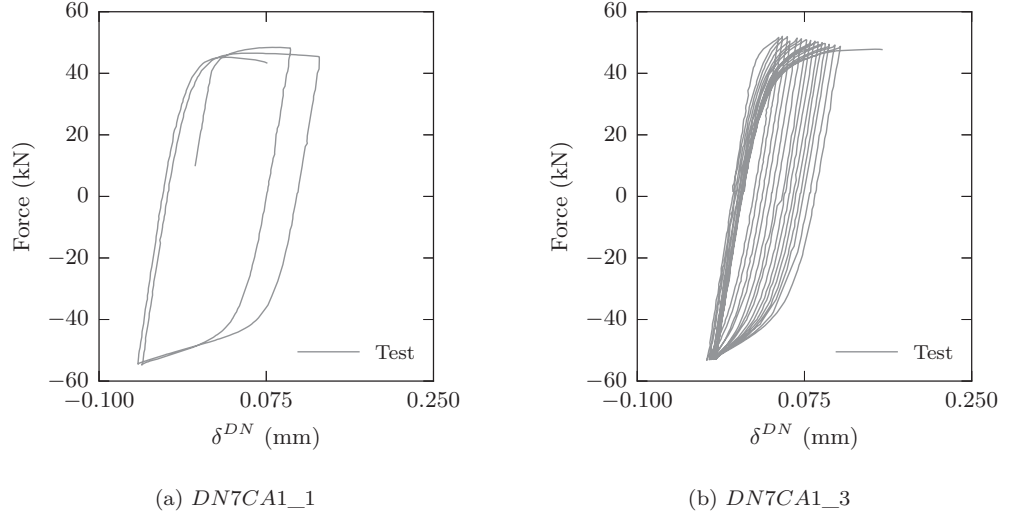


Figure 3.30 – Comparison of hysteresis curves in double notch specimens for path 1

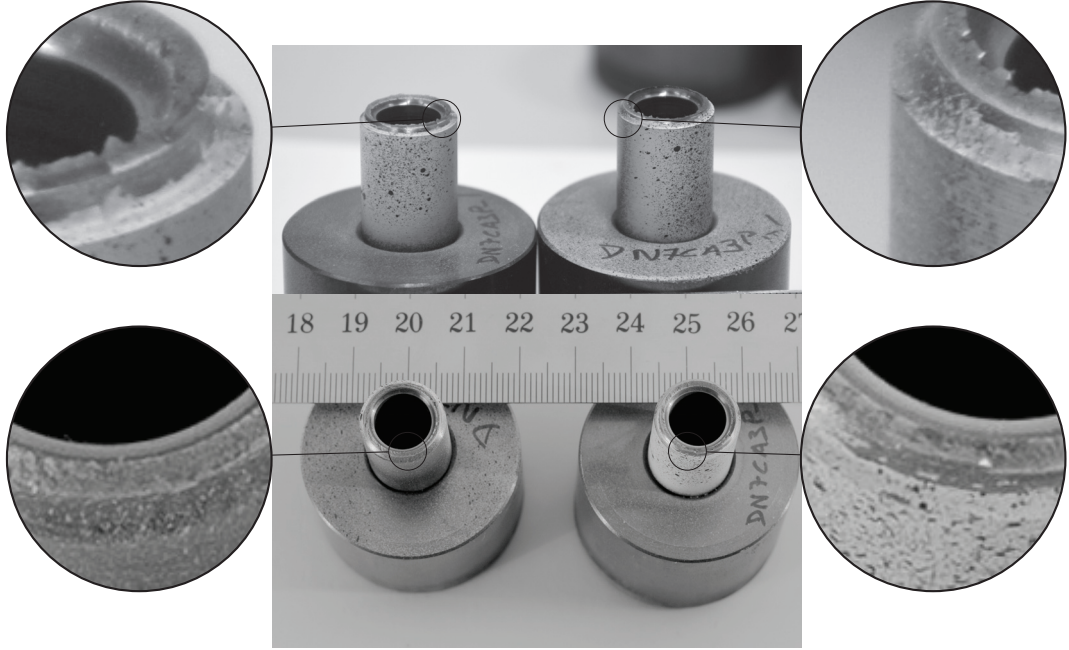


Figure 3.31 – Fracture surface in cyclic for load path 3 in double notched specimens

<sup>10</sup>octahedral strains ( $\dot{\gamma}_{oct}^p$ ) are related to the equivalent plastic strain ( $\dot{\varepsilon}_{eq}^p$ ) by a constant factor:  $\dot{\gamma}_{oct}^p = \sqrt{2}\dot{\varepsilon}_{eq}^p$

## 3.5 Conclusions

This chapter presented the results of an experimental campaign on small scale specimens to characterize key material properties of high strength S770QL steel.

Methods for obtaining key internal variables in micromechanical models for void growth and coalescence such as porosity, aspect ratio and distance to nearest neighbor were presented and quantified:

1. Inclusion volume ratio for base material was found to be on the average close to  $3e - 3$ . Since not all tend to nucleate voids, an order of magnitude for the initial void volume ratio of  $1e - 3$  is assumed to be a reasonable estimate.
2. Based on statistics of elongated inclusions no clear preferential direction was observed. Initial spherical voids are thus assumed.
3. An average inclusion ligament size ratio close to 0.2 is considered to be a reasonable estimate.

An attempt to describe the fracture behavior of S770QL steel was made by performing tests on single notch round bars and double notched tubes. Experimental observations corroborate some of the findings reported in literature. Key takeaways are as follows:

1. It can be argued, although not conclusively, that critical porosity (*i.e.* leading to failure) is higher in large amplitude cyclic loading than in monotonic loading of single notched specimens. Interrupted tests under ULCF are of interest in order to clarify this issue and in doing so provide better failure criteria.
2. Analysis of fracture surfaces show shallower dimples when compared to monotonic loading in single notched specimens, which is in line with observations by [Kanvinde and Deierlein, 2004].
3. Tests conducted in double notched specimens show a significant dependency of material ductility on the stress state for monotonic loading. A greater ductility is observed in pure shear cases than in pure tension. These findings are in accordance with [Faleskog and Barsoum, 2013].

4. Difficulties in carrying out reliable large amplitude cyclic loading in double notched specimens were presented. As a result, observations such as the ones in [Yokobori et al., 1965] that thin-walled tubes in pure torsion tests have a greater resistance than in tension in low cycle fatigue, will be assumed to hold true for the ultra low cycle fatigue regime of base material.

## 4 Welded component behavior

The main objective of this chapter, as opposed to the work done on smaller scale specimens described in the previous chapter, is to assess the impact of particular features of welded components at a reasonable scale in estimating fatigue life at high strain amplitudes under a variety of loading conditions. By reasonable scale it is meant that the thicknesses studied in this chapter (8 mm) can be seen as being used in the base plate of liquid storage tanks, for example. Though not at the scale of critical bridge components where one often sees thicknesses three to four times as large.

The main features of welded components can arguably be summarized up in four fundamental categories: the welding procedure (which is non obvious in high strength steels due to their heat treated microstructure), residual stresses imposed by the welding process, the weld profile (*e.g.* partial or full penetration welds and their resulting traits) and imperfections (*e.g.* porosities or initial microcracks). It is important at this point to revisit the scope of this work and underline some key assumptions. Insofar as from the structural engineering point of view the main objective is to arrive at a satisfactory criterion for design, and even though one recognizes the paramount importance of the welding procedure, it will be assumed (as will be shown to be a satisfactory assumption in chapter 6) that the resistance provided by the welding process is sufficient to attain yielding of the base material. Furthermore, due to high strain amplitudes, *i.e.* amplitudes that significantly surpass elastic strains into the plastic regime, the impact of residual stresses is assumed to be quite small and therefore will be neglected in forthcoming analyses.

To study the problem of welded components a testing campaign was undertaken and the results are presented herein. The chapter will start by describing the specimens, the testing apparatus and measurement instruments. Afterwards, a description of the loading protocols is given and is followed by the presentation of results and their discussion.

## 4.1 Test Setup

A welded tube to plate joint was chosen to study ultra low cycle fatigue (ULCF) behavior under multiaxial states under constant and variable amplitude loading. The main reason to use this kind of specimens is the uniformity with which one can apply a shear stress/strain field thus avoiding issues that can arise from stress/strain risers (*e.g.* corners) in the load transfer process in planar plate specimens.

The test setup consists of a welded circular tube ( $101.6 \times 10\text{mm}$ ) to plate ( $300 \times 200 \times 25\text{mm}$ ) specimen bolted<sup>1</sup> to a stiffened HEB360 column. The tube is made of high strength S770QL steel and, due to the unavailability of S770 steel plates, the base plate is made from S690 steel<sup>2</sup>. Sketches of the test setup are presented in Figures 4.1, 4.2 and 4.3 with all dimensions in figures are in millimeters).

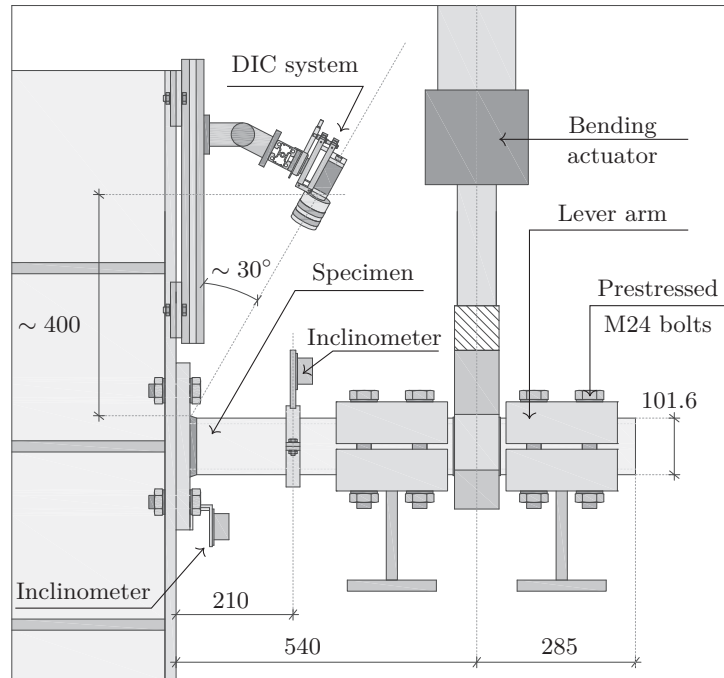


Figure 4.1 – Tube to plate test setup - side view

The specimen is loaded in bending and torsion with the use of two hydraulic actuators. These actuators have  $\pm 200$  kN nominal capacity and  $\pm 250$  mm stroke.

The first actuator, used for bending, has a jack head with a circular opening of 105.0 mm diameter through which the specimen can pass - see Fig. 4.4. This opening sits on a spherical

<sup>1</sup>4 M30 bolts prestressed at 1600N.m coupling moment

<sup>2</sup>the undermatching of the base plate and the tube is deemed insignificant in the subsequent analyses because all failures occurred at the weld toe on the side of the tube



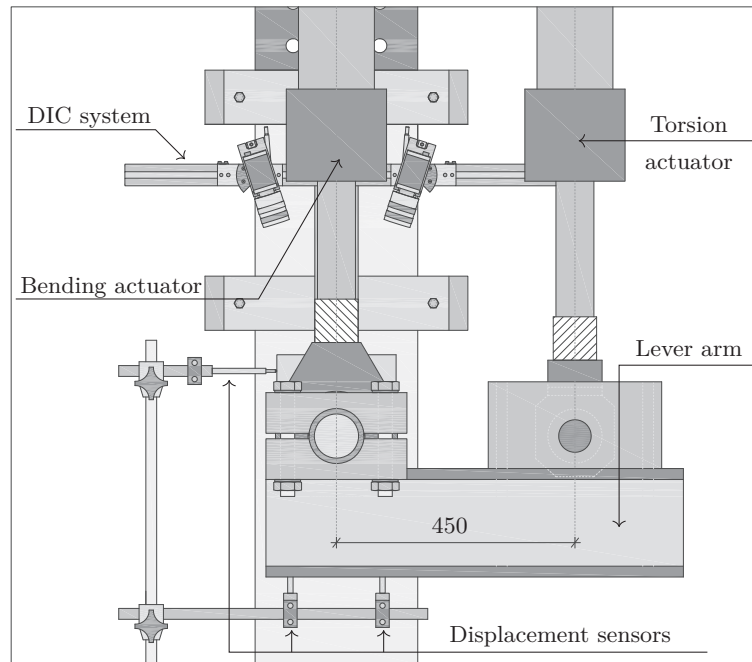


Figure 4.2 – Tube to plate test setup - front view

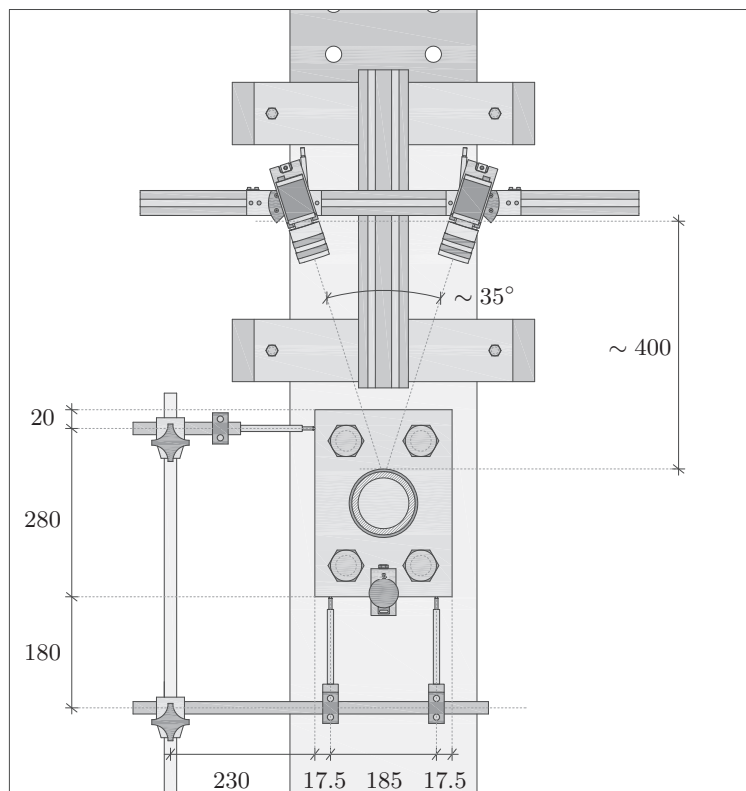


Figure 4.3 – Tube to plate test setup - front view cut just before tube inclinometer

mount that is able to rotate on all three-axes. The difference between the diameter of the tube and the diameter of the jack head leaves a  $1.7\text{mm}$  gap around the tube and a total clearance of  $3.4\text{mm}$  when the tube is touching the surface of the jack's head. For the bending tests this difference is not at all negligible (as will be shown) and allowance in the treatment of the data should be made for this gap <sup>3</sup>.

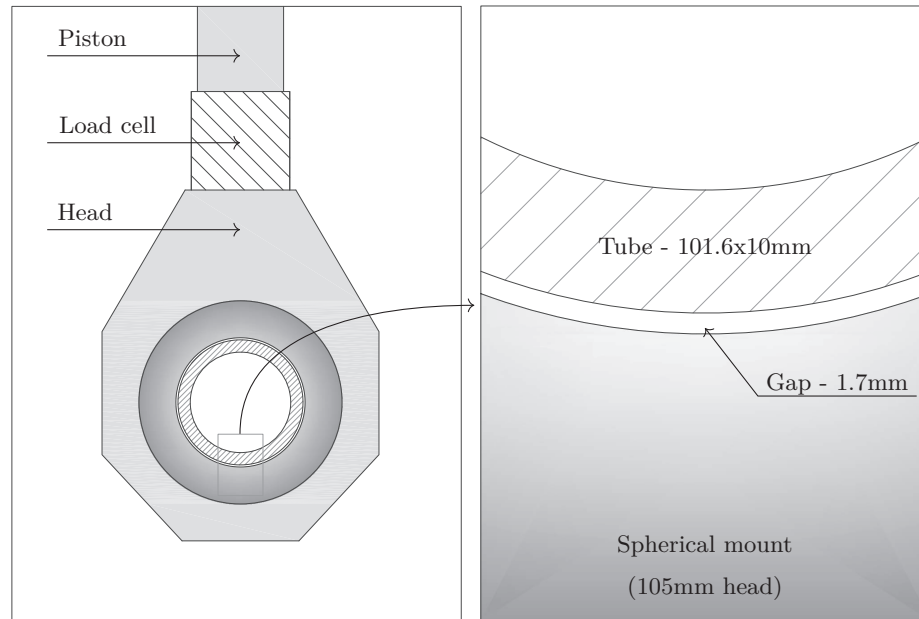


Figure 4.4 – Detail of gap in the bending actuator's head

Torsion is applied by a second actuator, residing in a plane perpendicular to the tube's longitudinal axis, through a lever arm - see Fig. 4.2. The nominal length between axes is 450 mm. The lever arm was custom built for this test setup. Torsion is applied by friction to the tube with four massive blocks of steel carved with a circular concave shape of diameter equal to the tube's own. These pieces constitute two pairs of clamps that are then prestressed together (each pair by 4 M24 bolts prestressed at 1000N.m torque moment) so as to be able to mobilize a significant amount of friction between the surfaces of the blocks and the tube. Each pair reside on opposite sides of the bending jack's head. The blocks are then welded to two 'I' beams that make the span of the lever arm. At the end of the arm, the 'I' beams are stiffened by multiple plates between them so as to create an as rigid a block as possible - see Fig. 4.5. An additional piece made up of steel plates is welded on the upper flanges of the beams so as to make up for the height difference between the center of the tube and the axis that passes through the torsion actuator's head - see Fig 4.2 and 4.5.

<sup>3</sup>Incidentally, such a small gap of  $1.7\text{mm}$  around the tube was not able to be corrected because one could not arrive at an effective mechanism to do so. Ironically if the gap were larger it would have been much easier since one could fabricate a system of tapered circular rings that would do trick

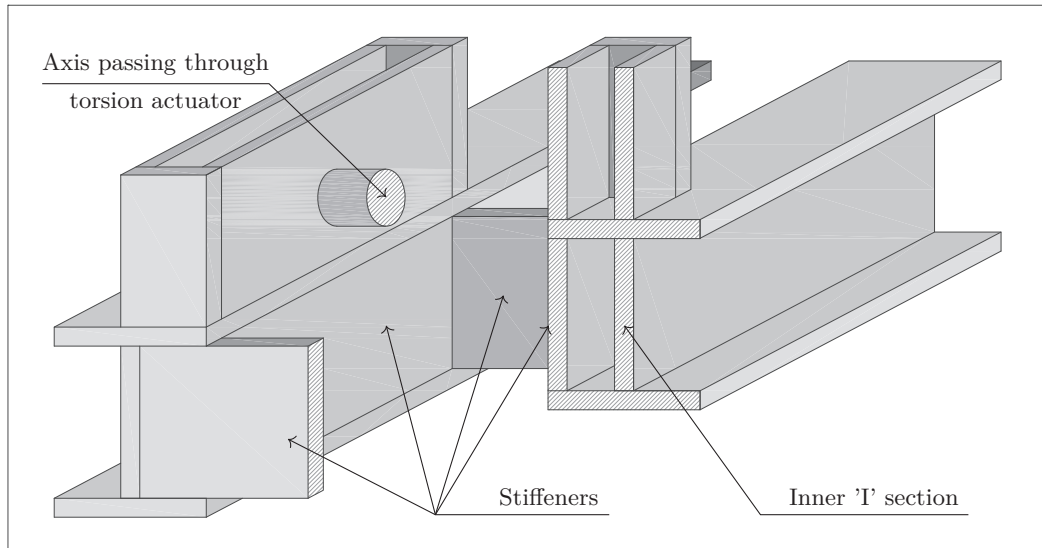


Figure 4.5 – Schematic of the lever arm around the torsion actuator

In order to concentrate yielding near the weld region, the section was reduced from 10 mm to 8 mm according to the geometry outlined in Fig.4.6. A composite of nearly 800 micrographs of the weld toe resulting in a 890MPx image can be seen in Fig. 4.7.

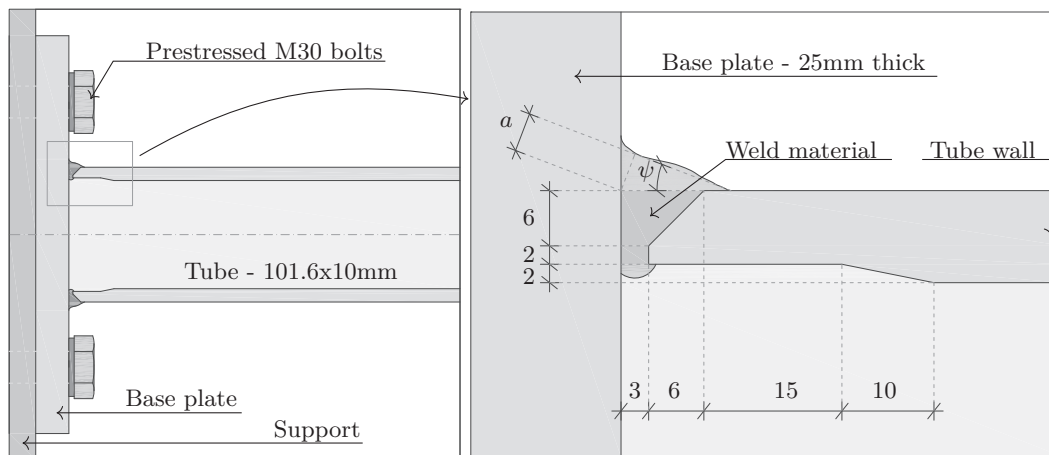


Figure 4.6 – Detail of weld region

With respect to instrumentation, each of the two actuators was equipped with a load cell and displacement transducer. Two vertical and one horizontal displacement sensors were used to quantify slipping of the base plate in relation to the column see - Fig. 4.3.

Due to the observed flexibility of the column to which the specimens were bolted on, two inclinometers were also used: one attached to the base plate<sup>4</sup> and another connected to a

<sup>4</sup>either glued or bolted

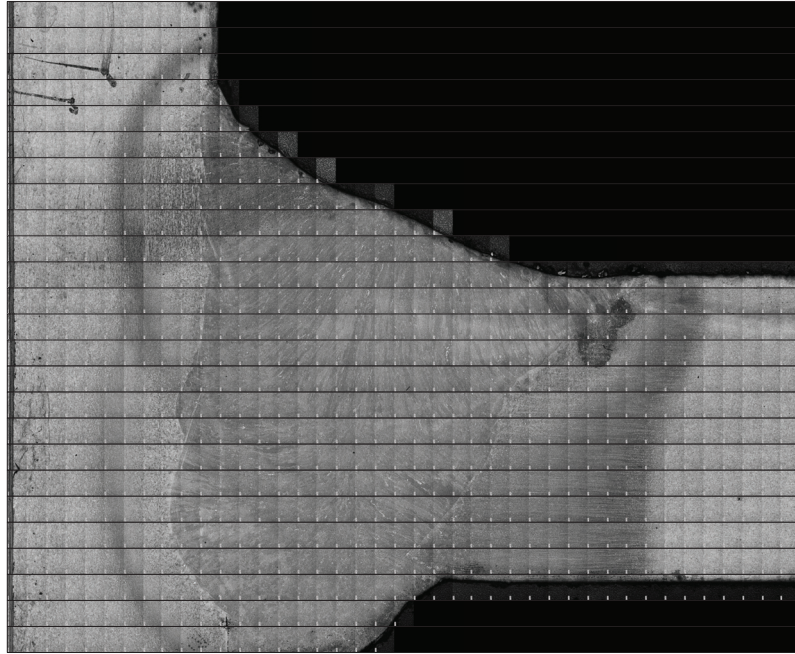


Figure 4.7 – Composite of micrographs around the weld toe - Nital 2%

section of the tube at approximately  $210\text{mm}$  from each other - see Fig. 4.1. The difference in rotation between the two provide an effective measure of the rotation the tubes are subjected to - see Fig. 4.8. The rotation due to the flexibility of the support was found not to be as insignificant as one might think. In fact in the first pure torsion tests that were conducted, by using data from the displacement sensors at the base plate one could see that  $\sim 40\%$  of the rotation measured at the  $210\text{mm}$  section was lost due to this flexibility.

Fig. 4.9 illustrates schematically the deformation to which the welded tube to plate specimens were subjected to.

### 4.2 Digital image correlation

Chiefly important in the resistance characterization of these tests is the use of digital image correlation (DIC). Localized strain measurements were taken at the surface of the weld toe, the results of which are of great importance in framing an appropriate failure criterion, as will be shown in the results and discussion section.

This system was used to measure the geometry, surface strain history of the weld region and to register any observable cracks within its field of view. Since the DIC's field of view only covers a small part of the perimeter of the tube one can expect that the critical crack leading to failure will not always be within it - particularly in the case of pure torsion loading.

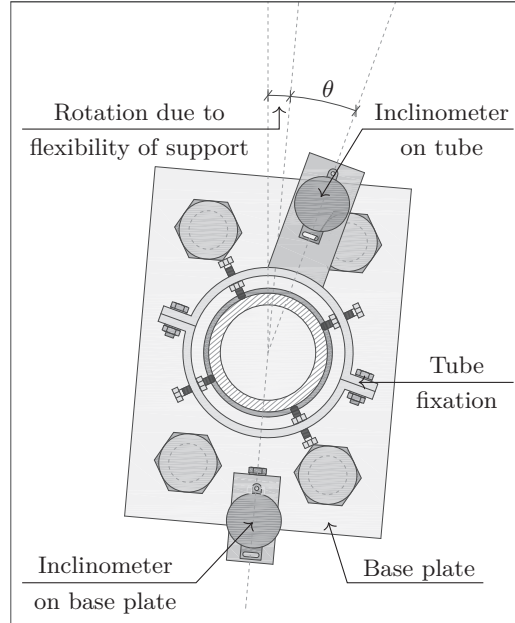


Figure 4.8 – Definition of effective rotation  $\theta$

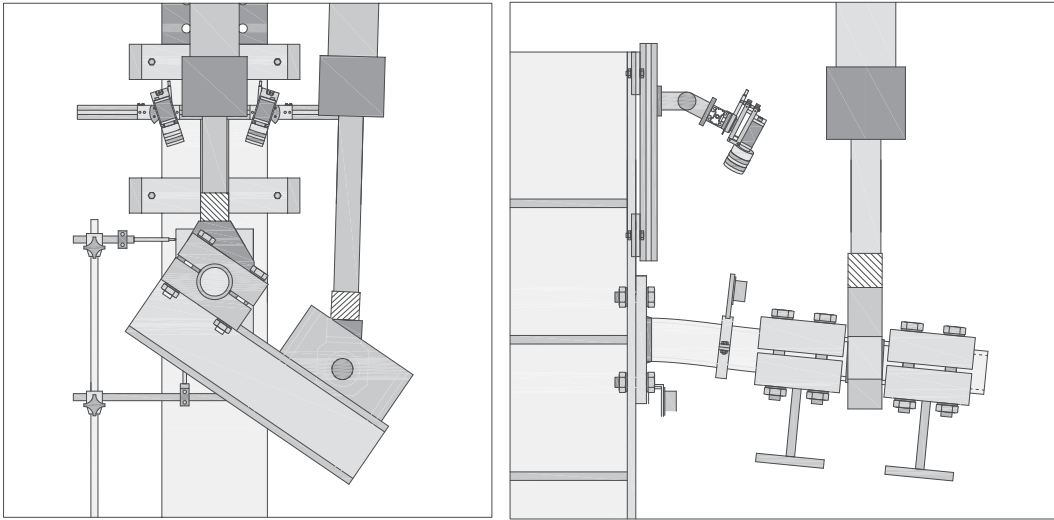


Figure 4.9 – Deformed view of the test setup

The DIC setup consists of two Manta G-504B/C cameras with a  $2452 \times 2056$  pixel CCD sensor used together with two Fujinon 50 mm focal length lenses. Images were processed using the software Video Image Correlation in 3-D (VIC3D v7.0 - Correlated Solutions) [McGowan et al., 2001].

Calibration of the system in order to identify the relative position between the two cameras and their absolute distance to the weld toe was conducted with the help of a standardized grid of  $12 \times 9$  circular dots at  $2\text{mm}$  spacing.

Small variations in the position of the cameras with respect to the weld toe, the focal length, aperture (because of lighting conditions) and the size of the camera sensor set the resolution of the system to 1 pixel corresponding between  $[0.03, 0.045]mm$ . Key options step size and filter size were set to 7 pixels and 7 data points, respectively <sup>5</sup>, across all specimens so as to provide a uniform basis of comparison. This essentially means that full-field calculations are based on a grid of points spaced out of 7 pixels and then averaged over a window of 7 by 7 data points *i.e.* approximately  $[1.5, 2.2]$  by  $[1.5, 2.2]$  mm (49 by 49 pixels). Correlation of data points between images in the reference and the deformed configuration is more dependent on the speckle pattern on the surface of the tube, and thus subset size varies slightly between specimens (around 27 by 27 pixels).

An adequate speckle pattern for high strain amplitudes and for the resolution level which one has set is not an obvious thing to achieve. Firstly one has to properly prepare the surface of the specimen so as to remove the mill scale without damaging the surface roughness and clean any oily deposits with a solvent. This can be done with a sufficiently rough but non-abrasive brush. Damaging the surface with abrasive materials runs the risk of localized reflections on the surface rendering it useless for a DIC analysis. Secondly one has to select a paint composition that is able to sustain large deformations. Acrylic-based paints are good in this respect. Thirdly and perhaps most importantly is the pattern itself. A good pattern should have two characteristics: good contrast between black and white, and a randomized set of positions between black and white areas. Implementing this typically involves providing a uniform colored base (usually white) and spraying black ink over that base. The problem with this is that at high strains this uniform base layer is easily damaged. The solution to this requires one to abandon the idea of a base layer. What follows unfortunately is a procedure that is far from systematic and therefore involves a lot of trial and error. This procedure consist of multiple and quite small spraying passes interchangeably between black and white at a considerable distance from the area of interest (between half to one meter or so). Its purpose: to have small and thin droplets of ink scattered on the surface. Luckily in this setting, with the ink's viscosity and the right spray nozzle one can arrive at suitable droplet size (in the order of 0.1mm) and suitable density with respect to the subset size. Here perhaps it is relevant to mention what is meant by suitability.

Consider Fig. 4.10 which shows strain measurements on a picture of an unloaded specimen with respect to a reference picture (equally unloaded). Since both pictures (the reference and the one shown) are at rest, the resulting strain field has to be noise in the signal and thus provide a measure of the precision involved in the analyses. A range slightly higher than what is shown in Fig. 4.10 of  $\pm 0.08\%$  was what was typically observed in the DIC

---

<sup>5</sup>background to comprehend these key options is given in chapter 2

analyses. Though not irrelevant when compared with elastic strains of 0.4% for this steel, at the levels of plastic strain amplitudes that these specimens were submitted to this is deemed acceptable.

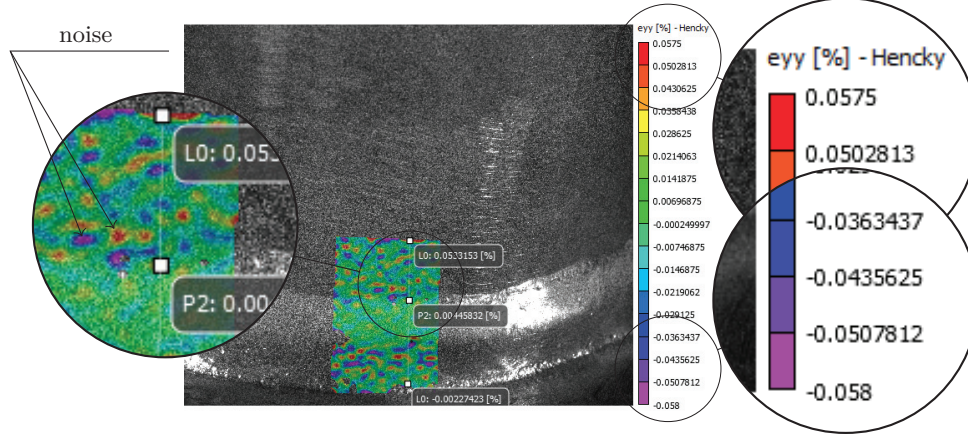


Figure 4.10 – Precision in  $\varepsilon_{yy}$  DIC measurements for specimen B7CA1\_3 - pictures at rest vs reference picture

There is another source of measurement error that is palpable in some cases, though it is not easily quantifiable, and has to do with the performance of the speckle pattern during loading. Debonding of the paint from surface of the specimen is a legitimate concern for the high strain levels at which these tests were operated, though the risk is significantly diminished with the procedure outlined above. Moreover the presence of small cracks that are not sufficiently large to invalidate the full-field calculations have a tendency to inflate the strain values. Put this way, the reader might indeed be skeptical of these measurements and rightly so in the author's opinion. The question then becomes whether one can make meaningful predictions with these measurements even taking into account the facts aforementioned. In the results and discussion section a reasonable case is presented that one can.

### 4.3 Loading protocols

Let us define  $\delta$  as the displacement of the bending actuator minus the average displacement of the two vertical displacement sensors<sup>6</sup> and the 3.4mm maximum clearance in the spherical mount, and  $\theta$  as the difference between the angles measured in the two inclinometers. Tests were conducted under displacement and rotation control: the controlling variable for the bending actuator was its piston's displacement (not  $\delta$ ); the displacement of the torsion actuator was controlled by  $\theta$ . It is worth emphasizing that tests were indeed performed

<sup>6</sup>this accounts for slipping



## Chapter 4. Welded component behavior

discounting the torsional flexibility of the support by controlling the test with the difference between the two inclinometers. In the few tests (two that were conducted without an inclinometer at the base plate), the test was controlled solely with the inclinometer at 210mm from the support. The effective rotation in these cases was calculated *ad hoc* using the displacement sensors at the base plate.

The following structure for specimen designation will be followed,

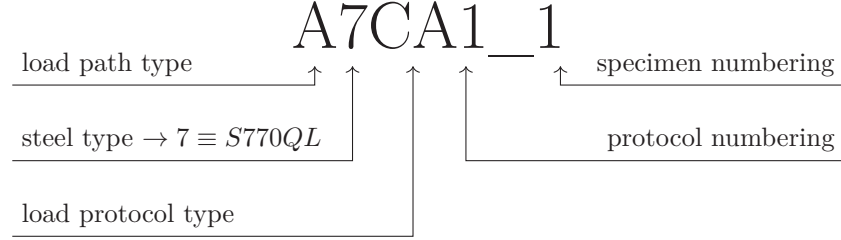


Figure 4.11 – Specimen designation for welded tube to plate tests

Table 4.1 presents the test matrix with 56 tests in constant amplitude (CA) loading. Five different ratios (A,B,C,D and F) between  $\delta$  and  $\theta$  in proportional loading were used and are represented graphically in Fig. 4.12a. Additionally 9 tests (labelled E) were conducted under a non-proportional load path with ranges of  $\Delta\delta$  and  $\Delta\theta$  similar to load type C - see Fig. 4.12b.

Table 4.1 – Constant amplitude test matrix

Type	Amp.	$\Delta\theta$ (Deg)	$\Delta\delta$ (mm)	# specimens
A (Torsion)	CA1	5.50	0.00	5
A (Torsion)	CA2	4.10	0.00	4
A (Torsion)	CA3	8.15	0.00	1
A (Torsion)	CA4	2.20	0.00	1
B (Bending)	CA1	0.00	38.50	5
B (Bending)	CA2	0.00	33.50	4
C	CA1	4.10	36.00	4
C	CA2	3.50	31.00	6
C	CA3	2.60	24.00	2
D	CA1	5.60	32.00	5
D	CA2	4.00	23.00	4
D	CA3	4.55	26.25	1
E	CA1	4.00	36.50	5
E	CA2	3.50	32.00	4
F	CA1	4.70	14.00	2
F	CA2	3.40	10.00	3
Total				56

Variable amplitude (VA) tests were conducted under two types of load histories: VA1



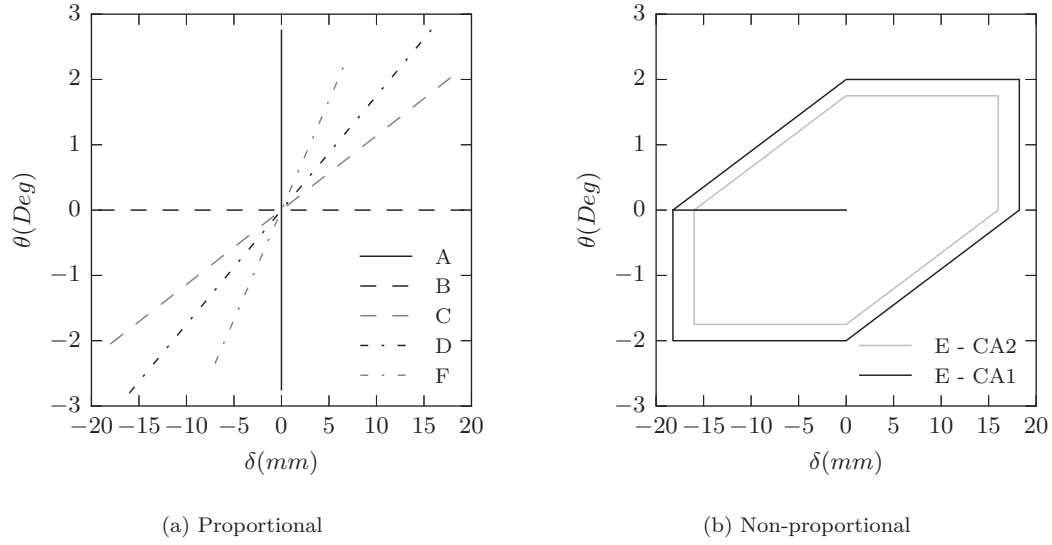


Figure 4.12 – Constant amplitude load paths

alternates between two different range levels and VA2 performs block loading of 3 cycles between ranges. 3 specimens under both VA1 and VA2 for load ratios A,B,C and D were performed, totaling 24 VA tests. Table 4.2 presents the range levels of  $\delta$  and  $\theta$  and Fig. 4.13 illustrates graphically the load protocols VA1 and VA2.

Table 4.2 – Variable amplitude test matrix

Type	Amp.	$\Delta\theta_1$ (Deg)	$\Delta\delta_1$ (mm)	$\Delta\theta_2$ (Deg)	$\Delta\delta_2$ (mm)	# specimens
A	VA1	5.50	0.00	4.00	0.00	3
A	VA2	5.50	0.00	4.00	0.00	3
B	VA1	0.00	33.00	0.00	29.00	3
B	VA2	0.00	33.00	0.00	29.00	3
C	VA1	4.00	36.00	3.55	31.50	3
C	VA2	4.00	36.00	3.55	31.50	3
D	VA1	5.55	32.00	4.00	23.50	3
D	VA2	5.55	32.00	4.00	23.50	3
Total						24

Even though the grand total of CA and VA is 80 tests, due to problems during testing (*e.g.* an inclinometer unglued from the base plate or paint on the surface of specimen was of insufficient quality) only 64 tests are considered valid for use in fatigue life estimation <sup>7</sup>.

<sup>7</sup>a few others were used to assess initiation life as defined in the results and discussion section

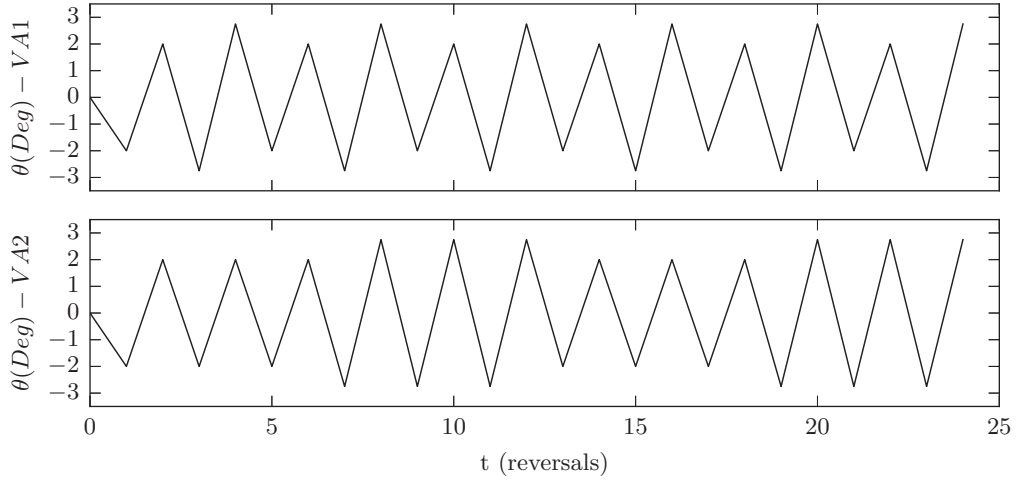


Figure 4.13 – Variable amplitude load protocols

## 4.4 Results and discussion

As one can gather due to the large amount of information collected in the testing campaign, only a few representative cases will be discussed in detail in this section. Relevant information on all the tests that were conducted can be consulted in annex E.

One begins by considering the case of a simple bending test (specimen *B7CA1\_3*) to illustrate the importance in the interpretation of results for the definition of what constitutes the failure of the specimen.

Fig. 4.14 shows two hysteresis curves for *B7CA1\_3*. The first shows the data as was collected from the test setup at the 5<sup>th</sup> cycle of loading. As one can see the 3.4mm clearance due to the gap shown in Fig. 4.4 has a very noticeable effect. The second shows the corrected hysteresis curve. In Fig. 4.14b one can observe a stable hysteretic loop on the part of the component. However, if one turns one's attention to Fig. 4.15, it can be seen that at the very same cycle a surface crack at the weld toe is detectable.

It is useful to underline two factors involved in the detection of a surface crack. The first is that this was done exclusively with pictures taken by the DIC system, which means that undetected cracks might have developed elsewhere along the periphery of the weld toe. The second is that there is a limitation in the perception of what is a crack. At the scale the pictures were taken, this limit can be stated to be in the order of 0.1mm of surface opening.

It can therefore be argued that since surface cracks were detected before any noticeable drop in the load carrying capacity of the component, establishing crack initiation as a criterion for

failure underestimates ULCF life estimations. This seemingly innocuous statement has a tremendous impact if one wishes to apply micromechanical ductile fracture criteria to welded steel components. Since the main justification to use micromechanical models is rooted in the fact that it is physics based (*i.e.* is representative of the physical process underlying fracture) and that the behavior it purports to capture is initiation <sup>8</sup>, the unsuitability of such models become apparent in the presence of high strain gradients and the emergence of surface cracks with no drop in the resistance typically observed in the testing of large scale structural components.

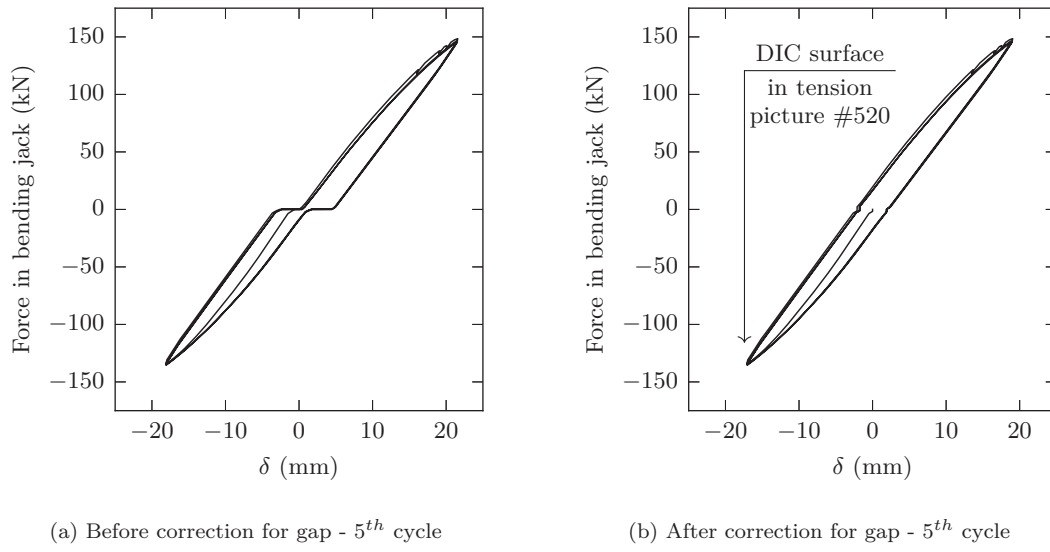


Figure 4.14 – Impact of gap in bending jack head in the hysteresis of specimen B7CA1\_3

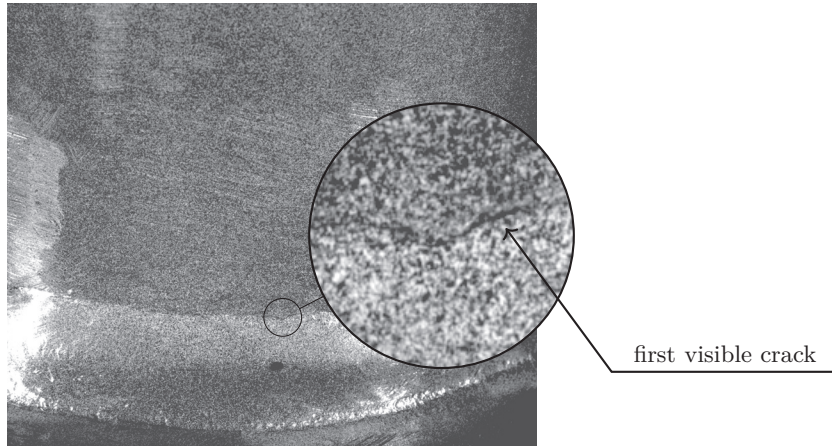


Figure 4.15 – First visible crack in specimen B7CA1\_3 at picture number 520 - 5<sup>th</sup> cycle

<sup>8</sup>in this context, the coalescence of an interligament crack between adjacent voids or second-phase particles under a fairly uniform strain field

## Chapter 4. Welded component behavior

At this point one needs to establish a definition of what constitutes failure of a specimen to guide the interpretation of the results. A resistance based criterion is used henceforth that establishes failure as a 10% drop in load carrying capacity of the specimen. Such a small threshold is used in order to limit the effects of significant crack propagation within the specimen - see Fig. 4.16. Fig. 4.17 shows a typical striation pattern that underlines significant crack propagation.

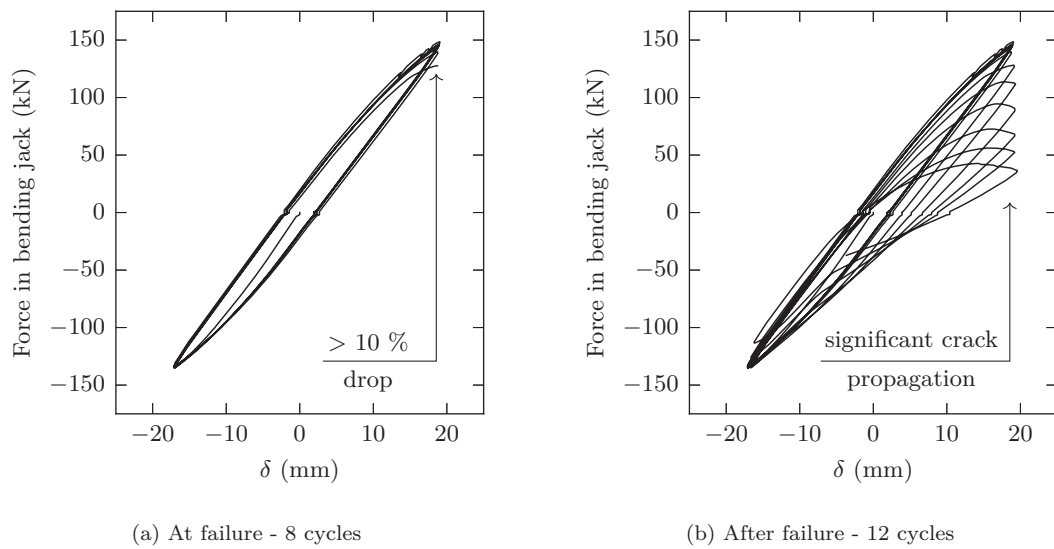


Figure 4.16 – Hysteresis curve for specimen B7CA1\_3

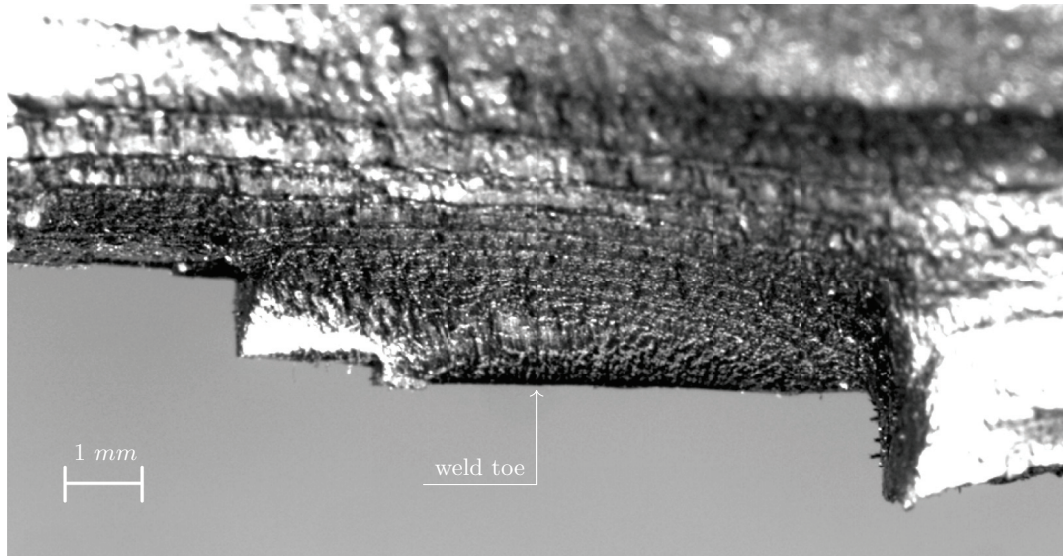


Figure 4.17 – Crack propagation on specimen B7CA2\_2

Considering that the number of cycles to which a crack was detected in DIC system is a

more than reasonable upper bound on the number of cycles to initiation ( $N_{init}$ ), one can define as initiation ratio  $N_{init}$  divided by the number of cycles to failure ( $N_f$ ). Fig. 4.18 plots this ratio for all specimens.

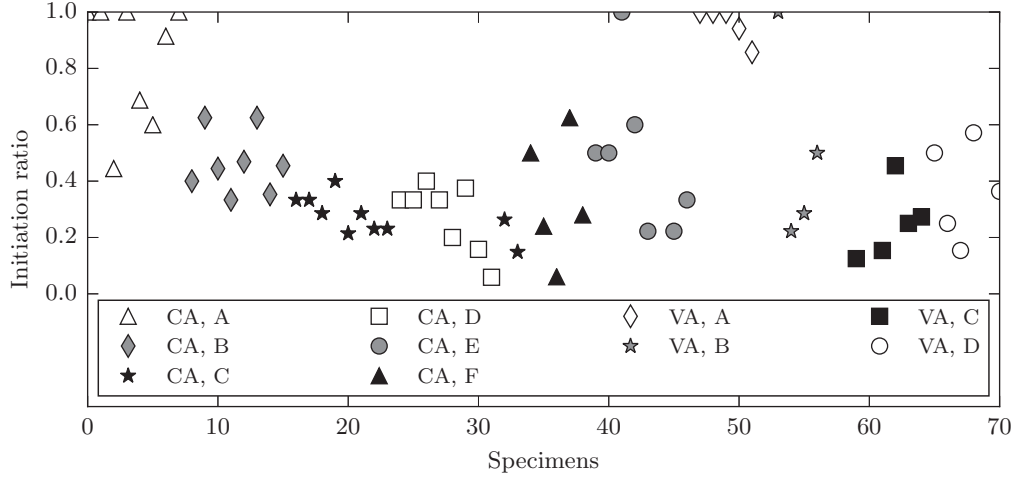


Figure 4.18 – Initiation ratios for tube to plate tests by test type

As one can see, it can be reasonably concluded that the initiation process constitutes at most and in rough terms only half to a third of the total life of this component; propagation then accounting for half to two thirds of the total life. Also worth taking note is the fact that for pure torsion tests it is much harder to detect a surface crack due to both limited surface opening and higher probability of a critical crack happening outside the field of view of the DIC system.

Without a meaningful way to link micromechanical models to failure of large scale components, it seems justifiable to fall back to more classical approaches to the problem such as types of relationships that relate strain to total life. Here, a pressing question arises: what strain measure to use in the presence of strain risers (*e.g.* the geometry imposed by the weld profile) and in the context of multiaxial fatigue? To begin formulating an answer to this question one should first consider the information that the DIC system can provide.

Fig. 4.19 shows an example of the full field measurement of  $\varepsilon_{yy}$  in B7CA1\_3 and Fig. 4.20 measurements of the geometry,  $\varepsilon_{yy}$  and a strain quantity  $\varepsilon_{eq}^*$  to be defined shortly, through a section parallel to the longitudinal direction of the tube and passing through the point of maximum  $\varepsilon_{yy}$ .

The geometric effect of the weld is quite blatant in the strain concentrations observed at the weld toe. Strain gradients in this case are between 5 to 10 % per mm. Considering that these

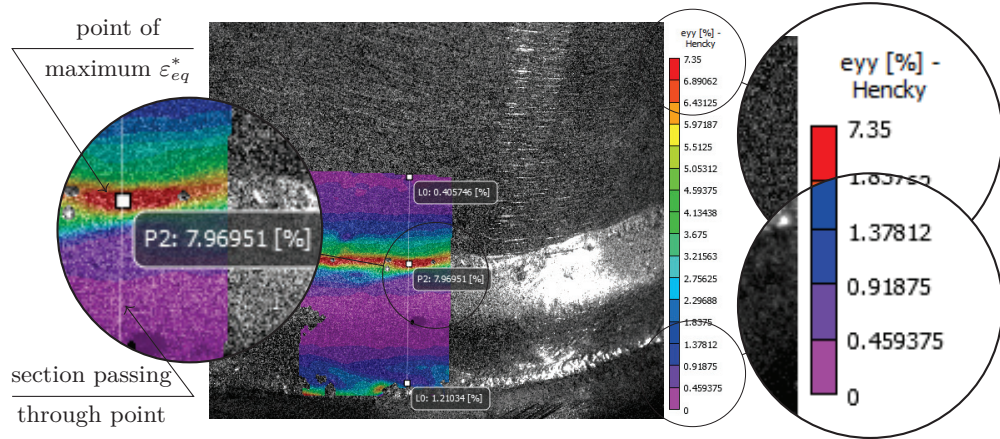


Figure 4.19 –  $\varepsilon_{yy}$  DIC measurements for specimen B7CA1\_3 at the peak of the first load excursion - picture number 50

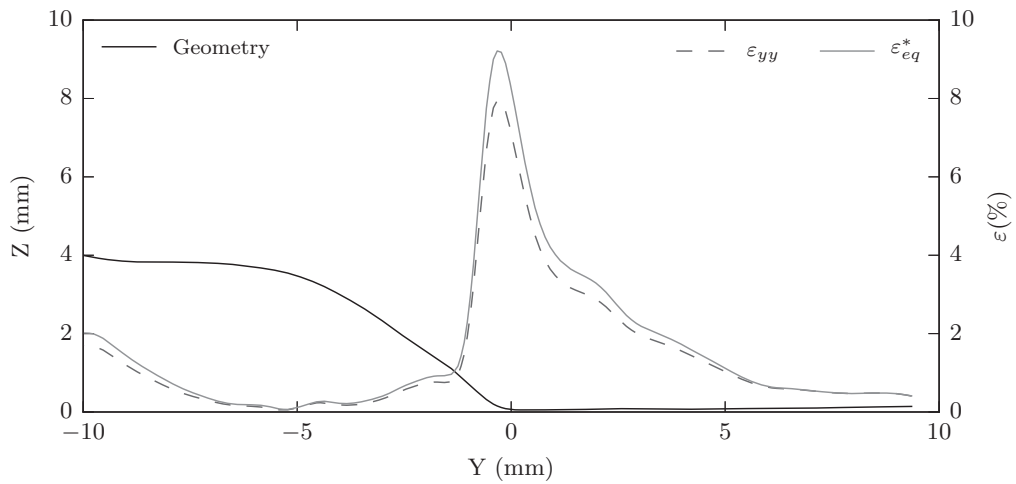


Figure 4.20 – DIC measurements at section through point of maximum  $\varepsilon_{yy}$  for specimen B7CA1\_3 at the peak of the first load excursion - picture number 50

values are averaged over a window of around  $1.5 \times 1.5 \text{ mm}^2$  (*cf.* section on DIC), local values can conceivably be higher. As an additional example of how fortuitous strain distributions can be when geometric effects are combined with the certain types of loading, consider Fig. 4.21 which depicts a 3D view of the weld geometry of specimen C7CA1\_2, as well as full field measurements of principal strain  $\varepsilon_1$  and the crack pattern at failure. Here, noticeable striations on the weld's surface can be seen in the 3D representation. As minor as these surface depressions caused by the welding process can be, strain concentrations can be seen along the troughs of those ridges.



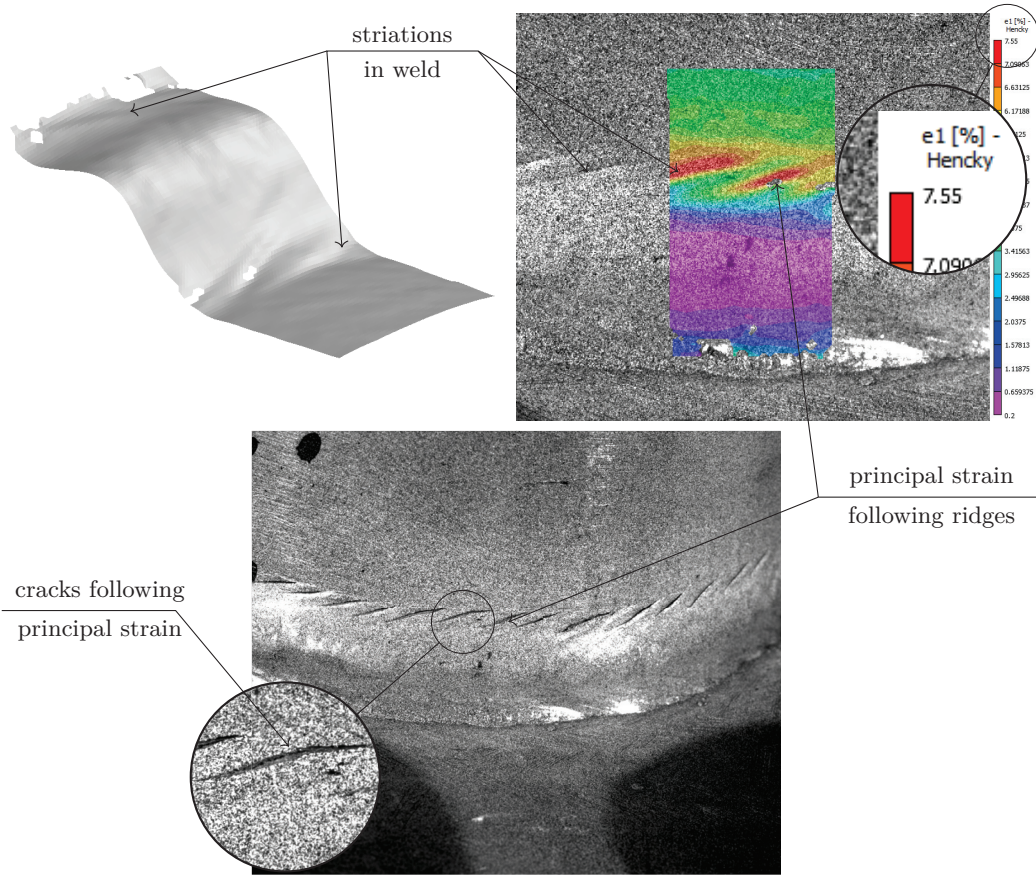


Figure 4.21 – Influence of geometry on strains at weld toe for specimen C7CA1\_2

Damage is a concept that often has different meanings depending on the context in which it is used. In fatigue it is commonplace to associate it with the counting of cycles and a quantity that is representative of the process leading to failure (*e.g.* stress ranges for high-cycle fatigue and strain amplitudes for low-cycle fatigue). Other approaches might define it as a critical crack length within the context of linear elastic fracture mechanics (LEFM), relating crack growth rates to stress intensity factor ranges. In the case of ultra-low cycle fatigue in multiaxial conditions, it necessary to define such a quantity in order to define damage. Here, intuitively, one will follow the proposition that the work dissipated by plastic straining is representative of that process. In a perfectly plastic material, a measure of that dissipation can be in fact the work conjugate of any stress measure. For the Von Mises stress, the equivalent plastic strain defined by the rate in Eq. 4.1 is such a measure. It should be noted that this measure is closely related to the octahedral shear strain (they differ by a factor of

$\sqrt{2}$ ) used in [Yokobori et al., 1965].

$$\dot{\varepsilon}_{eq}^p = \sqrt{\frac{2}{3} \dot{\varepsilon}_{ij}^p \dot{\varepsilon}_{ij}^p} \quad (4.1)$$

Consider also the introduction of another strain quantity, the equivalent strain  $\varepsilon_{eq}^*$ , given by Eq. 4.2.

$$\varepsilon_{eq}^* = \text{sign}(\varepsilon_{kl,rel}) \sqrt{\frac{2}{3} \varepsilon_{ij} \varepsilon_{ij}} \quad (4.2)$$

Note the differences between Eq. 4.2 and Eq. 4.1. Firstly Eq. 4.2 is expressed in terms of the total strain tensor ( $\varepsilon_{ij} = \varepsilon_{ij}^e + \varepsilon_{ij}^p$ ), which assumes that the elastic strain tensor is small when compared with the plastic strain. Secondly it expresses a base quantity as opposed to a rate quantity. Lastly, it is endowed with the sign of the most relevant strain tensor quantity with respect to the loading - *e.g.* for a pure torsion loading occurring in plane xy,  $\varepsilon_{kl,rel} \equiv \varepsilon_{xy}$ . The sole reason for this is to allow to keep track of the direction of the strain tensor with respect to the loading.

With equivalent strain defined in such a way, it is possible to define a time history from DIC surface measurements in the following way: keeping in mind the assumption that elastic strains are small with respect to the plastic, one can evoke the condition of volume conservation which states that  $\text{trace}(\varepsilon^p) = 0$  to approximate the strain depth component; secondly since there is no yielding in shear components except the one in the circumferential direction these are taken to be zero. All subsequent analyses are conducted with these assumptions and whenever *point measurements* are mentioned they always refer to the point in the full field measurements that shows the maximum equivalent strain range. Finding this point is the same as finding the points of maximum principal strain and therefore in the case of specimen C7CA1\_2 this point is found in the weld's striations.

A typical time history analysis taken the DIC system for the point of maximum strain can be seen in Fig. 4.22 for specimen B7CA1\_3.

The fact that local measurements are used instead of nominal section estimations, gives  $\varepsilon_{eq}^*$  added significance even if for no other reason than the added resolution in capturing the behavior, *i.e.* when taking local measurements one is also taking into account local features that can affect significantly  $\Delta \varepsilon_{eq}^*$ .



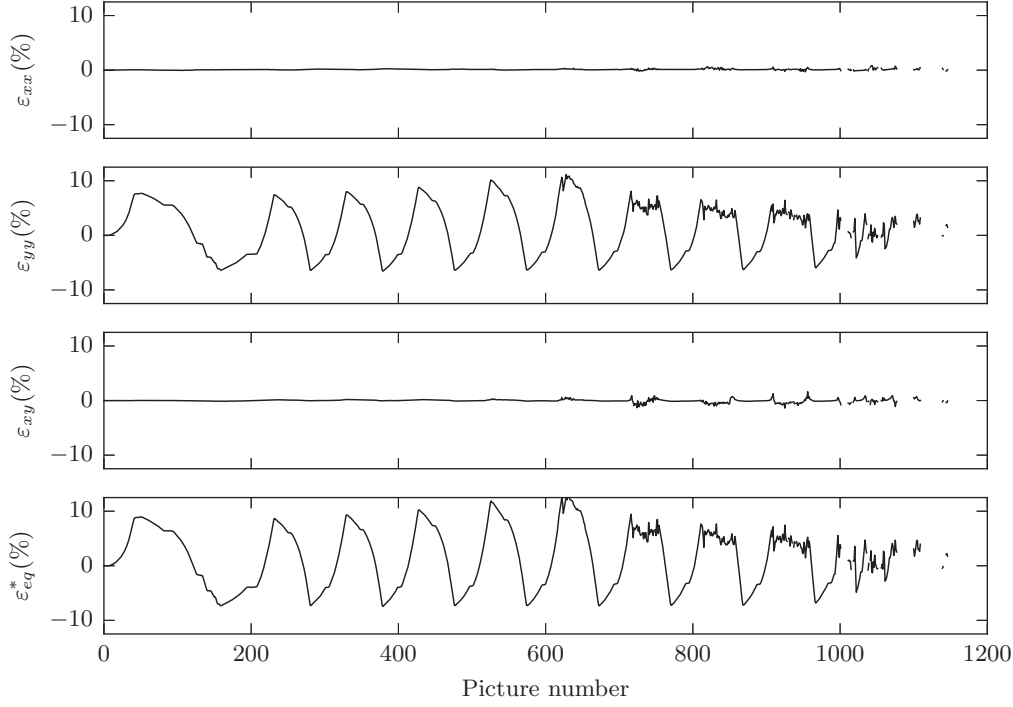


Figure 4.22 – DIC point measurements for specimen B7CA1\_3

Consider the Manson-Coffin type relation in Eq.4.3.

$$\frac{\Delta \varepsilon_{eq}^*}{2} = b(2N_f)^c \quad (4.3)$$

where,  $b$  is the fatigue ductility coefficient and  $c$  the ductility exponent (between -0.5 and -0.7 in many metals [ASM International, 1996] ).

Fig. 4.23 shows the results of constant amplitude proportional tests according to the assumptions previously stated - results in table form can be consulted in Appendix E as well as individual test reports. An important detail to mention is that the equivalent strain range can only be established by DIC within the initiation regime defined earlier for two main reasons: the first, once a surface crack starts to form these strains no longer meaningful (see *e.g.* Fig. 4.22 where the subtle increase from the 4<sup>th</sup> to the 5<sup>th</sup> cycle is due to the crack in Fig. 4.15); the second, with successive cycles paint might peel off. Therefore, the  $\Delta \varepsilon_{eq}^*$  in Fig. 4.23 is obtained only within early cycles and then assumed to hold its relevancy in the estimation of total life according to Eq.4.3. Number of cycles over which  $\Delta \varepsilon_{eq}^*$  is averaged is noted for each test in Appendix E as  $N_{ave}$ .

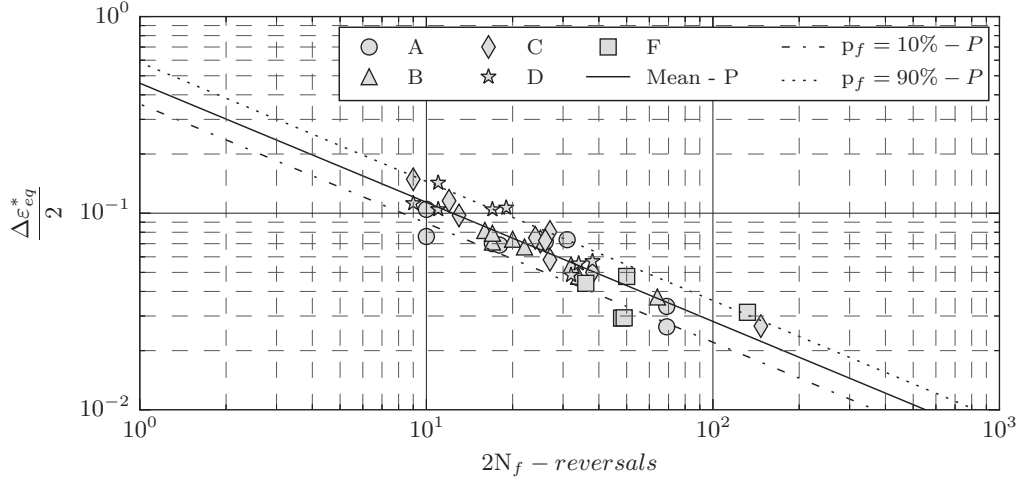


Figure 4.23 – Equivalent strain - life curve for tube to plate CA tests using slope from proportional (P) loading tests

Also depicted in Fig. 4.23 is the linear regression in log-scale of Eq. 4.3 in fitting the test results, as well as the 10<sup>th</sup> and 90<sup>th</sup> percentiles of the regression. The mean ductility coefficient was found to be around 0.458, whereas the ductility exponent  $c$  was found to be  $\simeq -0.6$ , well within expected bounds found in literature. This in itself is a surprising result, both justifying the assumption that this quantity is representative of the failure process and bringing closer this evaluation procedure to an already well established approach.

It is worth emphasizing that the fact that in this representation no noticeable distinctions between load types can be made, says nothing about the mechanisms leading to failure themselves. They are surely different if one thinks of them in the micromechanical sense and from what was concluded in Chapter 3. What this approach seems to indicate, however, is that they are sufficiently close to be considered together, statistically speaking. Justifications can be found in a number of factors that are not explicitly controlled. The effects of weld geometry associated with the load type, like the ones illustrated in Fig. 4.21, can be one of those factors. In this case location can play an important role as cracks can initiate in weld material or in the heat affected zone. Another is the different crack tip constraint conditions in mode-I and mode-II once a full-fledge crack is formed on the specimen. Here, again, location can play an important role as the crack can propagate in weld material, HAZ or in base material. However, bearing in mind that one of the main objectives of this thesis is to provide a simple but suitable criterion for design purposes, this approach is deemed acceptable.

For constant amplitude non-proportional loading (load type E), however, it does not seem

so reasonable to consider proportional together with the non-proportional tests - see Fig. 4.24 whose values can be consulted in Appendix E. Considering the same slope of -0.6, the mean ductility coefficient would be around 0.324, lower than 90<sup>th</sup> percentile for the proportional tests of 0.36. This suggests the failure mechanism is non-negligibly different for a non-proportional and worse.

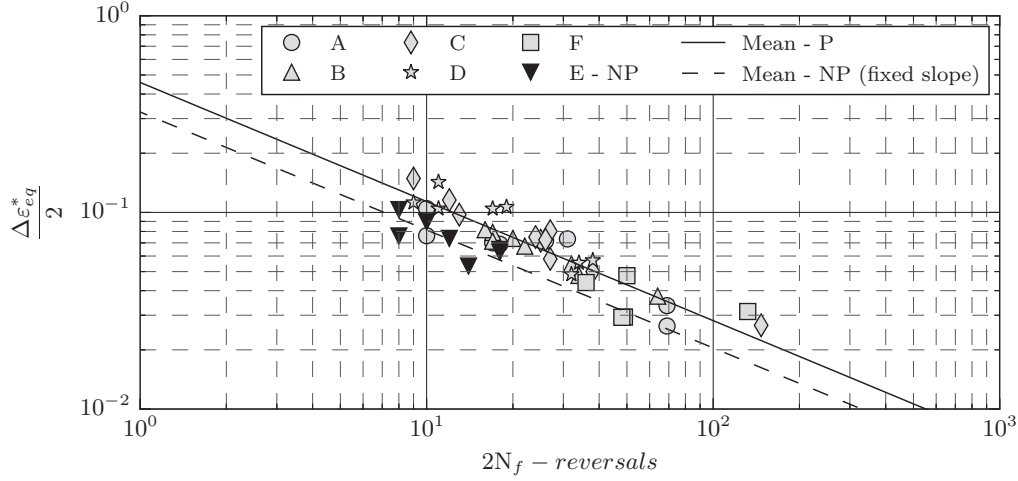


Figure 4.24 – Equivalent strain-life curve for tube to plate CA tests with non-proportional (NP) loading tests with a fixed slope of -0.6

With an acceptable basis for CA tests established, the problem of VA can be addressed in the form of a linear damage sum (Palmgren-Miner's rule -  $D$ ) following Eq.4.4, where  $N |_{\Delta\epsilon^*_{eq,i}}$  should be read as the number of applied cycles at ' $i$ -th' constant amplitude level of  $\epsilon^*_{eq}$ , and  $N_f$  given by Eq. 4.3 at the very same level.

$$D = \sum_i \frac{N |_{\Delta\epsilon^*_{eq,i}}}{N_f |_{\Delta\epsilon^*_{eq,i}}} \quad (4.4)$$

Fig. 4.25 shows the damage accumulation for both CA and VA loadings. The average value of damage for all tests is 1.03 with a coefficient of variation (CoV) of 29.15%. These results are consistent with damage sum distributions in high-cycle fatigue reported by [Wirsching, 1984], where it is recommended for fatigue reliability analyses to have  $D$  as a random variable with a log-normal distribution of mean 1.0 and CoV of 30%.

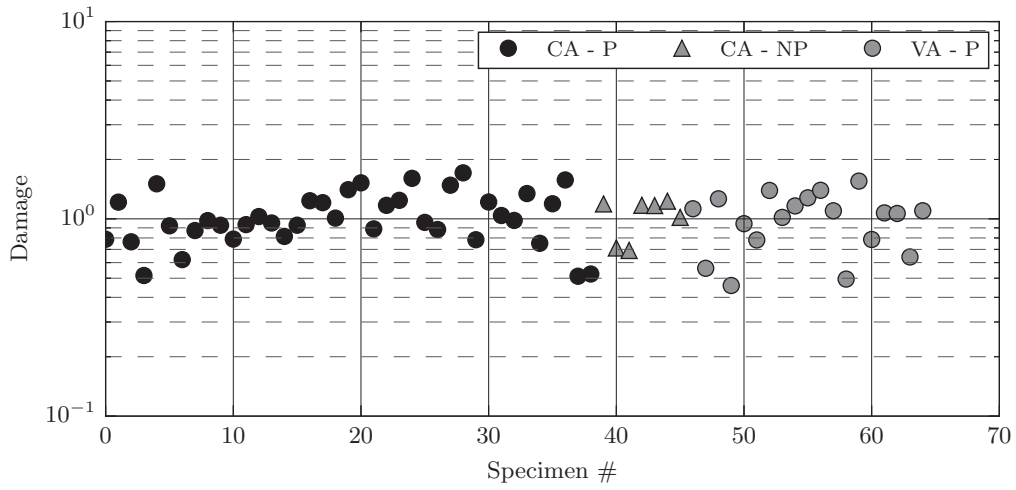


Figure 4.25 – Damage following Miner’s rule in Manson-Coffin model for tube to plate tests

## 4.5 Conclusion

This chapter presented the methodologies and the results obtained in the experimental program designed to study the behavior of a welded structural component in high-strength steel S770QL. The following concluding remarks are given:

1. One of the main observations of this test campaign was that in a large scale components one can observe surface cracking before any significant drop in the load carrying capacity of the specimen. This implies that physics based micromechanical models that are more suitable for fracture initiation are in principle unsuitable to describing these types of problems because a significant part of the component’s life is spent in propagation.
2. Initiation accounts for one third to a half of the life of a welded tube-to-plate specimen. Conversely, propagation is responsible for half to two thirds of ULCF life.
3. It was shown that classical approaches like the Manson-Coffin relationship for low cycle fatigue, that expresses fatigue resistance in total life <sup>9</sup> can be used for welded structural components using local digital image correlation measurements of strains.
4. Multiaxial loadings can be adequately represented in equivalent strain-life terms for proportional constant amplitude using local DIC measurements in high-strength structural steel.

<sup>9</sup>here failure arguably implies both initiation and propagation, though how much is spent in propagation is unclear since usually low-cycle fatigue tests that determine the ductility parameters are defined by the detection of a surface crack

5. Equivalent strain-life curves for proportional loadings with DIC measurements were observed to follow a slope of -0.6 which is well within the bounds found in literature for most metals [ASM International, 1996].
6. Non-proportional loading histories were found to be more damaging than proportional ones.
7. Variable amplitude time histories were found to be satisfactorily taken into account by linear damage sum according to Palmgren-Miner's rule.



## 5 A cyclic micromechanical material model

This chapter presents the development of a micromechanical material model to describe ductile fracture under large amplitude cyclic strains. It is divided by into three main sections. The first describes an extension of the GLD model to kinematic hardening and its implementation in a user-defined material model in Abaqus (UMAT). The second presents the validation of the material model through comparison with the UMAT implementation of Keralavarma-Benzerga (KB) material model presented in [Keralavarma and Benzerga, 2010] and implemented in Abaqus in [Kweon et al., 2016]. The third presents the performance of the material model using experimental data gathered in Chapter 3.

The main objective of this extension of the GLD model to incorporate kinematic hardening is to study void shape effects in a material's response to cyclic loading, particularly its effects in porosity ratcheting and therefore fracture incipience. Incorporating kinematic hardening in a porous material law is not an obvious task. A well-know issue, for example, is the influence of the hardening law's curvature under non-proportional loading as discussed in [Mear and Hutchinson, 1985]. Another is the choice of the backstress evolution law whose influence will be shortly presented. The extension submitted in this chapter will be phenomenological in nature with the objective of approximating as much as possible the behavior of the current GLD model for monotonic isotropic hardening *w.r.t.* both the evolution of the porosity and the void's aspect ratio. Having achieved this, the analysis of small scale specimens for both monotonic and cyclic loading will be presented.

A limit load on the inter-void ligament (the TBL model) will be used as a coalescence criterion and assumed to be representative of the incipience of fracture.

## 5.1 An extension of the GLD model to nonlinear kinematic hardening and its implementation

All the relevant quantities subsequently described should be interpreted as being incrementally rotated, following the hypoelastic formulation explained in Chapter 2. More specifically it should be underlined that these quantities follow Eq. 2.24 at the start of each step. Macroscopic quantities are represented by upper case letters (*e.g.* the plastic strain tensor becomes  $\mathbf{E}^p$ ).

### GLD yield criterion with backstresses

From Eq.2.47 one redefines the GLD function  $\phi^{GLD}(\boldsymbol{\Sigma}, \sigma_y, f, w, \boldsymbol{\Upsilon})$  to take into account the backstress ( $\mathbf{A} \rightarrow \phi^{GLD}(\boldsymbol{\Sigma}, \mathbf{A}, \sigma_y, f, w, \boldsymbol{\Upsilon})$ ), as shown in Eq. 5.1.

$$\begin{aligned} \phi^{GLD} = & C \frac{\|\boldsymbol{\Sigma}' - \mathbf{A}' + \eta \Sigma_h \mathbf{Q}\|^2}{\sigma_y^2} + \\ & 2q(g+1)(g+f) \cosh\left(k \frac{(\boldsymbol{\Sigma} - \mathbf{A}) : \mathbf{X}}{\sigma_y}\right) - \\ & (g+1)^2 - q^2(g+f)^2 \end{aligned} \quad (5.1)$$

with  $\Sigma_h = (\boldsymbol{\Sigma} - \mathbf{A}) : \mathbf{X}$ ,  $\|\mathbf{S}\| = \sqrt{3/2 \mathbf{S}' : \mathbf{S}'}$  and  $q$  a factor fit to unit cells calculations similarly to Eq. 2.63. In this thesis no corrections using  $q$  were used (*i.e.*  $q = 1.0$  in all calculations).

### Residuals and implicit integration scheme

Consider a strain increment (Eq. 2.14) defining the total strain  $\mathbf{E}_{n+1} = \mathbf{E}_n + \Delta \mathbf{E}$ , with strain assumed to be additively decomposed in elastic and plastic parts, following an associated flow rule for  $\Delta \mathbf{E}^p$  ( $\Delta \mathbf{E}^p = \lambda \partial \phi^{GLD} / \partial \boldsymbol{\Sigma}$ ). For a material to adhere to these assumptions, the following conditions (known in the context of convex optimization as the Karush-Kuhn-Tucker (KKT) conditions) have to be met,

$$\lambda \geq 0 \quad (5.2)$$

$$\phi^{GLD} \leq 0 \quad (5.3)$$

$$\lambda \phi^{GLD} = 0 \quad (5.4)$$



### 5.1. An extension of the GLD model to nonlinear kinematic hardening and its implementation

In succinct terms, these conditions ensure that when the step is elastic ( $\phi^{GLD} < 0$ ), by Eq. 5.4 no plastic strain occurs ( $\lambda = 0$ ), but when plastic strain occurs, also by Eq. 5.4, one must be on the yield function ( $\phi^{GLD} = 0$ ).

Let us define residual  $R_{n+1}^*$  as the error one makes in quantity  $*$  between configuration  $n$  and  $n + 1$  as the following,

$$R_{ij,n+1}^{\mathbf{E}^p} \equiv -E_{ij,n+1}^p + E_{ij,n}^p + \lambda \left. \frac{\partial \phi}{\partial \Sigma_{ij}} \right|_{n+1} \quad (5.5)$$

$$R_{n+1}^\phi \equiv \phi|_{n+1} \quad (5.6)$$

When the strain increment violates the KKT conditions, one must then get back to the yield surface, *i.e.* one must allow some part of the strain increment to be plastic<sup>1</sup> in order to decrease the value of the yield function so that Eq. 5.4 is satisfied. This is achieved by linearizing Eqs. 5.5 and 5.6 to obtain Eqs. 5.7 and 5.8,

$$R_{kl,n+1}^{\mathbf{E}^p} + \frac{\partial R_{kl,n+1}^{\mathbf{E}^p}}{\partial \Sigma_{ij}} d\Sigma_{ij} + \frac{\partial R_{kl,n+1}^{\mathbf{E}^p}}{\partial A_{ij}} dA_{ij} + \frac{\partial R_{kl,n+1}^{\mathbf{E}^p}}{\partial \sigma_y} d\sigma_y + \frac{\partial R_{kl,n+1}^{\mathbf{E}^p}}{\partial f} df + \frac{\partial R_{kl,n+1}^{\mathbf{E}^p}}{\partial w} dw + \frac{\partial R_{kl,n+1}^{\mathbf{E}^p}}{\partial \Upsilon_{ij}} d\Upsilon_{ij} \overset{\text{Neglected}}{\longrightarrow} = 0 \quad (5.7)$$

$$R_{n+1}^\phi + \frac{\partial R_{n+1}^\phi}{\partial \Sigma_{ij}} d\Sigma_{ij} + \frac{\partial R_{n+1}^\phi}{\partial A_{ij}} dA_{ij} + \frac{\partial R_{n+1}^\phi}{\partial \sigma_y} d\sigma_y + \frac{\partial R_{n+1}^\phi}{\partial f} df + \frac{\partial R_{n+1}^\phi}{\partial w} dw + \frac{\partial R_{n+1}^\phi}{\partial \Upsilon_{ij}} d\Upsilon_{ij} \overset{\text{Neglected}}{\longrightarrow} = 0 \quad (5.8)$$

Since  $\mathbf{A}$ ,  $\sigma_y$ ,  $f$  and  $w$  can be defined as a function of the plastic strain increment, one can write the solution of the set of Eq. 5.7 and 5.8 as,

$$d\Sigma_{ij} = \Xi_{ijkl} \left\{ -R_{kl}^{\mathbf{E}^p} - \frac{\partial R_{kl}^{\mathbf{E}^p}}{\partial \lambda} d\lambda \right\} \quad (5.9)$$

$$d\lambda = \frac{-\phi + \frac{\partial \phi}{\partial \Sigma_{ij}} \Xi_{ijkl} R_{kl}^{\mathbf{E}^p}}{\frac{\partial \phi}{\partial \lambda} - \frac{\partial \phi}{\partial \Sigma_{ij}} \Xi_{ijkl} \frac{\partial R_{kl}^{\mathbf{E}^p}}{\partial \lambda}} \quad (5.10)$$

where  $\Xi$  is the algorithmic tangent stiffness matrix defined in Eq.5.11 with  $\mathcal{C}$  being the elastic

<sup>1</sup>An important detail in this scheme is the direction in which that plastic increment is taken. In this implicit algorithm, normality is enforced at the end of the step *cf.* Eq. 5.5

stiffness matrix and,

$$\Xi = \left[ \mathcal{C}^{-1} + \lambda \frac{\partial^2 \phi}{\partial \Sigma^2} \right]^{-1} \quad (5.11)$$

$$\frac{\partial R_{kl}^{\mathbf{E}^p}}{\partial \lambda} = \frac{\partial R_{kl}^{\mathbf{E}^p}}{\partial A_{kl}} \frac{\partial A_{kl}}{\partial \lambda} + \frac{\partial R_{kl}^{\mathbf{E}^p}}{\partial \sigma_y} \frac{\partial \sigma_y}{\partial \lambda} + \frac{\partial R_{kl}^{\mathbf{E}^p}}{\partial f} \frac{\partial f}{\partial \lambda} + \frac{\partial R_{kl}^{\mathbf{E}^p}}{\partial w} \frac{\partial w}{\partial \lambda} \quad (5.12)$$

$$\frac{\partial \phi}{\partial \lambda} = \frac{\partial \phi}{\partial A_{kl}} \frac{\partial A_{kl}}{\partial \lambda} + \frac{\partial \phi}{\partial \sigma_y} \frac{\partial \sigma_y}{\partial \lambda} + \frac{\partial \phi}{\partial f} \frac{\partial f}{\partial \lambda} + \frac{\partial \phi}{\partial w} \frac{\partial w}{\partial \lambda} \quad (5.13)$$

This constitutes the core of the return-mapping algorithm [Simo and Hughes, 1998]. Derivatives are given in Appendix A. The implementation is also supplemented with a backtrack line search for increased numerical stability [Boyd and Vandenberghe, 2004].

### Rates and increments

Stress, strain and plastic multiplier at iteration *it* using Eqs. 5.10 and 5.9 are as follows,

$$\Sigma_{n+1}^{it} = \Sigma_{n+1}^{it-1} + d\Sigma \quad (5.14)$$

$$\lambda_{n+1}^{it} = \lambda_{n+1}^{it-1} + d\lambda \quad (5.15)$$

$$\mathbf{E}_{n+1}^{P,it} = \mathbf{E}_{n+1}^{P,it-1} + \mathcal{C}^{-1} d\Sigma \quad (5.16)$$

$$E_{eq,n+1}^{P,it} = E_{eq,n}^P + \chi \lambda_{n+1}^{it} \quad (5.17)$$

with  $\chi$  given by Eq. 5.18.

$$\chi = \sqrt{\frac{2}{3} \frac{\partial \phi}{\partial \Sigma} : \frac{\partial \phi}{\partial \Sigma}} \quad (5.18)$$

Internal variables are initiated as follows,

$$\Sigma_{n+1}^0 = \Delta \Lambda \Sigma_n \Delta \Lambda^T + \mathcal{C} \Delta \mathbf{E} \quad (5.19)$$

$$\mathbf{A}_{k,n+1}^0 = \Delta \Lambda \mathbf{A}_n \Delta \Lambda^T \quad (5.20)$$

$$\sigma_{y,n+1}^0 = \sigma_{y,n}; f_{n+1}^0 = f_n; w_{n+1}^0 = w_n \quad (5.21)$$

$$\Upsilon_{n+1}^0 = \Delta \Lambda \Upsilon_n \Delta \Lambda^T \quad (5.22)$$

### 5.1. An extension of the GLD model to nonlinear kinematic hardening and its implementation

---

#### Backstresses - $\mathbf{A}$

Nonlinear kinematic hardening is incorporated using the Chaboche model. Here, there exists two options in terms of backstress rates. The first following Eq. 2.38 (Eq. 5.23) the second following [Mear and Hutchinson, 1985] (Eq. 5.24)

$$\dot{\mathbf{A}}_k = \left( \frac{2}{3} C_k \frac{\partial \phi}{\partial \Sigma} - \gamma_k \mathbf{A} \chi \right) \dot{\lambda} \quad (5.23)$$

$$\dot{\mathbf{A}}_k = \left( \frac{C_k}{\sigma_y} (\Sigma - \mathbf{A}) - \gamma_k \mathbf{A} \right) \chi \dot{\lambda} \quad (5.24)$$

where 'k' is the k-th backstress and  $\mathbf{A} = \sum_k \mathbf{A}_k$ . Because of the yield surface's dependency on the hydrostatic pressure, the use of the rate in Eq. 5.23 reinforces the rate of change of the porosity leading to significant differences with respect to isotropic hardening. The rate in Eq. 5.24 mitigates this issue, updating internal variables much in the same way as isotropic hardening - see Section 5.2 on results. The algorithm is an implicit Newton method integration scheme, this means the derivatives in the final iteration are taken to be constant during the integration step (see Eqs. 5.5 and 5.6). With this and the differential equation in Eq. 5.24, it can be shown that the k-th backstress in step *it* ( $\mathbf{A}_{k,n+1}^{it}$ ) is given by,

$$\mathbf{A}_{k,n+1}^{it} = \frac{\mathbf{A}^* - \left\{ \mathbf{A}^* - \left( \frac{C_k}{\sigma_y} + \gamma_k \right) \mathbf{A}_{k,n} \right\} e^{-\left( \frac{C_k}{\sigma_y} + \gamma_k \right) \chi \lambda_{n+1}^{it}}}{\frac{C_k}{\sigma_y} + \gamma_k} \quad (5.25)$$

with,

$$\mathbf{A}^* = \frac{C_k}{\sigma_y} (\Sigma_{n+1}^{it} - \mathbf{A}_n + \mathbf{A}_{k,n}) \quad (5.26)$$

$\mathbf{A}^*$  is the variable that dictates the change in direction in which the step is taken and is constant throughout the increment step.

In so far as the evolution law for the backstress is postulated phenomenologically, a keen observer might take issue with the fact that it depends on the macroscopic equivalent plastic strain increment and not the microscopic one. By the Hill-Mandel lemma in Eq. 2.44 they differ by a factor of  $(1 - f)$ . The use of the macroscopic plastic strain rate  $\mathbf{D}^p$  to define the backstress evolution law is not unprecedented in phenomenological adaptations to kinematic hardening of the Gurson model *cf.* [Klingbeil et al., 2016]). There, however, the final backstress is multiplied by a factor of  $(1 - f)$  to ensure that it vanishes in the limit of  $f \rightarrow 1$ . Although no such considerations are made here, for the porosities used in this study

## Chapter 5. A cyclic micromechanical material model

---

this factor is deemed negligible. This issue is, nonetheless, important to bring to the reader's attention.

### Yield stress - $\sigma_y$

Nonlinear isotropic hardening was chosen to take the form of Eq.<sup>2</sup> 5.27.

$$\sigma_{y,n+1}^{it} = \sigma_{y,0} + K \left( E_{eq,n+1}^{p,it} \right)^n \quad (5.27)$$

### Porosity - $f$

From homogenization the rate of change of porosity is defined as,

$$\dot{f} = (1 - f) \frac{\partial \phi}{\partial \Sigma_{kk}} \dot{\lambda} \quad (5.28)$$

Following the same reasoning as in the backstress sub-section, the porosity at iteration  $it$  is given by,

$$f_{n+1}^{it} = 1 - (1 - f_n) e^{\frac{\partial \phi}{\partial \Sigma_{kk}} \lambda_{n+1}^{it}} \quad (5.29)$$

For cyclic loading, in the absence of a mechanism to incorporate particle-void interaction, a heuristic was implemented so that  $f$  is not smaller than the initial porosity  $f_0$  - Eq. 5.30. If indeed this were to be true, this would imply that the inclusions around which the voids form, would lose volume.

$$\begin{cases} f_{n+1}^{it} = f_{n+1}^{it} & , f_{n+1}^{it} > \epsilon \cdot f_0 \\ f_{n+1}^{it} = f_0 & , f_{n+1}^{it} \leq \epsilon \cdot f_0 \end{cases} \quad (5.30)$$

where  $\epsilon$  is a number close to unity (*e.g.*=0.9999) to ensure one is always tightly bound by the initial porosity level.

### Aspect ratio - $w$

Defining  $S = \ln(w)$ , the rate of change of S is taken from Eq. 2.52 as to be as Eq. 5.31

$$\dot{S} = \mathbf{Z} : \left[ (1 + k_w k_f k_T) \frac{\partial \phi}{\partial \Sigma} + \left( \frac{1}{f_{n+1}^{it}} \mathbf{X}_v - \mathbf{X} \right) \frac{\partial \phi}{\partial \Sigma_{kk}} \right] \dot{\lambda} \quad (5.31)$$

---

<sup>2</sup><sub>n</sub> as a superscript is associated with the material's hardening exponent

### 5.1. An extension of the GLD model to nonlinear kinematic hardening and its implementation

An important heuristic is here introduced. Following experimental observations in Chapter 3 and in [Kanvinde and Deierlein, 2004] that voids under ultra low cycle fatigue tend to be shallower than in monotonic cases, the rate of change of the aspect ratio is adjusted according to Eq. 5.32

$$\dot{S}^{cyclic} = \begin{cases} \dot{S} & , \frac{\partial \phi}{\partial \Sigma_{kk}} > 0 \\ \rho \dot{S} & , \frac{\partial \phi}{\partial \Sigma_{kk}} \leq 0 \end{cases} \quad (5.32)$$

In cases where the average volume increases (given by  $\partial \phi / \partial \Sigma_{kk}$ ), one falls to the GLD's rate of change. When the void decreases in volume, however, one changes the rate by a constant proportionality factor  $\rho$ . The aspect ratio at the end of the step is, therefore, given by,

$$w_{n+1}^{it} = w_n e^{\dot{S}^{cyclic} \lambda_{n+1}^{it}} \quad (5.33)$$

#### Void orientation

If the void is approximately spherical *i.e.*  $0.99 \leq w \leq 1.01$ , as per [Kweon et al., 2016], the void's orientation given by  $\mathbf{\Upsilon}$  follows the eigenvectors of the void's plastic strain tensor increment  $\Delta t \mathbf{D}_v$  with  $\mathbf{n}_3$  being the maximum stretch direction (corresponding to the maximum eigenvalue) with,

$$\Delta t \mathbf{D}_v = \left[ (1 + k_w k_f k_\tau) \frac{\partial \phi}{\partial \Sigma} + \left( \frac{1}{f_{n+1}^{it}} \mathbf{X}_v - \mathbf{X} \right) \frac{\partial \phi}{\partial \Sigma_{kk}} \right] \lambda \quad (5.34)$$

Outside this range two options present themselves as discussed in chapter 2. For the Jaumman-Zaremba rate, one should take care to correct for plastic distortions induced by the void. For the Green-McInnis-Naghdi rate, in the absence of a better approximation, one considers that voids rotates with the material, *i.e.* it follows Eq. 5.22 with Eq. 2.29. Simulations presented in this Chapter will only use the Green-McInnis-Naghdi rate. The choice to use this rate is justified with the increased sensitivity to shear oscillations in the Jaumann-Zaremba rate for shear loadings when kinematic hardening is used (illustration given in the validation section - Section 5.2, Fig. 5.6 ).

#### Convergence criterion

Convergence is said to be achieved when the residuals are within a specified tolerance. That tolerance is defined in this UMAT by  $\|R^{\mathbf{E}^P}\| / \|\mathbf{E}^P\| < Tol$  and  $\phi^{GLD} < Tol$ . Tolerance used was  $1e - 5$ .

### Void coalescence

Void coalescence was implemented as a failure indicator with the TBL model. Stresses are put into the void's frame of reference first by rotating tensor  $\boldsymbol{\Sigma} - \mathbf{A}$  back to the undeformed frame of reference, then changing the reference frame to match the void's orientation - see Eq. 5.35

$$\boldsymbol{\Sigma}^v = \mathbf{\Upsilon}^T \boldsymbol{\Lambda}^T (\boldsymbol{\Sigma} - \mathbf{A}) \boldsymbol{\Lambda} \mathbf{\Upsilon} \quad (5.35)$$

Two important assumptions will be made. The first concerns the size of the void considered in TBL's RVE: given a cylindrical void with radius  $R^{TBL}$  whose volume is defined by  $V_v^{TBL} = 2\pi w^{TBL} (R^{TBL})^3$ , one stipulates that the change in the void's volume is approximately equal to the change in the porosity defined by the GLD model ( $f$ ). This is expressed in Eq. 5.36.

$$\frac{f}{f_0} \approx \frac{V_v^{TBL}}{V_{v,0}^{TBL}} \quad (5.36)$$

The second assumption will be that the distance between voids RVE's remains roughly the same during loading *i.e.*  $L^{TBL} = L_0^{TBL}$ , and that the aspect ratio of the void in the GLD model is the same as in the TBL model. From Eq. 5.36 one can then arrive at Eq. 5.37.

$$\chi_{TBL} = \sqrt[3]{\frac{f}{f_0} \frac{w_0}{w}} \chi_{TBL,0} \quad (5.37)$$

This assumption arose from the need to have a criterion that provided good estimates in both monotonic and in cyclic loading, in which no obvious proposition can be made. Some justification, however, can be found in the fact that in a 2D random distribution of voids, the cells in its corresponding Dirichlet tessellation have an average aspect ratio of 1 and stay 1 throughout loading simply due to the random nature of the tiling [Benzerga, 2000].

TBL's yield function is then evaluated ( $\phi^{TBL}(\boldsymbol{\Sigma}^v, \chi_{TBL}, w)$  - see Eq. 2.58) and failure is defined in the FEM models when  $\phi^{TBL} = 0$  i.e. when  $\phi^{TBL}$  goes outside the elastic domain defined by its yield function.

### 5.1. An extension of the GLD model to nonlinear kinematic hardening and its implementation

---

#### Structure of the UMAT

Abaqus Standard supplies the following useful quantities:  $\Sigma_n$ ,  $DROT$ ,  $\mathbf{F}_n$ ,  $\mathbf{F}_{n+1}$  and  $SDV$  a vector for the user to store internal variables ( $\xi$ ). The stress tensor  $\Sigma_n$  as supplied by Abaqus, is already incrementally rotated by the Jaumann-Zaremba rate ( $DROT$ ). The first step in the analysis is to neutralize this rotation by Eq. 5.38 - superscript  $\sim$  means the rotated configuration from  $n$  to  $n + 1$ .

$$\Sigma_n = DROT^T \tilde{\Sigma}_n DROT \quad (5.38)$$

Subsequently relevant quantities like the strain increment  $\Delta \mathbf{E}$  and incremental rotation  $\Delta \Lambda$  are calculated with the deformation gradient  $\mathbf{F}_n$  and  $\mathbf{F}_{n+1}$  following what was outlined in Chapter 2.

Then quantities like the plastic strain tensor, the backstresses and  $\Lambda$  from the previous iteration that are stored in  $SDV$  are rotated following incremental objectivity.

The trial stress tensor is subsequently calculated and if the KKT conditions are violated, the step is plastic and one has to use the return mapping algorithm outlined previously to get back to the yield function.

Once on the yield function, voids are rotated and  $\phi^{TBL}$  evaluated. All relevant quantities at the end of the step ( $f, w, E_{eq}^p, \eta^v$ ,  $\mathbf{E}$ ,  $\mathbf{A}, \mathbf{E}^p, \mathbf{\Upsilon}, \mathbf{\Lambda}$ ,  $\mathbf{A}_k$  and  $\phi^{TBL}$  are then stored in  $SDV$ , the new stress supplied to Abaqus and one is now ready for the next step.

This procedure is summarized in Fig. 5.1

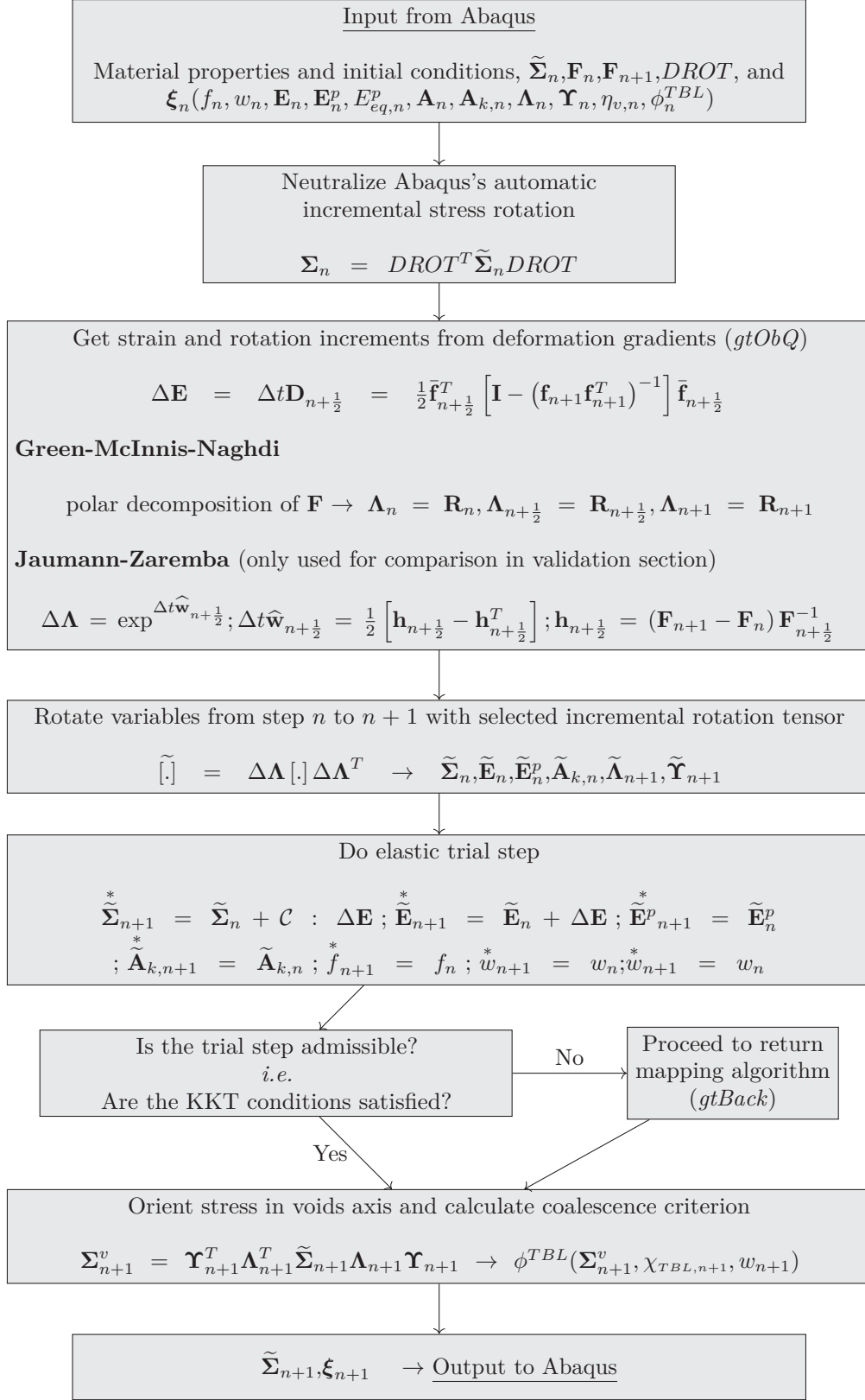


Figure 5.1 – Structure of the *gld* UMAT



## 5.2 Validation and additional comments

This section presents validation tests conducted on the UMAT developed for cyclic loading presented in the previous section. Validation is mostly achieved through comparison with the UMAT implementation of the KB material model presented in [Keralavarma and Benzerga, 2010] and implemented in an Abaqus UMAT discussed in [Kweon et al., 2016]. This material model is based on an extension of the GLD model to an anisotropic Hill matrix. To compare the performance of the two formulations, all anisotropic coefficients were set such that the material behavior is isotropic.

All comparisons have the same material response associated with it. By that statement, it is meant that whenever Isotropic or Kinematic hardening terms are employed the coefficients describing the hardening have been fit to material presented in Table 3.1. This includes backstress coefficients in the Chaboche model  $C_k$  and  $\gamma_k$ .

Validation tests were carried out on a single 3D cubic element (8 nodes) with reduced integration (C3D8R). The outcomes shown subsequently are results in the integration point of that element. Two loading cases are presented in Fig. 5.2. Although most of the examples shown will use only tension since there is a difference in the rotational formulation between this study and [Kweon et al., 2016], one example is made illustrating the difference between using the Jaumann-Zaremba stress rate and the Green-Mcinnis-Naghdi rate.

One begins, however, to illustrate a salient point in the kinematic hardening formulations of micromechanical models. It pertains to the choice of hardening direction presented in equations 5.23 and 5.24 (*i.e.* between the first term being in the direction of  $\Sigma - \mathbf{A}$  and  $\dot{\mathbf{D}}^p$ , respectively). Consider Fig. 5.3 in which the choices are compared. There it can be observed that  $\dot{\mathbf{D}}^p$  leads to significantly different predictions on the porosity. This is justified by considering that micro-mechanical models of porous ductile media are inherently not volume preserving (*i.e.*  $E_{kk} \neq 0$ ). If the term  $E_{kk} \neq 0$  then this has the most visible effect of self-reinforcing the porosity rate.  $\Sigma - \mathbf{A}$  is the same as presented in [Mear and Hutchinson, 1985]. Henceforth, Eq. 5.24 will be used.

To show that this implementation of the GLD model with kinematic hardening is behaving well in the limit of the Gurson model, one need only to show that for a circular void ( $S = 0$ ) and for  $\dot{S} = 0$  this model offers the same predictions as the Gurson model as implemented in Abaqus. This is done successfully in Fig. 5.4.

To include void shape effects, the GLD model will be compared with the KB UMAT. Table 5.1 presents the case studies performed for this comparison. Full presentation of the results

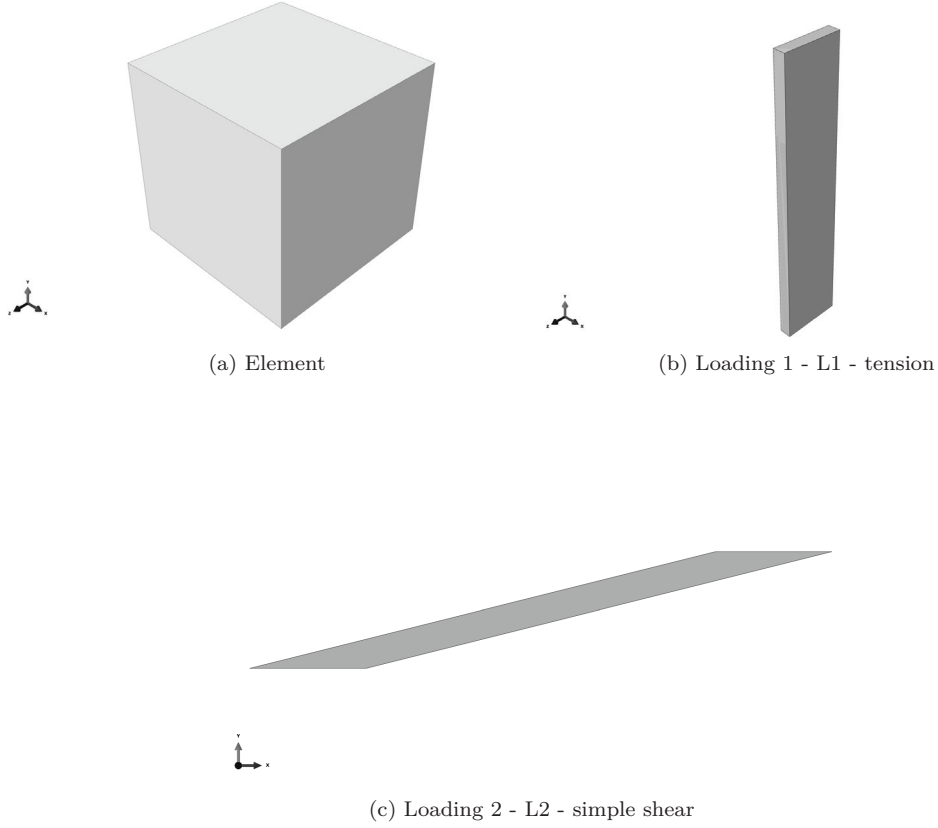


Figure 5.2 – Element(C3D8R) and loading cases used in validation of gld Umat in Abaqus

are too lengthy and referred to Appendix A. One presents however a representative case in Fig. 5.5 for tension load transverse to a prolate void. Small differences are attributed mostly to the disparities in the integration scheme and the derivatives between the two formulations. They are deemed acceptable for the purposes of this study, *i.e.* they capture with sufficient accuracy the interactions between porosity and void shape effects for initially spherical, oblate and prolate voids with loadings parallel and transverse to their main axis.

Lastly, one should comment on the choice of the Green-McInnis-Naghdi rate for this formulation. Consider the case of a loading in simple shear and the material response with the two different rates shown in Fig. 5.6. Here, one can observe the extent to which the Jaumann-Zaremba rate is more sensitive to shear oscillations than the Green-McInnis-Naghdi rate <sup>3</sup>.

---

<sup>3</sup>The detection of this problem arose in an attempt to model the double notched tubes in Chapter 3 in a 2D axisymmetric model enriched with an extra degree of freedom that allows for torque. The material model used was the nonlinear kinematic hardening supplied with Abaqus. The methodology is similar to the one followed by [Faleskog and Barsoum, 2013]. Even though the intended material law was an ever increasing power law, material softening was observed.

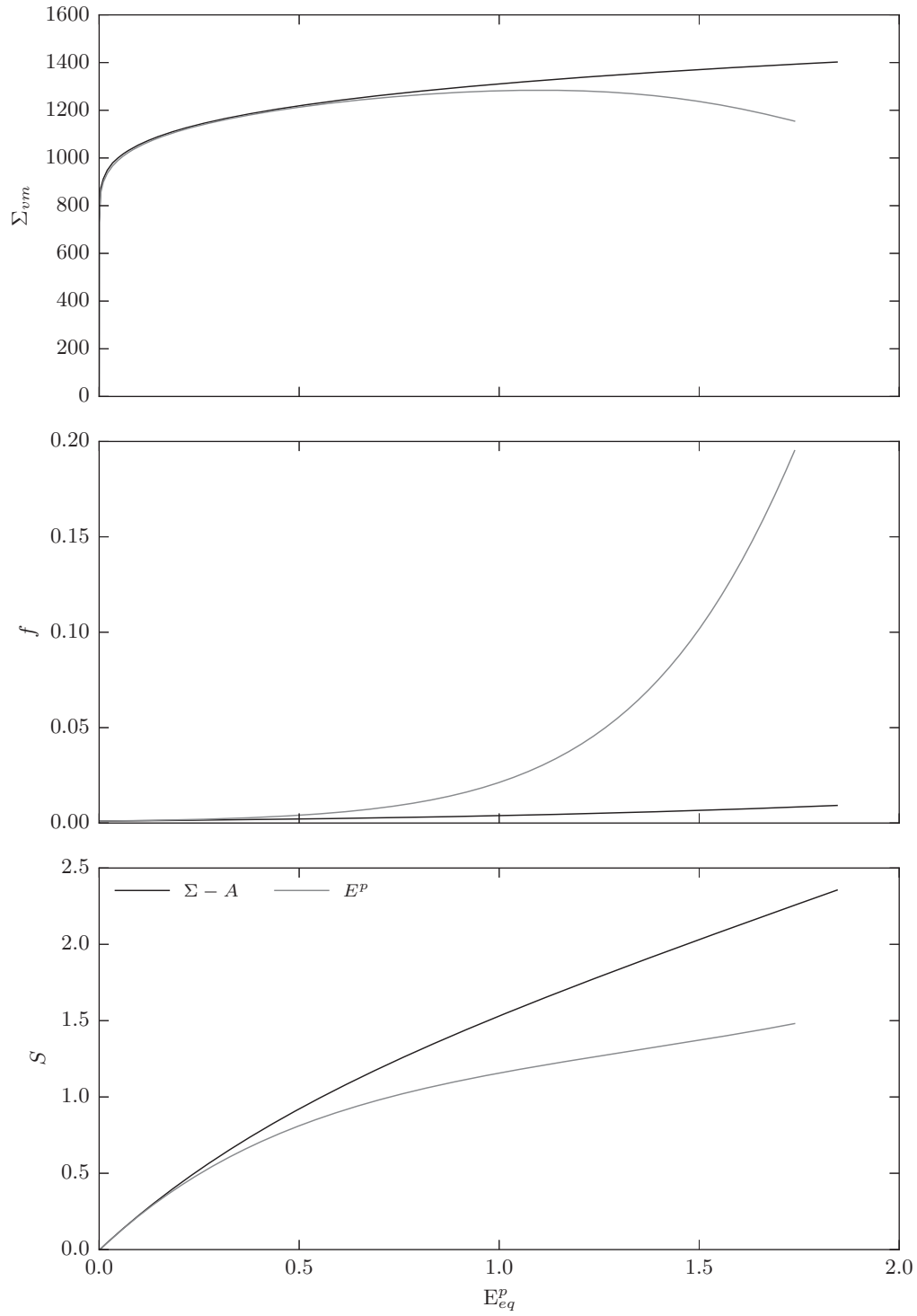


Figure 5.3 – Comparison between hardening directions

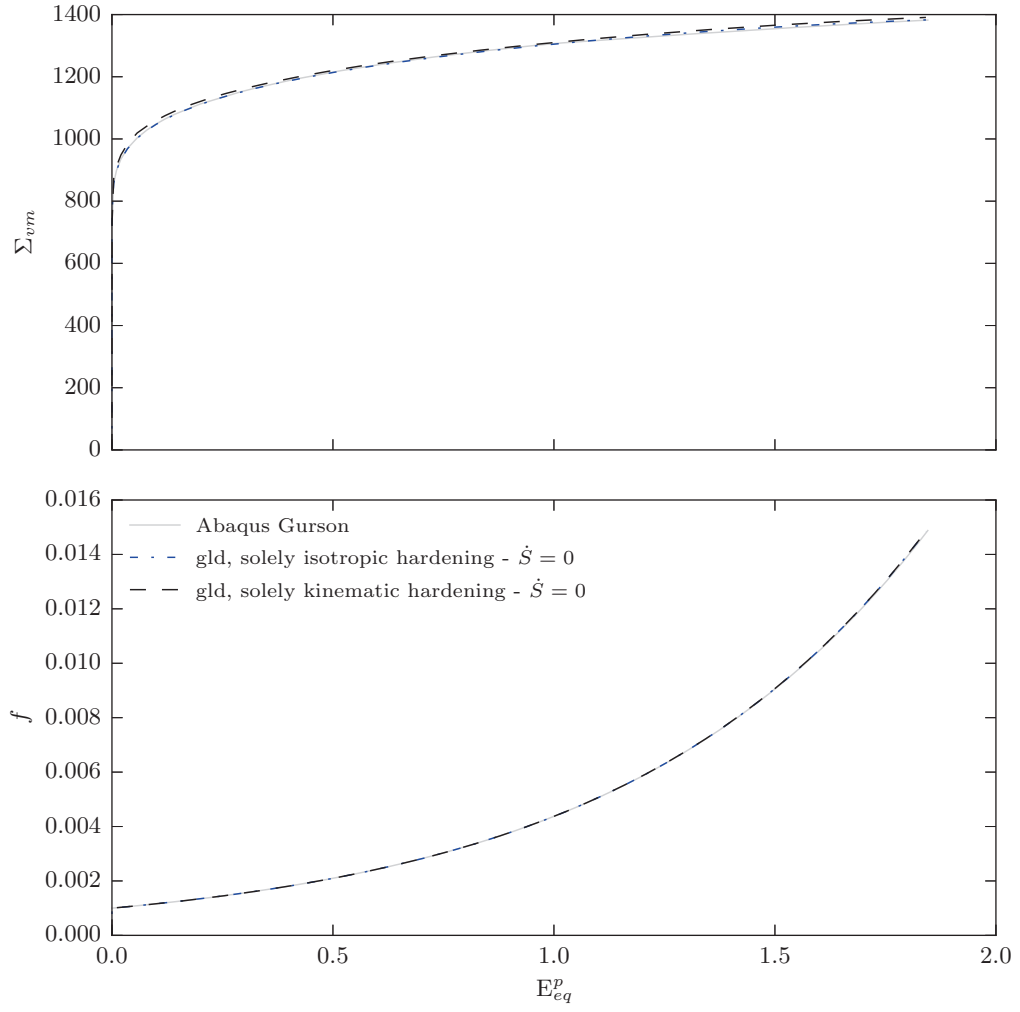


Figure 5.4 – Comparison between GLD Umat and Abaqus’s implementation of the Gurson model

Table 5.1 – Designation for internal variables used in the validation procedure with KB UMAT

Designation #	$f_0$	$S_0$	$\Upsilon$
1	1.0e-3	0.0	$\mathbf{n}_3 \equiv [0, 1, 0]$
2	5.0e-3	1.0	$\mathbf{n}_3 \equiv [1, 0, 0]$
3	1.0e-2	-1.0	-
4	1.5e-2	-	-

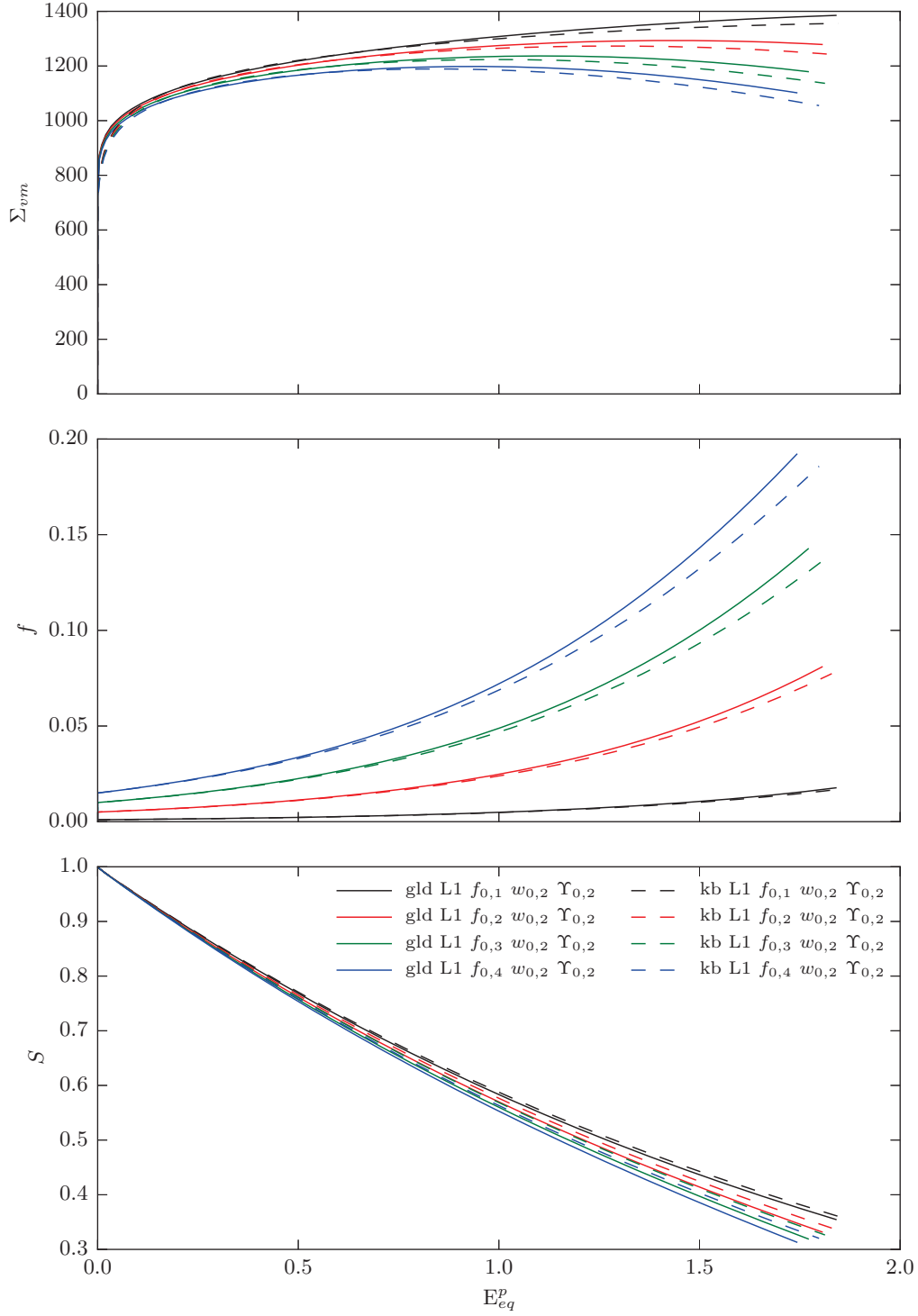


Figure 5.5 – Comparison between for tension load tranverse to prolapse void

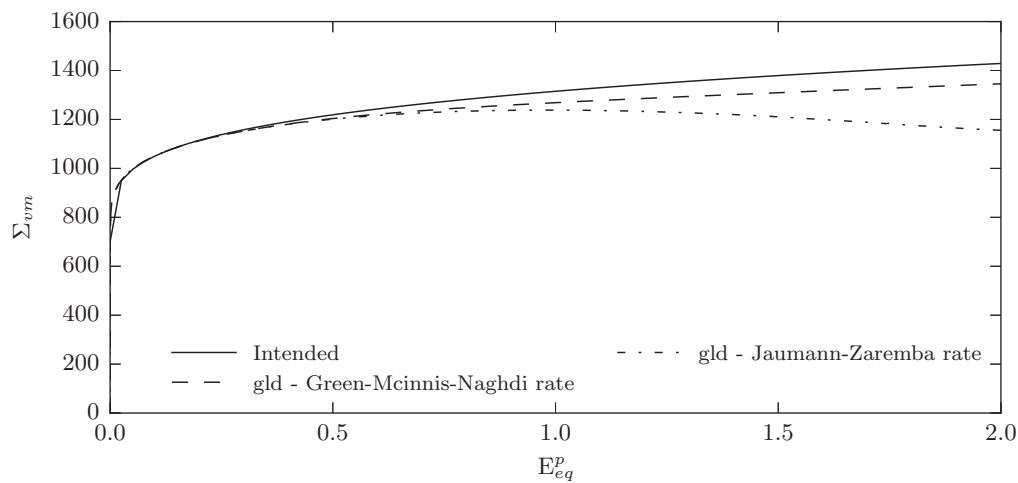


Figure 5.6 – Comparison between intended material response and different objective stress rates in kinematic hardening for simple shear

## 5.3 Analysis of small scale tests

This section discusses the application of the material model presented before. It first begins by discussing the results from the application to single notched tensile specimen followed by a discussion on its application to the double notched tubular specimens. In the latter case, it will be seen that its applications proved challenging, mainly for computational reasons and, as such, their results constitute merely a qualitative interpretation of the model. All finite element models follow the formulation shown in Section 5.1, *i.e.* a full 3D element formulation. All models are conducted solely with kinematic hardening. The Chaboche coefficients used in all models can be consulted in Table A.1, which were fit to the half cycle data shown in Table 3.1 with 8 backstresses.

### 5.3.1 Single notched bar specimens

One begins by describing the geometry of the models for single notched specimens. Geometric characteristics for all models follow caliper measurements for the notch area as well as scaled pictures (*c.f.* Section 2.2) from the target DIC data to calculate the local displacement at the notch. Since targets were not layed at precise distances for all specimens, loading was obtained for all specimens individually and so each test constitutes a single finite element model; distances from the center of each target to the corresponding notch edge were taken into account in its definition.

For computational reasons, only a quarter of the specimen was modeled. Boundary conditions were set as follows: the base corresponding to the lower DIC target was kept fixed, while at the upper top, the displacement measured by the difference between the DIC targets was applied to all nodes using a master-slave node formulation. Vertical boundary conditions at the sides of the model followed double symmetry.

Mesh size was kept constant throughout the notch cross section to avoid mesh dependency issues when comparing between different test results. Linear 3D cubic reduced integration isoparametric elements (C3D8R) of  $50\mu m$  and aspect ratio of approximately of 1 (cube) were used in all models. An example of a typical model is depicted in Fig. 5.7.

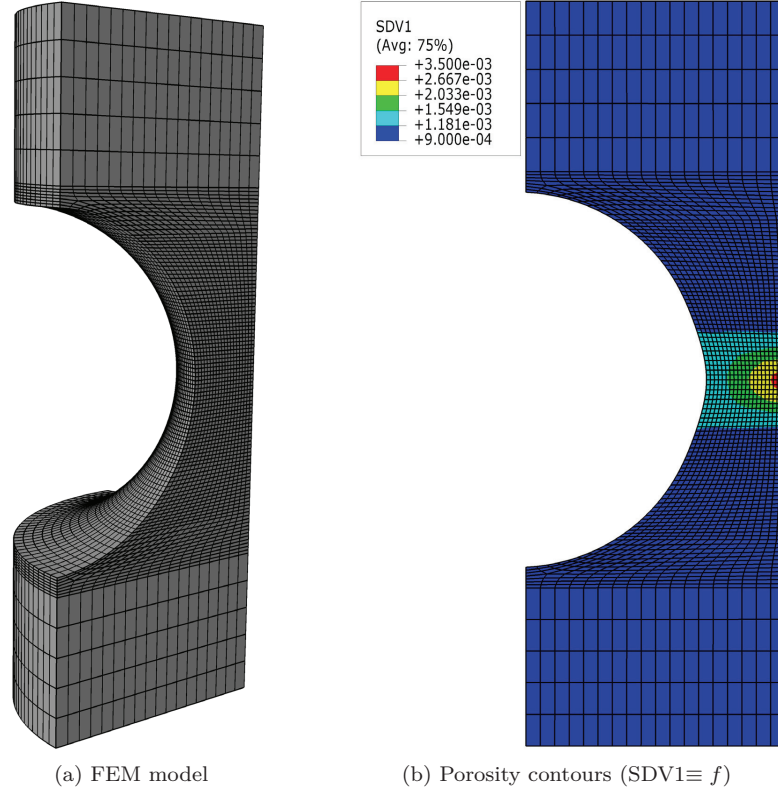


Figure 5.7 – FEM model and a typical porosity contour map for a single notched bar test (T2CA1\_7\_1 at the 17th half cycle)

### Monotonic

Fig. 5.8 presents the load displacements curves from the 6 monotonic tests that were conducted. The curves approximate tests to within a reasonable accuracy - consider the transition from the elastic regime into plasticity taking into account the non-linear drop in stiffness caused by necking of notch.

In Fig. 5.8 is also represented a coalescence criterion given by the condition set by the TBL micromechanical model ( $\phi^{TBL} = 0$ ). Parameters governing this criterion were set as follows. First micro-mechanical internal variables were set using the observations presented in Section 3.2 :  $f_0 = 1e - 3$ ,  $w_0 = 1.0$ . Subsequently, one test (T2M\_7\_2) was picked where the objective was to find the initial ligament ratio ( $\chi_{TBL,0}$ ) that corresponded  $\phi^{TBL} = 0$  through the heuristic outlined previously. The result was a ligament ratio of 0.25. This quite close to the estimate obtained in Section 3.2 for the inclusion ligament size ratio ( $\chi_{inc}$ ).

Table 5.2 shows a summary of the monotonic test results where a comparison is made between the failure displacement (as defined by a significant drop in stiffness in the necking phase)



Table 5.2 – Data summary for monotonic tests

Specimen	$\delta_f^{SN,test}$ (mm)	$\delta_f^{SN,TBL}$ (mm)	$\delta_f^{SN}$ % diff.	$\bar{T}$	$E_{eq,f}^{p,TBL}$	$E_{eq,f}^{p,Test}$
T1M_7_1	0.608	0.506	16.7	1.02	0.47	0.6
T1M_7_2	0.554	0.479	13.5	1.03	0.45	0.54
T1M_7_3	0.519	0.482	7.1	1.02	0.48	0.52
T2M_7_1	0.561	0.580	3.6	0.89	0.70	0.66
T2M_7_2	0.598	0.595	0.5	0.89	0.70	0.70
T2M_7_3	0.655	0.608	7.1	0.88	0.74	0.8

$f_0 = 1e - 3, w_0 = 1.0, \chi_{TBL,0} = 0.25$ , and  $\bar{T}$  taken similarly as Eq. 3.11

and the displacement estimated by the FEM model with the TBL criterion. Also presented in Table 5.2 is the weighted average of the triaxiality during loading and the equivalent plastic strain as measured in the FEM models at the failure displacement estimated by the TBL criterion ( $E_{eq,f}^{p,TBL}$ ) and the test ( $E_{eq,f}^{p,Test}$ ). Average error in assessing  $E_{eq,f}^p$  between TBL and tests for T1 is on the order of 15.7%. The maximum percentage difference in displacement of 16.7% is justified by a greater error in assessing the elastic stiffness of the specimen. A model with smaller elastic stiffness would have a smaller  $E_{eq,f}^{p,TBL}$ , which is in line with the TBL estimates. These differences are considered acceptable for the purposes of this study.

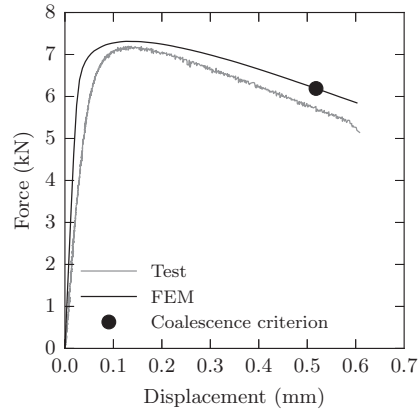
### Cyclic loading

Having established a reasonable criterion for monotonic failure, one proceeds to analyze the results of cyclic loading on single notch specimens.

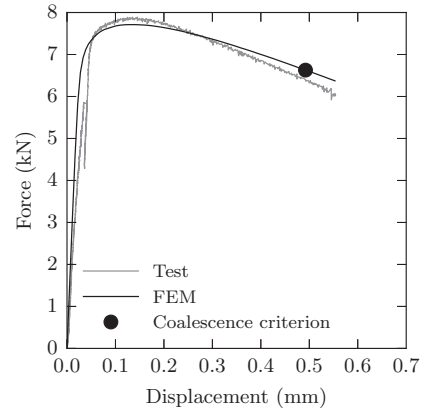
One begins by presenting a hysteresis curve of a typical test with the GLD UMAT in Fig. 5.9. Artifact in test result was explained in Chapter 3. It is considered that the GLD UMAT with non-linear kinematic hardening as described by the Chaboche model accurately represents the hysteresis response.

Consider now Fig. 5.10 which depicts the evolution of the failure criterion  $\phi^{TBL}$ , the porosity  $f$  and the aspect ratio as measured by  $S = \ln(w)$  as a function of the correction  $\varrho$  to the GLD evolution law of the aspect ratio. A range of +/- 10% of  $\phi^{TBL}$  is also plotted for visual guide.

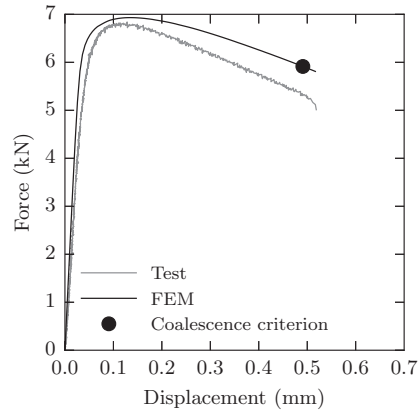
With no correction, there is no noticeable effect on the range in which the void's shape and porosity change their values. However, when one adds a small correction to  $\dot{S}$  in compression one immediately notices its effect on the evolution of  $f$  and  $S$ . Corrections on the other order of 10% to the compression evolution law of  $S$  are sufficient to reach  $\phi^{TBL} = 0$  within an acceptable number of half cycles. This is due to two important effects of this correction:



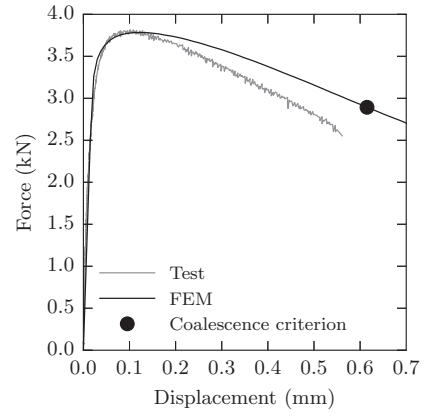
(a) T1M\_7\_1



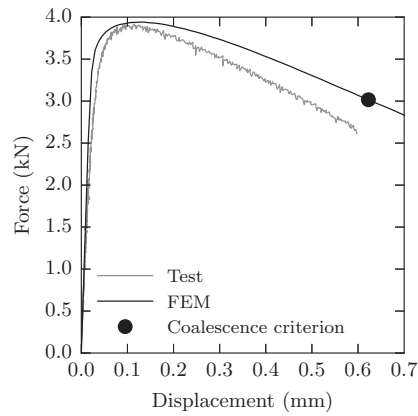
(b) T1M\_7\_2



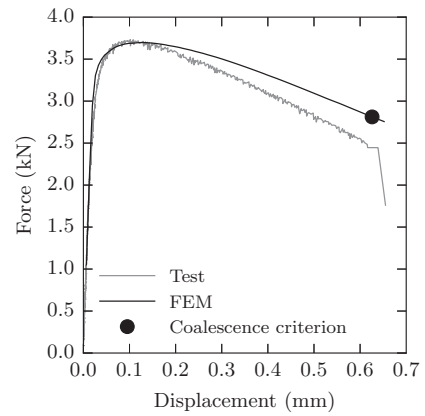
(c) T1M\_7\_3



(d) T2M\_7\_1



(e) T2M\_7\_2



(f) T2M\_7\_3

Figure 5.8 – Simple notched tensile tests - experimental results vs modeling

1 - an exponential increase in the porosity; 2 - the formation of shallower voids. The former is a typical behavior in ULCF, because it implies an exponential decrease in resistance (*c.f.* Section 2.4). The latter is supported by experimental observations in Chapter 3 and in [Kanvinde and Deierlein, 2004].

Fig. 5.11 shows results through the notch cross section for  $\varrho = 1.125$  at the end of the last three half cycles. There one can observe that the length in which  $\phi^{TBL} = 0$  is activated increases significantly between half cycles close to that failure criterion, suggesting that adding a material length scale (as suggested by [Kanvinde and Deierlein, 2004] with the factor  $l^*$ ) would not change the interpretation of results in a significant way.

Defining failure in tests as a 10% drop in the load carrying capacity of the specimen, one can compare results in terms of half cycles to failure. Performing an analysis for all cyclic tests using the same values of initial porosity, aspect ratio, void size, void spacing and  $\varrho = 1.125$  yields the summary Table 5.3. The results in this table show that the exponential decrease in resistance with amplitude as captured by this correction is able to approximate the failure half cycle to within an acceptable level of accuracy - see Fig. 5.12.

Discriminated results for each specimen can be found in Appendix C.

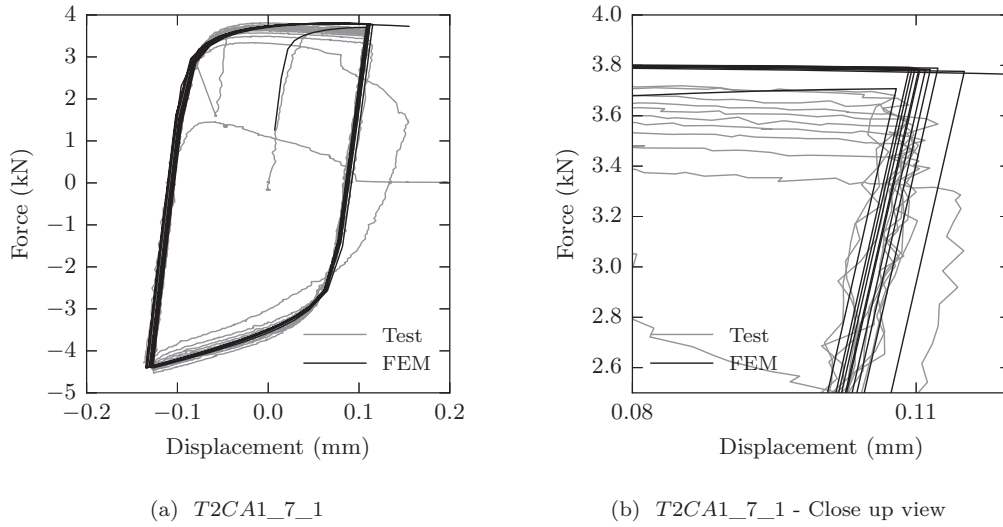


Figure 5.9 – Example of comparison of hysteresis curves between tests and the GLD UMAT -  $\varrho = 1.125$

Information in Table 5.3 is displayed graphically in Fig. 5.12

As much as it is useful to point out the good properties of this material model, it is also important to underline its shortcomings. Chiefly among them is the behavior that can be

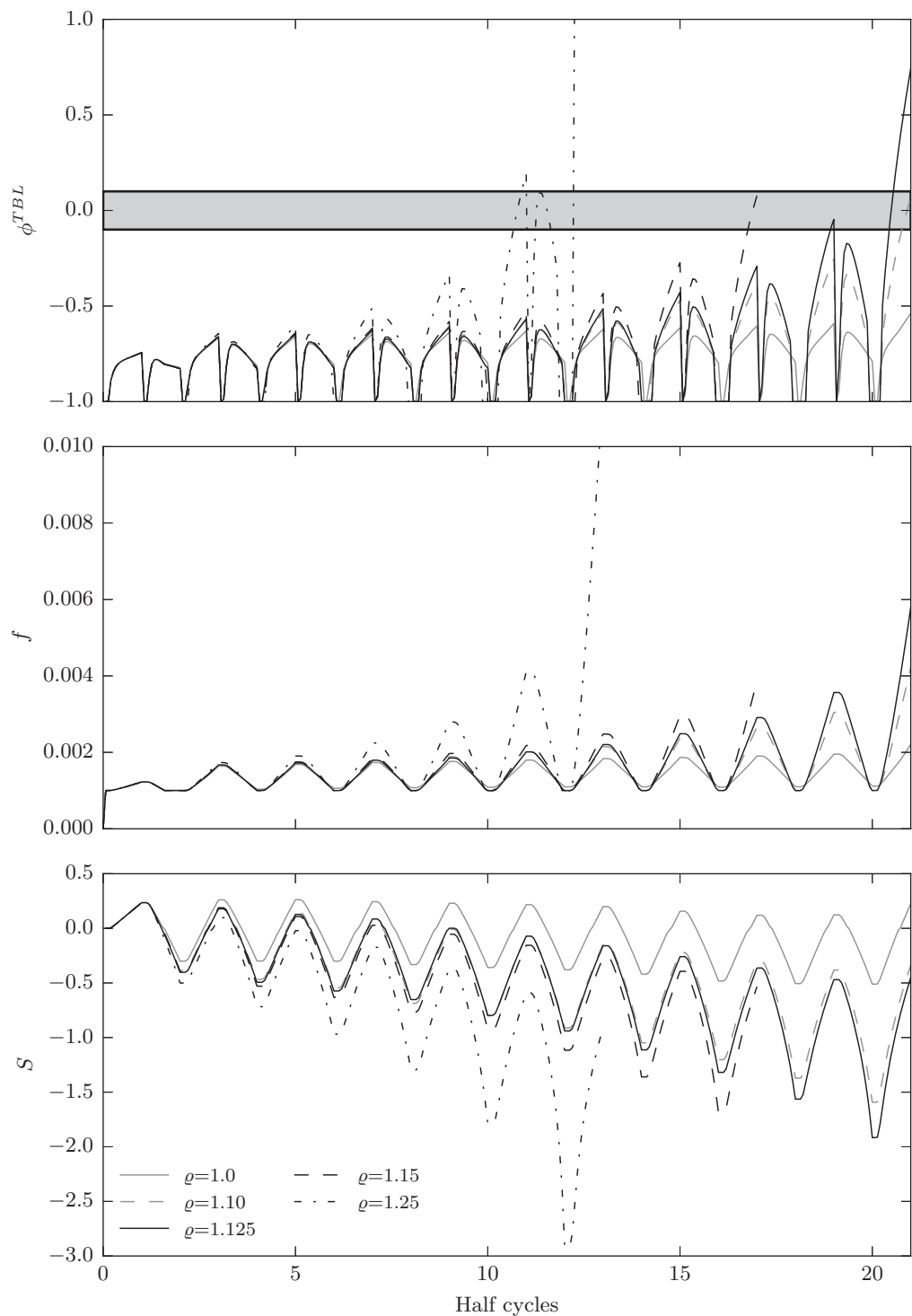


Figure 5.10 – Comparison of material model response at the integration point of the element at the center of the notch as a function of  $\varrho$  for specimen *T2CA1\_7\_1*

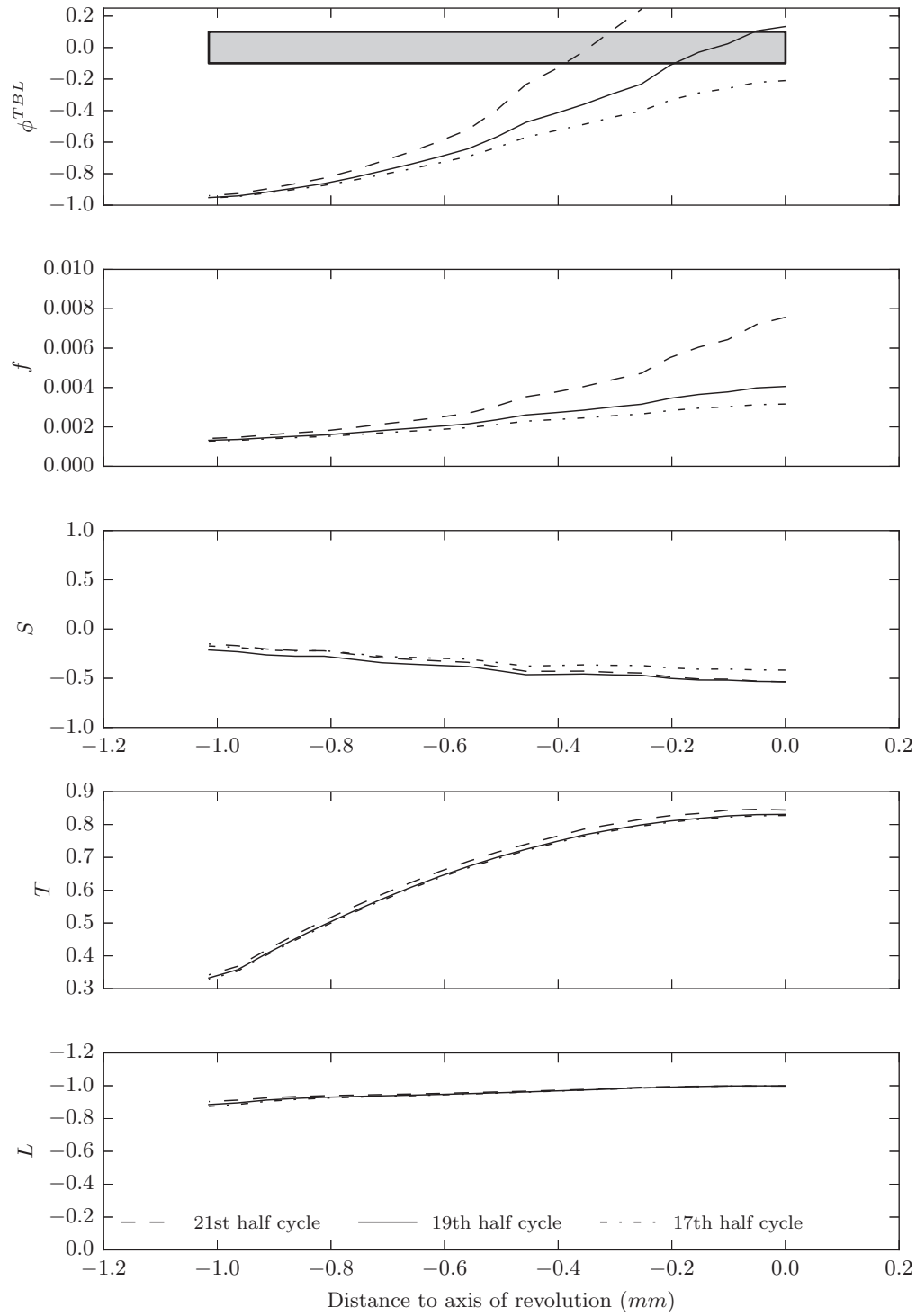

 Figure 5.11 – Nodal results through cross-section for specimen  $T2CA1\_7\_1$  with  $\varrho = 1.125$

Table 5.3 – Data summary for cyclic tests

Specimen	$\Delta\delta^{SN,test}$ (mm)	$H_c^{FEM}$	$H_c^{test}$
T1CA1_7_1	0.35	9	11
T1CA2_7_1	0.41	5	7
T1CA2_7_2	0.48	3	5
T2CA1_7_1	0.24	19	21
T2CA1_7_2	0.20	27	29
T2CA1_7_3	0.22	23	31
T2CA2_7_1	0.44	7	9
T2CA2_7_2	0.39	9	11

$f_0 = 1e - 3, w_0 = 1.0, \chi_{TBL,0} = 0.25, \varrho = 1.125$   
 $H_c$  stands for half cycle

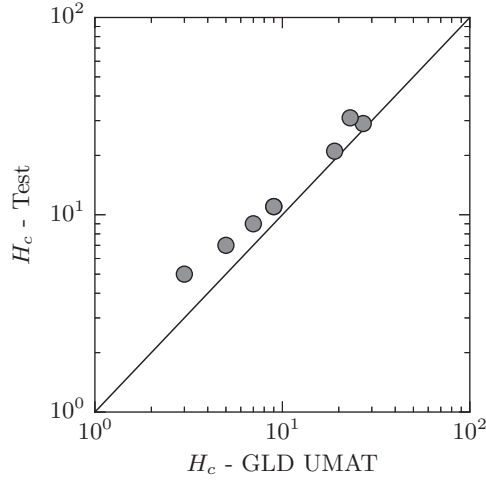


Figure 5.12 – Predicted number of half cycle versus experimental results

observed in Fig. 5.9b. The progressive decline in the ultimate load of the test, if not due to geometric non-linearities, could be explained by material softening subsequent to an increase in porosity. While one is able to capture an increase in the porosity of the material due to cyclic loading, this does not translate into a significant drop in the far-field measurement of the reaction force. Adding to this, significant assumptions were also made *w.r.t.* particle-void interactions, the coalescence criterion and the heuristic factor  $\varrho$ . The most consequential of them is arguably the adoption of the same coalescence criterion for ULCF as for monotonic loading which is, again arguably, at odds with the experimental observations in Fig 3.14 that seem to suggest a higher critical porosity in ULCF<sup>4</sup>.

<sup>4</sup>to be noted that this is merely an hypothesis based on larger sized dimples in ULCF. The extrapolation to higher porosities cannot be made conclusively without a series of interrupted ULCF tests in which the notch of SN specimens is opened and the porosity quantified

This model remains, therefore, merely an indicator for ULCF resistance for the way that it takes into account the interaction between void shape and porosity in cyclic loading which induces porosity ratcheting, not an actual full-fledged description of the physical process as manifested by Fig. 5.9b. This approach complements current cyclic micromechanical approaches that are able to reproduce qualitatively porosity ratcheting in unit cell models through time history dependent parameters as discussed in Section 2.4.

More refined models are envisioned where different coalescence criteria are adopted so as to either allow greater porosities inside the material through higher  $\rho$  coefficients in the cyclic GLD model (thereby capturing the material softening mentioned previously) or the implementation of two yield surface models, where growth and coalescence mechanisms compete for the material description. In the latter option, coalescence models, like the TBL, would be supplemented with their own evolution laws to capture this behavior more accurately.

### 5.3.2 Double notched tubular specimens

This section presents some results on the application of the GLD UMAT to the double notched tube experiments described in Chapter 3.

3D finite element models were built with the nominal geometry displayed in Fig. 3.15 with height equal to the DIC gauge length ( $h^{DN}$ ). Rigid boundary condition were set by a master-slave node disposition on the top and bottom of model. Master nodes were located on the axis of revolution separated by the gauge height. Slave nodes consisted of all the bottom and upper nodes, for the bottom and upper master node, respectively. Fixed conditions were set for the bottom master node, while loading in the form of displacement and rotation as measured by DIC over the gauge length, was set for upper master node. Similarly to single notched simulations, 8-node 3D reduced integration isoparametric elements (C3D8R) were used. However, due to the size of the model, larger elements than in the single notched specimens had to be employed. Elements in the notch region had a length of  $100\mu m$  through the cross section (*i.e.* radially),  $160\mu m$  circumferentially and  $80\mu m$  in height. The through cross-section size is double than the one used in SN specimens. Accurate estimates of plastic strain are, therefore, not expected. However, qualitative interpretations of those simulations will be given because they are judged to be of value. An illustration of the finite element model can be seen in Fig 5.13 with typical results in 5.14.

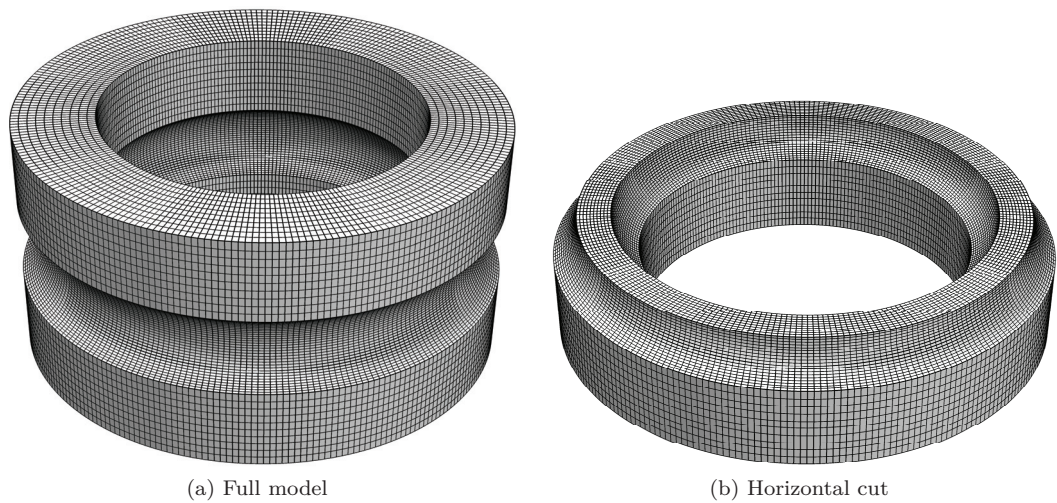


Figure 5.13 – FEM model for double notched tubes

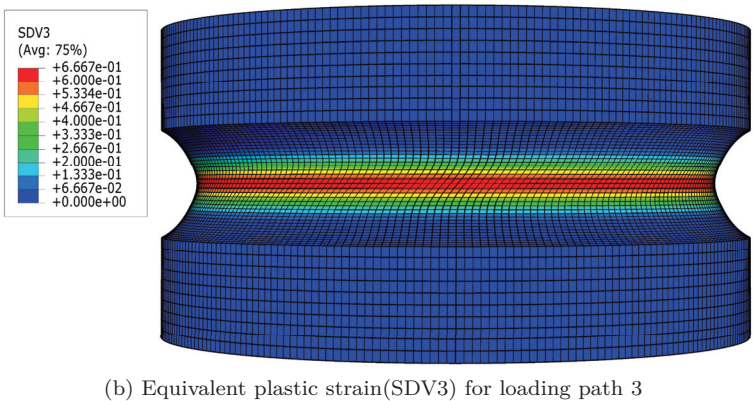
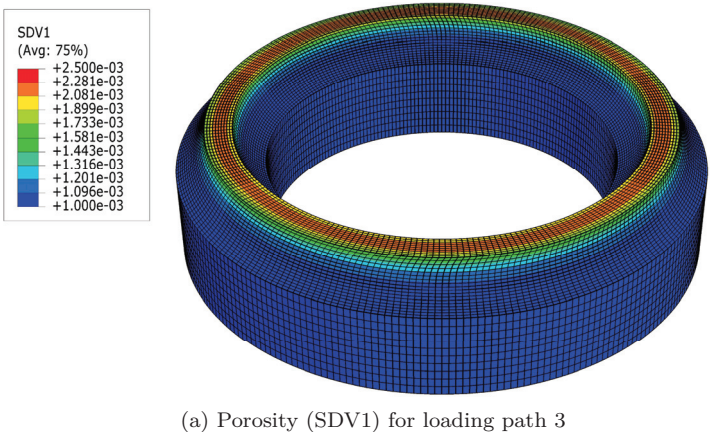


Figure 5.14 – Typical FEM results for a double notched tube simulation - *DN7M3\_1* at load step corresponding to fracture in experiments



#### Monotonic

One begins the discussion by taking note of the comparisons between force-displacement and moment rotation curves (in correspondence with the local loading level presented in Fig. 3.20b) in tests and in their corresponding finite element model using the GLD UMAT - see Fig. 5.15. Micromechanical variables used in the analysis were the same as in SN specimens. Notable in all these analyses is the correspondence of elastic stiffness as measured by the DIC system and the nominal geometry of the specimen described in the FEM - a testament to the precision of the DIC system.

For tensile loading (loading path 1) loss of stiffness due to necking of the cross-section is not sufficiently well modeled. This is due to an insufficient amount of elements in the cross section that don't fully capture the extent of plastic deformation across the notch.

For loading path 3, the apparently bizarre jumps in stiffness in the load-displacement/moment-rotation curves from the FEM are justified with the fact the local loading does not follow exactly a proportional path. Here the path was approximated in piece-wise linear segments and those jumps correspond to changes in the direction of load.

For loading path 4, although less perceptible, the load path was almost approximated by segments. After yielding there is a stark difference in the stiffness in both force-displacement moment-rotation curves. The over-stiffness in the moment-rotation from the FEM model corresponds to under stiffness in the force-displacement curve. This is possibly due to anisotropic plastic behavior of the material that could be addressed using a micromechanical model like the one in [Keralavarma and Benzerga, 2010].

Modeling pure torsion tests (loading path 2) remained unsatisfactorily resolved and will not be presented in this work. The large amounts of plastic deformation in shear (upwards of 40% if one takes loading 4 as a reference or even 120% if one is to take [Faleskog and Barsoum, 2013] tests on high-strength steel) for such a relatively coarse mesh tended to concentrate plasticity in only one element, leading to large element distortions and unrealistic plastic deformations.

With those caveats in mind, let's turn our attention to Fig. 5.16, 5.17 and 5.18 where the main focus is the performance of  $\phi^{TBL}$ . These figures show the loading history up to fracture of the integration point of the element with highest  $\phi^{TBL}$  at fracture. For load paths 3 and 4 it is also shown a measurement of how much these voids rotate as given by  $\eta_v$ , which is defined as the angle of the principal axis of the void from the initial to the current configuration. The initial axis of the voids was set to be parallel to the axis of revolution of the tube. However since voids are initially spherical, as soon as the material starts to yield and the void starts changing its shape, its axis will be changed and follow the direction of principal stretch as

discussed in the void orientation part of Section 5.1.

In Fig. 5.16 the performance of the coalescence criterion under-predicts fracture. One possible explanation is that one is not modeling plastic deformation properly<sup>5</sup>. Another however can be seen in the Lode parameter which is close to zero throughout most of the loading. This fact becomes more clear when one compares this loading to load path 3 whose loading happens with a higher Lode parameter. The performance of  $\phi^{TBL}$  here is much better.

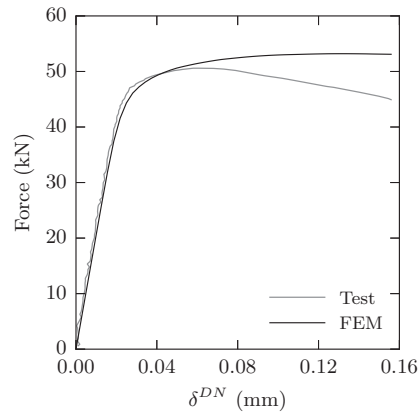
Another notable observation is that for load path 4 when Lode parameters are close to zero but stress triaxialities are also close to zero,  $\phi^{TBL}$  also performs relatively well *w.r.t.* load path 1.

### Cyclic

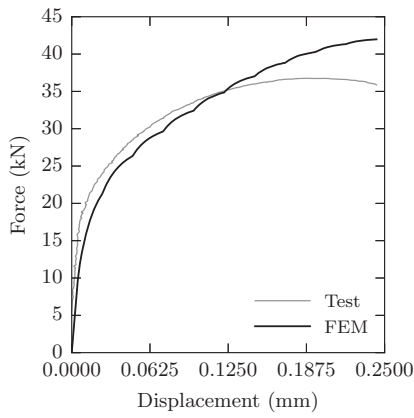
For cyclic loading no results are deemed worthy of reporting. Modelling ULCF in non-axisymmetric conditions using the micromechanical model developed herein proved to be challenging even in monotonic loading.

---

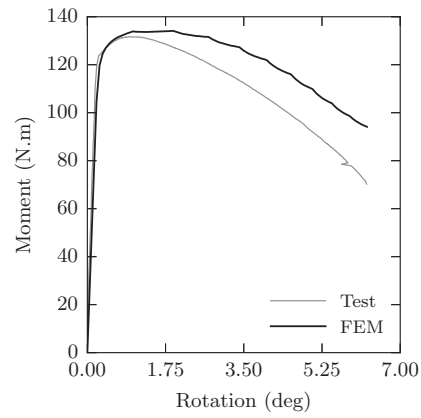
<sup>5</sup>although the results here are somewhat puzzling because simulations with a quarter of the model and twice the number of elements through the thickness of the notch, yield essentially the same predictions in terms of load-displacement, plastic strain and  $\phi^{TBL}$  values. One possible explanation is that one is not capturing the evolution of the slant mode of failure correctly (see Fig. 3.22)



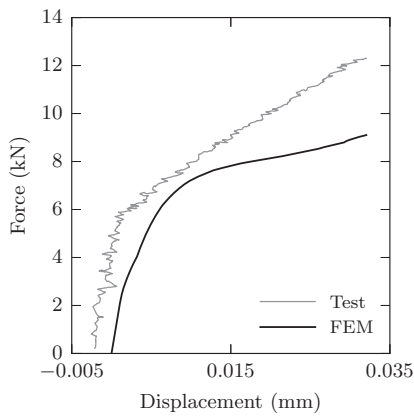
(a) DN7M1\_1 - Force-displacement



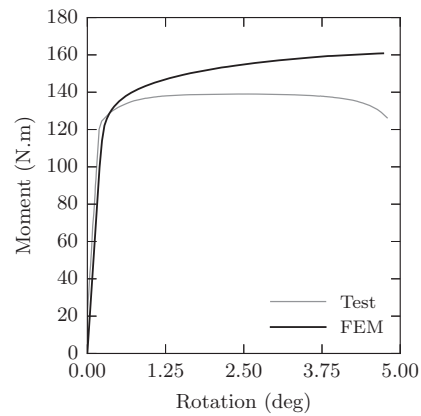
(b) DN7M3\_1 - Force-displacement



(c) DN7M3\_1 - Moment-rotation



(d) DN7M4\_3 - Force-displacement



(e) DN7M4\_3 - Moment-rotation

Figure 5.15 – Double notched tube tests - experimental results vs modeling

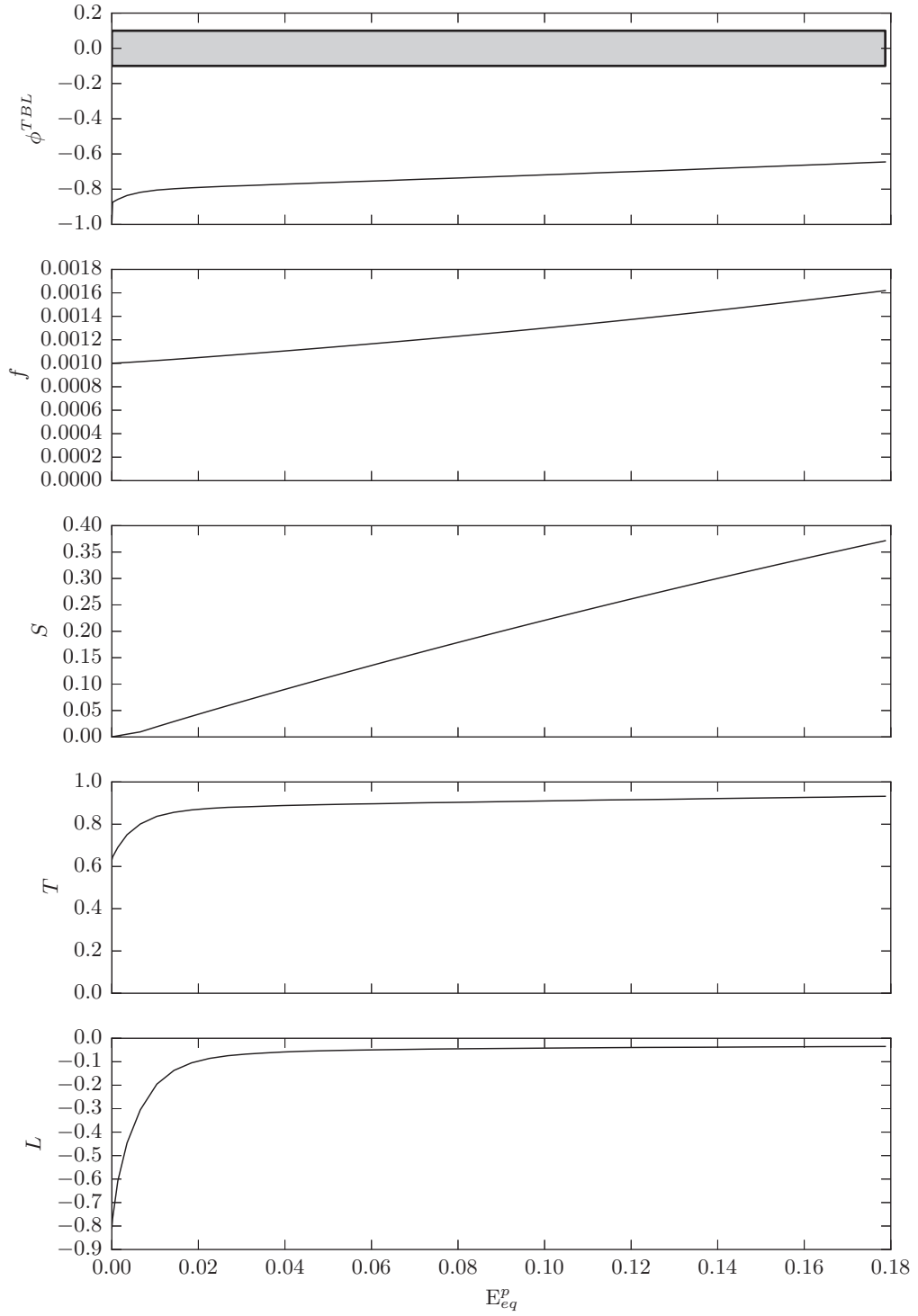


Figure 5.16 – Load history at the integration point of element of highest  $\phi^{TBL}$  for specimen DN7M1\_1

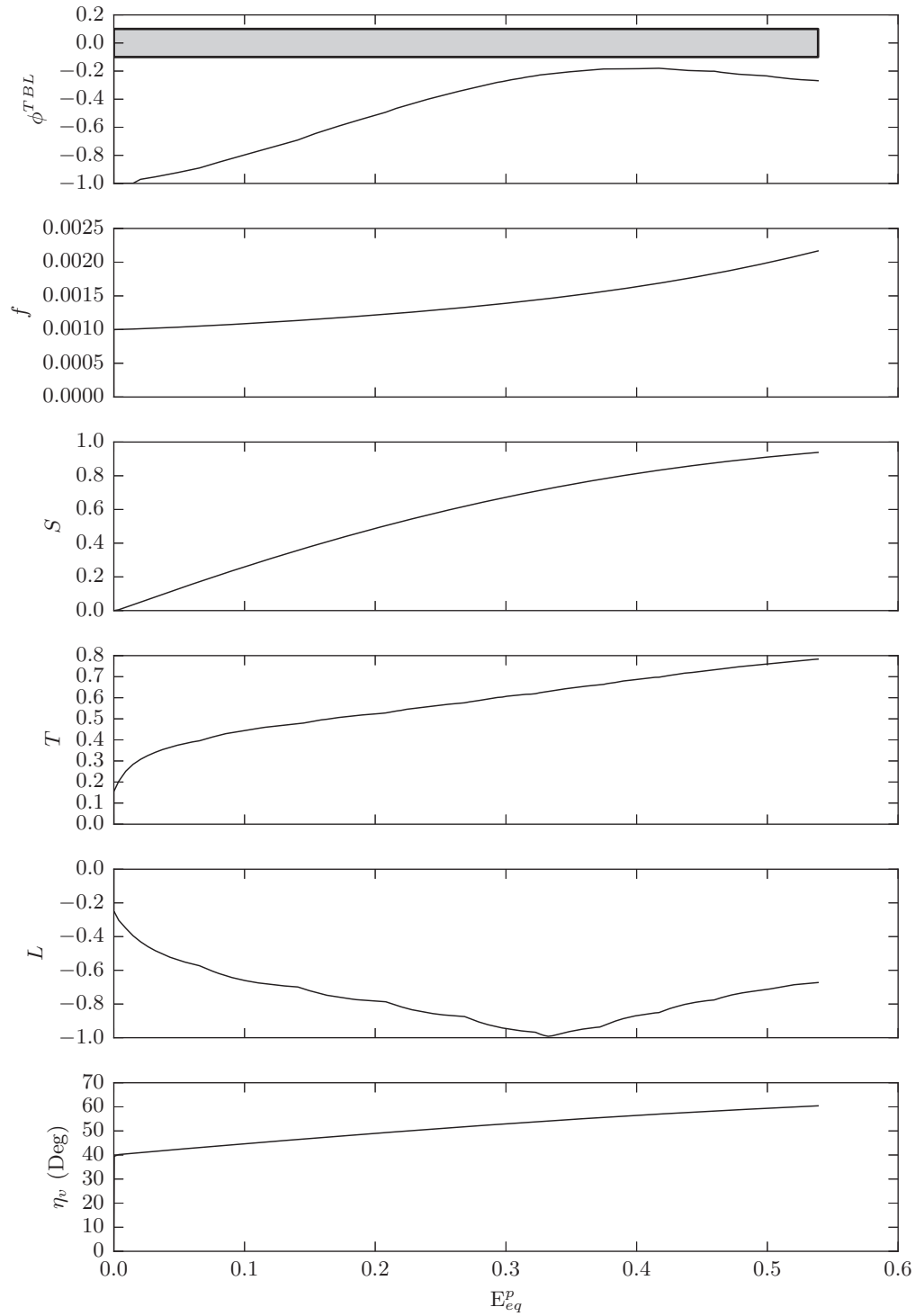


Figure 5.17 – Load history at the integration point of element of highest  $\phi^{TBL}$  for specimen DN7M3\_1

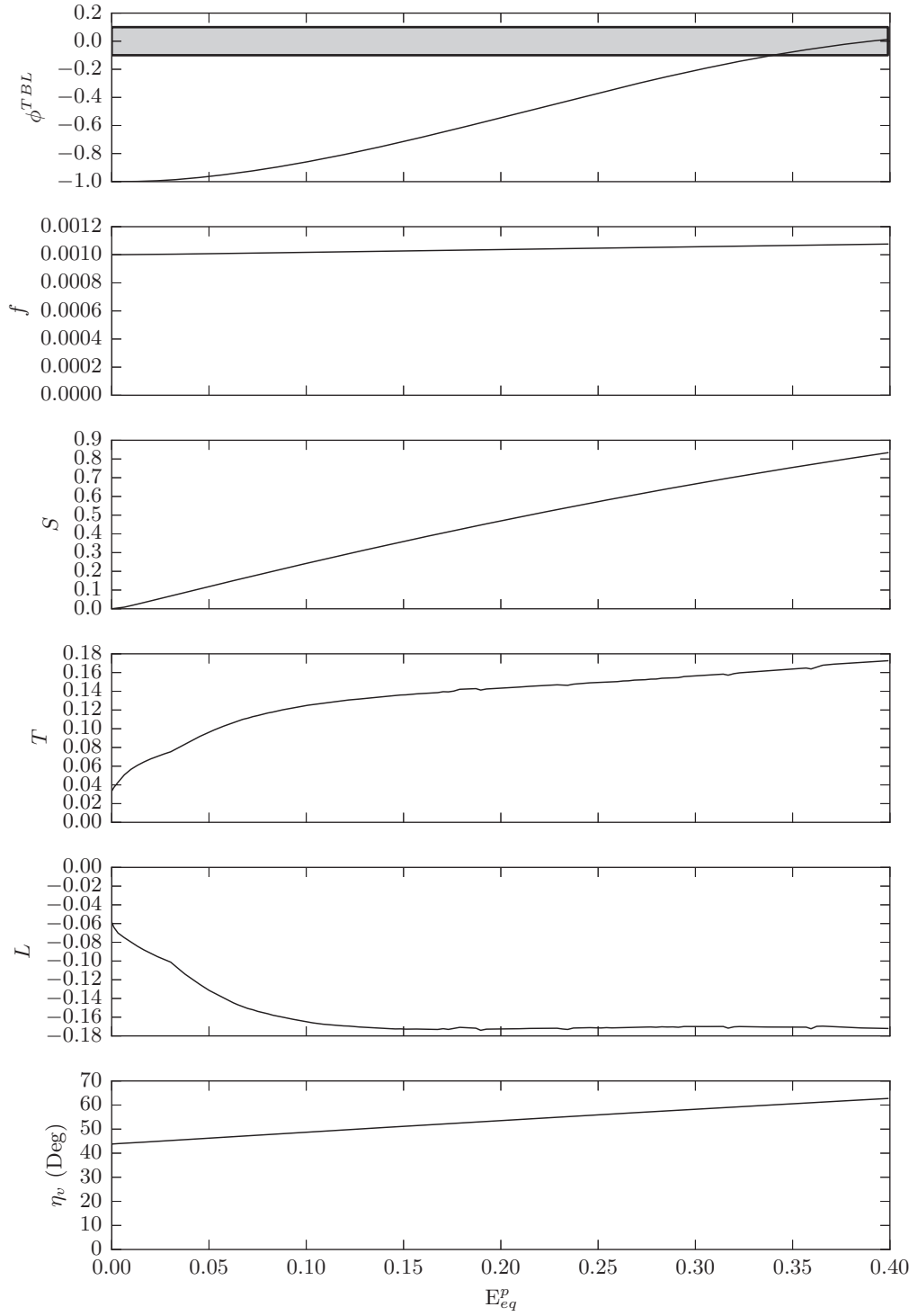


Figure 5.18 – Load history at the integration point of element of highest  $\phi^{TBL}$  for specimen DN7M4\_3

## 5.4 Conclusion

In this chapter a phenomenological extension of the Gologanu-Leblond-Devaux micromechanical model to non-linear kinematic hardening was developed. Its implementation in an Abaqus user defined material sub-routine was discussed and validated using an established UMAT in literature comparable to the GLD model. The gist of the matter is as follows,

1. A hypoelastic co-rotational implementation of the GLD model with kinematic hardening using the Green-McInnis-Naghdi stress rate was presented.
2. Backstress evolution laws have a significant impact in the evolution of internal variables.
3. An evolution law for the backstress was chosen so as to best approximate the behavior of the GLD model for isotropic hardening (co-directional with  $\Sigma - \mathbf{A}$  as per [Mear and Hutchinson, 1985]).
4. This model was compared with similar implementations<sup>6</sup> and found to reasonably approximate the GLD behavior for monotonic loading
5. Porosity ratcheting is modeled by different rates of change of voids aspect ratios, which is supported by experimental observations conducted in Chapter 3 and in [Kanvinde and Deierlein, 2004]
6. The following assumptions were also made:
  - (a) Voids rotate with the material as per the Green-McInnis-Naghdi rate;
  - (b) Porosity is enforced to have at minimum the initial void volume fraction;
  - (c) The same coalescence criterion for monotonic and cyclic loading with the TBL model was adopted by assuming an equal aspect ratio as in the GLD model and an equal ligament size at the beginning and at the end of the loading.

The performance of this model was assessed using experimental data from single notched and double notched test results.

For the single notched tests, key findings are as follows,

1. Micromechanical models that incorporate the interaction between porosity and void shape effects are able to capture a key characteristic of ULCF behavior: an exponential decrease in material resistance with cyclic loading.

---

<sup>6</sup>Abaqus's implementation of the Gurson model and the Keralavarma-Benzerga model implemented in a UMAT described in [Kweon et al., 2016]

2. An increased rate of change of voids aspect ratio in compression induces shallower voids and porosity ratcheting under cyclic loading.
3. The coalescence criterion with the assumptions outlined previously and with a  $\varrho$  calibrated on only one specimen provided a good estimate for the number of cycles to failure in single notched specimens with different amplitudes and notch geometries.
4. Despite this fact, this failure criterion remains an approximation to the physical mechanisms observed in the tests because does not capture the insidious decrease in load carrying capacity observed in specimens with a higher number of cycles (*cf.* Fig. 5.9b).

Application of this material model in the double notched tube tests proved challenging and no meaningful conclusive remarks can be offered. The discussion of monotonic tests are however of interest for their qualitative observations. The most relevant are the difficulty of modeling the tension tests which include a slant type of fracture and the relatively better performance of the TBL model as a fracture indicator in combined tension-torsion load paths (higher Lode parameters *i.e.* close to axisymmetric stress state).



## 6 Design approach for welded structural components

In Chapter 4 a procedure to evaluate ultra-low cycle fatigue (ULCF) resistance using digital image correlation (DIC) full-field measurements was presented. This method for characterizing resistance is intrinsically a local approach to fatigue. In high-cycle fatigue, local methods like the hot-spot ([Niemi et al., 2006]), effective notch stress ([Radaaj et al., 2006]), or [Xiao and Yamada, 2004] methods are to date quite established. In fact, the hot-spot method is allowed in high-cycle fatigue verifications in Eurocode 3 instead of using nominal stresses [European Committee for Standardization, 2005].

The main objective of this chapter will be to propose a local modeling approach that suitably approximates the full-field strain measurements of the DIC system. Since ULCF resistance can be characterized using local DIC data, one can arguably design for ULCF if one can reproduce the essence of those strain histories appropriately.

One will focus on the finite element representation of the tube to plate tests in chapter 4. Considering that for design purposes one should make things as simple as possible one is expected to make certain concessions on the modeling approach. The chapter will start by describing those root hypotheses and the modeling process as a whole. Following that introduction, a section on the results and their discussion will be presented and it will end in a short section summarizing the main conclusions of that discussion with an emphasis on the range and scope of the methodology.

### 6.1 Description of the modeling approach

When it comes to the finite element modeling of the tube to plate tests, there are several things that should be taken into account. The first is the description of the physical object,

which invariably leads to a discussion of its geometric and material properties. The second, the load and boundary conditions to which it is subjected to. The third is the scope of the finite element method (FEM) model itself, which by definition attempts to describe physical objects by partitioning them in discrete pieces. As will be shown, how they are partitioned and how those pieces (or elements) approximate the continuum mechanics problem is not insignificant for the issue at hand.

A successful estimation of strain histories with FE analyses requires two conditions: the first, an accurate simulation of the component level force-displacement/torque-rotation hysteresis curves; the second, reproducing the strain history measured by DIC with sufficient accuracy.

Starting with the simulation of the hysteresis curves, consider Fig. 6.1 that shows the FE representation of the tube to plate tests. The geometry of the model follows essentially the dimensions presented in chapter 4 with the exception of the base plate that, for simplicity, is generated along with the tube by a 360 degree revolution. Additionally, a detailed representation of the weld is both impractical and impossible <sup>1</sup> and, therefore, only the thickness and slope ( $a$  and  $\psi$  in Fig. 4.6, respectively) of the weld were explicitly taken into account when modeling different specimens - see Tables E.1 to E.3 . All other geometric properties such as the reduction of thickness near the weld toe are the same for all simulations and taken as nominal values - see Fig. 4.6.

Another simplification in these simulations concerns the material model used for plasticity. Here, the nonlinear kinematic hardening defined by the analysis software Abaqus [Dassault Systèmes, 2011] was used and not the material model developed in Chapter 5. Even though, as seen in previous chapters, this is based on the Chaboche model using the Jaumann-Zaremba stress rate, at the strain amplitudes in which the welded tube-to-plate tests were conducted shear oscillations are deemed to be negligible and therefore Abaqus's model was deemed acceptable to use - see Fig. 2.3 where the finite rotation of an element in simple does not significantly affect the material law for  $\varepsilon_{eq}^p < 50\%$ . Furthermore, a single material was defined for the whole model using backstress parameters calibrated for the base metal law defined in chapter 3. It is important to underline this assumption, *i.e.* the fact that one is neglecting the material behavior of the weld metal and the heat affected zone (HAZ). Later it will be shown that this is justifiable due to the adequate simulation of the hysteresis curves using solely this material law. The hardening coefficients used in the Chaboche model are based in half-cycle data presented in Table 3.1 and can be consulted in Table A.1.

With respect to loading and boundary conditions, let's turn our attention to Fig. 6.2 that

---

<sup>1</sup>DIC measurements were only made for a small portion of the perimeter of the tubes

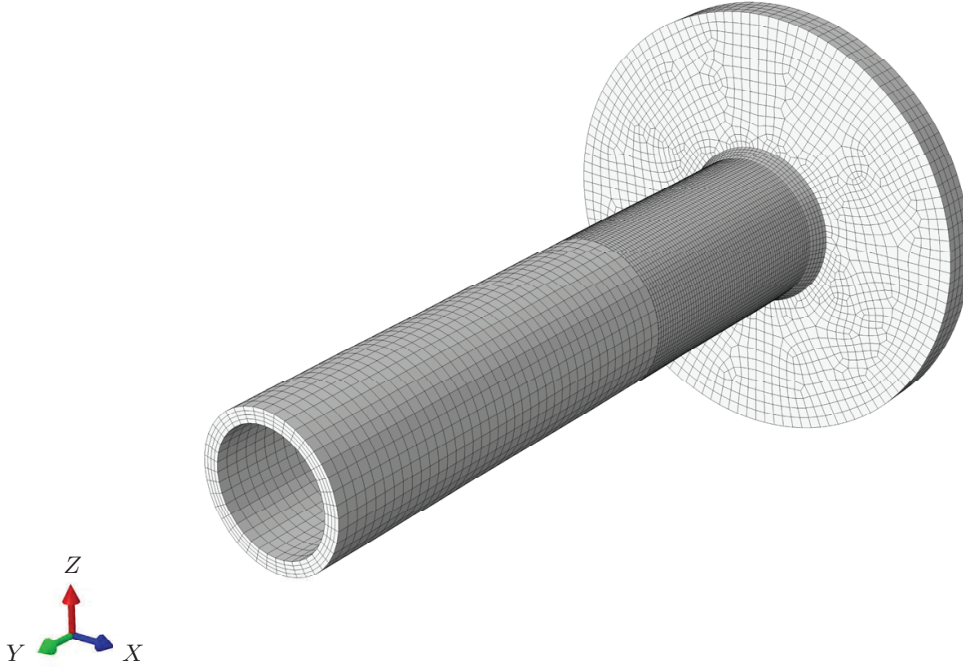


Figure 6.1 – FEM model of tube to plate test - general view, all elements C3D8R

depicts a cut of the FEM model and three notable points along its revolution axis. All three points act as *master nodes* with the nodes at their corresponding cross section (*i.e.* perpendicular to the 'Y' axis) acting as *slave nodes*. Master and slave nodes are connected together by rigid ties, which means that slave nodes will follow the displacement imposed on the master node as well as turn about it as their center of rotation. The node at the tip of the tube (indicated in Fig. 6.2 by  $\delta$ ) is located at approximately the same distance as the centerline of the bending jack (*cf.* Fig. 4.1) is from the support. The node tied to the double arrow, where rotation  $\theta$  is applied, is at a distance approximately from the tube inclinometer to the support (*cf.* Fig. 4.1 and 4.8). The support master node is tied to all the nodes at the back of the base plate. It is at the support master node that the boundary conditions for the model are set and their reactions compared with the forces measured in the tests. Of note on this point is the fact that the column support's flexibility is not something that can be discarded. Flexibility associated with bending imposed by  $\delta$  is taken into account in the model by an elastic rotational spring around the 'X' axis -  $K_\delta$ . For the flexibility associated with the torque imposed by  $\theta$  much of it is already taken into account because  $\theta$  is defined by the difference between base plate and tube inclinometers. Nevertheless, some elastic flexibility in the modeling was observed which can be explained by some minor flexibility of the plate itself. This was also modeled by a rotational elastic spring at the support master node but around the 'Y' axis -  $K_\theta$ . Values for  $K_\delta$  and  $K_\theta$  are presented in Table 6.1

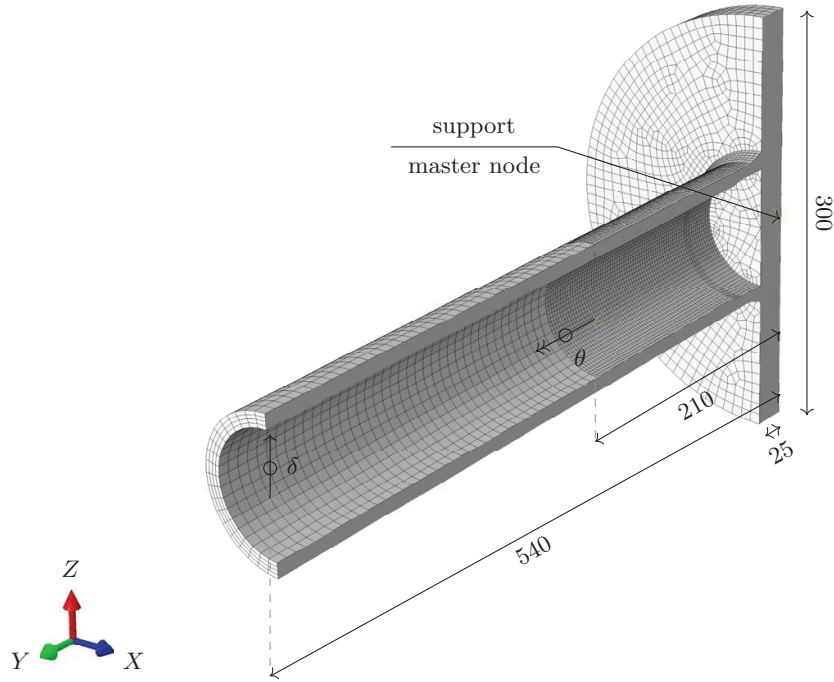


Figure 6.2 – FEM model of tube to plate test - cut and boundary conditions

All models with the tube to plate connection modeled explicitly (named henceforth as *global* models), have been meshed as can be seen in Fig. 6.1 and 6.2. It consists of a relatively coarse mesh from  $\delta$  to  $\theta$  whose sole purpose is to carry the bending moment between those two points. From  $\theta$  to the base plate, a more refined mesh of 2.5mm 3D 8-node linear reduced integration elements is used. Even though this was observed to be sufficient to capture the behavior of the hysteresis curves of force-displacement/torque-rotation, for the weld toe strain time history comparison with a much finer mesh was needed. Due to computational constraints, a submodelling approach was adopted whereby a small portion around the weld was extracted from the global model; the boundaries shaping this *submodel* were subjected to the displacement field of the global model on those very same boundaries. A graphical depiction of the submodel can be seen in Fig. 6.3. In the subsequent section a convergence study will be presented on the element size and type that was found to best fit the DIC measurements. This approach is similar to the one presented in Chapter 2 suggested by [Myers et al., 2009].

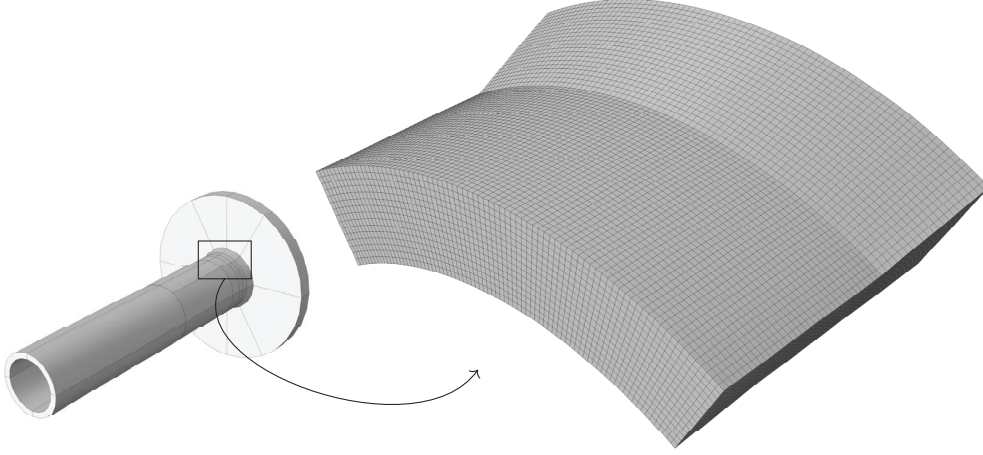


Figure 6.3 – FEM submodel of weld toe region

## 6.2 Results and discussion

One will begin by showing results for a simple bending test: first for the global model and later for the submodel. Fig. 6.4 shows the hysteresis curves on test B7CA1\_3 - here '*force in bending jack*' should be read as the vertical reaction in the FEM model. Rotational stiffness of the support ('X' direction;  $K_\delta$ ) was fit to a value of  $5e6$  N.mm/rad. Both curves can be seen to match sufficiently well, by which one means that the elastic stiffness is approximately correct and the work dissipated in each cycle is also approximately the same. Here one should bear in mind that the plastic work associated with each cycle is mainly occurring on the top and bottom parts of the tube near the weld (reduced thickness region). This concentration increases the sensitivity of the weld strains to meshing and loading conditions as well as material properties. The small difference in the maximum load that can be seen in compression between the model and the test is therefore expected to have some consequences when one begins to inquire into the submodels.

Consider Fig. 6.5 and 6.6 that show a vertical cut ('YZ' plane) along the tube's axis at the first and second load reversal and the corresponding equivalent strain measurements in both DIC and the FEM models. For clarification and in order to be consistent with DIC measurements,  $\varepsilon_{eq}^*$  was computed in the FEM with the total strain tensor (the logarithmic or Hencky strain). One can observe in these pictures distributions of  $\varepsilon_{eq}^*$  taken from the nodal results (*i.e.* extrapolated from the integration points and averaged) for different element sizes and type<sup>2</sup> in the weld region. Weld geometry was approximated in the FEM model linearly between the weld toe and the base plate with the angle  $\psi$  taken from the DIC measurements

<sup>2</sup>*LinR*  $\equiv$  linear 3D 8-node reduced integration element with enhanced hourglass control (C3D8R); *QuadR*  $\equiv$  quadratic 20-node reduced integration element (C3D20R)

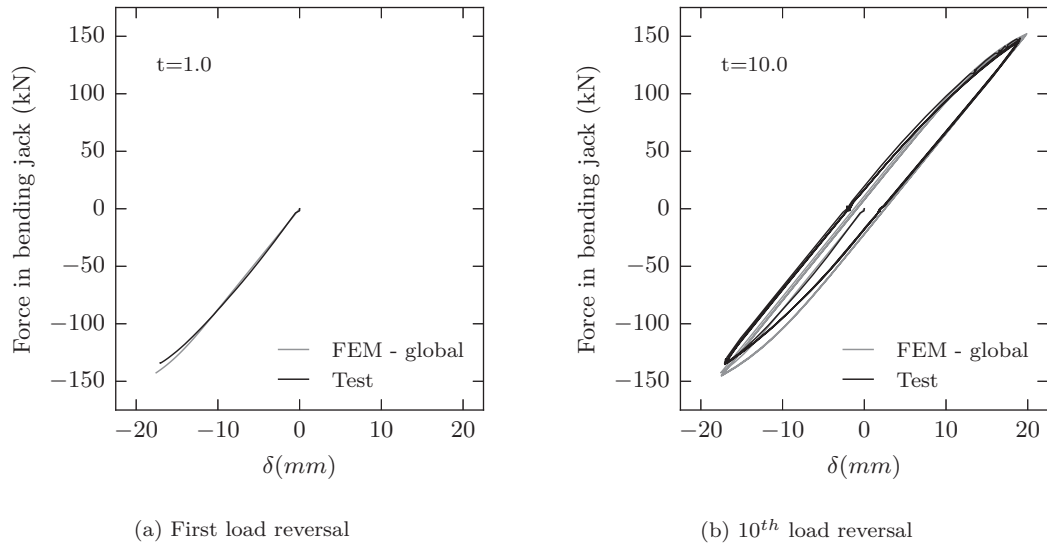


Figure 6.4 – FEM comparison of hysteresis curves for specimen B7CA1\_3

- *c.f.* Tables E.1 to E.3. A sharp transition was used instead of a radius because for shallow angles (less than 30 degrees) this has a negligible influence on the equivalent plastic strain [de Castro e Sousa and Nussbaumer, 2015].

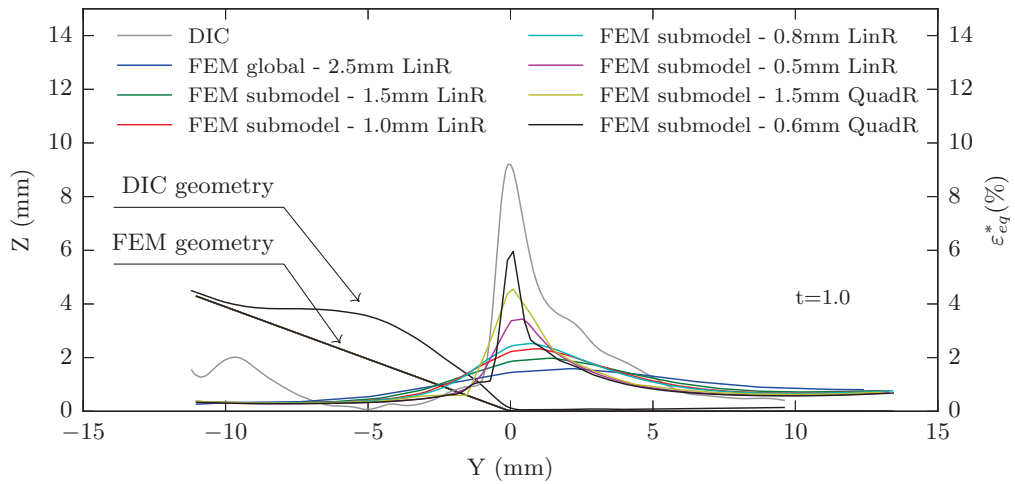


Figure 6.5 – Comparison of DIC measurements and FEM results for specimen B7CA1\_3 through a cut at weld toe at first displacement reversal (tensile)

The influence of size and type of elements are immediate in the figures shown above. Commenting on the results from the global model, where a fairly coarse mesh (with respect to the weld's size) was used, one notices that the strain concentration at the toe is barely

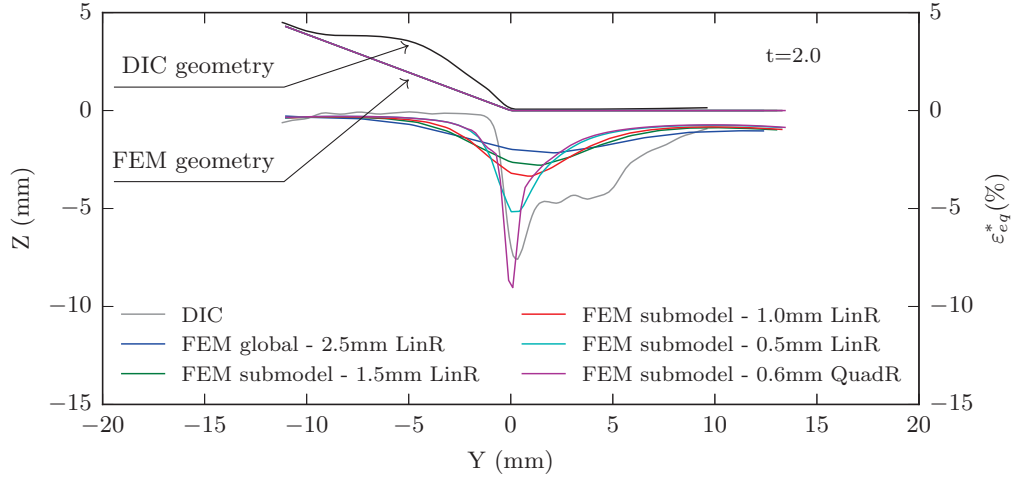


Figure 6.6 – Comparison of DIC measurements and FEM results for specimen B7CA1\_3 through a cut at weld toe at second displacement reversal (compression)

noticeable. As the mesh size decreases one can detect a corresponding increase in  $\varepsilon_{eq}^*$ . It can also be observed that the type of element has a significant influence in the strain evaluation.

Turning one's attention to Fig. 6.7, the time history of the point with maximum  $\varepsilon_{eq}^*$  amplitude is shown along with the corresponding point in the FEM submodel with 0.6mm size quadratic reduced integration (C3D20R). It can be seen that although DIC and the FEM submodel do not match perfectly <sup>3</sup>, their amplitudes only differ slightly (around 1.25% in percentage difference) which is considered to be an adequate reflection of the dissipation of the global model and the DIC measurements. An anecdotal indication that this size of an element is a natural selection to base further analyses is the fact that the distance between integration points is of the same order as the distance between data points in the DIC ( $7px \approx 0.3mm$ ). This distance is also within the range of the characteristic length  $l^*$  for most structural steels as given by [Kanvinde and Deierlein, 2004] (between  $60\mu m$  and  $500\mu m$ ). As shown in Chapter 2, the element type is the same as used in [Myers et al., 2009], although with roughly double the element size. The element size in [Kanvinde and Deierlein, 2004] was fixed so as to be within the range defined by [Myers et al., 2009]. Here element type and size are fixed with direct surface measurements made by DIC. One will proceed with these analyses by considering the same mesh size and type for subsequent submodels and comment on the consequences.

In pure torsion tests (load path A) it was also found that an additional rotational elastic spring should be considered in the model to account for some flexibility of the base plate

<sup>3</sup>presumably due to the initial small difference in the global model's first reversal

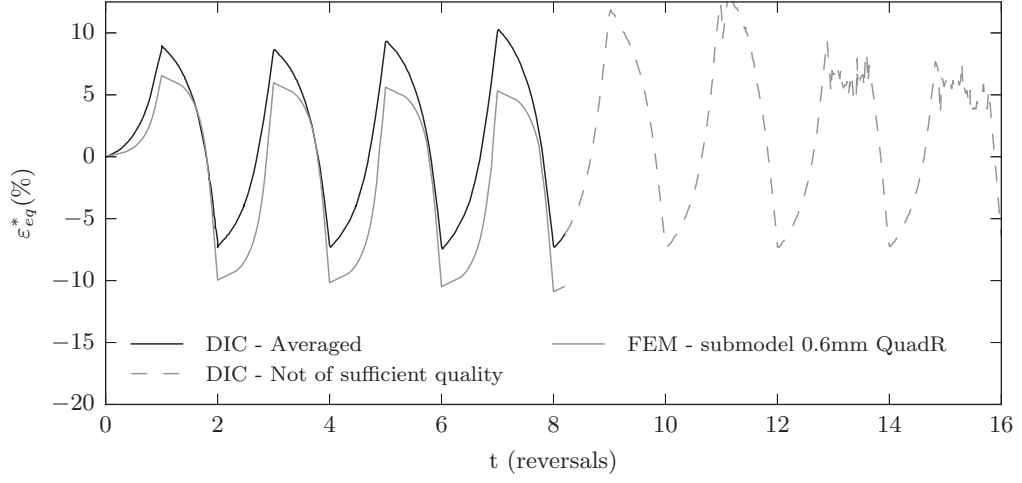


Figure 6.7 – Comparison of DIC measurements and FEM results for specimen B7CA1\_3 - time history of point at the weld toe

to torque. Fig. 6.8 presents the torque-rotation hysteresis curve for test A7CA1\_3 and the FEM global model with a stiffness of  $1.5e7$  N.mm/rad in the 'Y' direction -  $K_\theta$ . The results are quite encouraging on the global model. Having calibrated the elastic stiffness with the stiffness of the support, the plastic behavior matches equally well, lending some justification to the approximation of using the same material model for the weld as for the base material.

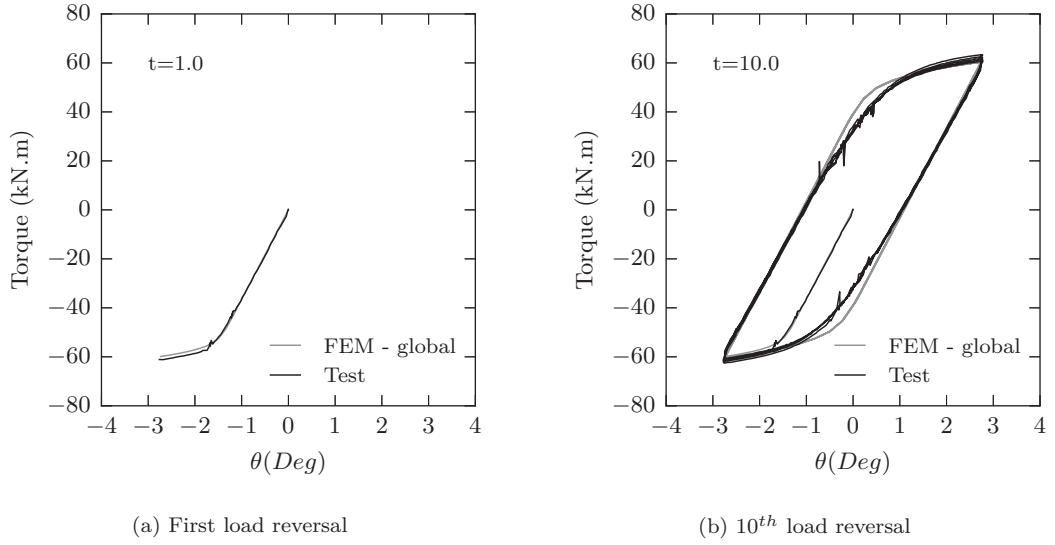


Figure 6.8 – FEM comparison of hysteresis curves for specimen A7CA1\_3

Consider the results in Fig. 6.9 that depicts the time history of  $\varepsilon_{eq}^*$  for A7CA1\_3 from a submodel using the same mesh size and element type as the one used in the simple bending



test. Here, it can be seen that the strain time history matches remarkably well. This observation seems to lead to the following conclusion: if one captures the hysteretic global behavior of the component accurately, the submodelling technique with 0.6mm quadratic elements will provide a representative time history of the strains at the weld toe with respect to the DIC measurements.

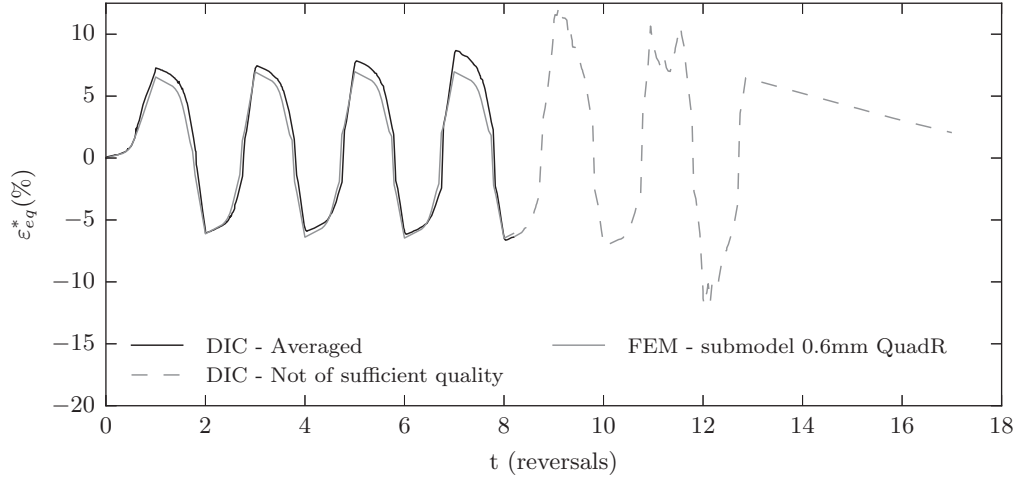


Figure 6.9 – Comparison of DIC measurements and FEM results for specimen A7CA1\_3 - time history of point at the weld toe

Following the consequences of that statement, additional FEM models were conducted for other load paths and amplitudes but keeping the same modeling principles. Not all tests were modeled due to time constraints. Representative tests for different amplitudes and load paths were performed (8 CA and 1 VA). Fig. 6.10 depicts the results from the CA tests simulations and Table 6.1 summarizes their key quantities.

Table 6.1 – Summary of CA FEM parameters and results

Specimen	$K_\delta$	$K_\theta$	$\Delta\epsilon_{eq,DIC}^*$	$\Delta\epsilon_{eq,FEM}^*$	$p_{dif,\epsilon_{eq}^*}$	$D_{DIC}$	$D_{FEM}$
A7CA1_3	-	1.5e7	14.01	13.22	5.94	0.76	0.70
A7CA2_2	-	1.5e7	5.29	6.40	-17.47	0.62	0.85
B7CA1_3	5e6	-	16.44	16.24	1.23	0.94	0.92
C7CA1_1	5e6	1.5e7	23.12	20.29	13.96	1.24	1.00
C7CA3_2	5e6	1.5e7	5.33	4.70	13.50	1.60	1.30
D7CA1_2	1.35e7	1.5e7	28.55	25.16	13.57	1.34	1.09
F7CA1_1	4e7	1.5e7	8.80	11.09	-20.70	0.75	1.10
F7CA2_2	4e7	1.5e7	5.86	5.58	4.96	0.51	0.47
$\Delta\epsilon_{eq}^*$ - % taken over $N_{ave}$ ; K - N.mm/rad; $p_{dif} \equiv$ percentage difference - %							

As can be seen in Fig. 6.10, the results from the FEM simulations provide a reasonably

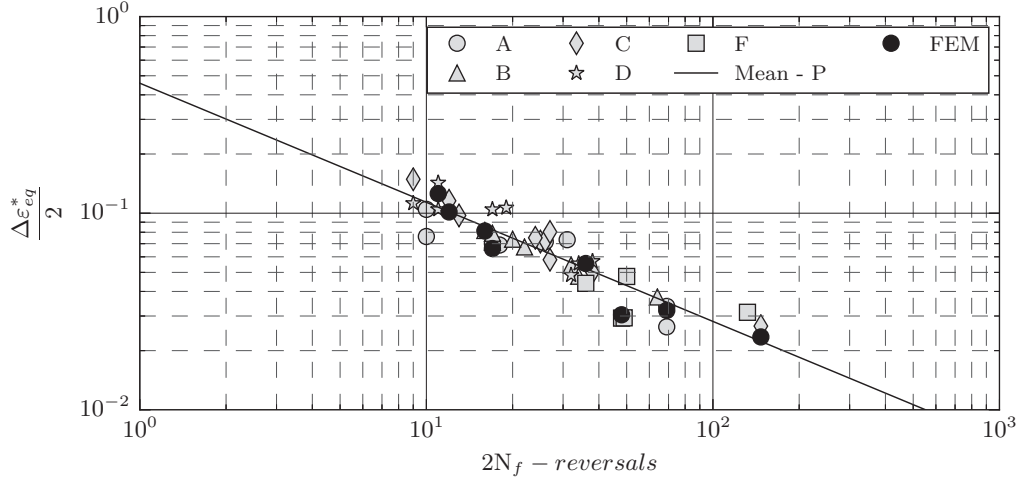


Figure 6.10 – Manson-Coffin curve for proportional constant amplitude tests with FEM results

close description of the model given by Eq. 4.3 because it is precisely descriptive of the DIC measurements. The maximum percentage difference between  $\Delta\varepsilon_{eq}^*$ , as taken by DIC or FEM, in Table 6.1 of  $-20.70\%$  is acceptable given the power law nature of the model, as shown by the differences in Fig. 6.10 when depicted in double log-scale. Damages calculated using FEM strain amplitudes with Eq. 4.3 and Eq. 4.4 are naturally also quite acceptable. The average value of  $D_{FEM}$  is 0.93 with a sample standard deviation of 0.24, *i.e.* a CoV of 26.0%.

At this point one should discuss the conspicuously different bending rotational stiffnesses used for the global models of test paths 'D' and 'F'. For this it is necessary to observe Fig. 6.11 that shows the force history of the bending and torsion jacks, and their sum (total vertical reaction) for test F7CA1\_1. Here, taking stiffness roughly speaking as the bending jack force divided by its displacement  $\delta$ , one can see a sudden change in this stiffness because of the gap in the jack's displacement, *i.e.* the loss of contact between the jack's head and the tube causes the force in it to be zero. The tube itself is moving at the  $\delta$  section, but only due to the displacement imposed by the movement of the torsion jack. The loss of contact indicates that the stiffness of both acting together is different from just the torsion jack acting by itself. This maybe to due to the fact that the lever arm's size is not inconsequential with respect to the test setup and specimen size thereby conferring an additional stiffness.

To simplify this potentially complicated situation the following judgment was made. Considering that the rotational stiffness associated with the torque is unambiguously defined by the elastic stiffness of the plate, this, once defined, should be kept constant throughout all

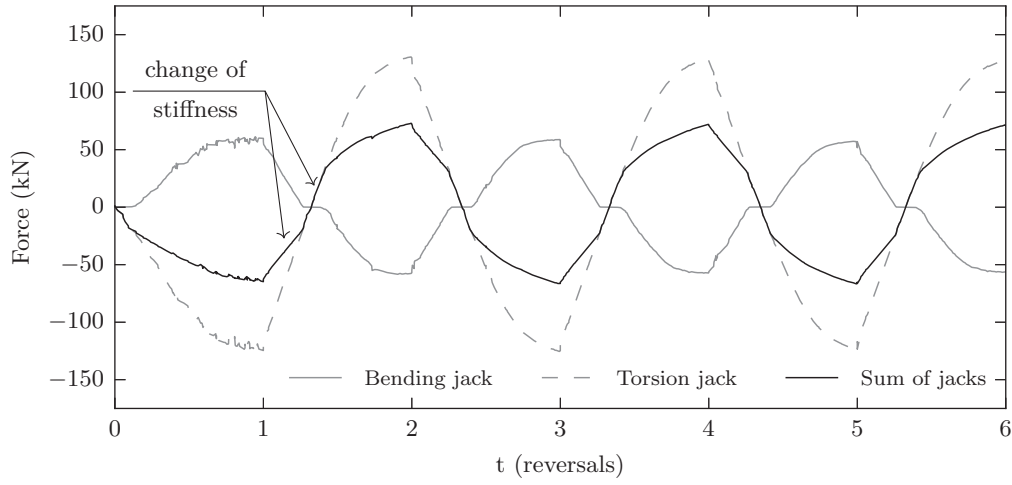


Figure 6.11 – Illustration of the bending stiffness issue for test F7CA1\_1 through loading history

the simulations. Moreover, the most important feature in modeling the global component behavior lies in respecting the time history of the forces measured during the test. This implies that at rotation  $\theta$  one should have in the model the same vertical reaction as the one measured in the test. With this in mind, the bending rotational stiffness ( $K_\delta$ ) was adjusted so as to provide the best match to this time history. An example of this can be seen in Fig. 6.12 for specimen F7CA1\_1, where the torsion jack force compares with the torque reaction in FEM model divided by the lever arm length.

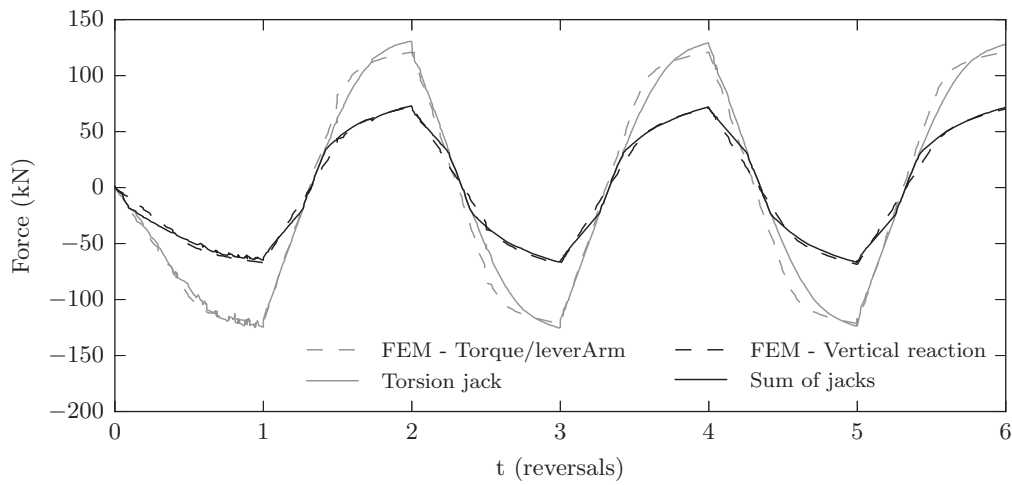


Figure 6.12 – Comparison of loading history and FEM results for test F7CA1\_1

An additional simulation with variable amplitude loading was conducted to assess if this methodology also holds for these cases. Fig. 6.13 shows the hysteresis torque-rotation curves for specimen A7VA1\_2 and the corresponding global model results, and Fig. 6.14 the time history of  $\varepsilon_{eq}^*$  as measured by DIC and in the FEM submodel.

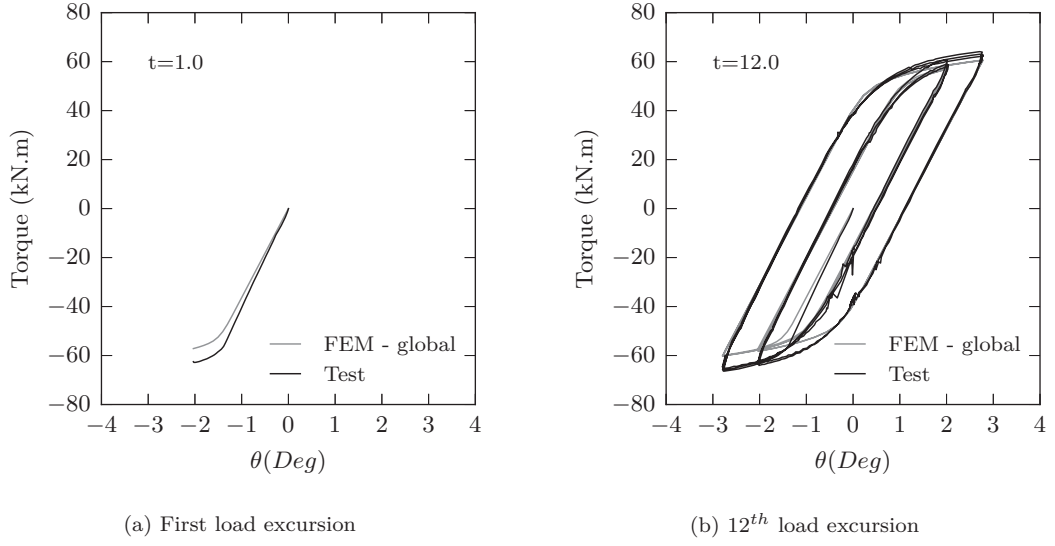


Figure 6.13 – FEM comparison of hysteresis curves for specimen A7VA1\_2

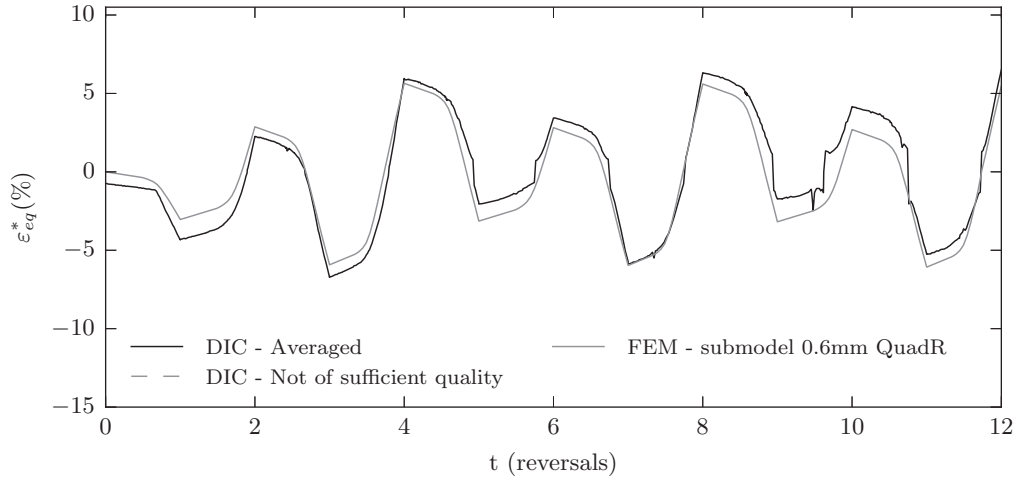


Figure 6.14 – Comparison of DIC measurements and FEM results for specimen A7VA1\_2 - time history of point at the weld toe

With respect to the Fig. 6.13, the global model was calculated maintaining the same rotational stiffness for torque of  $1.5e7$  N.mm/rad and the resulting hysteresis curve in matches test results sufficiently well. The average  $\varepsilon_{eq}^*$  ranges that can be extracted from Fig. 6.14 have

the following values:  $\Delta\varepsilon_{eq,1,DIC}^* = 12.18\%$ ,  $\Delta\varepsilon_{eq,1,FEM}^* = 11.6\%$ ,  $\Delta\varepsilon_{eq,2,DIC}^* = 5.98\%$ ,  $\Delta\varepsilon_{eq,2,FEM}^* = 5.92\%$ . Damage values calculated on the mean curve in Fig. 6.10, given by Eq. 4.3, with DIC and FEM strain amplitudes yields:  $D_{DIC} = 0.56$  and  $D_{FEM} = 0.52$ . With the proximity of such results one concludes that the method is suitable to be applied to variable amplitude loading.

A relevant question therefore arises: among a significant amount of simplifications, is a model that underestimates ULCF life by 50% (*e.g.* the damage sum computed for A7VA1\_2) acceptable? To give an answer to this question one will take the point of view of code requirements in the design of high cycle fatigue, namely the Eurocode [European Committee for Standardization, 2005].

A typical design in high cycle fatigue is carried using a nominal stress approach, whereby the code defines the characteristic resistance (FAT) according to the type of component being loaded. Resistance can be said to follow Eq. 6.1. The code sets three values for each type of detail:  $m$ ,  $\Delta\sigma$  and its corresponding  $N_f$  (the last two are equivalent to defining the constant  $C_{FAT}$ ).

$$N_f = C_{FAT} \Delta\sigma^m \quad (6.1)$$

For the sake of argument, let us consider a specific detail: a longitudinal attachment, which consists of a plate loaded on its longitudinal direction, and welded perpendicular to it is another plate of length  $L$  greater than 100mm. Fig. 6.15 depicts a sketch of this detail as well as a collection of over 700 test results that can be found in literature (*c.f.* [Baptista, 2016] for a complete list of references) and serve as the basis for the code's category definition of 56MPa stress range at  $2e6$  cycles (FAT56) with slope -3<sup>4</sup>. As one can see, the variability is considerable and if one equivalently plots the damage (with respect to the mean curve) for each specimen one can see that this approach, even though it is sanctioned by the code, typically yields values below 50%. The same conclusion could arguably be reached by selecting subsets from that database. In other words, such variability in fatigue is both expected and accepted. The reason for this is because one cannot in practical terms take into account all the relevant parameters that can influence this behavior in design.

It is, therefore, for this reason that the approach outlined in this chapter presents itself as a reasonable method for design. Fig. 6.17 shows the suggested design values based on the CA proportional tests given by a 5% probability of failure ( $p_f$ ) with a 75% confidence interval on the mean ( $CI_{mean}$ ) [IIW-JWG-XIII-XV, 2013]. Table 6.2 summarizes the recommended design values for S770QL steel to be used in this local approach with Eq. 4.3.

---

<sup>4</sup>which, parenthetically, is the same as the one commonly used for steels in Paris Law

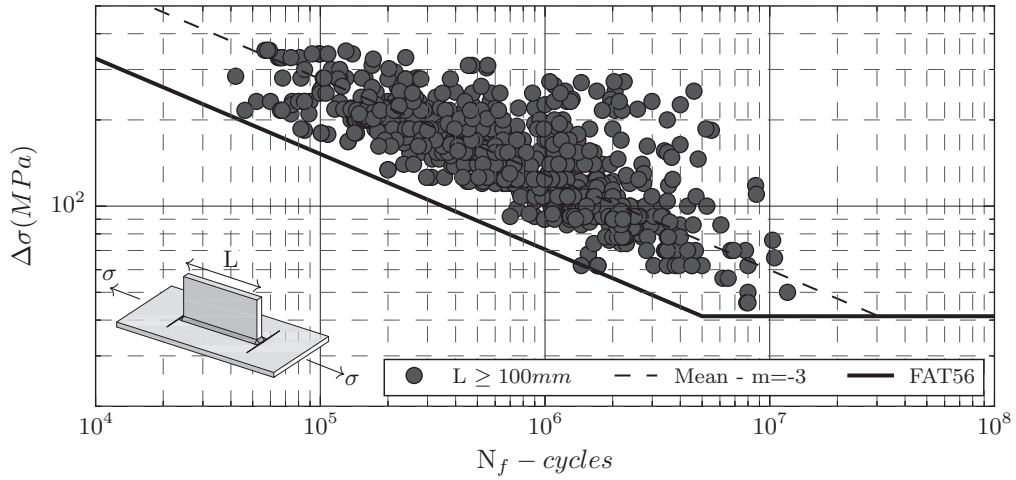


Figure 6.15 – Stress - life curve (SN) for longitudinal attachments in high cycle fatigue - one refers to [Baptista, 2016] for full list of references

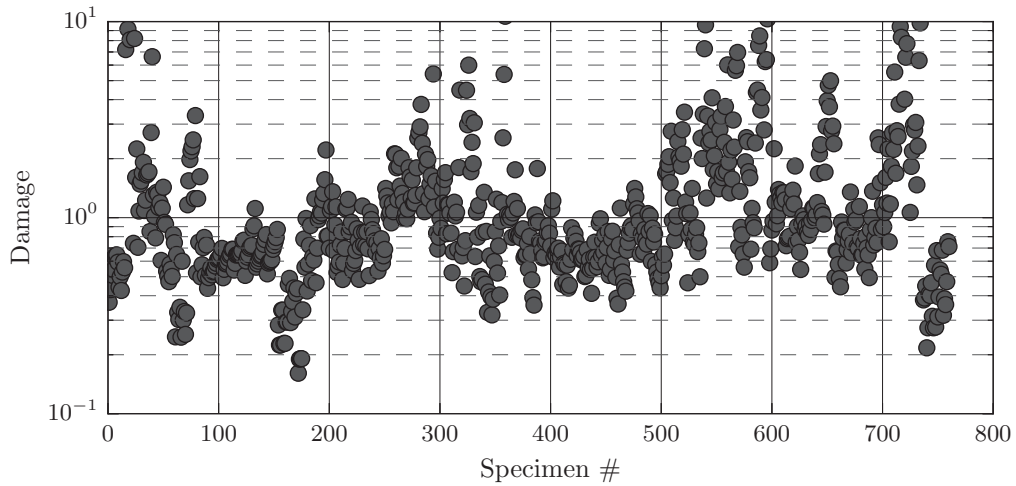


Figure 6.16 – Damage following Miner's rule in SN curve for longitudinal attachment

It should be noted that from what was concluded in Chapter 4 regarding VA loading, namely that the Palmgren-Miner's damage sum was sufficient for VA loading (*c.f.* Fig. 4.25), and considering that the submodeling approach also captures sufficiently well strain amplitudes under ULCF, the design curve in Fig. 6.17 is also valid for VA loading.

It is also important to discuss the scope and range of application of this methodology. Due to the fact of being a local method its objective hopes to give an estimate to ultra low cycle fatigue life that is decoupled from particular geometric effects imposed by different

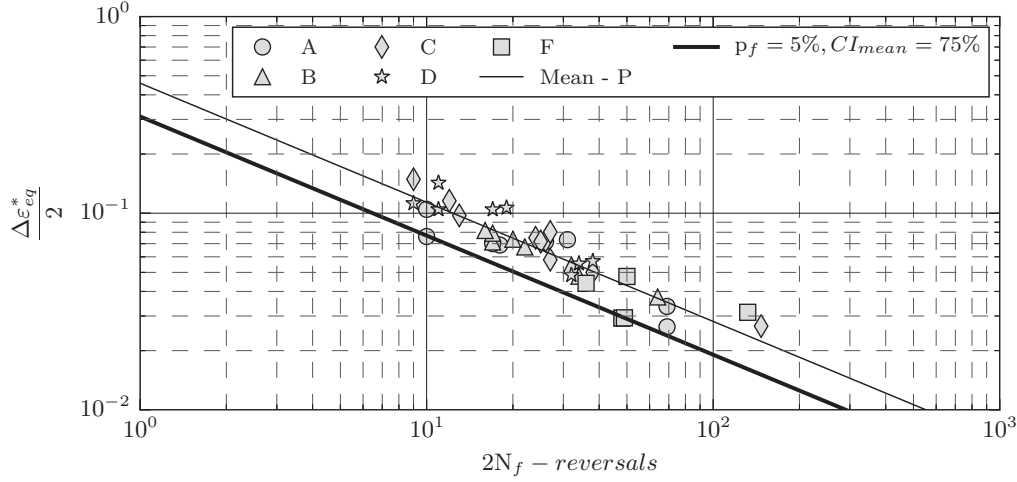


Figure 6.17 – Manson-Coffin curve for constant amplitude proportional tests and design value

Table 6.2 – Design values of M-C curve for local approach for components with thicknesses below 10mm under proportional loading histories for S770QL

Material	$b$	$c$
S770QL	0.31	-0.6
<i>cf.</i> Eq. 4.3		

components. In principle, its greatest advantage lies in the fact that for components where a high degree of geometric nonlinearity is expected, failure can be decided locally at certain critical points. That being said, its limitations arise from the simplifications involved in the evaluation process.

First and foremost is the fact that resistance is a function of total life (*i.e.* comprising both initiation and propagation). The fact that propagation accounts for a significant part of the total life, means that one will inexorably come across some sort of scale effect because the load carrying capacity of a structural component is intrinsically related to the relationship of the thickness of its constitutive parts and its overall geometry. Quantifying this effect is not straightforward and further testing on components of a different scale and nature is needed to assess the impact of this issue. This explains the limit on Table 6.2.

Another relevant factor is the material properties of the steel in question. Since different microstructures have different plastic dissipation capacities, it is both conceivable and expected that the steel type will have a noticeable impact on the ULCF resistance.

Lastly, one would be remiss if no comment on non-proportional loading cases was given. In

chapter 4, one observed that for non-proportional load path 'E' the average value of the ductility coefficient was 0.32 which is roughly the design value that one obtained for all the proportional constant amplitude tests. As was previously stated, this suggests that the mechanisms involved in the deterioration of the component's resistance are significantly worse than those present in the proportional load paths. Therefore, it is unsuitable to consider these loading cases when using the resistance curve defined by Table 6.2 and further research should be made on this subject.

### 6.3 Conclusion

This chapter provided a framework for the assessment of ULCF resistance in welded steel joints. Essential features of this approach are as follows,

1. The presence of stress/strain risers such as welds lead to significant strain gradients close to those notches. Continuum-based FEM are known to suffer from mesh sensitivities close to discontinuities. To mitigate those effects, and using detailed 3D FEM at the area close to the notch, a specific mesh size and type was calibrated with surface strains measurements made by DIC (*cf.* Chapter 4). Those are,
  - (a) 3D 20-node quadratic reduced integration elements, in line with [Myers et al., 2009]
  - (b) Approximately cubic in aspect ratio with 0.6 millimeters in size.
2. The use of base material hardening properties and a simplified weld geometry in the FEM submodel was sufficient to yield estimates close to the mean resistance curve of the Manson-Coffin law (*cf.* Fig. 6.10).
3. Design values for the high-strength S770QL steel are given in Table 6.2
4. This approach was tested in proportional constant and variable amplitude ULCF loading conditions and deemed acceptable when compared to current design practice for high cycle fatigue.
5. Nonproportional load paths cannot be used in the same design curve and further research should be conducted to mitigate this weakness.

Although this design framework is based on local strain measurements and therefore less dependent on specimen geometry, there is the risk it will suffer from the same component dependent deficiencies as other models because so much of the fatigue life is spent in propagation. Further analysis is needed to bound the application range of this approach. Prominently among those concerns are,



1. The weld profile, because the weld angles in this detail are not very aggressive ( $\psi < 30\text{Deg}$ )
2. The component thickness, which is of natural interest when so much of the fatigue life spent in propagation
3. The material properties, mainly for two reasons:
  - (a) The high-strength steel studied in this thesis exhibits little to no isotropic hardening, limited ductility and a small hardening exponent. Steels with other characteristics can have significantly different hysteretic behaviors which can affect a clear evaluations of strain amplitudes.
  - (b) As pointed out by [Kanvinde and Deierlein, 2004] fracture is usually defined as happening within a minimum volume of material associated with its microstructural properties. This is what leads to the definition of a characteristic length of material ( $l^*$ ). In this approach that characteristic length is something that is implicitly taken into account in the mesh size and in the choice of the DIC parameters. Although the volume spanned by the integration points in the element size of this approach fall within the values recommended for most structural steels in [Kanvinde and Deierlein, 2004], care should be taken for significantly different materials.



## 7 Conclusion and future work

The work presented in this thesis had the main objective of understanding the behavior of welded structural components in situations susceptible to multiaxial ultra low cycle fatigue and provide suitable method for their design. The material studied in this document is the high-strength structural steel S770QL.

### Summary and conclusions from Chapter 2

This chapter provided some background on topics such as finite strain plasticity which are important under large scale yielding and thus quite relevant for ULCF. Also discussed are the basic principles in digital image correlation to understand key aspects of the experimental programs in this document. Finally a review of a continuum mechanics approach to ductile fracture and ULCF was given.

From that presentation the following remarks are deemed important:

1. Finite rotations can have a sizable impact on the plastic behavior of material models. Kinematic hardening models are particularly sensitive to this issue.
2. Under monotonic loading there a strong dependency of fracture strain to the stress state has been reported in literature. This is commonly measured by two parameters: the triaxiality and the Lode parameter. The former provides a measure of the ratio of hydrostatic to the deviatoric part of the stress state and the latter a measure of the state of axisymmetry. Investigations into the effects of low triaxialities and the Lode parameter are fairly recent developments in the state of the art of ductile fracture.
3. Differences on the low-cycle fatigue resistance between tension and torsion tests in small thin walled tubes of base material have been reported in literature.

## Chapter 7. Conclusion and future work

---

4. From the continuum mechanics perspective, there are two common choices on how to approach the problem of ULCF:
  - (a) Empirical formulae associated with Manson-Coffin type expressions
  - (b) A more physical oriented approach through micromechanical models based on the nucleation of voids around impurities in the material and their subsequent growth and coalescence.

### Summary and conclusions from Chapter 3

Here, the results of an experimental campaign on small scale specimens to characterize key material properties of high strength S770QL steel was presented. They can be summarized as follows,

1. Internal variables in micromechanical models for void growth and coalescence such as porosity, aspect ratio, and inclusion ligament size ratio were determined.
2. SEM micrographs of the fracture surfaces of single notched specimens suggest two important conclusions:
  - (a) The presence of shallower voids under cyclic loading *w.r.t.* monotonic, in line with [Kanvinde and Deierlein, 2004].
  - (b) It can be argued, although not conclusively, that critical porosity (*i.e.* leading to failure) is higher in large amplitude cyclic loading than in monotonic loading of single notched specimens.
3. Tests conducted on double notched tubular specimens confirmed the dependence of material ductility (as measured by the fracture strain) on the stress state.

### Summary and conclusions from Chapter 4

This chapter presented methodologies and results of a welded tube-to-plate connection loaded in bending and in torsion. Different ratios of longitudinal and shear strain were applied by varying the ratio between bending and torsion. Results were mostly interpreted by the use of digital image correlation measurements on the surface of the joint near the weld toe region. The following points summarize the main conclusions of that chapter,

1. One can detect surfaces cracks on the welded component without a large decrease in the load carrying capacity of the connection.

- 
2. This initiation phase was found to be within a third to a half of the life of the specimen. Conversely, propagation can be from half to almost to two thirds of the total ULCF life.
  3. To the extent that a continuum mechanics based approach can approximate total life (*i.e.* initiation plus propagation<sup>1</sup>), empirical methods such as Manson-Coffin are worth considering.
  4. The suitability of a Manson-Coffin approach using an equivalent strain measure deduced from DIC was tested and it was found that this approach does indeed provide a good estimate for total life under proportional constant amplitude multiaxial loadings.
  5. In contrast to the tests of base material on the double notched tubes presented in Chapter 3, the dependence of ULCF life on the stress state in welded joints of high-strength steel was found to be negligible
  6. The application of the Palmgren-Miner's rule for variable amplitude loading was found to be a suitable approach
  7. Nonproportional load paths were found to be more severe than proportional ones.

## Summary and conclusions from Chapter 5

In this chapter a micromechanical model that incorporates kinematic hardening was presented that allows for the consideration of void shape interactions with the porosity. This model is a heuristic extension of the GLD micromechanical model. Main conclusions are as follows,

1. The decrease in fracture strain observed for cyclic loading *w.r.t.* to monotonic loading can be modeled by porosity ratcheting induced by progressively shallower voids. This assertion is supported by the experimental observations presented in Chapter 3.
2. A simplified approach considering as a coalescence criterion another micromechanical model (the TBL model) was presented. Although it provides reasonable estimates for ULCF in single notched tests, by virtue of its assumptions a complete description of the ULCF phenomenon remains elusive (*cf.* Chapter 5 for more details).
3. Difficulties in modeling double notched tubular specimens were registered. Of particular interest is the mode of failure associated with pure tension tests. Here, a pronounced slanted fracture surface can be observed in the tests and is associated with low Lode

---

<sup>1</sup>which is arguably better modeled by a fracture mechanics approach - *e.g.* cohesive zone modeling or J-integral approaches

parameters in the notched section as obtained through FEM modeling. The non-axisymmetry of the stress state in pure tension is further confirmed with elongated dimples along the circumferential direction that can be seen in the fractography presented in Chapter 3 (*c.f.* Fig. 3.24). It is in this context that the FEM models presented in this Chapter tend not to perform so well under pure tension load paths. However, under increased Lode parameters, results are more encouraging as the models tend to perform better.

### Summary and conclusions from Chapter 6

This chapter presented a design approach for the assessment of ULCF resistance in welded steel joints. This approach is inspired by the work of [Myers et al., 2009] albeit a different failure criterion is recommended (the Manson-Coffin approach). The gist of this design proposal is as follows,

1. The presence of stress/strain risers such as welds lead to significant strain gradients close to those notches. Continuum-based FEM are known to suffer from mesh sensitivities close to discontinuities. To mitigate those effects, and using detailed 3D FEM at the area close to the notch, a specific mesh size and type was calibrated with surface strains measurements made by DIC (*c.f.* Chapter 4).
2. A design curve to be used in models following those specific mesh requirements was given for the high-strength S770QL steel (*c.f.* Chapter 6 for more details on the range of application).
3. This approach was tested in proportional constant and variable amplitude ULCF loading conditions and deemed acceptable when compared to current design practices for high cycle fatigue.

### Future work

With respect to micromechanical models the following recommendations are made,

1. Given the experimental observations that fracture under ULCF have shallower voids than under monotonic loading and the effectiveness of the fact observed in Chapter 5 that increasingly oblate voids induce higher porosities, a unit cell study to quantify these effects on the heuristic factor  $\varrho$  introduced in Chapter 5 is warranted.
2. It's worth noting that ratcheting can also be achieved by history dependent parameters in the hardening laws of the deviatoric and hydrostatic components of the GLD criterion

---

similarly to [Leblond et al., 1995]. This can be used as complement to induce porosity ratcheting if unrealistic aspect ratios are observed.

3. A more precise failure criterion in ULCF is needed. The physical mechanisms involved in this phenomenon are, however, less clear. Interrupted tests under ULCF are of interest in order to clarify this issue and would provide guidance on the definition of better failure criteria.
4. A comprehensive study of the influence of hardening parameters in the hysteretic behavior of both the porosity, the void aspect ratio and the failure criterion can also be of worth for selecting materials for specific applications involving ULCF.
5. For non-axisymmetric conditions, an extension to kinematic hardening of void growth models that include void shape effects for ellipsoidal voids (like [Madou and Leblond, 2013a], [Madou and Leblond, 2013b]) is also of interest for ULCF applications.

Concerning the more practical approach to design with Manson-Coffin type laws in welded joints, the following lines of inquiry are suggested,

1. Given the successful application of DIC measurements in assessing strains at the weld toes of components subjected to ULCF, different weld geometries are recommended to validate the expected increase in plastic strain as predicted by FEM in the presence of more aggressive weld toe geometries and validate mesh size requirements.
2. Due to the significant weight of crack propagation in ULCF, size effects related to plate thickness are expected and should be investigated
3. The impact of material properties is also deemed worthy of further investigation. The fact that a specific mesh was used, albeit calibrated with DIC measurements, has implicitly defined a length scale associated with fracture process of the material. To which extent this would change the mesh requirements is worth investigating using the same methodology for different materials. This would allow the development of a more systematic approach using a non-local method for added robustness (*e.g.* where the length scale would be defined by a volume averaging and not a specific mesh size).
4. Although no visible difference was registered using an equivalent strain approach in evaluating ULCF resistance of welded joints of high-strength steel under multiaxial loading, material properties could have an influence on this behavior, and should thus be examined

5. The effects of non-proportional loading should also be investigated. Here energy methods like [Garud, 1981] or critical plane models like [Fatemi and Socie, 1988] can provide insights for addressing this issue.



## A.1 Cyclic GLD yield function and defining parameters

The cyclic yield function and defining parameters were adapted from [Benzerga and Leblond, 2010].

$f$  is the porosity and  $w$  is the aspect ratio of spheroidal void with principal axis  $\mathbf{n}_3$ .  $w < 1$  are oblate voids.  $w > 1$  are prolate voids.  $S = \ln w$ .

$$\begin{aligned} \phi^{GLD}(\boldsymbol{\Sigma}, \mathbf{A}, \sigma_y, f, w, \Upsilon) = & C \frac{\|\boldsymbol{\Sigma}' - \mathbf{A}' + \eta \Sigma_h \mathbf{Q}\|^2}{\sigma_y^2} + \\ & 2q(g+1)(g+f) \cosh\left(k \frac{(\boldsymbol{\Sigma} - \mathbf{A}) : \mathbf{X}}{\sigma_y}\right) - \\ & (g+1)^2 - q^2(g+f)^2 \end{aligned} \quad (\text{A.1})$$

with,  $\Sigma_h = (\boldsymbol{\Sigma} - \mathbf{A}) : \mathbf{X}$

$$g = 0 \quad (w > 1) \quad , \quad g = f \frac{(1 - w^2)^{\frac{3}{2}}}{w} \quad (w < 1) \quad (\text{A.2})$$

$e_1$  and  $e_2$  are defined as the eccentricities of the void and the representative volume element of the GLD, respectively. Numerical implementations of  $e_2$  can be done with approximate closed form solutions but they are generally numerically unstable for prolate voids. In this UMAT implementation  $e_2$  is determined by a numerical root finding algorithm using Halley's

## Appendix A. UMAT

---

method.

$$e_1 = \begin{cases} \sqrt{1 - \exp(-2S)} & , (w > 1) \\ \sqrt{1 - \exp(2S)} & , (w < 1) \end{cases} ; \quad \frac{(1 - e_2^2)^n}{e_2^3} = \frac{1}{f} \frac{(1 - e_1^2)^n}{e_1^3} ; \quad n = \begin{cases} 1 & , (w > 1) \\ \frac{1}{2} & , (w < 1) \end{cases} \quad (\text{A.3})$$

$$k = \begin{cases} \left[ \frac{1}{\sqrt{3}} + \frac{1}{\ln f} \left( (\sqrt{3} - 2) \ln \frac{e_1}{e_2} \right) \right]^{-1} & , (w > 1) \\ \frac{3}{2} \left[ 1 + \frac{(g_f - g_1) + \frac{4}{5}(g_f^{5/2} - g_1^{5/2}) - \frac{3}{5}(g_f^5 - g_1^5)}{\ln \frac{g_f}{g_1}} \right]^{-1} & , (w < 1) \end{cases} \quad (\text{A.4})$$

$$g_f = \frac{g}{g + f} \quad , \quad g_1 = \frac{g}{g + 1} \quad (\text{A.5})$$

$$\alpha_1 = \begin{cases} \frac{[e_1 - (1 - e_1^2) \tanh^{-1} e_1]}{2e_1^3} & , (w > 1) \\ \frac{[-e_1(1 - e_1^2) + \sqrt{1 - e_1^2} \sin^{-1} e_1]}{2e_1^3} & , (w < 1) \end{cases} \quad (\text{A.6})$$

$$\alpha_2 = \begin{cases} \frac{1 + e_2^2}{(1 + e_2^2)^2 + 2(1 - e_2^2)} & , (w > 1) \\ \frac{(1 - e_2^2)(1 - 2e_2^2)}{(1 - 2e_2^2)^2 + 2(1 - e_2^2)} & , (w < 1) \end{cases} \quad (\text{A.7})$$

$$\alpha_1^G = \begin{cases} \frac{1}{3 - e_1^2} & , (w > 1) \\ \frac{1 - e_1^2}{3 - 2e_1^2} & , (w < 1) \end{cases} \quad (\text{A.8})$$

$$H^* = 2(\alpha_1 - \alpha_2) \quad ; \quad Q^* = 1 - f \quad ; \quad sh = \sinh(kH^*) \quad ; \quad ch = \cosh(kH^*) \quad (\text{A.9})$$

$$\eta = -\frac{2}{3} \frac{kQ^*(g + 1)(g + f)sh}{(g + 1)^2 + (g + f)^2 + (g + 1)(g + f)[kH^*sh - 2ch]} \quad (\text{A.10})$$

$$C = -\frac{2}{3} \frac{k(g + 1)(g + f)sh}{(Q^* + \frac{3}{2}\eta H^*)\eta} \quad (\text{A.11})$$

## A.2 TBL yield function and defining parameters

Yield function and defining parameters can be found in [Torki et al., 2015].

$$\phi^{TBL,mod} = \begin{cases} \frac{(|\Sigma_{33}| - t\Sigma^{surf})^2}{b^2(\Sigma^{vol})^2} + 4\frac{\Sigma_{31}^2 + \Sigma_{32}^2}{l^2\tau^2} - 1 & , |\Sigma_{33}| \geq \Sigma^{surf} \\ 4\frac{\Sigma_{31}^2 + \Sigma_{32}^2}{l^2\tau^2} - 1 & , |\Sigma_{33}| \leq \Sigma^{surf} \end{cases} \quad (A.12)$$

with,  $\Sigma^{vol}$ ,  $\Sigma^{surf}$

$$\Sigma^{vol} = \frac{\sigma_y}{\sqrt{3}} \left[ 2 - \sqrt{1 + 3\chi_{TBL}^4} \ln \frac{1 + \sqrt{1 + 3\chi_{TBL}^4}}{3\chi_{TBL}^2} \right] \quad (A.13)$$

$$\Sigma^{surf} = \frac{\sigma_y}{3\sqrt{3}} \frac{\chi_{TBL}^3 - 3\chi_{TBL} + 2}{\chi_{TBL} w_{TBL}} \quad (A.14)$$

$$\tau = \frac{2\sigma_y}{\sqrt{3}} (1 - \chi_{TBL}^2) \quad (A.15)$$

$$\chi_{TBL} = \frac{R^{TBL}}{L^{TBL}} \quad , \quad w_{TBL} = \frac{h^{TBL}}{R^{TBL}} \quad , \quad \lambda_{TBL} = \frac{H^{TBL}}{L^{TBL}} \quad (A.16)$$

$$t = \frac{(t_0 + t_1\chi_{TBL}) w_{TBL}}{1 + (t_0 + t_1\chi_{TBL}) w_{TBL}} \quad (A.17)$$

TBL parameter values in the UMAT are set as follows:  $t_0 = -0.84, t_1 = 12.9, b = 0.9, l = 1.0$

## A.3 Derivatives in return mapping algorithm

$$\frac{\partial R_{ij}^{E^p}}{\partial A_{kl}} = \lambda \frac{\partial^2 \phi^{GLD}}{\partial \Sigma_{ij} \partial A_{kl}} \quad ; \quad \frac{\partial R_{ij}^{E^p}}{\partial \sigma_y} = \lambda \frac{\partial^2 \phi^{GLD}}{\partial \Sigma_{ij} \partial \sigma_y} \quad (A.18)$$

$$\frac{\partial R_{ij}^{E^p}}{\partial f} = \lambda \frac{\partial^2 \phi^{GLD}}{\partial \Sigma_{ij} \partial f} \quad ; \quad \frac{\partial R_{ij}^{E^p}}{\partial w} = \lambda \frac{\partial^2 \phi^{GLD}}{\partial \Sigma_{ij} \partial w} \quad (A.19)$$

$$\Sigma_h = (\Sigma - \mathbf{A}) : \mathbf{X} \quad ; \quad \Sigma'_{kl} = \Sigma_{kl} - \frac{1}{3} \Sigma_{mm} \delta_{kl} \quad ; \quad \partial \Sigma'_{kl} / \partial \Sigma_{ij} = \delta_{ik} \delta_{jl} - \frac{1}{3} \delta_{ij} \delta_{kl}$$

$$\begin{aligned}
 \frac{\partial \phi^{GLD}}{\partial \Sigma_{ij}} &= \frac{3C}{\sigma_y^2} \left\{ (\Sigma'_{kl} - A'_{kl} + \eta \Sigma_h Q_{kl} - \frac{1}{3}(\Sigma'_{mm} - A'_{mm} + \eta \Sigma_h Q_{mm}) \delta_{kl}) \right. \\
 &\quad \left. [\delta_{ik} \delta_{jl} - \frac{1}{3} \delta_{ij} \delta_{kl} + \eta X_{ij} Q_{kl} - \frac{1}{3} \delta_{kl} X_{ij} Q_{mm}] \right\} + \\
 &\quad 2q(g+1)(g+f) \sinh \left( k \frac{\Sigma_h}{\sigma_y} \right) \frac{k}{\sigma_y} X_{ij}
 \end{aligned} \tag{A.20}$$

$$\begin{aligned}
 \frac{\partial^2 \phi^{GLD}}{\partial \Sigma_{ij} \partial \Sigma_{kl}} &= \frac{3C}{\sigma_y^2} \left\{ [\delta_{im} \delta_{jn} + \frac{1}{3} \delta_{ij} \delta_{mn} + \eta X_{ij} Q_{mn} - \frac{1}{3} \delta_{mn} X_{ij} Q_{oo}] \right. \\
 &\quad \left. [\delta_{km} \delta_{ln} + \frac{1}{3} \delta_{kl} \delta_{mn} + \eta X_{kl} Q_{mn} - \frac{1}{3} \delta_{mn} X_{kl} Q_{oo}] \right\} + \\
 &\quad 2q(g+1)(g+f) \cosh \left( k \frac{\Sigma_h}{\sigma_y} \right) \frac{k^2}{\sigma_y^2} X_{ij} X_{kl}
 \end{aligned} \tag{A.21}$$

$$\begin{aligned}
 \frac{\partial \phi^{GLD}}{\partial A_{ij}} &= -\frac{3C}{\sigma_y^2} \left\{ (\Sigma'_{kl} - A'_{kl} + \eta \Sigma_h Q_{kl} - \frac{1}{3}(\Sigma'_{mm} - A'_{mm} + \eta \Sigma_h Q_{mm}) \delta_{kl}) \right. \\
 &\quad \left. [\delta_{ik} \delta_{jl} - \frac{1}{3} \delta_{ij} \delta_{kl} + \eta X_{ij} Q_{kl} - \frac{1}{3} \delta_{kl} X_{ij} Q_{mm}] \right\} - \\
 &\quad 2q(g+1)(g+f) \sinh \left( k \frac{\Sigma_h}{\sigma_y} \right) \frac{k}{\sigma_y} X_{ij}
 \end{aligned} \tag{A.22}$$

$$\begin{aligned}
 \frac{\partial^2 \phi^{GLD}}{\partial \Sigma_{ij} \partial A_{kl}} &= -\frac{3C}{\sigma_y^2} \left\{ [\delta_{im} \delta_{jn} + \frac{1}{3} \delta_{ij} \delta_{mn} + \eta X_{ij} Q_{mn} - \frac{1}{3} \delta_{mn} X_{ij} Q_{oo}] \right. \\
 &\quad \left. [\delta_{km} \delta_{ln} + \frac{1}{3} \delta_{kl} \delta_{mn} + \eta X_{kl} Q_{mn} - \frac{1}{3} \delta_{mn} X_{kl} Q_{oo}] \right\} - \\
 &\quad 2q(g+1)(g+f) \cosh \left( k \frac{\Sigma_h}{\sigma_y} \right) \frac{k^2}{\sigma_y^2} X_{ij} X_{kl}
 \end{aligned} \tag{A.23}$$

$$\frac{\partial \phi^{GLD}}{\partial \sigma_y} = -2C \frac{\|\mathbf{\Sigma}' - \mathbf{A}' + \eta \Sigma_h \mathbf{Q}\|^2}{\sigma_y^3} - \frac{2q(g+1)(g+f)k\Sigma_h}{\sigma_y^2} \sinh \left( k \frac{\Sigma_h}{\sigma_y} \right) \tag{A.24}$$

### A.3. Derivatives in return mapping algorithm

$$\begin{aligned}
\frac{\partial^2 \phi^{GLD}}{\partial \Sigma_{ij} \partial \sigma_y} = & -\frac{6C}{\sigma_y^3} \left\{ (\Sigma'_{kl} - A'_{kl} + \eta \Sigma_h Q_{kl} - \frac{1}{3}(\Sigma'_{mm} - A'_{mm} + \eta \Sigma_h Q_{mm}) \delta_{kl}) \right. \\
& \left. [\delta_{ik} \delta_{jl} - \frac{1}{3} \delta_{ij} \delta_{kl} + \eta X_{ij} Q_{kl} - \frac{1}{3} \delta_{kl} X_{ij} Q_{mm}] \right\} - \\
& 2q(g+1)(g+f)kX_{ij} \left[ \frac{k\Sigma_h}{\sigma_y^3} \cosh\left(k \frac{\Sigma_h}{\sigma_y}\right) + \frac{1}{\sigma_y^2} \sinh\left(k \frac{\Sigma_h}{\sigma_y}\right) \right] \quad (A.25)
\end{aligned}$$

Since there are a great deal of coefficients on  $\phi^{GLD}$  that depend on  $f$  and  $w$ , numerical estimates using a complex step derivative approximation [Martins et al., 2003] were used for the derivatives in Eq. A.26.

$$\frac{\partial \phi^{GLD}}{\partial f} \quad ; \quad \frac{\partial \phi^{GLD}}{\partial w} \quad ; \quad \frac{\partial^2 \phi^{GLD}}{\partial \Sigma_{ij} \partial f} \quad ; \quad \frac{\partial^2 \phi^{GLD}}{\partial \Sigma_{ij} \partial w} \quad (A.26)$$

$$\frac{\partial A_{ij,k}}{\partial \lambda} = \left( C_k \frac{\Sigma_{ij} - A_{ij}}{\sigma_y} - \gamma_k A_{ij,k} \right) \chi \quad (A.27)$$

$$\frac{\partial \sigma_y}{\partial \lambda} = nK (E_{eq}^p)^{n-1} \chi \quad (A.28)$$

$$\frac{\partial f}{\partial \lambda} = (1-f) \frac{\partial \phi^{GLD}}{\partial \Sigma_{kk}} \quad (A.29)$$

$$\frac{\partial S}{\partial \lambda} = \mathbf{Z} : \left[ (1 + k_w k_f k_\tau) \frac{\partial \phi}{\partial \Sigma} + \left( \frac{1}{f_{n+1}^{it}} \mathbf{X}_v - \mathbf{X} \right) \frac{\partial \phi}{\partial \Sigma_{kk}} \right] \quad (A.30)$$

$$\frac{\partial S^{cyclic}}{\partial \lambda} = \begin{cases} \frac{\partial S}{\partial \lambda} & , \frac{\partial \phi}{\partial \Sigma_{kk}} > 0 \\ \varrho \frac{\partial S}{\partial \lambda} & , \frac{\partial \phi}{\partial \Sigma_{kk}} \leq 0 \end{cases} \quad (A.31)$$

$$\frac{\partial w}{\partial \lambda} = \frac{\partial w}{\partial S^{cyclic}} \frac{\partial S^{cyclic}}{\partial \lambda} = w \frac{\partial S^{cyclic}}{\partial \lambda} \quad (\text{A.32})$$

## A.4 Hardening parameters

The material model used throughout the thesis is based solely on nonlinear kinematic hardening with the Chaboche model except where otherwise explicitly indicated. The coefficients for this model can be seen in A.1 which are in correspondence with Table 3.1 and Fig. 3.2 up to sufficiently high equivalent plastic strains (here taken at 400%).

Table A.1 – Chaboche model backstress coefficients used throughout the thesis

Backstress #	$C$ (MPa)	$\gamma$
1	100465.56	1107.87
2	16124.16	460.41
3	6492.09	142.14
4	2613.95	44.098
5	1055.04	13.20
6	435.25	3.97
7	189.27	0.99
8	81.47	0.126

## A.5 Validation

Table A.2 – Numbering for internal variables used in the validation procedure

#	$f_0$	$S_0$	$\mathbf{\Upsilon}$
1	1.0e-3	0.0	$\mathbf{n}_3 \equiv [0, 1, 0]$
2	5.0e-3	1.0	$\mathbf{n}_3 \equiv [1, 0, 0]$
3	1.0e-2	-1.0	-
4	1.5e-2	-	-

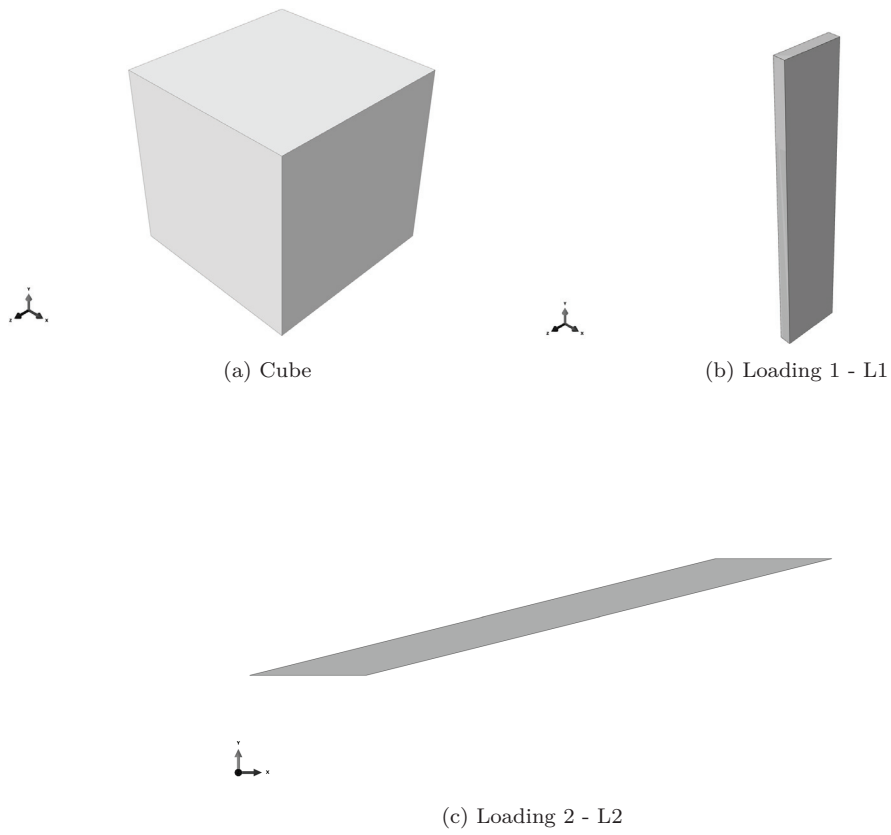


Figure A.1 – Element(C3D8R) and loading cases used in validation of gld Umat in Abaqus

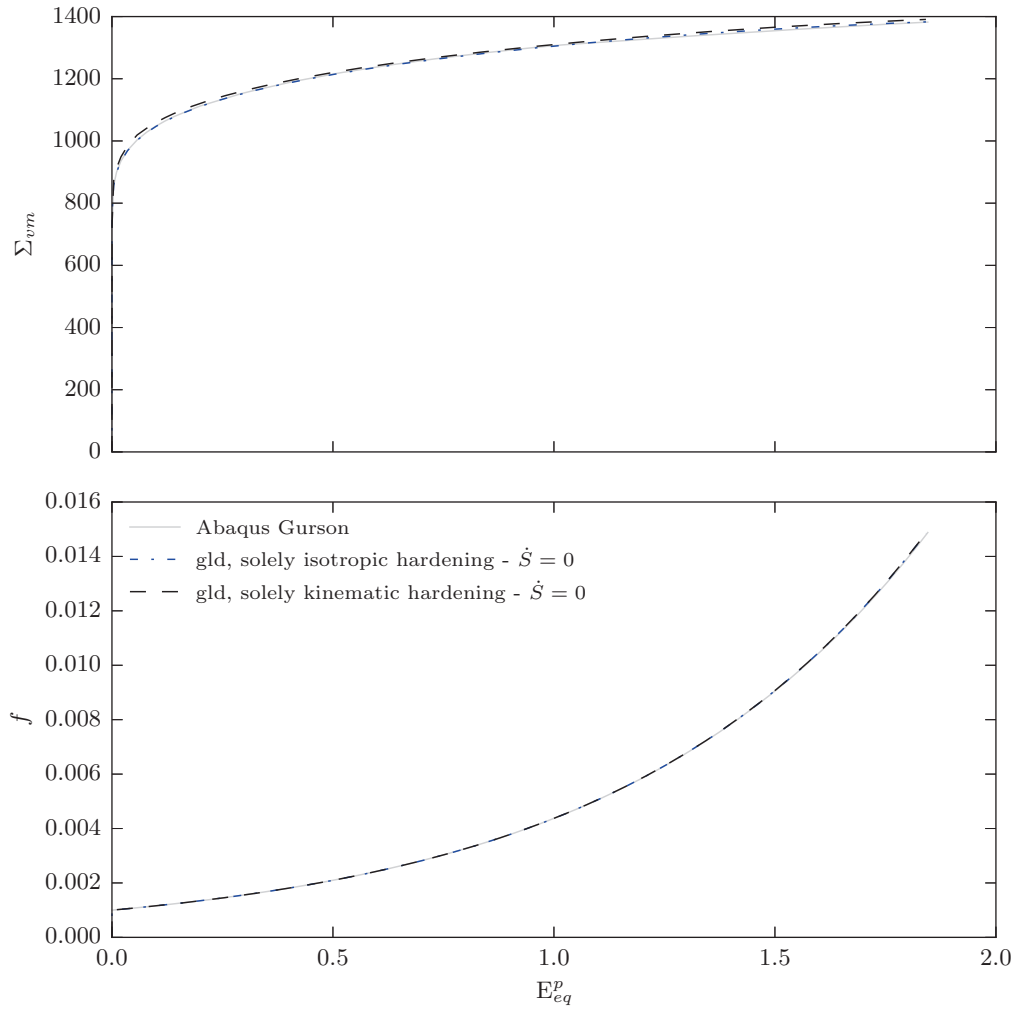


Figure A.2 – Comparison between gld Umat and Abaqus’s implementation of the Gurson model



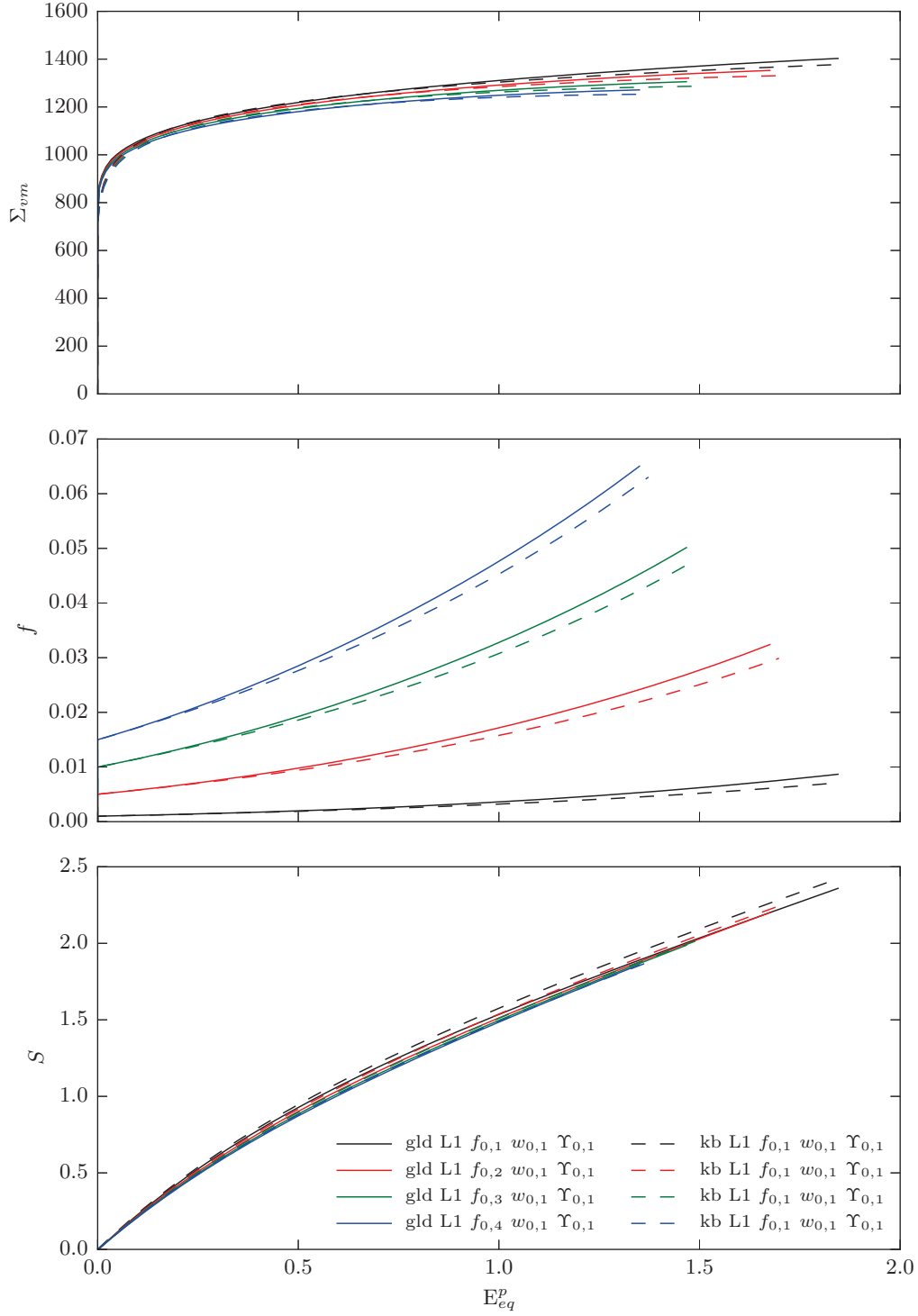


Figure A.3 – Comparison between gld and kb Umat for loading: Tension; direction: Parallel to voids; initial void shape: Spherical

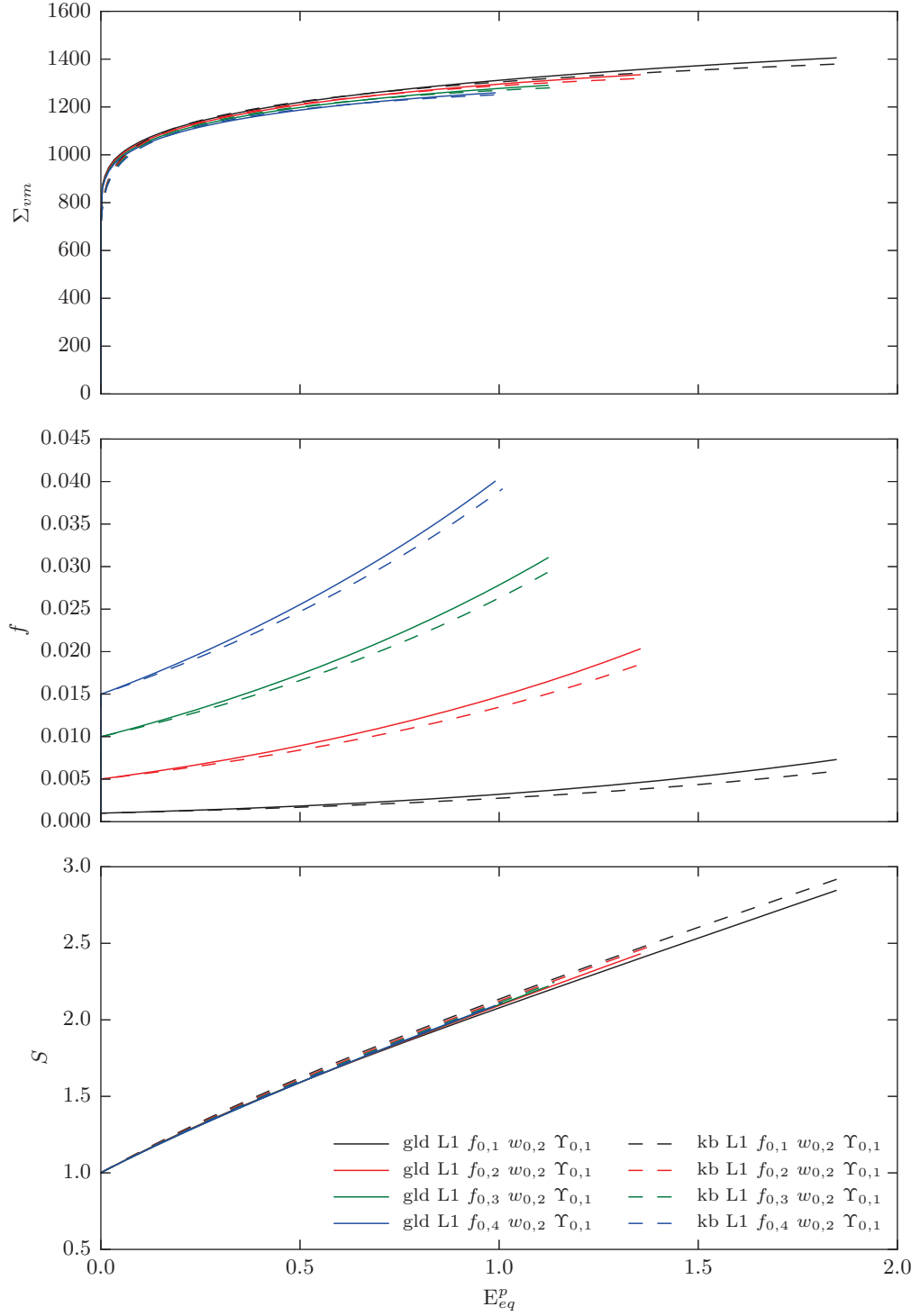


Figure A.4 – Comparison between gld and kb Umat for loading: Tension; direction: Parallel to voids; initial void shape: Prolate

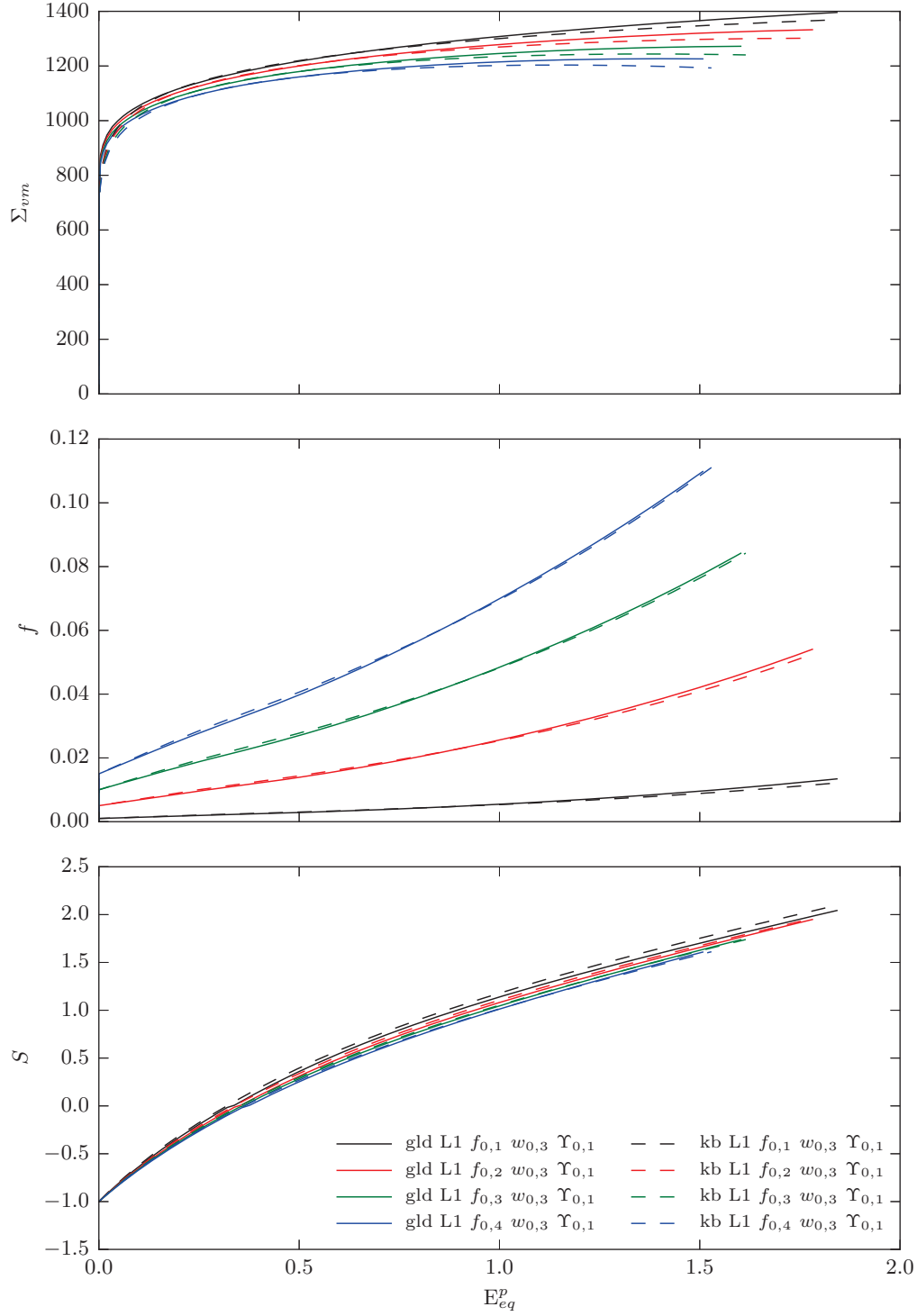


Figure A.5 – Comparison between gld and kb Umat for loading: Tension; direction: Parallel to voids; initial void shape: Oblate

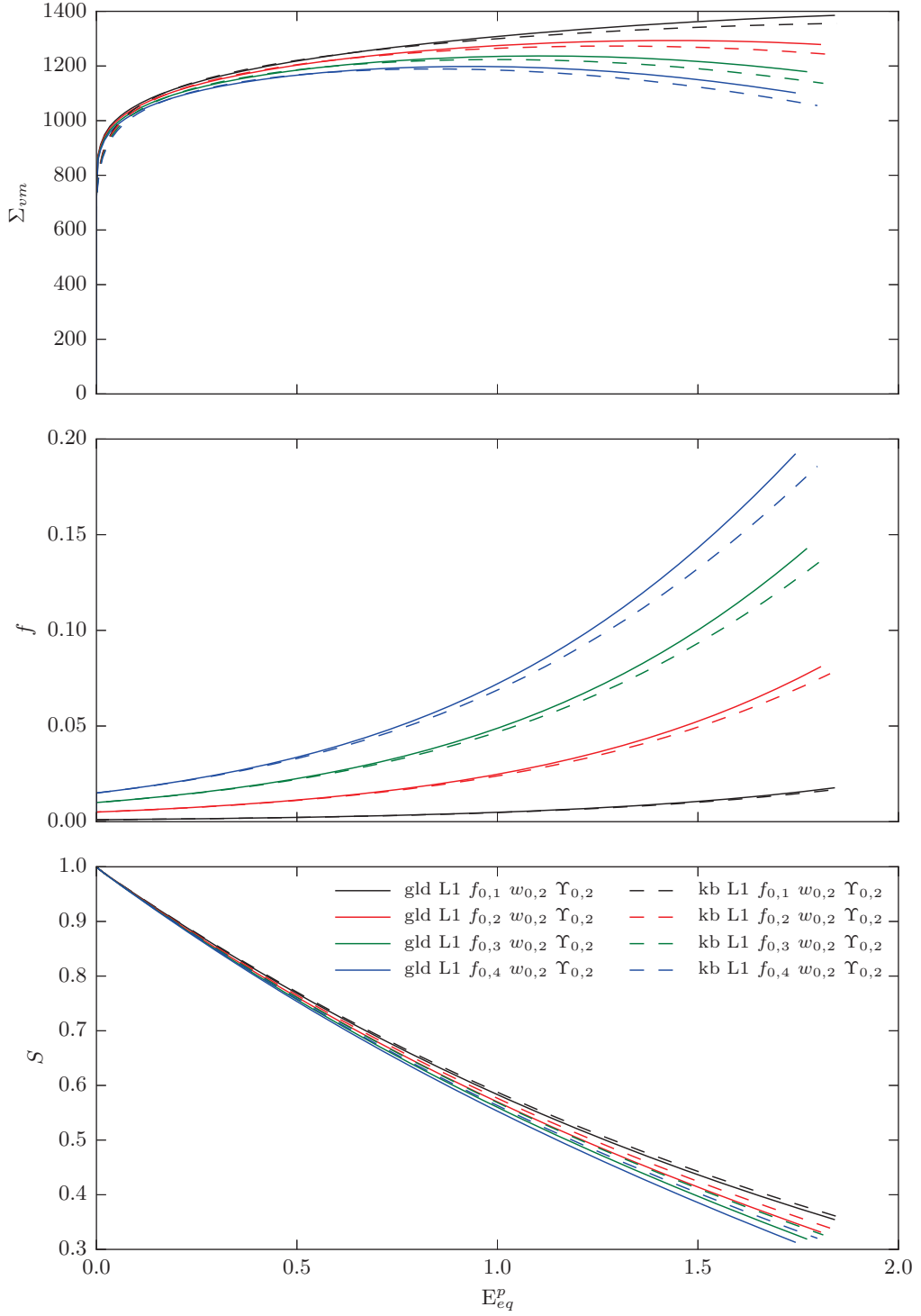


Figure A.6 – Comparison between gld and kb Umats for loading: Tension; direction: Transverse to voids; initial void shape: Prolate

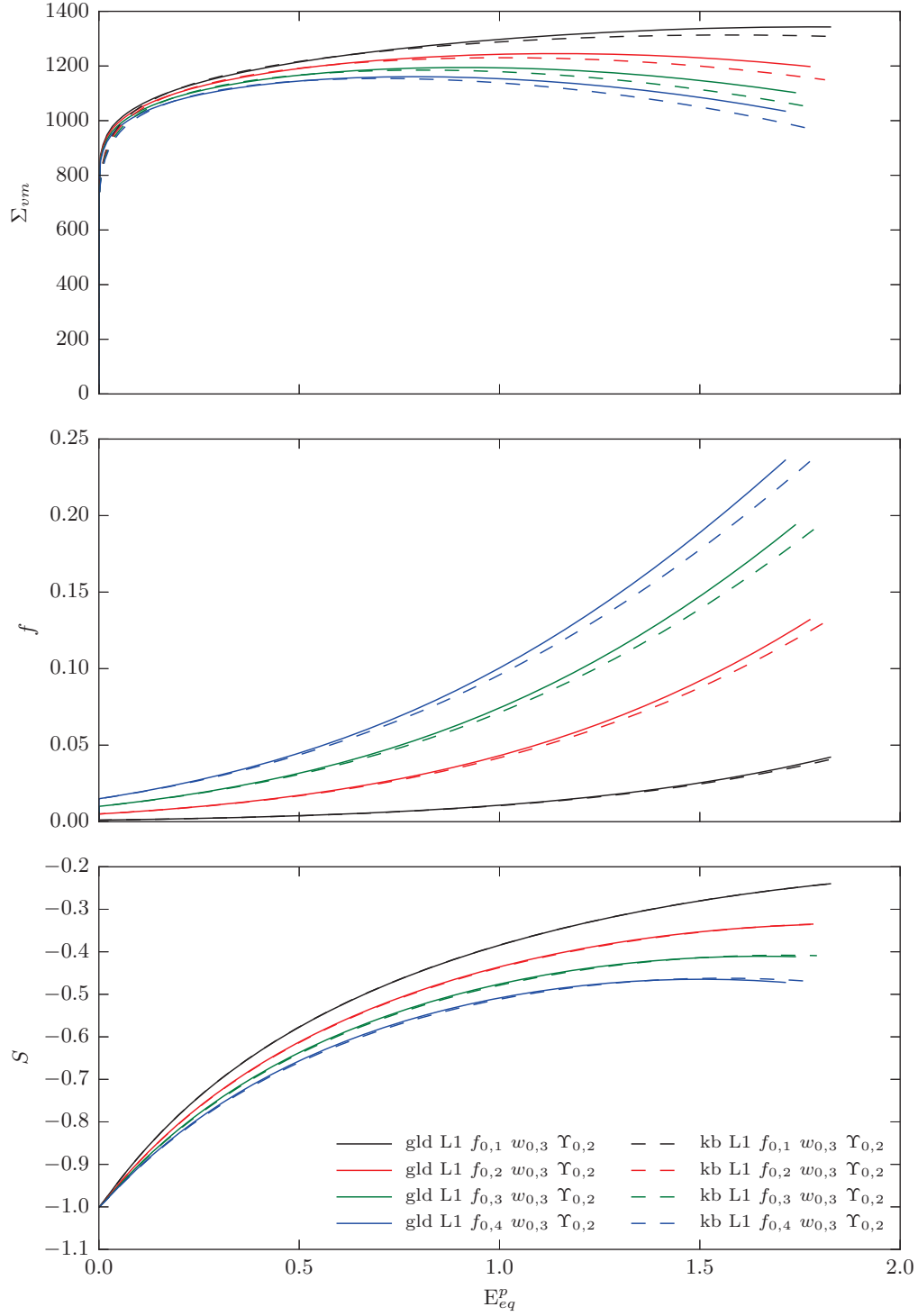


Figure A.7 – Comparison between gld and kb Umats for loading: Tension; direction: Transverse to voids; initial void shape: Oblate



# B Summary of data from metallographic analyses

## B.1 Specimen designation and definitions

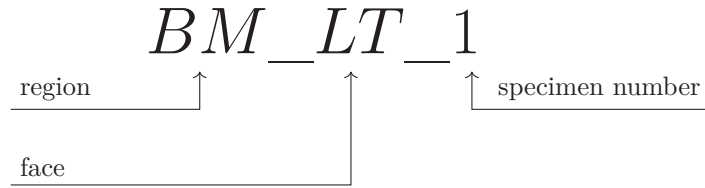


Figure B.1 – Specimen designation for metallographic analyses

Region designations: BM - base material; W - weld material; WT - near weld toe of a loaded tube specimen. For WT cases, unfortunately representative samples near the weld toe were hard to get, leading to sampling away from the weld toe (around 2.5 to 5 mm). This means that the statistics presented herein are closer to the BM than to the actual weld toe.

The following distributions were used:

1. Generalized extreme value (GEV) distribution cumulative distribution function,

$$F(x; \mu_{GEV}, \sigma_{GEV}, \xi_{GEV}) = \exp \left\{ - \left[ 1 + \xi_{GEV} \left( \frac{x - \mu_{GEV}}{\sigma_{GEV}} \right) \right]^{-1/\xi_{GEV}} \right\} \quad (B.1)$$

2. Beta distribution probability density function for  $0 < x < 1$  and shape parameters

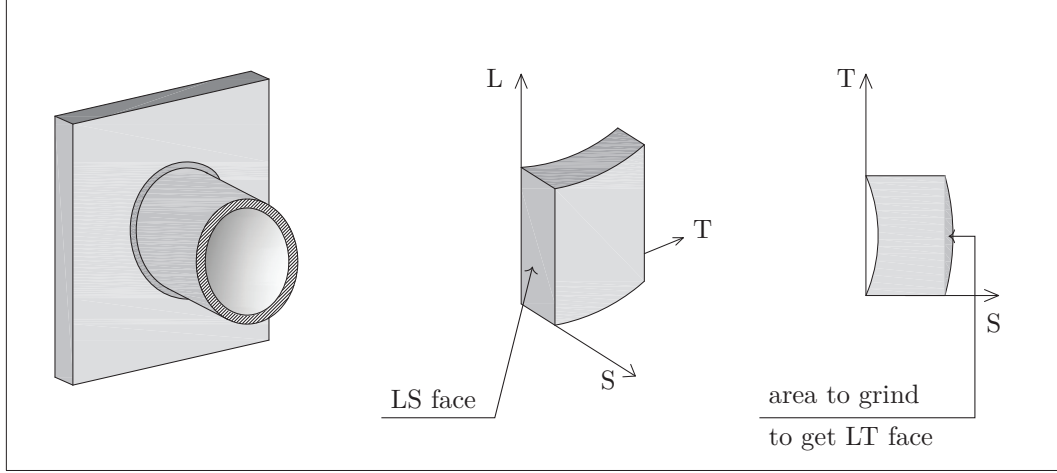


Figure B.2 – Orientation of micrographs *w.r.t.* to tube sample

$\alpha_{be} > 0$  and  $\beta_{be} > 0$ ,

$$f(x; \alpha_{be}, \beta_{be}) = \frac{x^{\alpha_{be}-1} (1-x)^{\beta_{be}-1}}{\int_0^1 u^{\alpha_{be}-1} (1-u)^{\beta_{be}-1} du} \quad (\text{B.2})$$

Nearest neighbor calculations were conducted with SCIPY using a spatial KDTree search, which organizes a set of spatial points according to the closest euclidean distance. Searches were conducted using both circles and ellipses drawn over micrographs.

## B.2 Summary tables



Table B.1 – Chemical Composition of S770QL

	C	Mn	Si	Ni	Cr	Mo	V	Cu	P	S	$C_{eq}^{IIW}$	$C_{eq}^{AWS}$
$101.6 \times 10mm$	0.16%	1.44%	0.39%	0.54%	0.10%	0.37%	0.07%	0.17%	0.012%	0.002%	0.55%	0.61%
$219.1 \times 22.2mm$	0.15%	1.37%	0.25%	0.12%	0.40%	0.45%	0.00%	0.16%	0.012%	0.001%	0.57%	0.61%

Table B.2 – Summary of inclusion statistics

Specimen	# circles	% $A_{circles}$	# ellipses	% $A_{ellipses}$	$\overline{D}_{inc}(\mu m)$	$\overline{L}_{nn}(\mu m)$	$\overline{AR}$	$\overline{\chi}_{inc}$	$f_0^{CAD}$	$f_0^{AIP}$
BM_LT_1	743	76.64	92	23.36	5.50	63.00	0.65	0.15	0.0023	0.0038
BM_LS_1	1229	45.58	682	54.42	3.07	38.43	0.42	0.16	0.0016	0.0026
BM_LT_2	3543	91.46	346	8.54	6.57	36.00	0.52	0.28	0.0080	0.0047
BM_LS_2	1527	57.17	664	42.83	7.01	37.45	0.57	0.29	0.0108	0.0033
BM_LS_3	1068	59.62	190	40.38	4.47	53.89	0.61	0.12	0.0027	0.0026
WT_LT_1	2069	79.88	347	20.12	4.66	31.50	0.54	0.31	0.0038	0.0037
WT_LT_1	3658	94.31	128	5.69	3.30	31.52	0.43	0.17	0.0026	0.0013
WT_LT_2	3188	85.49	375	14.51	5.76	31.50	0.59	0.29	0.0083	0.0036
WT_LS_1	1406	83.86	378	16.14	7.40	41.91	0.57	0.28	0.0096	0.0042

(over line indicates the average measurement)

## Appendix B. Summary of data from metallographic analyses

Table B.3 – Summary of circular inclusions statistics

Specimen	Inclusion diameters ( $D_{inc}$ ) - GEV					
	$Q_{0.05} (\mu m)$	$Q_{0.50} (\mu m)$	$Q_{0.95} (\mu m)$	$\xi_{GEV}$	$\mu_{GEV}$	$\sigma_{GEV}$
BM_LT_1	1.80	4.71	12.02	-0.1676	3.91	2.11
BM_LS_1	1.80	2.84	5.11	-0.0983	2.57	0.74
BM_LT_2	3.46	5.91	11.95	-0.1594	5.24	1.77
BM_LS_2	2.59	5.47	17.11	-0.3894	4.59	2.24
BM_LS_3	1.76	3.89	9.20	-0.1634	3.31	1.54
W_LT_1	2.33	4.16	8.65	-0.1536	3.66	1.32
WT_LT_1	2.02	3.13	5.18	-0.0140	2.85	0.77
WT_LT_2	2.95	5.15	10.58	-0.1576	4.55	1.59
WT_LS_1	2.83	5.30	17.47	-0.4790	4.51	1.97

$Q_x$  stands for quantile  $x$  of the distribution

Table B.4 – Summary of distance to nearest neighbor statistics

Specimen	Distance to nearest neighbor - $L_{nn}$ - GEV					
	$Q_{0.05} (\mu m)$	$Q_{0.50} (\mu m)$	$Q_{0.95} (\mu m)$	$\xi_{GEV}$	$\mu_{GEV}$	$\sigma_{GEV}$
BM_LT_1	13.94	55.89	135.76	-0.0332	45.20	29.01
BM_LS_1	5.57	31.88	93.78	-0.1357	24.79	18.86
BM_LT_2	7.84	31.82	78.04	-0.0392	25.69	16.62
BM_LS_2	6.32	30.38	94.66	-0.1963	23.69	17.60
BM_LS_3	16.14	49.52	106.04	0.0244	41.28	22.60
W_LT_1	4.72	19.40	135.41	-0.6896	14.25	12.37
WT_LT_1	8.18	28.16	66.09	-0.0320	23.07	13.81
WT_LT_2	7.08	28.08	67.16	-0.0222	22.76	14.46
WT_LS_1	5.94	35.27	100.85	-0.1111	27.48	20.85

$Q_x$  stands for quantile  $x$  of the distribution

Table B.5 – Summary of aspect ratios statistics

Specimen	Aspect ratio (AR) - Beta				
	$Q_{0.05}$	$Q_{0.50}$	$Q_{0.95}$	$\alpha_{be}$	$\beta_{be}$
BM_LT_1	0.33	0.66	0.90	4.219	2.308
BM_LS_1	0.17	0.42	0.70	3.519	4.770
BM_LT_2	0.28	0.52	0.76	5.570	5.182
BM_LS_2	0.28	0.57	0.83	4.406	3.363
BM_LS_3	0.37	0.61	0.82	6.989	4.550
W_LT_1	0.25	0.55	0.82	3.921	3.309
WT_LT_1	0.17	0.43	0.72	3.378	4.405
WT_LT_2	0.32	0.60	0.84	5.209	3.570
WT_LS_1	0.27	0.58	0.84	4.013	3.049

$Q_x$  stands for quantile  $x$  of the distribution

## B.2. Summary tables

Table B.6 – Summary of inclusion ligament ratio ( $\chi_{inc}$ ) statistics

Specimen	Inclusion ligament ratio $\chi_{inc}$ - GEV					
	$Q_{0.05} (\mu m)$	$Q_{0.50} (\mu m)$	$Q_{0.95} (\mu m)$	$\xi_{GEV}$	$\mu_{GEV}$	$\sigma_{GEV}$
BM_LT_1	0.03	0.10	0.52	-0.574864	0.072830	0.056501
BM_LS_1	0.04	0.10	0.50	-0.603674	0.077643	0.051500
BM_LT_2	0.08	0.21	0.77	-0.399571	0.169522	0.105326
BM_LS_2	0.06	0.20	0.93	-0.485679	0.157258	0.115961
BM_LS_3	0.03	0.09	0.35	-0.442155	0.069974	0.045710
W_LT_1	0.05	0.21	1.15*	-0.577493	0.155311	0.126154
WT_LT_1	0.05	0.12	0.44	-0.414294	0.102356	0.057191
WT_LT_2	0.08	0.22	0.78	-0.386716	0.175160	0.108744
WT_LS_1	0.06	0.19	0.92	-0.540647	0.143446	0.105816

$Q_x$  stands for quantile  $x$  of the distribution

\* - not physically admissible (GEV isn't bounded, but Beta led to a worst fit in this region)



## C Summary of data from single notched bar tests

This annex presents a summary of the data gathered in the single notched round bar tests. Fig. C.2 presents the designations in describing the geometry of each specimen. Displacement at time  $t$  is defined as the difference between  $h^{SN}(t)$  and  $h^{SN}(t_0)$  and is denoted as  $\delta^{SN}$ . When the designation *FEM* is evoked in this annex it is referring to the model described in chapter 5 and annex A.

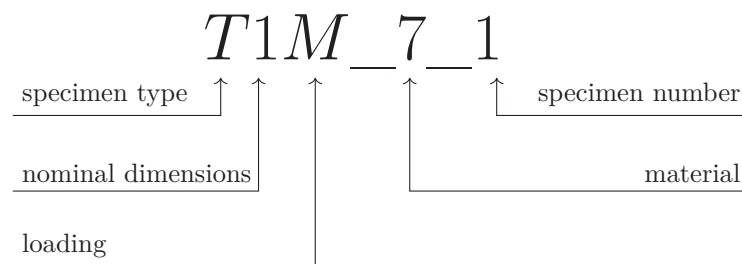


Figure C.1 – Specimen designation for single notched specimens

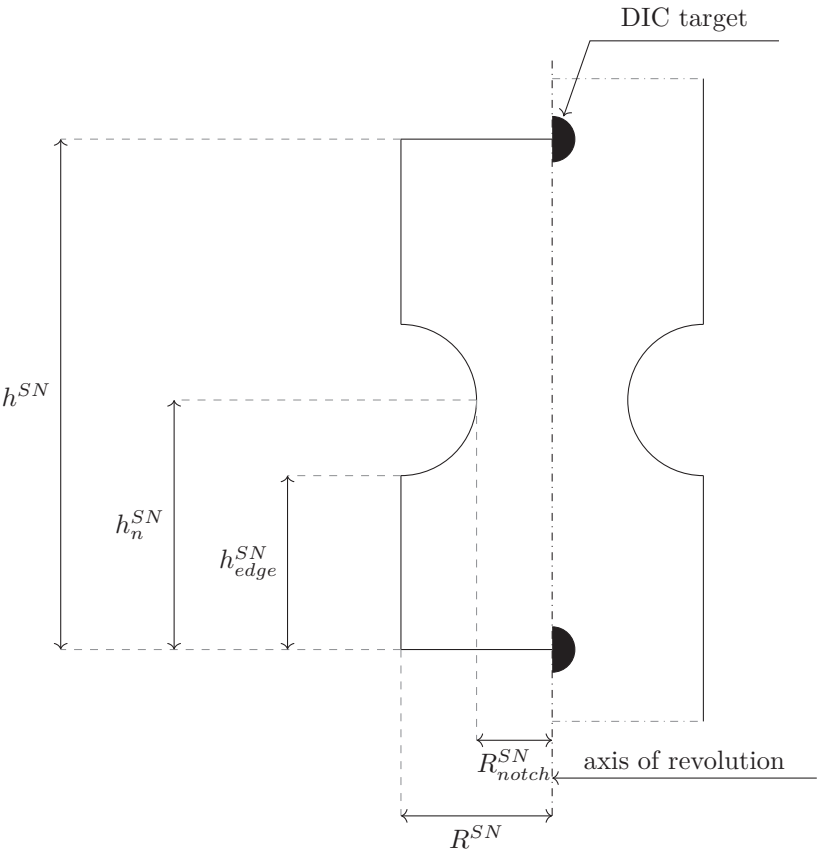


Figure C.2 – Geometry of single notched specimens

Table C.1 – Data summary for monotonic tests

Specimen	$h^{SN}$	$h_{edge}^{SN}$	$h_n^{SN}$	$R^{SN}$	$R_{notch}^{SN}$	$\delta_f^{SN,test}$	$\delta_f^{SN,FEM}$	% difference
T1M_7_1	10.71	3.35	5.05	3.07	1.37	0.608	0.506	16.7
T1M_7_2	9.84	3.19	4.82	3.03	1.40	0.554	0.479	13.5
T1M_7_3	15.29	5.78	7.37	3.05	1.33	0.519	0.482	7.1
T2M_7_1	10.70	3.76	5.83	3.09	1.02	0.561	0.580	3.6
T2M_7_2	11.52	4.10	6.18	3.12	1.04	0.598	0.595	0.5
T2M_7_3	11.67	3.96	6.07	3.10	1.01	0.655	0.608	7.1

$f_0 = 1e - 3, w_0 = 1.0, \chi_0 = 0.25$ ; all dimensions in  $mm$

Table C.2 – Data summary for cyclic tests

Specimen	$h^{SN}$	$h_{edge}^{SN}$	$h_n^{SN}$	$R^{SN}$	$R_{notch}^{SN}$	$\Delta\delta^{SN,test}$	$H_c^{FEM}$	$H_c^{test}$
T1CA1_7_1	8.13	2.64	4.23	3.02	1.53	0.35	9	11
T1CA2_7_1	7.29	1.92	3.49	3.05	1.43	0.41	5	7
T1CA2_7_2	7.65	2.00	3.64	3.09	1.36	0.48	3	5
T2CA1_7_1	8.93	2.17	4.39	3.14	1.02	0.24	19	21
T2CA1_7_2	8.60	2.25	4.28	2.99	1.02	0.20	27	29
T2CA1_7_3	8.45	2.15	4.34	3.13	1.02	0.22	23	31
T2CA2_7_1	8.29	1.99	4.17	3.08	1.02	0.44	7	9
T2CA2_7_2	8.75	2.26	4.36	3.06	1.03	0.39	9	11

$f_0 = 1e - 3, w_0 = 1.0, \chi_0 = 0.25, \varrho = 1.125$ ; all dimensions in  $mm$

$H_c$  stands for half cycle to failure

C.1 SEM micrographs

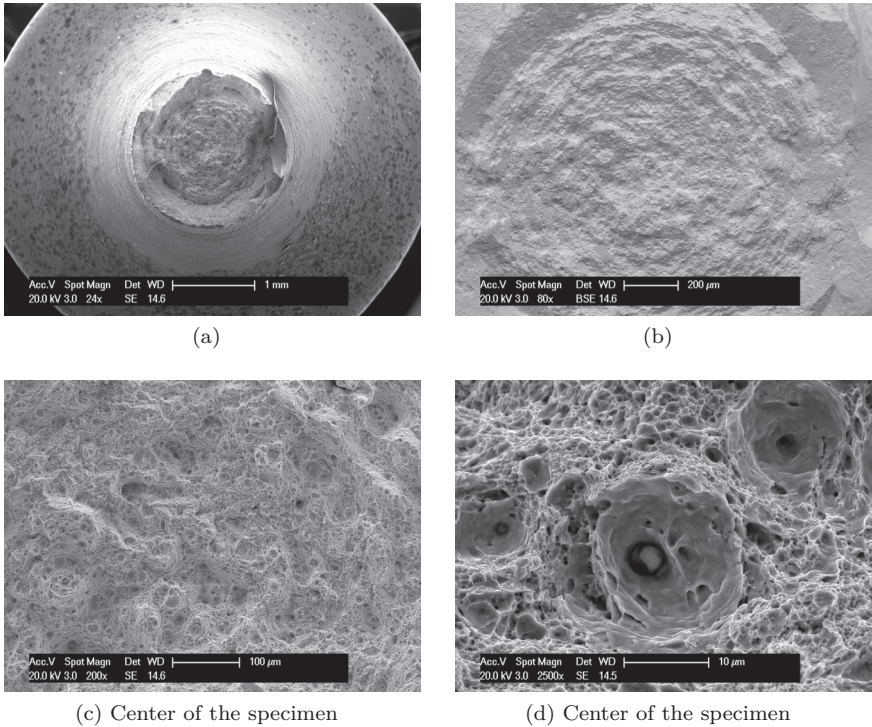


Figure C.3 – SEM micrographs of fracture surface for specimen T1M\_7\_1



### C.1. SEM micrographs

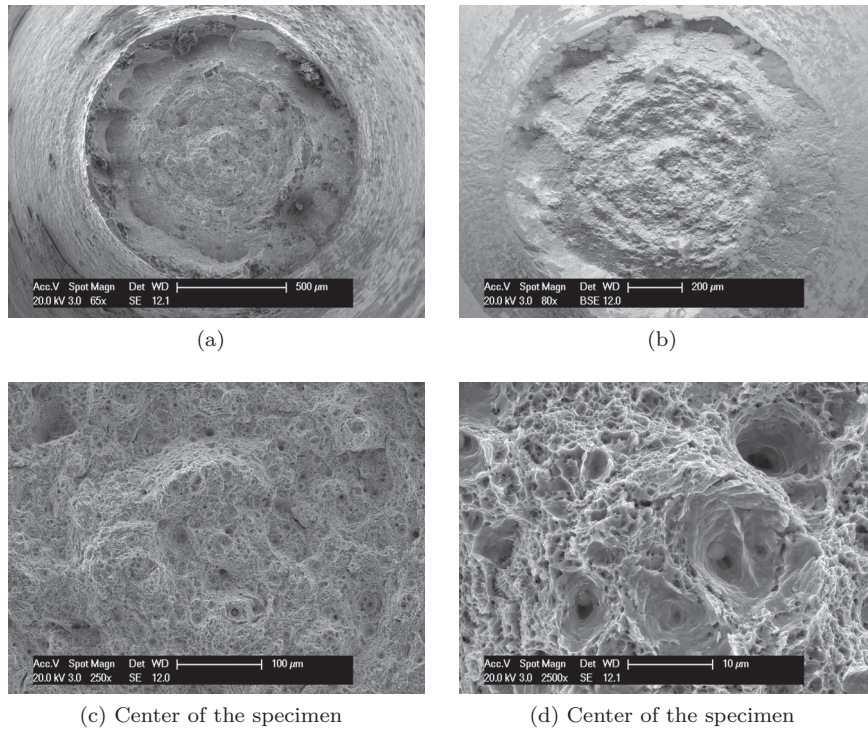


Figure C.4 – SEM micrographs of fracture surface for specimen T2M\_7\_3

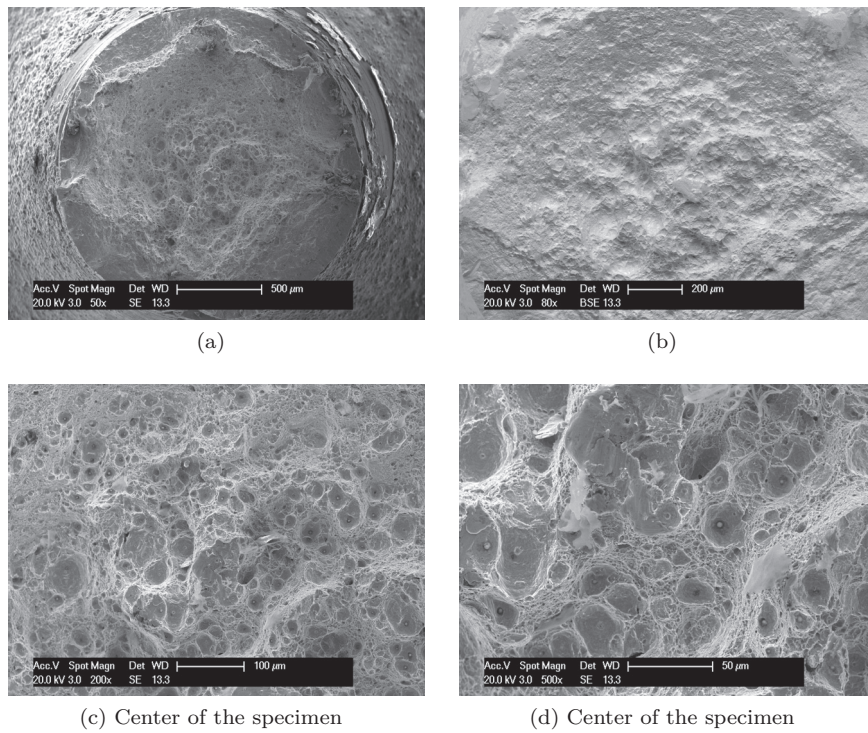


Figure C.5 – SEM micrographs of fracture surface for specimen T2CA1\_7\_2

Appendix C. Summary of data from single notched bar tests

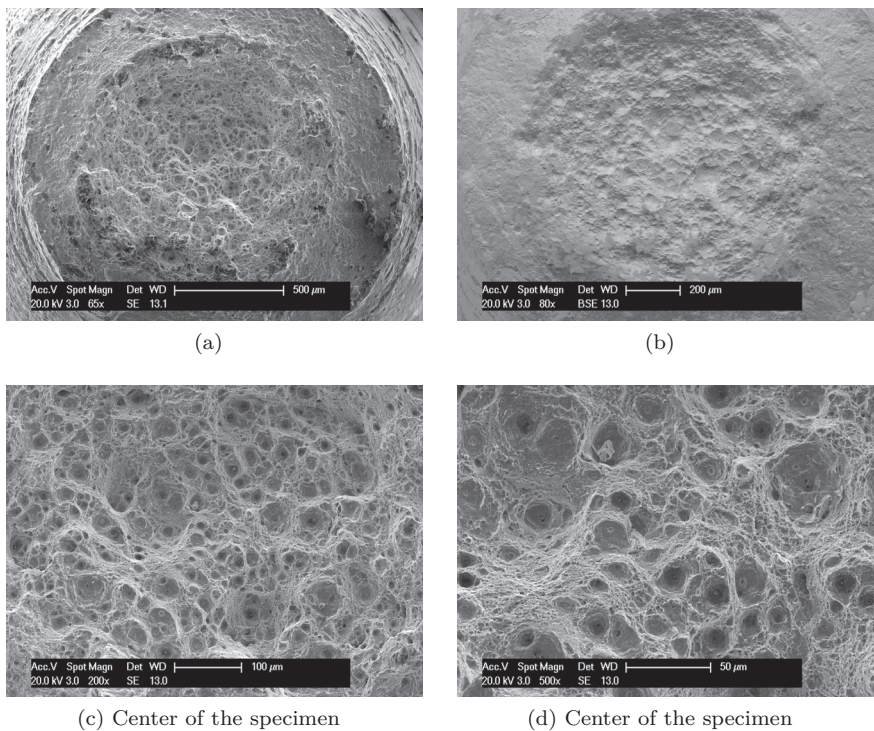


Figure C.6 – SEM micrographs of fracture surface for specimen T2CA2\_7\_2

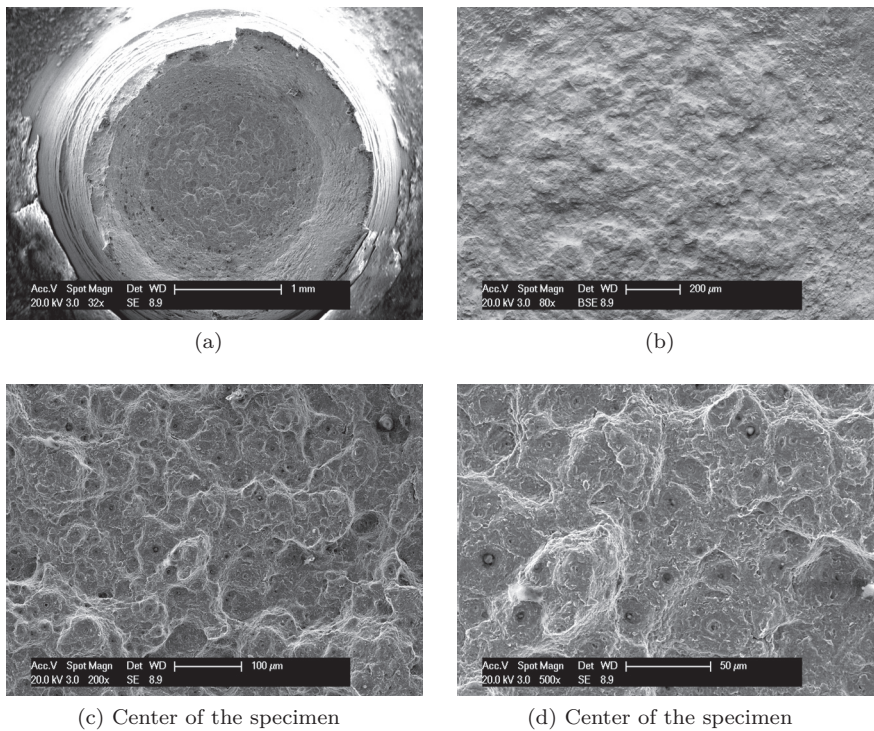


Figure C.7 – SEM micrographs of fracture surface for specimen T1CA1\_7\_1



# D Summary of data from double notched tube tests

## D.1 Fracture surfaces

### D.1.1 Monotonic

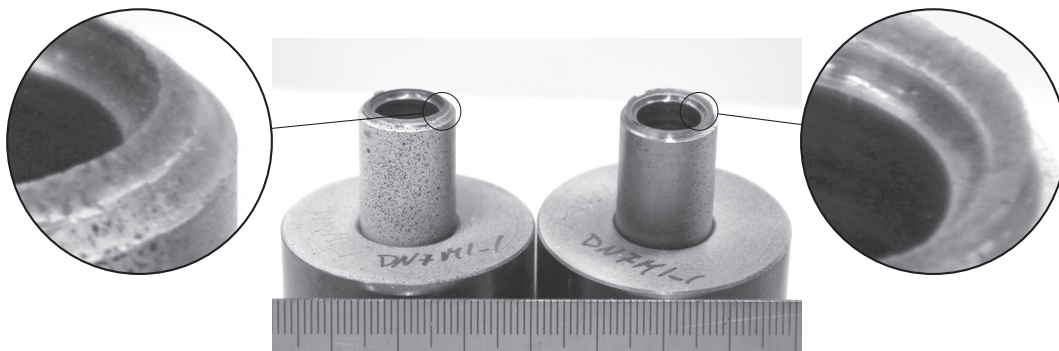


Figure D.1 – Slant fracture in monotonic pure tension (path 1) double notched specimens

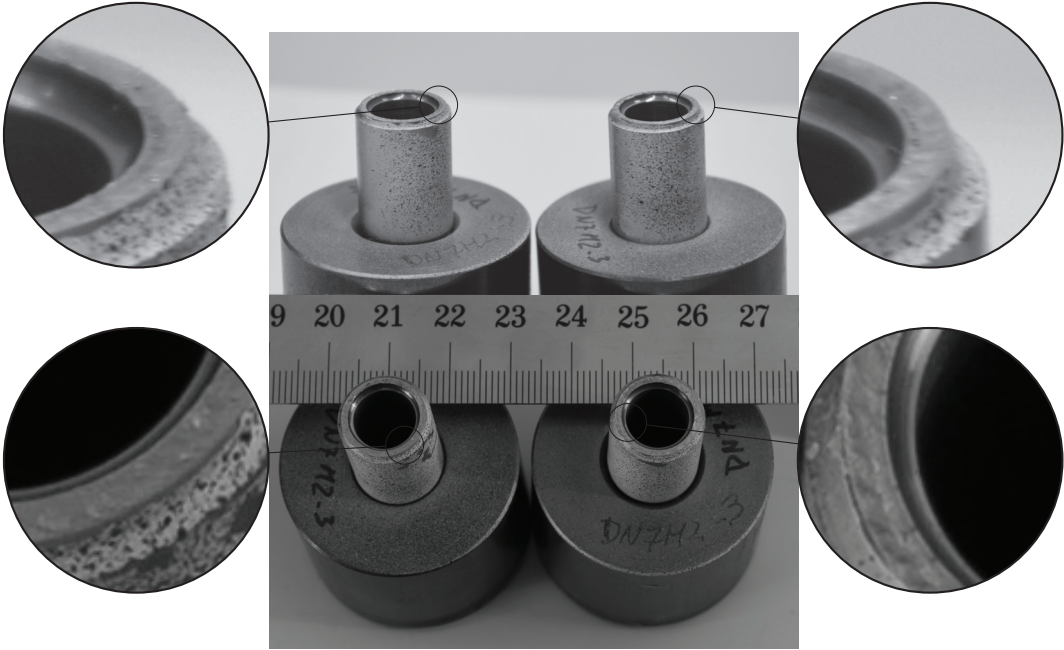


Figure D.2 – Slant fracture in monotonic pure torsion (path 2) double notched specimens

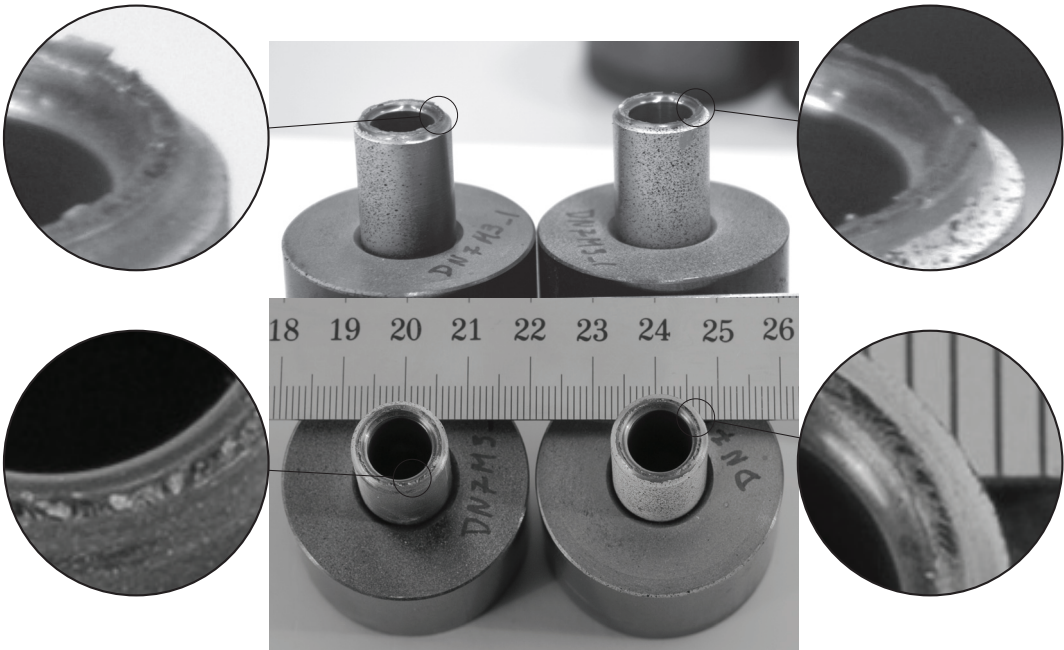


Figure D.3 – Fracture surface in monotonic for load path 3 in double notched specimens

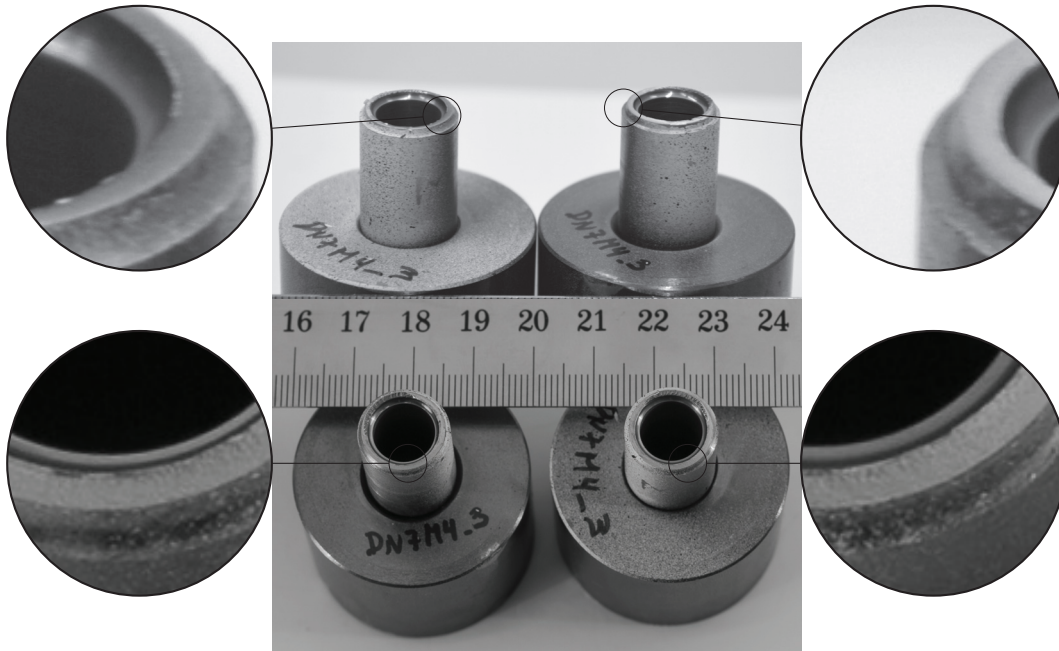


Figure D.4 – Fracture surface in monotonic for load path 4 in double notched specimens

D.1.2 Large amplitude cyclic loading

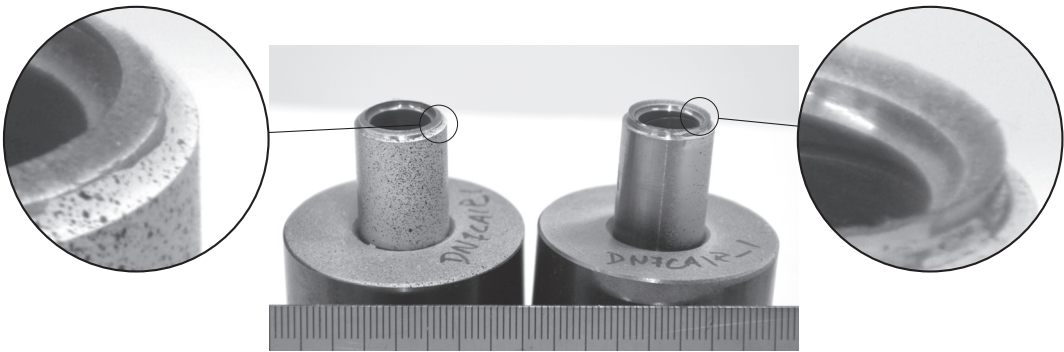


Figure D.5 – Slant fracture in cyclic pure tension (path 1) double notched specimens

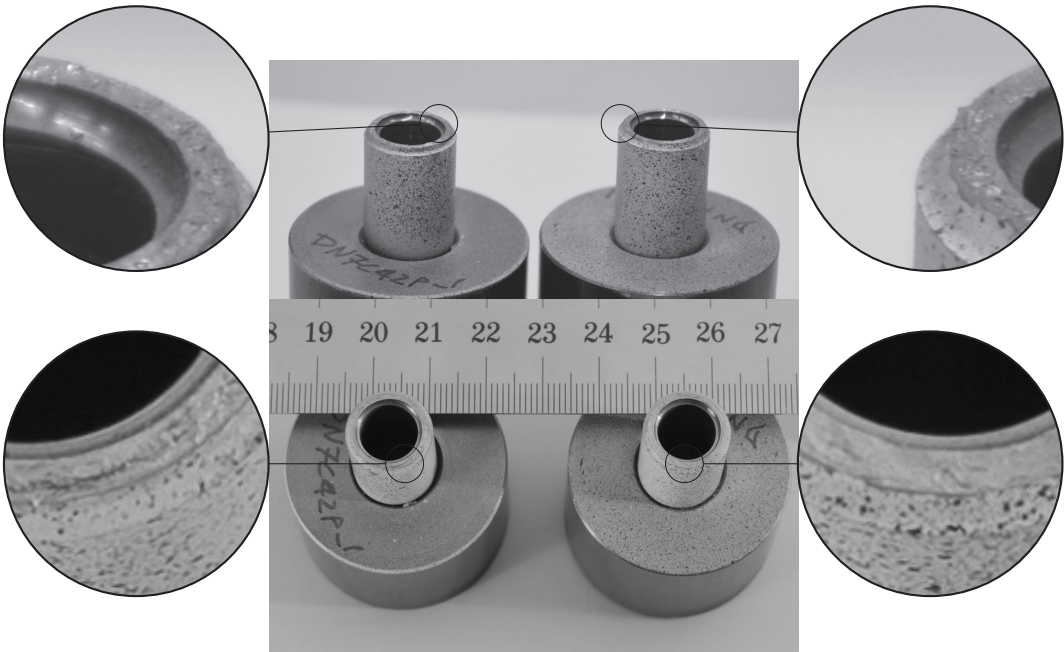


Figure D.6 – Fracture surface in cyclic for load path 2 in double notched specimens



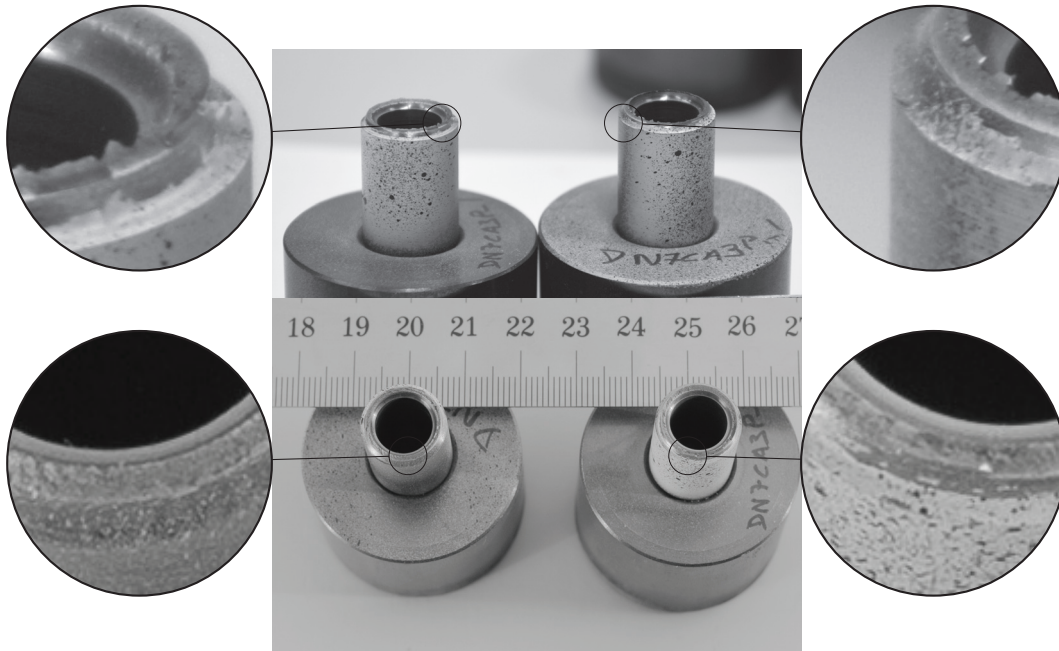


Figure D.7 – Fracture surface in cyclic for load path 3 in double notched specimens

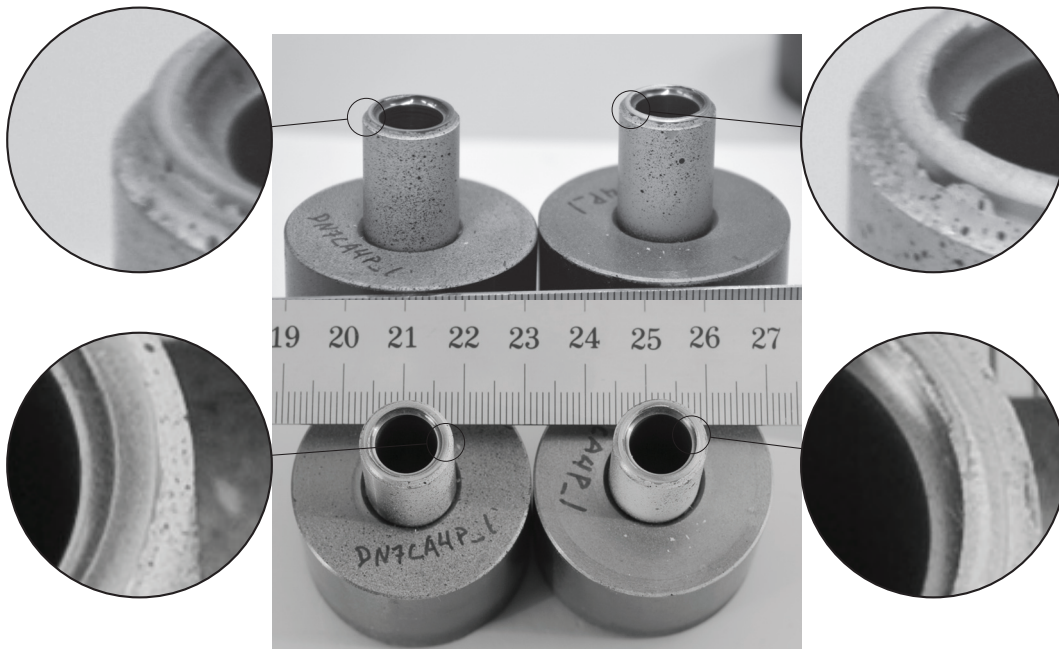


Figure D.8 – Fracture surface in cyclic for load path 4 in double notched specimens

## D.2 SEM micrographs

### D.2.1 Monotonic loading

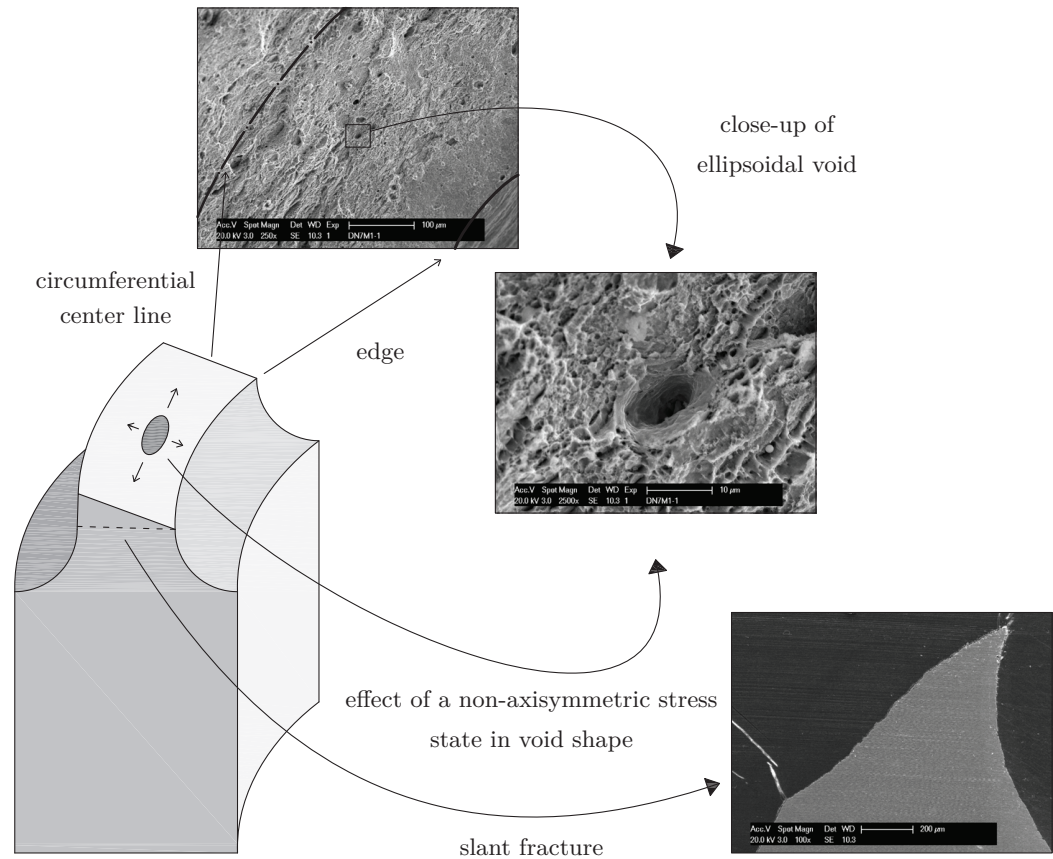


Figure D.9 – Fractography of a double notched specimen loaded in monotonic pure tension - *DN7M1\_1*



## D.2. SEM micrographs

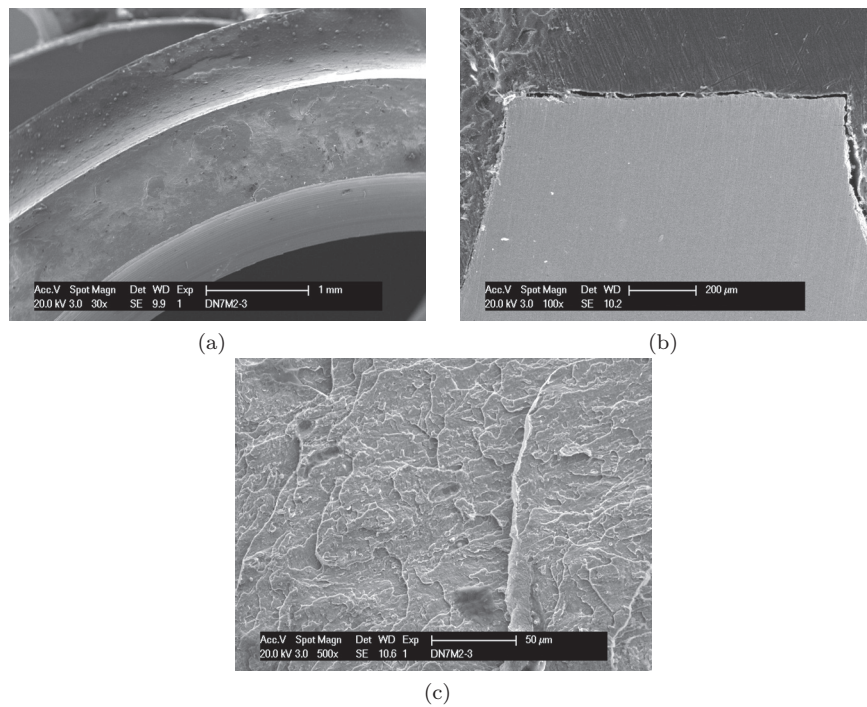


Figure D.10 – SEM micrographs of fracture surface for specimen DN7M2\_3

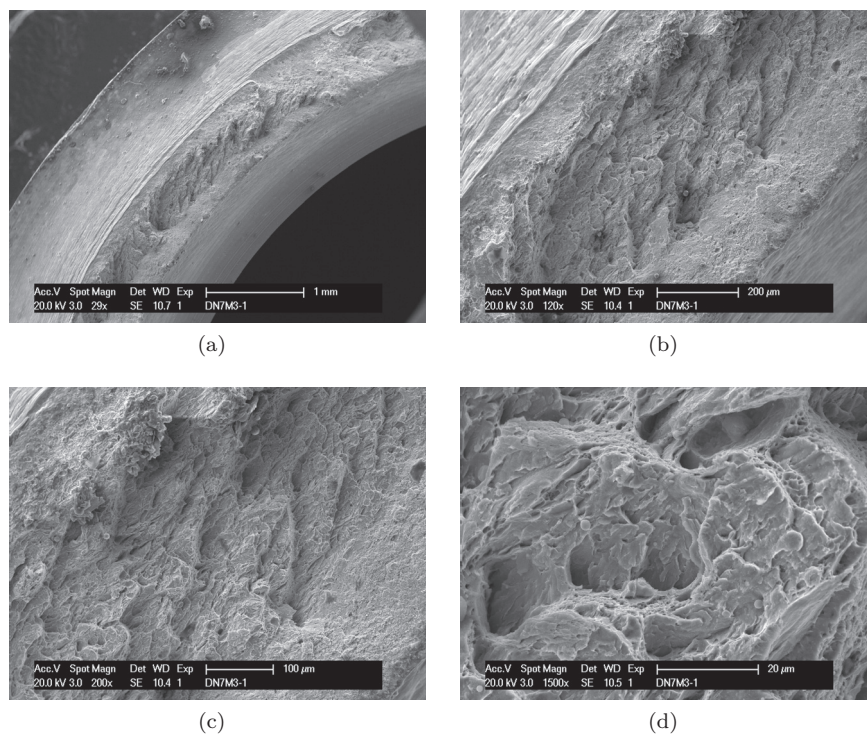


Figure D.11 – SEM micrographs of fracture surface for specimen DN7M3\_1

Appendix D. Summary of data from double notched tube tests

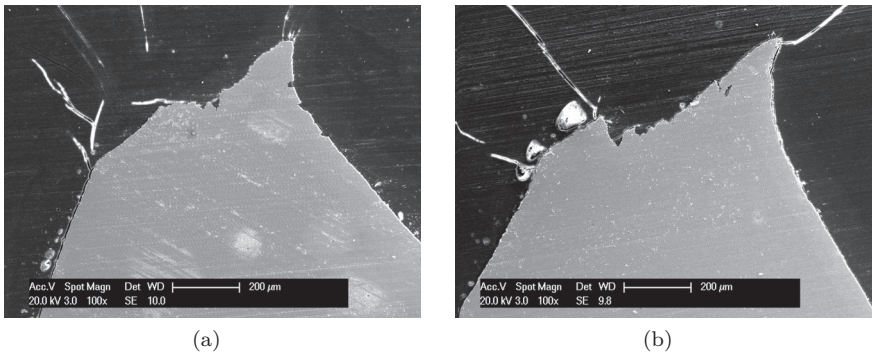


Figure D.12 – SEM micrographs of fracture surface through cross section for specimen DN7M3\_1

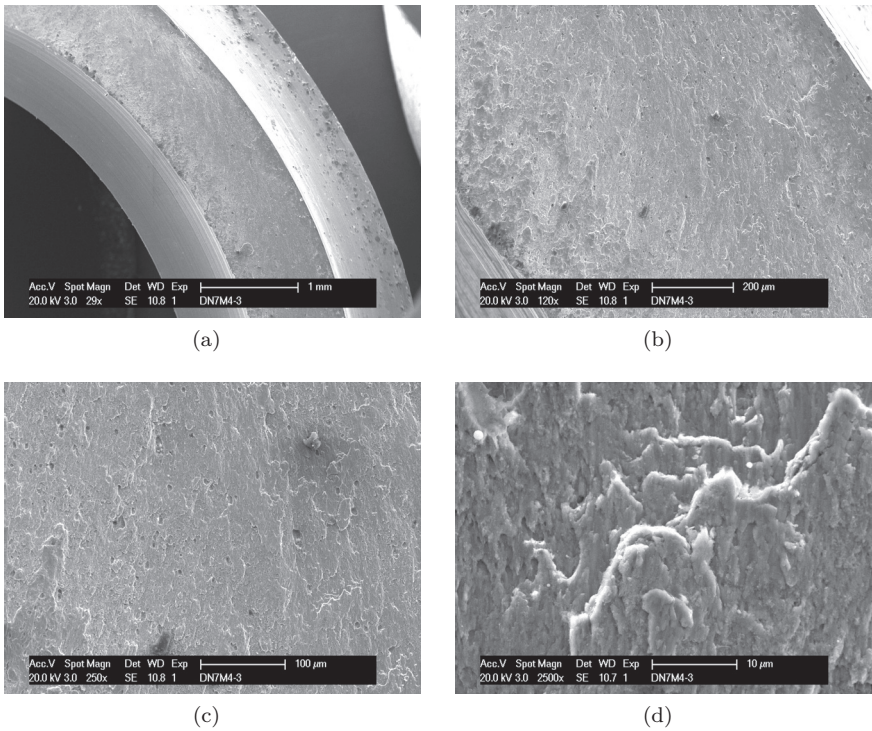


Figure D.13 – SEM micrographs of fracture surface for specimen DN7M4\_3

## D.2. SEM micrographs

---

### D.2.2 Large amplitude cyclic loading

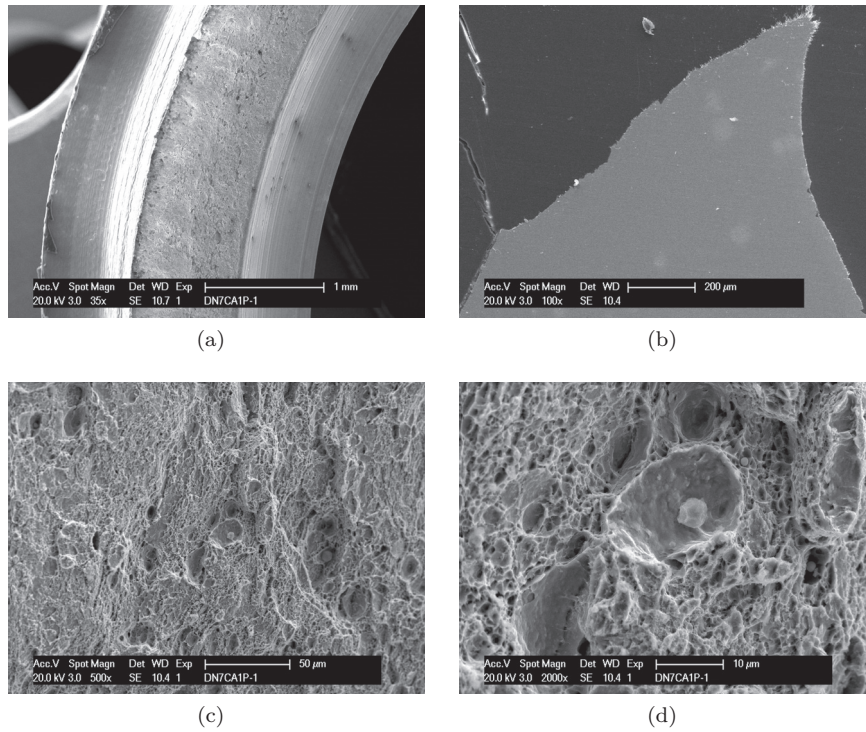


Figure D.14 – SEM micrographs of fracture surface for specimen DN7CA1\_1



Appendix D. Summary of data from double notched tube tests

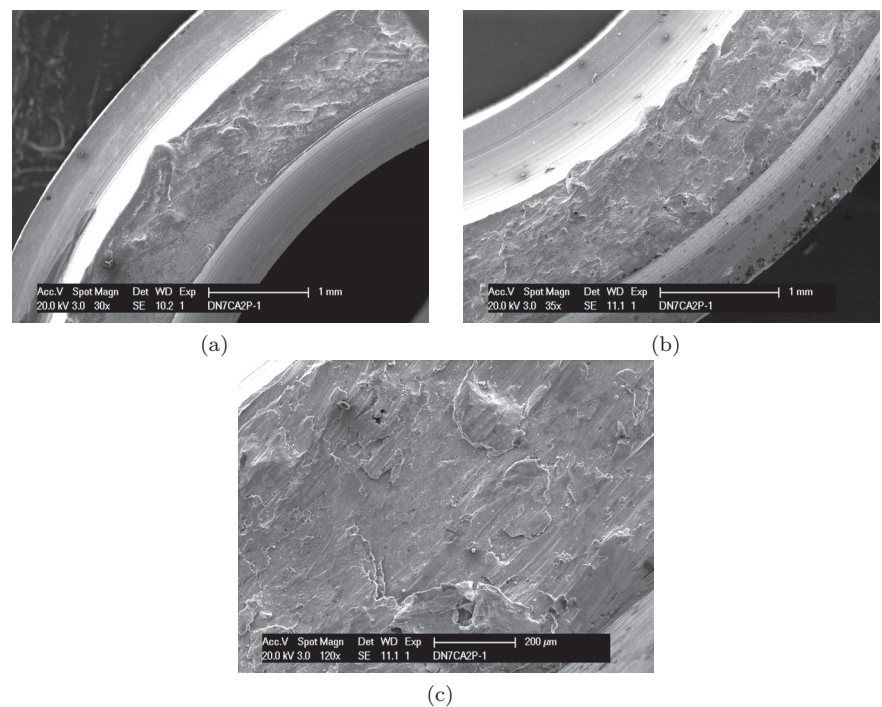


Figure D.15 – SEM micrographs of fracture surface for specimen DN7CA2\_1

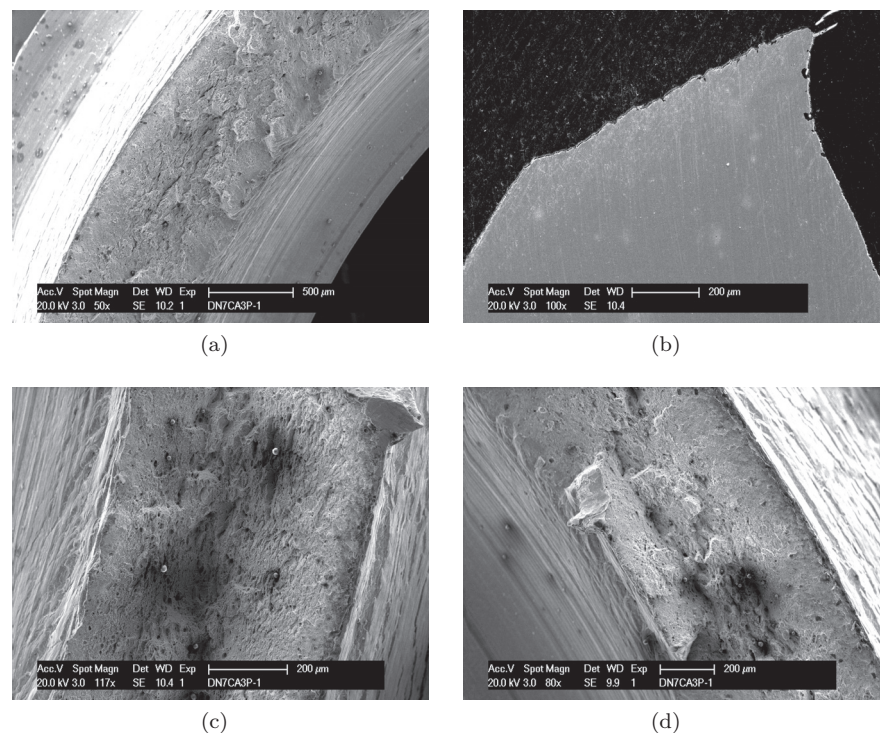


Figure D.16 – SEM micrographs of fracture surface for specimen DN7CA3\_1

## D.2. SEM micrographs

---

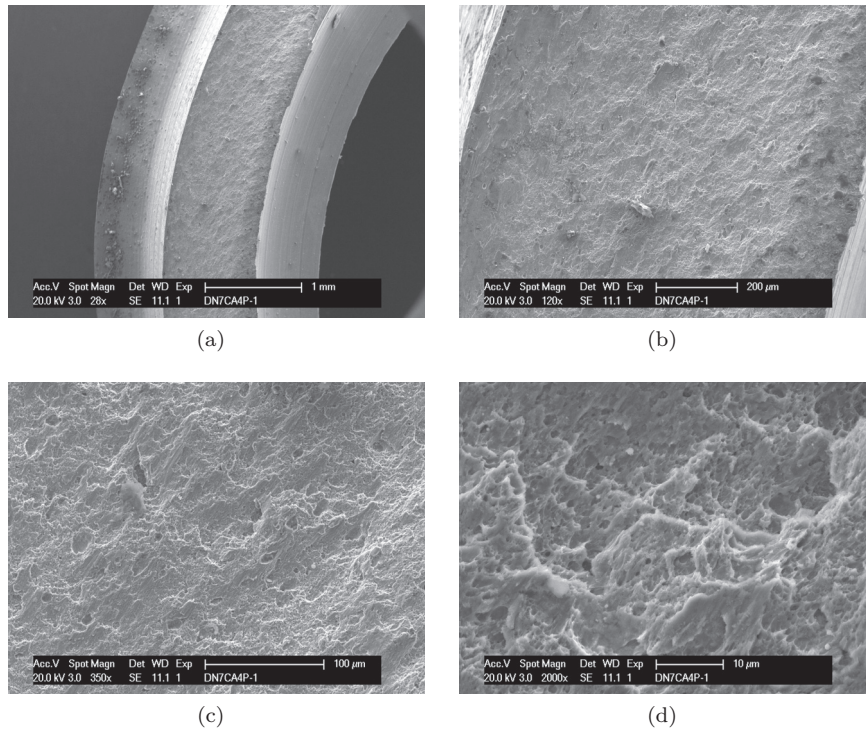


Figure D.17 – SEM micrographs of fracture surface for specimen DN7CA4\_1



## E Summary of data from tube to plate tests

This annex provides a summary of each tube to plate test.

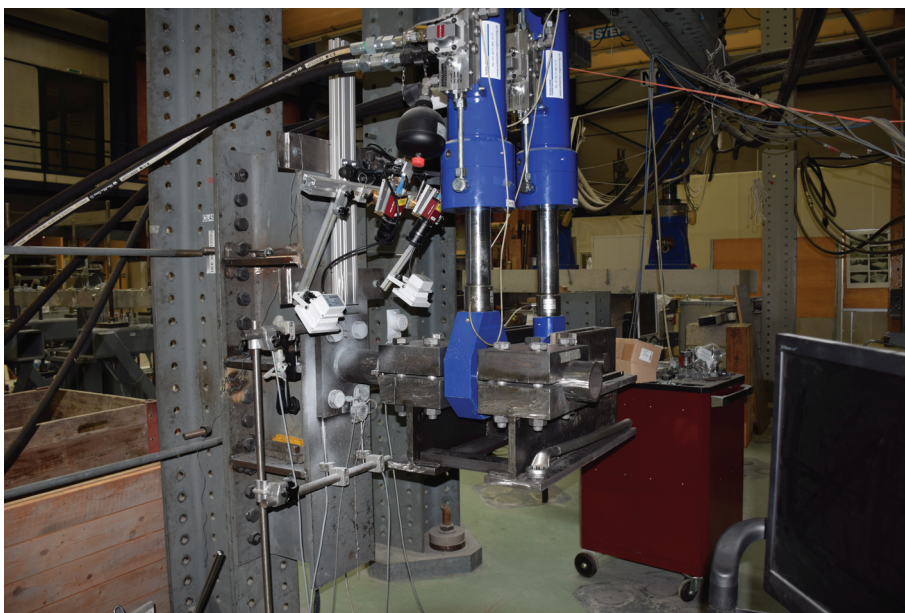


Figure E.1 – Photograph of tube-to-plate test setup





Table E.1 – Summary of tube to plate constant amplitude test results

#	Specimen	$\bar{\Delta}\delta$	$\bar{\Delta}\theta$	$\bar{\Delta}\varepsilon_{xx}$	$\bar{\Delta}\varepsilon_{xy}$	$\bar{\Delta}\varepsilon_{yy}$	$\bar{\Delta}\varepsilon_{eq}^*$	$\bar{\Delta}\varepsilon_{eq, FEM}^*$	$N_{init}$	$N_f$	$N_{ave}$	FZ→DIC	Paint Ok?	$a$	$\psi$
0	A7CA1_1	0.00	5.48	0.00	11.11	0.00	13.78	-	9	9	9	No	Yes	3.94	19.52
1	A7CA1_2	0.00	5.25	2.10	11.90	2.60	14.33	-	13	13	9	No	Yes	4.14	20.18
2	A7CA1_3	0.00	5.49	0.85	11.07	2.46	14.01	13.22	4	9	4	Yes	Yes	4.45	20.54
3	A7CA1_4	0.00	5.47	1.10	11.96	3.91	15.22	-	5	5	3	No	Yes	4.06	21.57
4	A7CA1_5	0.00	5.52	0.44	12.23	1.24	14.67	-	11	16	2	Yes	Yes	4.44	28.47
5	A7CA2_1	0.00	4.20	1.10	5.77	1.18	6.71	-	21	35	21	Yes	Yes	2.79	33.13
6	A7CA2_2	0.00	4.24	1.38	3.61	2.01	5.29	5.77	32	35	29	Yes	Yes	3.02	14.23
-	A7CA2_3	0.00	3.97	0.00	2.08	0.00	2.57	-	18	30	6	Yes	No quality	3.71	19.58
-	A7CA2_4	0.00	3.97	0.00	7.10	1.15	8.35	-	22	31	1	No	No quality	3.91	18.80
7	A7CA3_1	0.00	8.15	0.00	17.77	1.58	20.92	-	5	5	4	No	Yes	4.37	21.18
8	B7CA1_2	38.22	0.00	0.00	0.00	12.78	14.74	-	4	10	5	No	Yes	4.32	18.73
9	B7CA1_3	35.79	0.00	0.00	0.00	14.17	16.34	16.24	5	8	5	No	Yes	4.44	21.26
10	B7CA1_4	38.37	0.00	0.00	0.00	12.46	14.28	-	4	9	5	No	Yes	3.33	18.55
11	B7CA1_5	38.37	0.00	0.00	0.00	14.36	15.82	-	3	9	3	No	Yes	3.74	18.32
12	B7CA2_1	32.92	0.00	0.00	0.00	6.37	7.50	-	15	32	11	Yes	Yes	3.78	18.17
13	B7CA2_2	33.82	0.00	0.00	0.00	9.46	10.91	-	10	16	12	No	Yes	4.19	18.52
14	B7CA2_3	33.94	0.00	0.00	0.80	8.20	9.56	-	6	17	8	No	Yes	3.57	18.72
15	B7CA2_4	33.54	0.00	0.00	0.00	11.51	13.47	-	5	11	7	No	Yes	4.45	25.25
16	C7CA1_1	36.25	4.58	1.48	8.57	17.26	23.12	20.29	2	6	3	No	Yes	4.46	19.46
17	C7CA1_2	35.58	4.08	0.00	2.50	12.66	14.99	-	4	12	3	No	Yes	3.37	16.07

$\delta$  - mm ;  $\theta$  - Deg ;  $\varepsilon$  - % ;  $a$  - mm ;  $\psi$  - Deg; Continued on next page

# Appendix E. Summary of data from tube to plate tests

#	Specimen	$\bar{\Delta}\delta$	$\bar{\Delta}\theta$	$\bar{\Delta}\varepsilon_{xx}$	$\bar{\Delta}\varepsilon_{xy}$	$\bar{\Delta}\varepsilon_{yy}$	$\bar{\Delta}\varepsilon_{eq}^*$	$\bar{\Delta}\varepsilon_{eq,FEM}^*$	$N_{init}$	$N_f$	$N_{ave}$	FZ→DIC	Paint Ok?	$a$	$\psi$
18	C7CA1_3	35.45	4.10	0.00	5.06	16.04	19.48	-	2	7	1	Yes	Yes	3.96	18.58
19	C7CA1_4	36.57	4.05	0.00	8.40	23.83	29.76	-	2	5	2	Yes	Yes	5.25	29.22
20	C7CA2_1	31.00	3.56	0.00	4.86	12.64	16.06	-	3	14	3	No	Yes	4.42	22.50
21	C7CA2_3	31.07	3.56	0.00	5.67	7.76	11.59	-	4	14	4	Yes	Yes	4.77	34.96
22	C7CA2_4	30.99	3.56	0.00	3.46	12.10	14.35	-	3	13	4	Yes	Yes	3.69	17.73
23	C7CA2_6	31.37	3.54	0.00	3.70	12.11	14.52	-	3	13	2	No	Yes	3.04	15.33
24	D7CA1_2	31.87	5.59	0.00	13.88	19.70	28.55	21.33	2	6	3	Yes	Yes	4.15	22.75
25	D7CA1_4	31.98	5.57	0.00	6.51	17.17	20.91	-	2	6	2	Yes	Yes	3.54	18.10
26	D7CA1_5	31.79	5.58	0.00	8.66	18.09	22.46	-	2	5	1	Yes	Yes	4.91	23.45
27	D7CA3_1	26.24	4.55	0.00	8.34	16.44	20.90	-	3	9	2	Yes	Yes	3.94	19.11
28	D7CA2_1	23.47	4.08	0.00	6.56	17.10	21.32	-	2	10	2	Yes	Yes	4.22	24.72
29	D7CA2_2	23.35	4.02	0.00	4.17	7.21	9.69	-	6	16	6	No	Yes	3.79	16.89
30	D7CA2_3	23.47	4.02	0.00	5.84	7.67	11.40	-	3	19	6	No	Yes	4.11	19.18
31	D7CA2_4	23.55	4.03	0.00	3.78	8.78	11.08	-	1	17	4	No	Yes	3.40	18.19
32	C7CA3_1	25.23	2.81	0.06	2.53	8.23	10.01	-	5	19	5	No	Yes	4.38	23.16
33	C7CA3_2	21.50	2.39	0.08	0.99	4.55	5.33	4.30	11	74	10	Yes	Yes	4.37	22.59
34	F7CA1_1	14.39	4.82	0.92	4.89	6.21	8.80	11.09	9	18	9	No	Yes	3.58	19.87
35	F7CA1_2	13.77	4.61	0.07	4.86	7.46	9.53	-	6	25	6	No	Yes	3.82	21.98
36	F7CA2_1	9.75	3.30	0.54	3.81	4.37	6.27	-	4	66	4	Yes	Yes	4.23	21.18
37	F7CA2_2	10.67	3.60	0.10	3.96	4.24	5.86	5.56	15	24	12	Yes	Yes	4.50	22.18
38	F7CA2_3	9.73	3.31	0.28	2.96	4.48	5.87	-	7	25	6	No	Yes	4.20	24.18
39	E7CA1_2	36.97	4.04	0.33	3.27	17.66	20.67	-	2	4	2	Yes	Yes	3.97	20.45

$\delta$  - mm ;  $\theta$  - Deg ;  $\varepsilon$  - % ;  $a$  - mm ;  $\psi$  - Deg; Continued on next page

#	Specimen	$\bar{\Delta}\delta$	$\bar{\Delta}\theta$	$\bar{\Delta}\varepsilon_{xx}$	$\bar{\Delta}\varepsilon_{xy}$	$\bar{\Delta}\varepsilon_{yy}$	$\bar{\Delta}\varepsilon_{eq}^*$	$\bar{\Delta}\varepsilon_{eq,FEM}^*$	$N_{init}$	$N_f$	$N_{ave}$	FZ→DIC	Paint Ok?	$a$	$\psi$
40	E7CA1_3	37.06	4.03	0.61	4.15	12.10	15.18	-	2	4	2	Yes	Yes	4.02	21.40
41	E7CA1_4	37.10	4.05	0.39	1.90	10.35	10.66	-	7	7	4	No	Yes	3.66	18.94
42	E7CA1_5	37.02	4.06	0.18	4.95	14.69	17.91	-	3	5	2	Yes	Yes	4.04	20.45
43	E7CA2_1	32.62	3.54	0.15	3.11	10.27	12.56	-	2	9	4	Yes	Yes	3.08	18.22
-	E7CA2_2	32.60	3.56	0.06	3.01	15.65	18.67	-	2	9	2	Yes	No quality	4.66	23.78
44	E7CA2_3	32.53	3.56	1.15	4.06	10.77	12.96	-	2	9	2	Yes	Yes	4.82	15.12
45	E7CA2_4	32.55	3.57	0.36	4.15	11.89	14.75	-	2	6	2	Yes	Yes	3.37	19.88

$\delta$  - mm ;  $\theta$  - Deg ;  $\varepsilon$  - % ;  $a$  - mm ;  $\psi$  - Deg

Table E.2 – Summary of tube to plate variable amplitude test results - part 1

#	Specimen	$\bar{\Delta}\delta_1$	$\bar{\Delta}\theta_1$	$\bar{\Delta}\delta_2$	$\bar{\Delta}\theta_2$	$\bar{\Delta}\varepsilon_{xx,1}$	$\bar{\Delta}\varepsilon_{xy,1}$	$\bar{\Delta}\varepsilon_{yy,1}$	$\bar{\Delta}\varepsilon_{xx,2}$	$\bar{\Delta}\varepsilon_{xy,2}$	$\bar{\Delta}\varepsilon_{yy,2}$	$\bar{\Delta}\varepsilon_{eq,1}^*$	$\bar{\Delta}\varepsilon_{eq,2}^*$	$\bar{\Delta}\varepsilon_{eq,1/2,FEM}^*$
46	A7VA1_1	0	5.57	0	4.46	0	12.74	1.26	0	7.98	0.96	14.91	9.41	-
47	A7VA1_2	0	5.56	0	4.05	0	10.22	1.2	0	4.88	0.46	12.18	5.98	11.56
48	A7VA1_3	0	5.48	0	4.06	1.55	12.29	1.83	1	7.14	1.54	14.62	8.49	-
49	A7VA2_1	0	5.56	0	4.06	0.98	7.22	1.2	0.49	3.67	0.7	8.51	4.32	-
50	A7VA2_2	0	5.55	0	4.05	1.03	13.31	2.23	0.6	6.78	1.24	15.71	8.12	-
-	A7VA2_3	0	5.56	0	4.05	-	-	-	-	-	-	-	-	-
51	B7VA1_1	32.89	0.00	29.36	0.00	0	0	6.14	0	0	4.4	7.08	5.06	-
52	B7VA1_2	32.79	0.00	29.48	0.00	0	0	12.68	0	0	9.08	14.75	10.6	-
53	B7VA1_3	33.08	0.00	29.39	0.00	0	0	9.75	0	0	6.89	11.24	7.97	-
54	B7VA2_1	32.96	0.00	29.37	0.00	0	0	11.31	0	0	6.89	13.1	9.65	-

$\delta$  - mm ;  $\theta$  - Deg ;  $\varepsilon$  - % ; Continued on next page

Appendix E. Summary of data from tube to plate tests

#	Specimen	$\Delta\delta_1$	$\Delta\theta_1$	$\Delta\delta_2$	$\Delta\theta_2$	$\Delta\epsilon_{xx,1}$	$\Delta\epsilon_{xy,1}$	$\Delta\epsilon_{yy,1}$	$\Delta\epsilon_{xx,2}$	$\Delta\epsilon_{xy,2}$	$\Delta\epsilon_{yy,2}$	$\Delta\epsilon_{eq,1}^*$	$\Delta\epsilon_{eq,2}^*$	$\Delta\epsilon_{eq,1/2, FEM}^*$
-	B7VA2_2	32.8	0.00	29.04	0.00	0	0	6.68	0	0	5.25	7.77	6.09	-
-	B7VA2_3	-	0.00	-	0.00	-	-	-	-	-	-	-	-	-
55	C7VA1_2	35.85	4.06	31.82	3.53	0	6.92	18.37	0	5.02	13.49	22.72	16.64	-
-	C7VA1_3	36.05	4.05	31.27	3.56	-	-	-	-	-	-	-	-	-
56	C7VA1_4	36.21	4.05	31.37	3.55	0	5.2	13.48	0	3.95	10.41	17.33	13.36	-
57	C7VA2_1	36.17	4.04	31.45	3.54	0	5.01	14.14	0	3.73	10.77	17.04	12.99	-
58	C7VA2_2	35.69	4.06	31.52	3.56	0	4.33	9.94	0	3.36	7.52	13.1	9.89	-
59	C7VA2_3	36.05	4.05	31.36	3.55	0	5.14	18.5	0	3.66	13.08	21.73	15.29	-
60	D7VA1_1	32.08	5.55	23.35	4.04	0	8.19	16.68	0	5.6	10.56	21.02	13.63	-
61	D7VA1_2	32.17	5.55	23.08	4.05	0	9.93	16.85	0	6.62	9.33	22.12	12.71	-
62	D7VA1_3	32.38	5.56	23.49	4.04	2.8	7.19	10.56	1.86	4.78	6.63	16.44	10	-
63	D7VA2_1	32.38	5.54	23.25	4.04	0	6.58	13.96	0	4.1	7.12	17.21	9.21	-
-	D7VA2_2	32.15	5.56	23.47	4.04	-	-	-	-	-	-	-	-	-
64	D7VA2_3	32.27	5.55	23.44	4.04	1.76	9.25	14.47	0.95	5.84	7.47	19.23	10.58	-

$\delta$  - mm ;  $\theta$  - Deg ;  $\epsilon$  - %

Table E.3 – Summary of tube to plate variable amplitude test results - part 2

#	Specimen	$N_{init}$	$N_1$	$N_2$	$N_f$	$N_{ave,1}$	$N_{ave,2}$	FZ in DIC	Paint Ok?	$a$	$\psi$
46	A7VA1_1	15	8	7	15	3	3	No	Yes	3.92	17.08
47	A7VA1_2	12	6	6	12	3	3	No	Yes	3.11	14.62
48	A7VA1_3	19	9	10	19	1	2	No	Yes	3.91	18.94

$a$  - mm ;  $\psi$  - Deg ; Continued on next page

#	Specimen	$N_{init}$	$N_1$	$N_2$	$N_f$	$N_{ave,1}$	$N_{ave,2}$	FZ in DIC	Paint Ok?	$a$	$\psi$
49	A7VA2_1	16	9	8	17	3	3	No	Yes	2.87	18.54
50	A7VA2_2	12	6	8	14	4	6	No	Yes	3.55	14.82
-	A7VA2_3	4	6	5	11	0	0	No	No quality	4.29	21.08
51	B7VA1_1	34	17	17	34	4	4	No	Yes	4.12	22.58
52	B7VA1_2	4	9	9	18	3	3	Yes	Yes	4.50	21.45
53	B7VA1_3	6	10	11	21	3	3	Yes	Yes	4.91	23.88
54	B7VA2_1	9	9	9	18	4	6	Yes	Yes	4.14	22.19
-	B7VA2_2	12	11	12	23	4	6	No	No quality	3.76	20.30
-	B7VA2_3	-	-	-	-	-	-	-	No quality	3.53	16.30
55	C7VA1_2	1	4	4	8	1	1	Yes	Yes	4.86	21.16
-	C7VA1_3	1	4	4	8	0	0	Yes	No quality	4.56	22.01
56	C7VA1_4	2	7	6	13	2	2	Yes	Yes	3.95	23.11
57	C7VA2_1	5	5	6	11	1	3	Yes	Yes	2.68	15.66
58	C7VA2_2	2	3	5	8	2	3	No	Yes	4.05	20.87
59	C7VA2_3	3	5	6	11	1	4	Yes	Yes	4.78	20.28
60	D7VA1_1	3	3	3	6	1	1	No	Yes	4.25	20.66
61	D7VA1_2	2	4	4	8	1	1	Yes	Yes	3.91	22.19
62	D7VA1_3	2	6	7	13	3	3	Yes	Yes	2.74	18.61
63	D7VA2_1	4	4	3	7	3	3	No	Yes	4.08	21.12
-	D7VA2_2	3	4	3	7	0	0	No	No quality	4.60	22.98
64	D7VA2_3	4	5	6	11	2	3	No	Yes	2.95	12.89

$a$  - mm ;  $\psi$  - Deg



# Bibliography

- [Argon and Im, 1975] Argon, A. and Im, J. (1975). Separation of Second Phase Particles in Spheroidized 1045 Steel, Cu-0.6pct Cr Alloy, and Maraging Steel in Plastic Straining. *Metallurgical Transactions*, 6A.
- [Armstrong and Fredrick, 1966] Armstrong, P. and Fredrick, C. (1966). A Mathematical Representation of the Multiaxial Bauschinger Effect - Report RD/B/N 731. Technical report, Central Electricity Generating Board.
- [ASM International, 1996] ASM International (1996). *ASM Handbook Vol. 19 - Fatigue and Fracture*.
- [ASTM, 2013a] ASTM (2013a). E45-13: Standard Test Methods for Determining the Inclusion Content of Steel.
- [ASTM, 2013b] ASTM (2013b). E8/E8M - 13a - Standard Test Methods for Tension Testing of Metallic Materials 1.
- [Bao and Wierzbicki, 2004] Bao, Y. and Wierzbicki, T. (2004). On fracture locus in the equivalent strain and stress triaxiality space. *International Journal of Mechanical Sciences*, 46(1):81–98.
- [Baptista, 2016] Baptista, C. (2016). *Multiaxial and variable amplitude fatigue in steel bridges*. PhD thesis, Ecole Polytechnique Federale de Lausanne.
- [Barsoum and Faleskog, 2007] Barsoum, I. and Faleskog, J. (2007). Rupture mechanisms in combined tension and shear—Experiments. *International Journal of Solids and Structures*, 44(6):1768–1786.
- [Barsoum et al., 2012] Barsoum, I., Faleskog, J., and Pingle, S. (2012). The effect of stress state on ductility in the moderate stress triaxiality regime of medium and high strength steels. *International Journal of Mechanical Sciences*, pages 203–212.

## Bibliography

---

- [Becker and Shipley, 2002] Becker, W. and Shipley, R., editors (2002). *ASM Handbook Volume 11: Failure Analysis and Prevention*. ASM International.
- [Benzerga, 2000] Benzerga, A. A. (2000). *Rupture ductile des tôles anisotropes*. Phd thesis, École Nationale Supérieure des Mines de Paris.
- [Benzerga, 2002] Benzerga, A. A. (2002). Micromechanics of coalescence in ductile fracture. *Journal of Mechanics and Physics of Solids*, 50(6):1331–1362.
- [Benzerga and Leblond, 2010] Benzerga, A. A. and Leblond, J.-b. (2010). Ductile Fracture by Void Growth to Coalescence. *Advances in Applied Mechanics*, 1(44):169–305.
- [Besson and Guillemer-Neel, 2003] Besson, J. and Guillemer-Neel, C. (2003). An extension of the Green and Gurson models to kinematic hardening. *Mechanics of Materials*, 35(1-2):1–18.
- [Bhate et al., 2012] Bhate, D., Mysore, K., and Subbarayan, G. (2012). An Information Theoretic Argument on the Form of Damage Accumulation in Solids. *Mechanics of Advanced Materials and Structures*, 19(1-3):184–195.
- [Boyd and Vandenberghe, 2004] Boyd, S. and Vandenberghe, L. (2004). *Convex optimization*. Cambridge University Press.
- [Chaboche et al., 1979] Chaboche, J., Dang Van, K., and Codier, G. (1979). Modelization of the Strain Memory Effect on the Cyclic Hardening of 316 Stainless Steel. In *Structural mechanics in reactor technology - SMiRT 5*, page L11.
- [Chu and Needleman, 1980] Chu, C. C. and Needleman, a. (1980). Void nucleation effects in biaxially stretched sheets. *Journal of Engineering Materials and Technology*, 102(3):249.
- [Coffin, 1954] Coffin, L. F. J. (1954). A study of the effect of cyclic thermal stresses on a ductile metal. *Trans. ASME*, 76:931–950.
- [Cooke and Kanvinde, 2015] Cooke, R. J. and Kanvinde, a. M. (2015). Constitutive parameter calibration for structural steel: Non-uniqueness and loss of accuracy. *Journal of Constructional Steel Research*, 114:394–404.
- [Cortes et al., 2011] Cortes, G., Nussbaumer, A., Berger, C., and Lattion, E. (2011). Experimental determination of the rotational capacity of wall-to-base connections in storage tanks. *Journal of Constructional Steel Research*, (67):1174–1184.
- [Danas and Castaneda, 2012] Danas, K. and Castaneda, P. P. (2012). Influence of the Lode parameter and the stress triaxiality on the failure of elasto-plastic porous materials. *International Journal of Solids and Structures*, 49(1112):1325–1342.



- [Dassault Systèmes, 2011] Dassault Systèmes (2011). Abaqus Standard and Abaqus Documentation for version 6.11-2.
- [de Castro e Sousa and Nussbaumer, 2015] de Castro e Sousa, A. and Nussbaumer, A. (2015). The influence of weld geometry on plastic strain history in cyclic loading – a parametric study. In *2015 International Conference on Steel and Composite Structures, Incheon, South Korea, August 25-29, 2015*.
- [de Castro e Sousa and Nussbaumer, 2017] de Castro e Sousa, A. and Nussbaumer, A. (2017). Ultra low cycle fatigue of welded steel joints under multiaxial loading - extended test data and analysis, EPFL-Report-225939. Technical report, École polytechnique fédérale de Lausanne.
- [Devaux et al., 1997] Devaux, J., Gologanu, M., Leblond, J.-b., and Perrin, G. (1997). On continued void growth in ductile metals subjected to cyclic loadings. In Willis, J., editor, *IUTAM Symposium on Nonlinear Analysis of Fracture*, number 2, pages 299–310. Kluwer Academic Publishers.
- [Dunand and Mohr, 2011] Dunand, M. and Mohr, D. (2011). Optimized butterfly specimen for the fracture testing of sheet materials under combined normal and shear loading. *Engineering Fracture Mechanics*, 78(17):2919–2934.
- [European Committee for Standardization, 2005] European Committee for Standardization (2005). Eurocode 3: Design of Steel Structures - Part 1-9 Fatigue.
- [European Committee for Standardization, 2006a] European Committee for Standardization (2006a). EN10210-1: Hot finished structural hollow sections of non-alloy and fine grain steels - Part 1: Technical delivery conditions.
- [European Committee for Standardization, 2006b] European Committee for Standardization (2006b). Eurocode 8 - Design of structures for earthquake resistance - Part 4: Silos, tanks and pipelines.
- [European Committee for Standardization, 2007] European Committee for Standardization (2007). Eurocode 3 - Design of steel structures - Part 1-6: Strength and Stability of Shell Structures.
- [European Committee for Standardization, 2009] European Committee for Standardization (2009). EN 10025-6:2004+A1 - Hot rolled products of structural steels - Part 6 Technical delivery conditions for flat products of high yield strength structural steels in the quenched and tempered condition.

## Bibliography

---

- [Faleskog and Barsoum, 2013] Faleskog, J. and Barsoum, I. (2013). Tension–torsion fracture experiments—Part I: Experiments and a procedure to evaluate the equivalent plastic strain. *International Journal of Solids and Structures*, 50(25-26):4241–4257.
- [Fatemi and Socie, 1988] Fatemi, A. and Socie, D. F. (1988). A critical plane approach to multiaxial fatigue damage including out-of-phase loading. *Fatigue and fracture of engineering materials & structures*, 11:149–165.
- [Fell et al., 2008] Fell, B. V., Kanvinde, A. M., and Deierlein, G. G. (2008). Large-scale testing and simulation of earthquake-induced ultra low cycle fatigue in bracing members subjected to cyclic inelastic buckling. (172).
- [Garud, 1981] Garud, Y. (1981). A New Approach to the Evaluation of Fatigue Under Multiaxial Loadings. *Journal of engineering materials and technology*, 103(2):118–125.
- [Gilles et al., 1992] Gilles, P., Jullien, B., and Mottet, G. (1992). Analysis of cyclic effects on ductile tearing strength by a local approach of fracture. In *Advances in Fracture/Damage Models for the Analysis of Engineering Problems*, volume 137, pages 269–284. ASME Publication AMD.
- [Gologanu, 1997] Gologanu, M. (1997). *Etude de quelques problèmes de rupture ductile des métaux*. Phd thesis, Université Paris 6.
- [Gologanu et al., 1994] Gologanu, M., Deveau, J., and Leblond, J.-B. (1994). Approximate Models for Ductile Metals Containing Nonspherical Voids — Case of Axisymmetric Oblate Ellipsoidal Cavities. *Journal of Engineering Materials and Technology*, 116(3):290–297.
- [Gologanu and Leblond, 1993] Gologanu, M. and Leblond, J.-B. (1993). Approximate models for Ductile Metals Containing Non-Spherical voids - Case of Axisymmetric Prolate Ellipsoidal Cavities. *Journal of Mechanics and Physics of Solids*, 41(11):1723–1754.
- [Gologanu et al., 1997] Gologanu, M., Leblond, J.-b., Perrin, G., and Devaux, J. (1997). Recent Extensions of Gurson’s Model for Porous Ductile Metals. In *Continuum Micromechanics*. Springer Vienna.
- [Gurson, 1975] Gurson, A. (1975). Continuum theory of ductile rupture by void nucleation and growth. Part I. Yield criteria and flow rules for porous ductile media. *Journal of Engineering Materials and Tecnology*, 99:2–15.
- [Hancock and Mackenzie, 1976] Hancock, J. W. and Mackenzie, A. (1976). On the Mechanisms of Ductile Failure in High Strength Steels Subjected to Multi-Axial Stress-States. *Journal of Mechanics and Physics of Solids*, 24:147–169.

- [Hughes and Winget, 1980] Hughes, T. J. R. and Winget, J. (1980). Finite rotation effects in numerical integration of rate constitutive equations arising in large-deformation analysis. *International Journal for Numerical Methods in Engineering*, 15(12):1862–1867.
- [IIW-JWG-XIII-XV, 2013] IIW-JWG-XIII-XV (2013). Recommendations for fatigue design of welded joints and components - XIII-2460-13/XV-1440-13. Technical report, International Institute of Welding - IIW/IIS.
- [Kailasam and Castaneda, 1998] Kailasam, M. and Castaneda, P. (1998). A general constitutive theory for linear and nonlinear particulate media with microstructure evolution. *Journal of the Mechanics and Physics of Solids*, 46(3):427–465.
- [Kanvinde et al., 2007] Kanvinde, A. M., Asce, A. M., Deierlein, G. G., and Asce, F. (2007). Cyclic Void Growth Model to Assess Ductile Fracture Initiation in Structural Steels due to Ultra Low Cycle Fatigue. 133(6):701–712.
- [Kanvinde and Deierlein, 2004] Kanvinde, A. M. and Deierlein, G. G. (2004). *Micromechanical Simulation of Earthquake Induced Fracture in Steel Structures*. Number 145. Blume Center, Stanford University, Stanford, Ca.
- [Kanvinde et al., 2011] Kanvinde, A. M., Grilli, D. A., and Marshall, K. (2011). A Framework for Forensic Examination of Earthquake- Induced Steel Fracture Based on the Field Failures in the 2011 Christchurch Earthquake.
- [Keralavarma and Benzerga, 2010] Keralavarma, S. and Benzerga, A. A. (2010). A constitutive model for plastically anisotropic solids with non-spherical voids. *Journal of the Mechanics and Physics of Solids*, 58(6):874–901.
- [Klingbeil et al., 2016] Klingbeil, D., Svendsen, B., and Reusch, F. (2016). Gurson-based modelling of ductile damage and failure during cyclic loading processes at large deformation. *Engineering Fracture Mechanics*, 160:95–123.
- [Koplik and Needleman, 1988] Koplik, J. and Needleman, A. (1988). Void growth and coalescence in porous plastic solids. *International Journal of Solids and Structures*, 24(8):835–853.
- [Kuroda, 2002] Kuroda, M. (2002). Extremely low cycle fatigue life prediction based on a new cumulative fatigue damage model. *International Journal of Fatigue*, 24(6):699–703.
- [Kweon et al., 2016] Kweon, S., Sagsoy, B., and Benzerga, A. A. (2016). Constitutive relations and their time integration for anisotropic elasto-plastic porous materials. *Comput. Methods Appl. Mech. Engrg.*, 310:495–534.

## Bibliography

---

- [Leblond et al., 1995] Leblond, J.-b., Perrin, G., and Devaux, J. (1995). An improved Gurson-type model for hardenable ductile metals. *European Journal of Mechanics and Solids*, 14(4):499–527.
- [Lubliner, 2008] Lubliner, J. (2008). *Plasticity Theory*. Dover Publications, Minealo, N.Y., U.S.A.
- [Ludwik, 1909] Ludwik, P. (1909). *Elemente der technologischen Mechanik*. Springer-Verlag, Berlin.
- [Madou and Leblond, 2013a] Madou, K. and Leblond, J.-B. (2013a). Numerical studies of porous ductile materials containing arbitrary ellipsoidal voids - I : Yield surfaces of representative cells Numerical studies of porous ductile materials containing arbitrary ellipsoidal voids - I : Yield surfaces of representative c. *European Journal of Mechanics and Solids*.
- [Madou and Leblond, 2013b] Madou, K. and Leblond, J.-B. (2013b). Numerical studies of porous ductile materials containing arbitrary ellipsoidal voids - II : Evolution of the length and orientation of the void axes Numerical studies of porous ductile materials containing arbitrary ellipsoidal voids - II : Evolution of t. *European Journal of Mechanics and Solids*, (April).
- [Manson, 1953] Manson, S. S. (1953). Behaviour of Materials under Conditions of Thermal Stress. Technical report, National Advisory Committee for Aeronautics.
- [Martins et al., 2003] Martins, J. R. R. a., Sturdza, P., and Alonso, J. J. (2003). The complex-step derivative approximation. *ACM Trans. Math. Softw.*, 29(3):245–262.
- [McClintock, 1968] McClintock, F. A. (1968). A Criterion for Ductile Fracture by the Growth of Holes. *Journal of Applied Mechanics*, 35(2):363–371.
- [McGowan et al., 2001] McGowan, D. M., Ambur, D. R., Hanna, T. G., and McNeill, S. R. (2001). Evaluating the Compressive Response of Notched Composite Panels Using Full-Field Displacements. *Journal of Aircraft*, 38(1):122–129.
- [Mear and Hutchinson, 1985] Mear, M. and Hutchinson, J. (1985). Influence of yield surface curvature on flow localization in dilatant plasticity. *Mechanics of Materials*, 4:395–407.
- [Mohr and Henn, 2007] Mohr, D. and Henn, S. (2007). Calibration of Stress-triaxiality Dependent Crack Formation Criteria: A New Hybrid Experimental–Numerical Method. *Experimental Mechanics*, 47(6):805–820.
- [Myers et al., 2009] Myers, A. T., Deierlein, G. G., and Kanvinde, A. M. (2009). Testing and probabilistic simulation of ductile fracture initiation in structural steel components

- and weldments. Technical Report 170, John A. Blume Earthquake Engineering Center, Stanford Univ., Stanford, CA.
- [Myers et al., 2010] Myers, A. T., Kanvinde, A. M., Asce, A. M., Deierlein, G. G., and Asce, M. (2010). Calibration of the SMCS Criterion for Ductile Fracture in Steels : Specimen Size Dependence and Parameter Assessment. (November):1401–1410.
- [Myers et al., 2014] Myers, A. T., Kanvinde, A. M., Deierlein, G. G., and Baker, J. W. (2014). Probabilistic Formulation of the Cyclic Void Growth Model to Predict Ultralow Cycle Fatigue in Structural Steel. *Journal of Engineering Mechanics*, 140.
- [Myers et al., 2005] Myers, A. T., Kanvinde, A. M., and Ibarra, L. (2005). Maximum Likelihood based Parameter Estimation of Constitutive Models for Earthquake Engineering cyclic simulation. (1):1–6.
- [Nahshon and Hutchinson, 2008] Nahshon, K. and Hutchinson, J. (2008). Modification of the Gurson Model for shear failure. *European Journal of Mechanics and Solids*, 27(1):1–17.
- [Niemi et al., 2006] Niemi, E., Fricke, W., and Maddox, S. (2006). *Fatigue Analysis of Welded Components - Designer's Guide to the Structural Hot-Spot Stress Approach*. Woodhead Publishing.
- [Nip et al., 2010a] Nip, K. H., Gardner, L., Davies, C., and Elghazouli, A. Y. (2010a). Extremely low cycle fatigue tests on structural carbon steel and stainless steel. *Journal of Constructional Steel Research*, 66(1):96–110.
- [Nip et al., 2010b] Nip, K. H., Gardner, L., and Elghazouli, A. Y. (2010b). Cyclic testing and numerical modelling of carbon steel and stainless steel tubular bracing members. *Engineering Structures*, 32(2):424–441.
- [NZSEE, 2009] NZSEE (2009). Seismic Design of Storage Tanks.
- [Oliphant, 2007] Oliphant, T. E. (2007). Python for Scientific Computing. *Computing in Science & Engineering*, 9(3).
- [Pérez and Granger, 2007] Pérez, F. and Granger, B. E. (2007). IPython: A System for Interactive Scientific Computing. *Computing in Science & Engineering*, 9(3).
- [Pineau et al., 2016] Pineau, a., Benzerga, a. a., and Pardoën, T. (2016). Failure of metals I: Brittle and ductile fracture. *Acta Materialia*, 107:424–483.
- [Prinz and Nussbaumer, 2012a] Prinz, G. S. and Nussbaumer, A. (2012a). Fatigue analysis of liquid-storage tank shell-to-base connections under multi-axial loading. *Engineering Structures*, 40:75–82.

## Bibliography

---

- [Prinz and Nussbaumer, 2012b] Prinz, G. S. and Nussbaumer, A. (2012b). On the low-cycle fatigue capacity of unanchored steel liquid storage tank shell-to-base connections. *Bulletin of Earthquake Engineering*.
- [Radaaj et al., 2006] Radaaj, D., Sonsino, C., and Fricke, W. (2006). *Fatigue Assessment of Welded Joints by Local Approaches*. Woodhead Publishing.
- [Raphael and Smith, 2003] Raphael, B. and Smith, I. F. C. (2003). A direct stochastic algorithm for global search. *Applied Mathematics and Computation*, 146(2-3):729–758.
- [Rice and Tracey, 1969] Rice, J. and Tracey, D. (1969). On the ductile enlargement of voids in triaxial stress fields. *Journal of the Mechanics and Physics of Solids*, 17:201–217.
- [Schreier et al., 2009] Schreier, H., Orteu, J.-J., and Sutton, M. A. (2009). *Image Correlation Shape, Motion and deformation Measurements*. Springer US.
- [Simo and Hughes, 1998] Simo, J. C. and Hughes, T. J. R. (1998). *Computational inelasticity*. Springer-Verlag, New York.
- [Smith et al., 2014] Smith, C. M., Deierlein, G. G., and Kanvinde, A. M. (2014). *A Stress-Weighted Damage Model for ductile fracture initiation in structural steel under cyclic loading and generalized stress states*. Number December. Blume Center, Stanford University, Stanford, Ca.
- [Socie and Marquis, 1999] Socie, D. and Marquis, G. (1999). *Multiaxial Fatigue*. SAE International.
- [Tateishi et al., 2007] Tateishi, K., Hanji, T., and Minami, K. (2007). A prediction model for extremely low cycle fatigue strength of structural steel. *International Journal of Fatigue*, 29(5):887–896.
- [Thomason, 1985] Thomason, P. (1985). Three-dimensional models for the plastic limit-loads at incipient failure of the intervoid matrix in ductile porous solids. *Acta Metallurgica*, 33(6):1079–1085.
- [Torki et al., 2015] Torki, M. E., Benzerga, A. A., and Leblond, J.-B. (2015). On Void Coalescence Under Combined Tension and Shear. *Journal of Applied Mechanics*, 82(7):071005.
- [Tvergaard, 1982] Tvergaard, V. (1982). On localization in ductile materials containing spherical voids. *International Journal of Fracture*, 18(4):237–252.
- [Tvergaard, 1990] Tvergaard, V. (1990). Material Failure by Void Growth to Coalescence. *Advances in Applied Mechanics*, 27.

- [Tvergaard and Needleman, 1984] Tvergaard, V. and Needleman, A. (1984). Analysis of the Cup Cone Fracture in a Round Tensile Bar. *Acta Materialia*, 32(1):157–169.
- [Vassilaros et al., 1980] Vassilaros, M., Joyce, J., and Gudas, J. (1980). Effects of specimen geometry on the Ji-R curve for ASTM A533B steel. *Astm Stp 700*, pages 251–270.
- [Wirsching, 1984] Wirsching, P. H. (1984). Fatigue reliability for offshore structures. *Journal of structural engineering*, 110(10):2340–2356.
- [Xiao et al., 2006] Xiao, H., Bruhns, O. T., and Meyers, A. (2006). Elastoplasticity beyond small deformations. *Acta Mechanica*, 182(1-2):31–111.
- [Xiao and Yamada, 2004] Xiao, Z.-G. and Yamada, K. (2004). A method of determining geometric stress for fatigue strength evaluation of steel welded joints. *International Journal of Fatigue*, 26:1277–1293.
- [Xue, 2008] Xue, L. (2008). A unified expression for low cycle fatigue and extremely low cycle fatigue and its implication for monotonic loading. *International Journal of Fatigue*, 30(10-11):1691–1698.
- [Yokobori et al., 1965] Yokobori, T., Yamanouchi, H., and Yamamoto, S. (1965). Low-cycle fatigue of thin-walled hollow cylindrical specimens of mild steel in uniaxial and torsional tests at constant strain amplitude. *International journal of fracture mechanics*, 1(1):3–13.
- [Zhou et al., 2012] Zhou, H., Wang, Y., Shi, Y., Xiong, J., and Yang, L. (2012). Extremely low cycle fatigue prediction of steel beam-to-column connection by using a micro-mechanics based fracture model. *International Journal of Fatigue*, 48:90–100.
- [Zhou et al., 2014] Zhou, H., Wang, Y., Yang, L., and Shi, Y. (2014). Seismic low-cycle fatigue evaluation of welded beam-to-column connections in steel moment frames through global-local analysis. *International Journal of Fatigue*, 64:97–113.





# Glossary

## A

macroscopic backstress tensor. 32, 90

$a$

weld thickness as defined in Fig. 4.6. 69

$\alpha$

microscopic backstress tensor. 15

$\alpha_1$

parameter defined by the geometry of a spheroidal void in the GLD model given in Appendix A. 26

$\alpha_1^G$

parameter defined by the geometry of a spheroidal void in the GLD model given in Appendix A. 26

$\alpha_2$

parameter defined by the geometry of a spheroidal void in the GLD model given in Appendix A. 24

$\mathcal{B}$

set defining the volume of a body. 9

$C_{eq}^{AWS}$

Equivalent carbon content as defined by the American Welding Society. 42

$C_{eq}^{IIW}$

Equivalent carbon content as defined by the International Institute of Welding. 42

## Glossary

---

$C$

parameter defined by the geometry of a spheroidal void in the GLD model given in Appendix A. 24

$\chi$

equivalent plastic strain proportionality coefficient associated with the plastic multiplier  $\lambda$ , given by Eq. 5.18. 92

$\chi_{inc}$

ligament size ratio as measured by the inclusion diameter divided by its corresponding nearest neighbor distance. 40, 106

$\chi_{TBL}$

inter-void ligament ratio in the TBL model. 28

$C_{\sigma}^{DN}$

axial elastic compliance in double notch tubular specimens. 54

$\mathcal{C}$

fourth-order elastic stiffness tensor. 13

$C_{\tau}^{DN}$

torsional elastic compliance in double notch tubular specimens. 54

$D$

damage according to Palmgren-Miner's rule. 85

$\delta^{DN}$

difference in the displacement (*w.r.t.* to undeformed configuration) between the average of two section above and below the notch for double notch specimens - see Fig. 3.17. At failure a subscript  $f$  is added.. 52

$\delta_f^{DN, machine}$

displacement at failure as measured at the machine level in double notch tubular specimens. 51

$\delta$

the displacement of the bending actuator minus the average displacement of the two vertical displacement sensors (to account for slipping) and the 3.4mm maximum clearance in the spherical mount, in welded tube to plate tests. 73

$D_{inc}$

inclusion diameter. 39, 41

$\delta_n^{DN}$

displacement over the notch in double notch tubular specimens, *i.e.* component from elastic displacement over the unnotched area between the gauge length is removed. 54

$\delta_n^{p,DN}$

plastic part displacement over the notch in double notch tubular specimens. 54

**d**

microscopic spatial rate of deformation tensor. 11

$DROT$

incremental rotation tensor as supplied by Abaqus Standard. 97

$\delta^{SN}$

difference in displacement between current and undeformed position of DIC upper and lower sights in single notched specimens. At failure a subscript  $f$  is added.. 167

$\varepsilon$

uniaxial microscopic logarithmic strain. 37

$\varepsilon_{eq}^p$

equivalent plastic strain. 15

$\Delta L/L_0$

Elongation to fracture. L stands for the length between two DIC targets - in single notched specimens this corresponds to  $h^{SN}$ . 36

$E_{mod}$

Young's modulus. 36

$\eta$

parameter defined by the geometry of a spheroidal void in the GLD model given in Appendix A. 24

$\eta_f^{cyclic}$

void growth index at fracture in cyclic loading. 30

## Glossary

---

$\eta_f^{mon}$

void growth index at fracture in monotonic loading. 29

$\eta_v$

angle between the principal axis of void from the initial to the deformed configuration:

$$\eta_v = \arccos \mathbf{n}_{3,0} \cdot \mathbf{n}_3 / (\|\mathbf{n}_{3,0}\|_2 \|\mathbf{n}_3\|_2). \quad 115$$

$\bar{\varepsilon}_f$

uniaxial round bar logarithmic strain given by  $2 \ln D_0/D_f$ , where  $D_0$  is the initial diameter and  $D_f$  the diameter after failure. 36

$f_0^{AIP}$

initial void volume fraction estimated from inclusion content through Automatic Image Processing. 39

$F^{DN}$

axial force in double notched specimens. 53

**F**

deformation gradient. 10

$f$

void volume fraction or porosity defined by the ratio of void volume to the total volume of an RVE. 23

**f**

relative deformation gradient. 11

$g$

parameter defined by the geometry of a spheroidal void in the GLD model given in Appendix A. 24

$h^{DN}$

difference between upper and lower sections in stereo correlated DIC for doubled notched specimens. Equal to 7.5mm centered at the notched height. 52, 53, 113

$h_n^{DN}$

notch height in double notched specimens. 51

$h^{SN}$

difference between upper and lower DIC sights in single notched specimens. 43, 44, 168

$H^{TBL}$

half the height of the cylindrical RVE in the TBL model. 27

$h^{TBL}$

half the height of the cylindrical void in the TBL model. 27

$K$

linear coefficient for isotropic hardening power law. 36

$K_\delta$

stiffness of the support in tube to plate global model associated with bending moment. 125, 127

$k^{DN}$

ratio between average axial stress and the shear stress at the notch in double notched specimens. 54

$k$

parameter defined by the geometry of a spheroidal void in the GLD model given in Appendix A. 24

$k_T^{DN}$

bounded ratio between average axial stress and the shear stress at the notch in double notched specimens. 54

$K_\theta$

stiffness of the support in tube to plate global model associated with bending moment. 125, 130

$\lambda_D$

parameter describing the rate of exponential decay in ULCF resistance under the cyclic void growth model. 30

$\Lambda$

general rigid body rotation. 12

$\lambda$

plastic multiplier. 15

## Glossary

---

$L_{nn}$

distance of an inclusion to its nearest neighbor. 40

$L$

Lode parameter. 20

$\mathbf{L}$

spatial velocity tensor. 11

$l^*$

material characteristic length. 30, 129, 139

$L^{TBL}$

radius of the cylindrical RVE in the TBL model. 27

$\frac{\Delta \epsilon^p}{2}$

plastic strain amplitude in M-C expression. 28

$M_t^{DN}$

torque in double notched specimens. 53

$n$

exponent for isotropic hardening power law. 36

$N_{ave}$

number of cycles over which the DIC measurements are averaged in welded tube-to-plate tests. 83, 131

$N_f$

number of cycles to failure. 28, 79

$N_{init}$

number of cycles to which a crack was detected in DIC system (approximately 0.1mm surface opening). 79

$\Omega$

rotation rate tensor. 12

$P^{DN}$

load path ratio as defined by Eq. 3.3. 51

$\varphi$

mapping function between point  $\mathbf{X}$  in the undeformed configuration and  $\mathbf{x}$  in the deformed configuration. 10

$\psi$

weld angle *w.r.t.* to tube as defined in Fig. 4.6. 69

$R_{ext}^{DN}$

radius of the double notch tube from axis of revolution to the external part of the wall. 51

$\rho$

parameter between 0 and 1 that weighs the amount of isotropic and kinematic hardening. 32

$\rho^{DN}$

load path ratio as defined by Eq. 3.3. 51

$R_{int}^{DN}$

radius of the double notch tube from axis of revolution to the internal part of the wall. 51

$R_m^{DN}$

radius of the double notch tube from axis of revolution to the mid-thickness of the wall. 51

$R_n^{DN}$

radius of internal and external notch in double notched specimens. 51

$\mathbf{R}$

rigid body rotation tensor from the polar decomposition of  $\mathbf{F}$ . 11

$R^{TBL}$

radius of the cylindrical void in the TBL model. 27

$\sigma$

uniaxial microscopic Cauchy stress also know as true stress. 37

$\sigma_n^{DN}$

average axial stress at the notch in double notched specimens. 54

## Glossary

---

$\sigma_h$

hydrostatic stress. 21

$\boldsymbol{\sigma}'$

deviatoric stress tensor, where the apostrophe implies  $\mathbf{S}' = \mathbf{S} - \frac{1}{3}S_{kk}\mathbf{I}$ . 14

$\sigma_{vm}$

Von Mises stress. 14

$\boldsymbol{\Sigma}^v$

stress tensor expressed in the void's frame of reference. 28

$\sigma_u$

Microscopic ultimate stress - maximum Cauchy stress measured in uniaxial round bar tensile test *i.e.* up to necking. 36

$\sigma_y$

Microscopic yield stress. 14, 36

$\tau_n^{DN}$

average shear stress at the notch in double notched specimens. 54

$t^{DN}$

thickness of double notch tube. 51

$\theta^{DN}$

difference in the rotation (*w.r.t.* to undeformed configuration) between the average of 200 points along two horizontal lines on the surface of double notch specimens above and below the notch - see Fig. 3.17 and 3.19. At failure a subscript  $f$  is added. 53

$\theta_f^{DN, machine}$

rotation at failure as measured at the machine level in double notch tubular specimens. 51

$\theta_{sec}^{DN}$

rotation (*w.r.t.* to undeformed configuration) of a point on the surface of a double notch specimens - see Fig. 3.17, 3.18 and 3.19. At failure a subscript  $f$  is added. x, 52, 53



$\theta_{ell}$

angle between the horizontal (either T- transverse or S - thickness) and the main axis of an ellipse that approximates the geometry of an inclusion. 39

$\theta_n^{DN}$

rotation over the notch in double notch tubular specimens, *i.e.* component from elastic rotation over the unnotched area between the gauge length is removed. 54

$\theta_n^{p,DN}$

plastic part of the difference in rotation above and below the notch over the gage length in double notch tubular specimens. 54

$\theta$

the difference between the angles measured in the two inclinometers in welded tube to plate tests. 73

$t_n^{DN}$

thickness of the notch in double notch tube. 51

$T$

stress triaxiality. 20

$\Upsilon$

matrix storing the orientation of spheroidal void, where the columns represent the unit vectors of the void's principal directions. 24

$\mathbf{U}$

right stretch tensor from the polar decomposition of  $\mathbf{F}$ . 11

$\varrho$

heuristic factor that scales the rate of change of the aspect ratio of a spheroidal void in the GLD model to distinguish the rate between tension and compression. 95

$\mathbf{V}$

left stretch tensor from the polar decomposition of  $\mathbf{F}$ . 11

$w$

aspect ratio of a spheroidal void, defined as the ratio between the height along the principal axis with the width along one of the other secondary axes.. 24

## Glossary

---

### W

material spin tensor. 11

$w_{TBL}$

aspect ratio of the cylindrical void in the TBL model. 28

### X

can define two quantities depending on the context: 1 - a point belonging to set  $\mathcal{B}$  that in the undeformed configuration; a tensor parameter defined by the geometry of a spheroidal void in the GLD model. 9, 24

### $\Xi$

algorithmic tangent stiffness matrix as defined by Eq.5.11. 91

### $\xi$

vector representing internal variable storage in the UMAT. 97

### x

point belonging to set  $\mathcal{B}$  that in the deformed configuration. 9

# Acronyms

## **AIP**

Automatic Image Processing. 39

## **AR**

Aspect Ratio. 39

## **BM**

Base Material. 38

## **CA**

Constant Amplitude. 52

## **CAD**

Computer-Aided Design. 39

## **CT**

Compact Tension. ix, 21, 22

## **DIC**

Digital Image Correlation. 5, 17, 36, 52, 205, 207

## **DN**

Double Notch. 50

## **EDX**

Energy Dispersed X-ray Spectroscopy. 36

## **FEM**

Finite Element Method. 16

## Acronyms

---

### GEV

Generalized Extreme Value. 40, 41

### GLD

Gologanu-Leblond-Devaux. viii, 24, 90, 91, 93, 95, 97

### HAZ

Heat Affected Zone. 30

### KB

Keralavarma-Benzerga. 89, 99

### KKT

Karush-Kuhn-Tucker. 90

### M-C

Manson-Coffin. 3, 28, 29

### PGSL

Probabilistic Global Search Lausanne. 38

### PP

Probability-Probability. 40

### PSO

Particle Swarm Optimization. 38

### RVE

Representative Volume Element(s). 23

### SEM

Scanning Electron Microscope. x, 36, 50

### SN

Single Notch. 43

### TBL

Torki-Benzerga-Leblond. 27, 41, 89

**ULCF**

Ultra Low Cycle Fatigue. 1

**UMAT**

user defined material model. 6

**W**

Weld. 38

**WT**

Weld Toe. 38



# albano de castro e sousa

structural engineer



## contact

albano.sousa@epfl.ch

## nationality

portuguese

## education

- since 2012 **Ph.D. candidate** - civil engineering École Polytechnique Fédérale de Lausanne (EPFL)  
Steel structures laboratory (ICOM) /  
Resilient steel structures laboratory (RESSLAB)  
Thesis: 'Ultra low cycle fatigue of welded steel joints under multiaxial loading'
- 2007–2009 **M.Sc.** - civil engineering Faculty of Engineering of the University of Porto (FEUP)  
Specialized in structural engineering  
Top 10% of the class (Grade A)  
Thesis: 'Aspects on nonlinear geometric and material analysis of three-dimensional framed structures'
- 2004–2007 **B.Sc.** - engineering sciences Faculty of Engineering of the University of Porto (FEUP)  
Civil engineering major

## industry experience

- 2009–2012 **structural engineer** afaconsult, Porto, Portugal  
Assumed primarily the role of designing and detailing reinforced concrete, prestressed concrete, steel and composite steel-concrete structures.

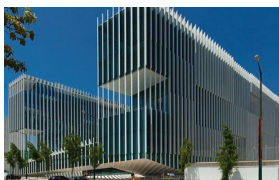
## teaching experience

- 2012–present **teaching assistant** École Polytechnique Fédérale de Lausanne (EPFL)  
In courses: analysis 2; analysis 3; steel structures; conceptual design of bridges; advanced steel design  
Supervised ten bachelor/semester projects and one master thesis

## selected projects



- Souto Moura **Lotto Rd** Milan, Italy  
Residential building by Pritzker laureate Eduardo Souto Moura as part of the Milan Fair requalification area. Involved in the structural design the building as well as coordinating tasks within the structural design group.



- Aires Mateus **EDP headquarters** Lisbon, Portugal  
Main office building for the portuguese power company EDP. Was responsible for the design and detailing of various parts of the building (namely the steel super-structure). The same architects recently won the contest to design the new Elysée/Mudac museums in Lausanne, Switzerland.

## publications

A. de Castro e Sousa, A. Nussbaumer

**Ultra low cycle fatigue of welded steel joints under multiaxial loading**

Proceedings of the the sixth international conference on Structural Engineering, Mechanics and Computation, Cape Town, South Africa, 5th-7th September 2016

A. de Castro e Sousa, A. Nussbaumer

**The influence of weld geometry on plastic strain history in cyclic loading – a parametric study**

Proceedings of the world congress on Advances in Structural Engineering And Mechanics; Incheon, South Korea; 25th-29th August 2015

G.S. Prinz, A. de Castro e Sousa

**Effect of slab stiffness on EBF link rotation demands and implications for ultra low cycle fatigue susceptibility**

Proceedings of the American Society of Civil Engineers Structures Congress; Boston, Massachusetts, U.S.A.; 3rd-5th April 2014

A. de Castro e Sousa, R.C. Barros

**Harmonizing effective length K-Factors between European and American codes of practice**

Integrity Reliability and Failure (Challenges and Opportunities), Editors: JF Silva Gomes and SA Meguid, INEGI editions; Porto, Portugal; 2009

A. de Castro e Sousa, M. Pereira, R.C. Barros

**Stiffness reduction factors for geometric and material nonlinearity of reinforced concrete beams and columns in short term loading**

Proceedings of the Twelfth International Conference on Civil, Structural and Environmental Engineering Computing; Funchal, Madeira, Portugal; 1st-4th September 2009

A. de Castro e Sousa, M. Pereira, R.C. Barros

**Simplified procedure for the assessment of second-order effects in three-dimensional framed structures**

Proceedings of the Twelfth International Conference on Civil, Structural and Environmental Engineering Computing; Funchal, Madeira, Portugal; 1st-4th September 2009



